SolidityONE
Leonardo da Vinci's Aerial Screw

Final Report

Group 3

January 28, 2020

Ensar Aşir
Kenny van Gaalen
Mark van den Ham
SeoungHoun Han
Thijs van Herwerden
Hugo Kerckhoffs
Rembert Kortenhorst
Nick Pauly
Teun Vleming
Rowan de Voogt

Delft University of Technology

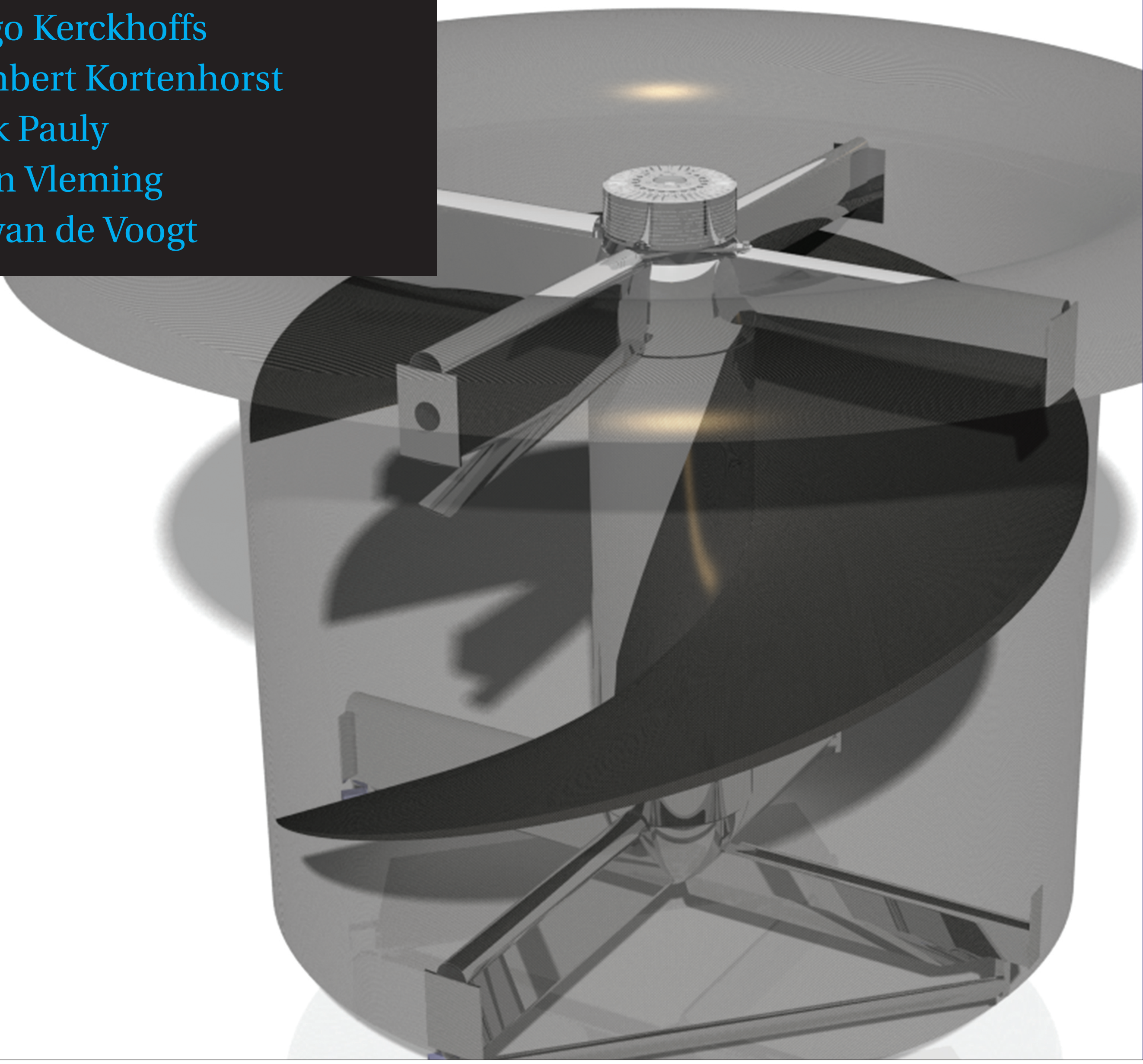

Delft University of Technology

Challenge the future

SolidityONE
Leonardo da Vinci's Aerial Screw

Final Report
Group 3
January 28, 2020

Faculty of Aerospace Engineering
Design Synthesis Exercise AE3200

Submitted in partial fulfillment
of the requirements for achieving
the Degree of
Bachelor of Science

by

Ensar Aşir	4530764
Kenny van Gaalen	4442679
Mark van den Ham	4442768
SeoungHoun Han	1397176
Thijs van Herwerden	4303296
Hugo Kerckhoffs	4433335
Rembert Kortenhorst	4390679
Nick Pauly	4550447
Teun Vleming	4556593
Rowan de Voogt	4544064

Supervised by

Dr. M.D. Pavel	Tutor
Ir. M. Coppola	Coach
Ir. C. Jux	Coach

Version history

Version	Changes	Date
Draft	Initial release	22-01-2020
Final	Final release	28-01-2020

TU Delft Delft University of Technology

Executive overview

This report provides an overview of the considerations and decisions made during the DSE project from the Faculty of Aerospace Engineering, arriving at the final design of the SolidityONE. The goal was to design a vertical take-off and landing vehicle according to the rules from the 37th annual student design competition by the Vertical Flight Society. This design proves the concept of a rotor with disk solidity equal to or larger than 1.0. Additionally, benefits this design has over existing rotorcraft mean it can be tailored to meet the needs of a specific market.

The mission

The designs of rotorcraft have been limited to and by a now standardised set of components: most predominantly the rotor and its controls. What is currently accepted as a rotorcraft, however, is not true to the first concept of manned vertical flight: namely, the aerial screw of Figure 1, as envisioned by Leonardo da Vinci in 1489. Utilising this concept of a new rotor geometry can provide an alternative rotorcraft design that can be sold as a proof of concept to existing manufacturers for new rotorcraft and personal aerial vehicle markets.

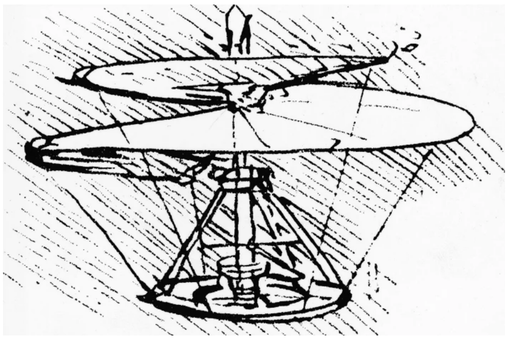

Figure 1: Leonardo da Vinci's aerial screw

To achieve this goal, research must be conducted and new models must be established. From this, the Mission Need Statement (MNS) and Project Objective Statements (POS) were formulated:

Mission Need Statement

Provide an alternative rotor design in the form of an aerial screw for vertical take-off and landing vehicles to overcome limitations such as noise, maintenance and/or safety of current rotorcraft.

Project Objective Statement

To design an aerial screw-inspired vehicle and win the 37th Vertical Flight Society Competition 2019-2020, by ten undergraduate students in ten weeks.

Requirements

After the goal of the project was set, requirements could be established. Following the analysis of the design competition, the mission profile in Figure 2 was created. It consists of take-off and initial climb followed by stationary hover at 1 metre altitude or higher. After hovering at least 5 seconds, the flight continues in forward motion of at least 20 metres distance, and for at least 1 minute. Then another hover at 1 metre for 5 seconds is required, following the descent and landing.

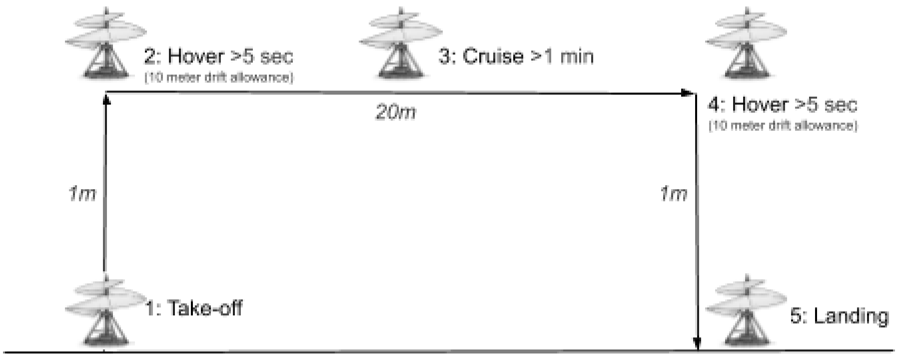

Figure 2: The mission profile

From the mission profile, requirements were determined. Since the design is not only designed for the competition, but also intended to be certified as a rotorcraft, the most current rotorcraft certification specifications have to be met. Two main sources of these specification are the FAR-27 and CS-27 by the American Federal Aviation Administration (FAA) and European Aviation Safety Agency (EASA), respectively. Further requirements based on the sustainability of the design and its life cycle have been created to reduce the carbon footprint and ecological impact. Finally the business aspects such as production and costs have been analysed to ensure a competitive design.

The following list describes the key requirements that have been identified for the success of the mission, where the keys "**Sc-F-Mis-**," "**Sc-F-VFS-**" and "**Sc-F-Sust-**" indicate the requirement origins mission profile, Vertical Flight Society and sustainability, respectively:

Key requirements

Sc-F-Mis-Takeoff *The vehicle shall be able to take-off vertically*
Sc-F-Mis-Hover-1 *The vehicle shall be capable of hover*
Sc-F-Mis-Hover-2 *The vehicle hover shall maintain its horizontal position to 10 m accuracy*
Sc-F-Mis-Cruise1 *The vehicle shall be able to fly at an altitude of at least 1 m*
Sc-F-Mis-Cruise2 *The vehicle shall fly for at least 1 min*
Sc-F-Mis-Cruise3 *The vehicle shall have a range of at least 20 m*
Sc-F-Mis-Landing *The vehicle shall be able to land vertically*
Sc-F-VFS-2 *The vehicle shall carry at least one occupant of 60 kg*
Sc-F-VFS-4 *The vehicle shall rely for its lift and thrust solely on one or more aerial screws*
Sc-C-VFS-5 *The aerial screw shall have a single blade*
Sc-C-VFS-6 *The aerial screw blade shall have continuous surface*
Sc-F-VFS-7 *The aerial screw shall have a blade solidity of at least 1*
Sc-F-VFS-8 *The vehicle shall fly without tethered power*
Sc-N-Sust-Cost-1 *The vehicle shall not cost more than €200,000*

These requirements set a baseline for further description of performance and functional requirements for the flight mission, systems and components.

THE DESIGN

In this section the design is presented and briefly described. Furthermore, the trade-off process and its outcomes are described. A render of the SolidityONE is shown in Figure 3, its rotor construction is shown in Figure 4 and the internal components and construction of the airframe are shown in Figure 5.

Figure 3: The SolidityONE concept

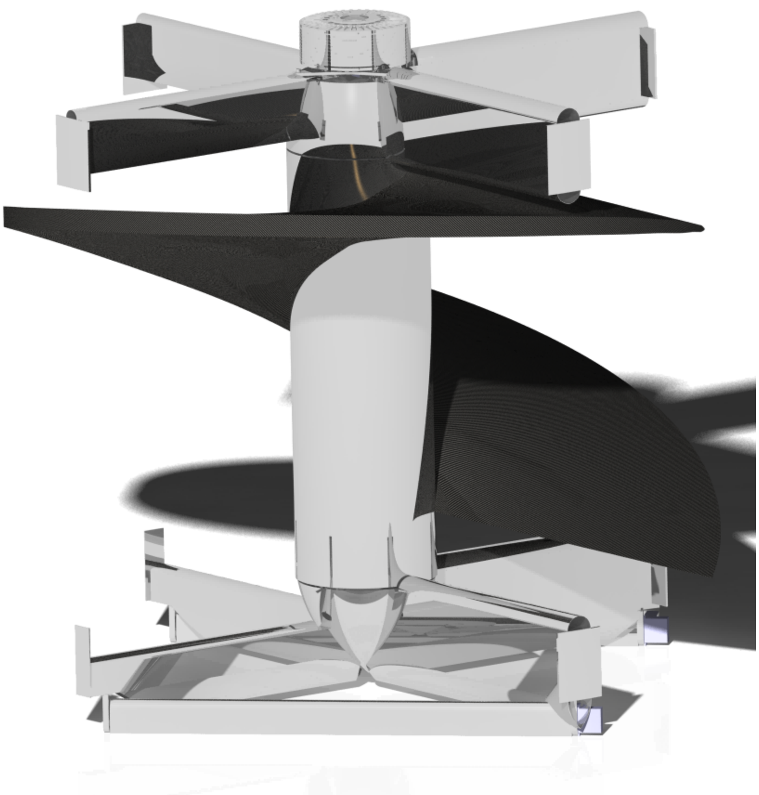

Figure 4: Render of an exposed rotor with supporting struts

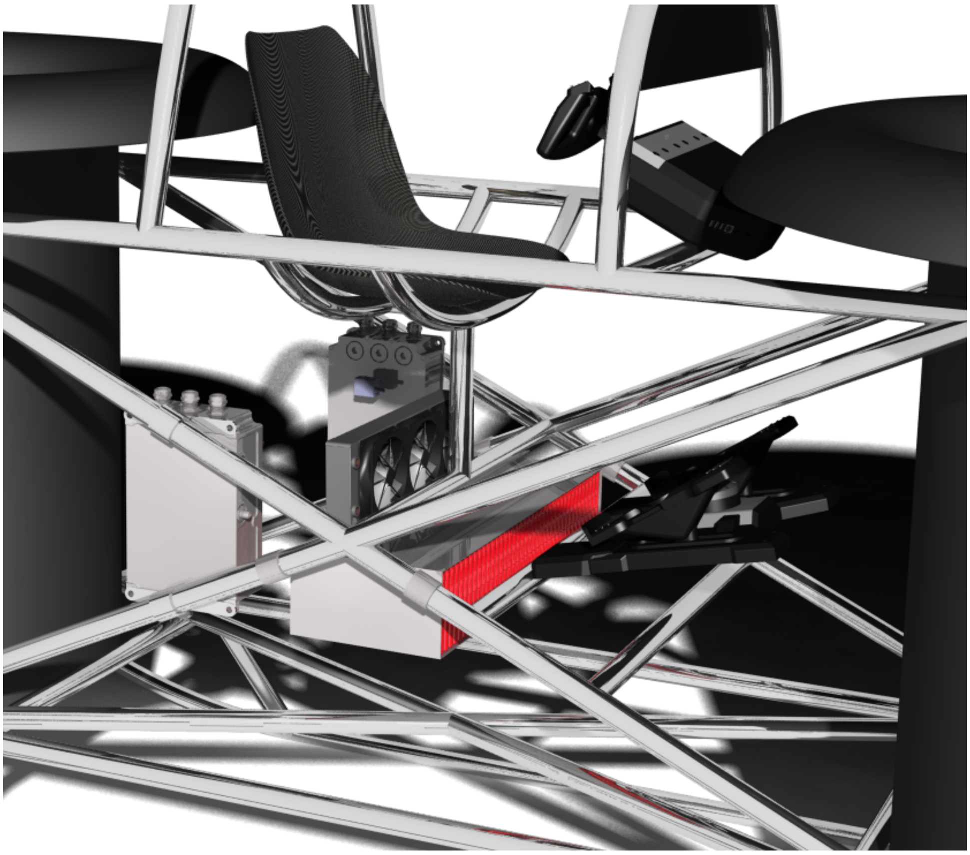

Figure 5: Internals of the airframe

The SolidityONE is shown in Figure 3. It has counter-rotating tandem rotors with a radius of 0.6 metres. The rotors are aerial screws with a pitch of 0.6 metres (the pitch being the height for this rotor design). A modified Blade Element Theory was developed which modelled the rotor as a series of circumferential airfoils which were then analyzed as flat-planar airfoils flying straight. These airfoils are depicted unwrapped in Figure 6 superimposed on a top-view of a 360 degree sweeping aerial screw.

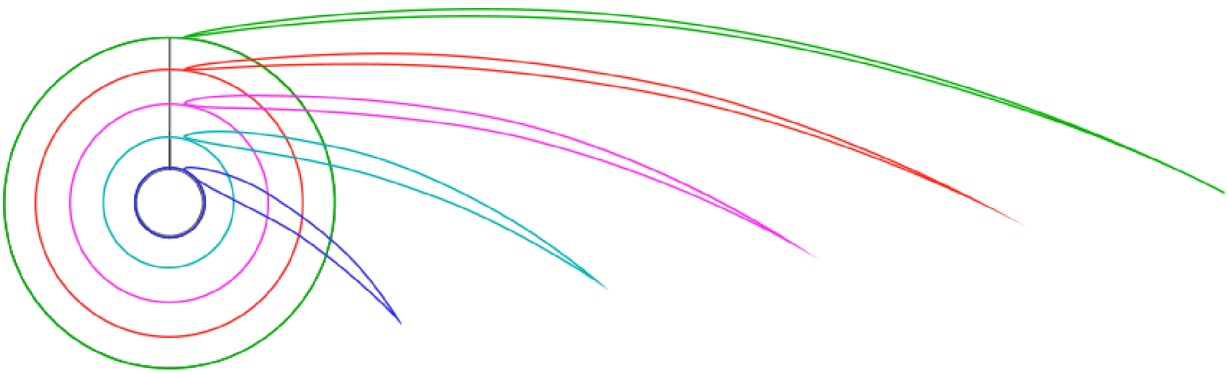

Figure 6: Blade element sections of an aerial screw

Airfoil optimisation with the use of Javafoil resulted in the selection of the NACA 8508 airfoil at the root, reducing in thickness to the NACA 8501 at the tip; where the last two digits indicate the thickness-to-chord ratio of the airfoil [1]. Its rotors are shrouded by a duct for performance enhancement and increased safety of bystanders. For control, the SolidityONE can vary its rotor speeds independently for vertical velocity and controlling the pitch of the full vehicle and has vanes below the ducts for yaw and roll control.

Furthermore, the structure is built predominantly using thin-walled aluminium and carbon fibre-based composite sandwich panels with foam core. Components selected off-the-shelf include the pilot control yoke and pedals, a motor by Emrax and a motor controller by Cascadia Motion. Additionally, a planetary gearbox by Anaheim Automation and battery cells by Sony have been selected. A mass distribution of the vehicle, broken down into payload and the systems is shown in Figure 7.

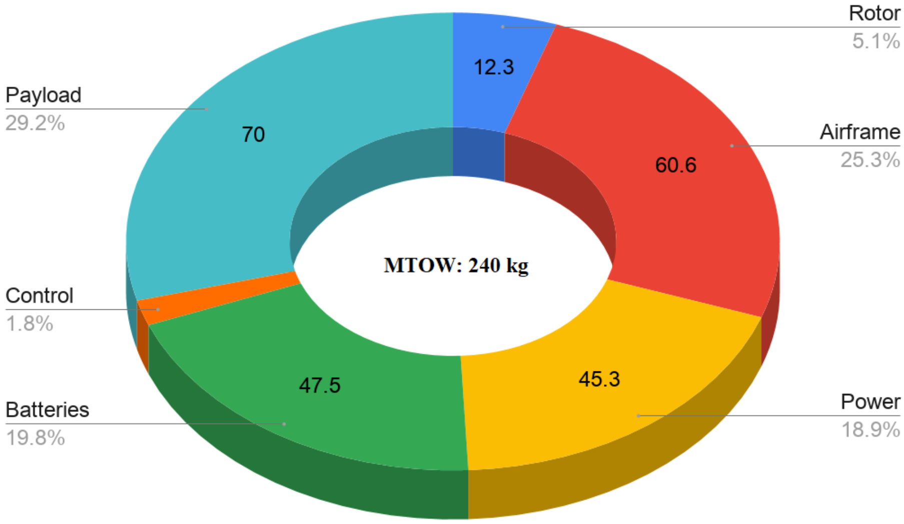

Figure 7: SolidityONE mass distribution

The SolidityONE is able to carry 70 kg, corresponding to a person of 60 kg with personal protection and a small mass contingency and can accelerate in 10 s to a horizontal velocity of 54 km h^{-1}. With this velocity, it can fly for 11 minutes and achieve a range of 10.2 km: greatly exceeding the previously described mission, which is shown in Figure 2. Further, the SolidityONE has an aerodynamic hover ceiling of 3.3 km altitude and climb vertically in 6.5 minutes from sea level to an altitude of 1.6 km and have enough time to descend to the ground. Furthermore, the SolidityONE can perform the mission in Figure 2 with an additional mass of 20 kg.

This design was the best of three concepts analysed, which resulted from a trade-off performed. Other concept configurations included a side-by-side rotor configuration similar to the tandem configuration and a nested co-axial helicopter. The prior was rejected over the tandem configuration predominantly to its lower forward velocity by lacking the differential thrust to maintain the required attitude. The former was rejected due to its additional complexity of design and overall poorer scoring in the trade-off.

Single rotor configurations with conventional anti-torque systems such as a tail rotor or NOTAR were rejected at an early stage due to the limitations in the control scheme. These limitations are the absence of conventional main rotor control in the form of cyclic and collective controls. Additionally, the torque was expected to be too large to counter effectively using a conventional tail-rotor.

Validation throughout development

The design process was validated in multiple ways: most evidently, an experiment was conducted in which the thrust produced on a scale-model aerial screw was measured for different RPMs. This validated the design tool of the aerodynamics of an aerial screw. The other include a noise estimation comparison to existing helicopters and a finite element method-analysis of various structural components in Abaqus: the analysis of the landing gear is displayed in Figure 8, where the U indicates the displacement.

Due to the unique nature of the rotor geometry, new software for the aerodynamic analysis had to be developed. Since statistics do not include this type of design, validation required extra resources. The test setup used for this validation is shown in Figure 9. The parameters analysed were solely the RPM versus thrust for the same geometry, both with and without duct. Though experiencing some vibrations, results could be obtained, which indicated that the software is conservative.

Figure 8: FEM analysis of the landing gear design where the deflected position is upwards

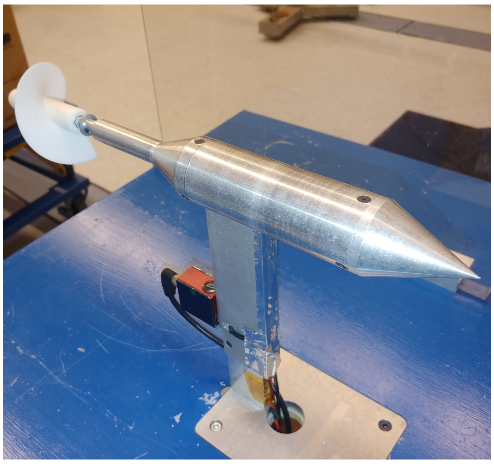

(a) Aerial screw mounted in test setup

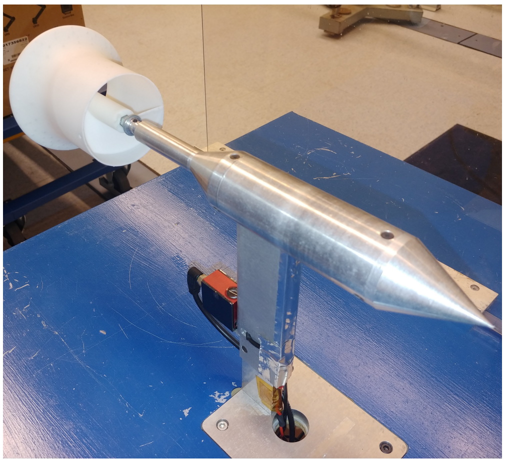

(b) Ducted aerial screw mounted in test setup

Figure 9: Both screws at test setup

In total, 98 requirements had to be met. While designing, the requirements and the functionality of the vehicle were the primary drivers for assumptions and design decisions. As a final check, all requirements are listed and individually explained how they are met.

Market impact

As in this design effort, the characteristics of the vehicle were yet unpredictable, no specific end-user was targeted yet. Instead the goal was to extensively evaluate the characteristics of the aerial screw. The actual target customers are helicopter manufacturers who want to adopt this technology and tailor it to a market of end-users.

The SolidityONE successfully is this small size proof of concept of an aerial screw vehicle. It shows the capability of using an aerial screw for lift generation in vertical take-off and landing vehicles.

In this design effort, expectations are exceeded. The vehicle performs better than expected. Noise reduction currently is an important objective of the helicopter industry and is an aspect on which the SolidityONE performs very well. Also the low rotor radius increases the usability of this type of vehicle. It is expected with confidence that in future development a helicopter manufacturer can tailor this rotor type to markets of end-users requiring either a small or silent vertical take-off and landing vehicle.

Designed for sustainability

Sustainability was considered as a vital component of a good design. Hence the three aspects of sustainability(economical, social and environmental impact) were considered throughout the project. For the economical aspect the project has to be long term profitable. The social aspect focuses on the impact of the product on the society in general. The environmental aspect considered the effect the entire life cycle of the vehicle has on the planet.

Throughout the design process the following measures were taken to result in a sustainable design:

Sustainable design measures

Low Emissions Electric motors were applied to provided the power to the rotor. This had a significant effect on the emissions, which are normally high for a rotorcraft.

Reusable A high degree of recyclable or reusable parts are applied in the design, which are listed in a parts map.

Low noise The rotor was designed to produce a low noise level compared to conventional rotors.

Safe and reliable A good RAMS analysis was made to ensure a safe and reliable design.

Resource management A MAI-plan was made to ensure an efficient production with limited waste of resources.

Bright future ahead

The goal for the VFS competition is to demonstrate the physics and feasibility of a rotor with an aerial screw geometry. Through this design exercise, it is proven that SolidityONE is able to fly. After competing in the VFS competition, the goal is to build a prototype and sell the concept, knowledge and prototype to helicopter manufactures or whom may be interested in production and selling aerial screw inspired vehicles.

The final proposal date of the VFS is due 31^{st} May, 2020. Before then, four action points have been identified that raise the level of detail and overall level of the report:

VFS improvements

FEM analysis and optimisation for total structure The structure is currently an assembly of numerous parts. A simulation of the total structure can lead to a more reliable and lighter design.

Improve control simulation A six degrees of freedom to gain more insights in the behaviour of the vehicle.

Perform additional tests can be used to cross check assumption and come up with factors that relate predicted performance with true performance.

CFD analysis and optimisation for the rotors The blade performance can be verified with the test; optimisation is possible through CFD analysis.

Combining the knowledge of CFD, FEM, control simulation, and tests, a more reliable and a detailed design can be made.

To get to the point where a helicopter manufacturer would be interested in buying the prototype and concept, more steps need to be taken. In chapter 14, manufacturing and the operations are described. Now, a clear planning and strategy is provided. The stages that this project is going to go through are listed below:

Market implementation

Acquire investment Besides man hours, an investment is needed to build the SolidityONE and convince helicopter manufacturers that this concept has a future. An investment of €48.000 has to be made. This is required to build the prototype.

Manufacturing The vehicle shall be designed and assembled at the TU Delft. This will be primarily done at the TU Delft Structures and Manufacturing lab or TU Delft Dreamhall, since the facilities necessary for composite and mechanical manufacturing are all present. The remaining parts are bought off-the-shelf.

Concept demonstration & selling First, companies should be contacted and get excited about this development. In the demonstration & selling phase, demonstrations are held. In this phase, companies should get enchanted by the demonstration and buy the concept and underlying theories for a price of €90.000.

Conclusion

SolidityONE is a vehicle that uses two fully solid aerial screws for propulsion. It was designed according to the VFS competition, as well as aviation regulations. After a trade-off period, a concept was chosen to design. To design the rotors, a custom adaption of Blade Element Momentum Theory was made, since there are no similar rotors in existence. The vehicle is designed with sustainability in mind. This led to the choice for electric motors and recycle-able materials with a low carbon footprint.

The result is a vehicle that flies on battery power. It was concluded that in terms of specific power consumption, this rotor type is less efficient than current state-of-the-art rotors. However, it is quieter than current helicopters. Also safety is improved due to the ducted rotor design, shielding the rotor from the environment. This opens a lot of opportunities in markets where noise is an issue. Further development could make this a successful product.

Acknowledgements

First of all, our team would like to thank Dr. Marilena Pavel, Ir. Constantin Jux and Ir. Mario Coppola for their valuable feedback during our meetings and support throughout our project. Their knowledge on designing, reporting and aerodynamics has been an amazing resource for which this project would not have existed without.

The team would furthermore thank the OSCC and Dr. Ir. Erwin Mooij on teaching and assisting with the system engineering related topics of designing. The feedback received helped the group greatly in effectively tackling the topics of system engineering.

We would also like to thank Gertjan Mulder and Dr. Calvin Rans, who took interest in the project by assisting with producing and testing of a scaled aerial screw; and advice on the structural analysis of the vehicle respectively.

Furthermore, the Vertical flight Society (VFS) for the proposal of the competition which has helped us as a team expand our knowledge on helicopter design.

Nomenclature

Abbreviations

$\vec{DP}$	Design parameter vector
$\vec{PP}$	Performance parameter vector
VFS	Vertical Flight Society
BMS	Battery management system
CFRP	Carbon fiber reinforced polymers
FBS	Functional breakdown structure
FFD	Functional flow diagram
MAI	Manufacturing, assembly and integration plan
PCB	Printed circuit board
RAMS	Reliability, availability, maintainability and safety
RPM	Revolutions per minute

Physics symbols

α	Angle of attack	[rad]
α_{tc}	Resistivity temperature coefficient	[K^{-1}]
ΔT_g	Additional thrust in ground effect	[-]
δ_{tip}	Tip clearance	[m]
η	Efficiency	[-]
$\frac{r}{R}$	Non-dimensional radius	[-]
γ	Flight path angle	[rad]
γ	Lock number	[-]
λ_c	Non-dimensional inflow velocity	[-]
λ_i	Non-dimensional induced velocity	[-]
μ	Preference value, advance ratio	[-]
Ω	Angular velocity	[rad s^{-1}]
ω	Normalized weight value	[-]
ϕ	Local inflow angle	[rad]
ψ	Duct inflow angle	[rad]
ψ	Rotor azimuth angle	[N]
ρ	Air density	[kg m^{-3}]
ρ_{res}	Resistivity	[Ωm]
σ_d	Diffuser expansion ratio	[-]
θ	Rotor blade pitch angle	[rad]
θ_0	Collective pitch angle	[rad]
θ_c	Angle of control plane w.r.t the shaft plane	[rad]
θ_d	Diffuser angle	[rad]
θ_f	Helicopter pitch angle	[rad]
a	Speed of sound	[m/s]
a	acceleration	[$m/2^2$]
C	Battery capacity	[Ah]
c	Rotor blade chord	[m]
C_l	Lift coefficient	[-]
C_M	Moment coefficient	[-]
C_P	Power coefficient	[-]
C_T	Thrust coefficient	[-]
C_{l_α}	Lift gradient	[rad^{-1}]
$C_{l_{max}}$	Maximum lift coefficient	[-]
$C_{P_{OR}}$	Power coefficient of open rotor	[-]
$C_{P_{SR}}$	Power coefficient of shrouded rotor	[-]
c_p	Specific heat	[J $kg^{-1}K^{-1}$]
$C_{T_{OR}}$	Thrust coefficient of open rotor	[-]
$C_{T_{SR}}$	Thrust coefficient of shrouded rotor	[-]
D	Drag	[N]
D_t	Duct inlet diameter	[m]
dD	Blade element drag	[N]
DL	Disc loading	[N m^{-2}]
dL	Blade element lift	[N]
dP	Blade element power	[W]
dQ	Blade element torque	[Nm]
dR	Blade element radial length	[m]
dS	Blade element surface area	[m^2]
dT	Blade element thrust	[N]
f	Frequency	[Hz
f/c	Airfoil camber to chord ratio	[-]

F_a	Force available	[N]
g	Gravitational acceleration	[m s^{-2}]
h	Height	[m]
h	Projected blade thickness	[m]
I	Current	[A]
I_N	Sound intensity of $N^{th} harmonic$	[dB
L	Lift, Length	[N]
L_d	Diffuser length	[m]
M	Mach number	[-]
M	Molar mass	[kg/mol]
M	Moment	[Nm]
m	Mass	[kg]
N	Number	[-]
n	Number of design parameters	[-]
P	Power	[kW]
P	Prandtl tip-loss factor	[-]
p	Rotor geometric pitch	[m]
PL	Power factor	[W N^{-1}]
Q	Torque	[Nm]
q	Number of performance parameters	[-]
q	pitch rate	[rad s^{-1}]
R	Rotor radius	[m]
r	Local radius	[m]
R^*	Universal gas constant	[J/molK]
r_{lip}	Duct inlet lip radius	[m]
ROC	rate of climb	[m/s]
SPL	Sound pressure level	[dB
St	Strouhal number	[-]
T	Temperature, thrust	[K]
$T(\psi)$	Thrust as a function of azimuth angle	[N]
t/c	Airfoil thickness to chord ratio	[-]
U	Voltage	[V]
u	Velocity in the X-Axis	[m s^{-1}]
V	Velocity	[m s^{-1}]
V_t	tip speed	[m s^{-1}]
V_{axial}	Rotor axial air velocity due to flight velocity	[m s^{-1}]
V_{tan}	Rotor tangential air velocity due to flight velocity	[m s^{-1}]
W	Weight	[N]
w	Velocity in the Z-Axis	[m s^{-1}]
X	Parameter value in linear fuzzification	
xf/c	Location of maximum airfoil camber	[-]
xt/c	Location of maximum airfoil thickness	[-]
z	Parameter value in quadratic fuzzification	

Subscripts

$0L$	Zero-lift
∞	Free-stream
al	Aluminium
aux	Auxiliary
avg	Time average
bc	Battery to controller cables
$cell$	Battery cell
cm	Controller to motor cables
esc	Electronic motor controller
gb	Gearbox
H	Horizontal component
i	Induced
$loss$	Loss
max	Maximum
MC	Maximum continuous
mot	Motor
P	Parallel (Electrical)
p	Profile
$rotor$	Rotor
S	Series (Electrical)
$stall$	Stall angle
$tilt$	angle w.r.t. inertial frame

tot	Total
V	Vertical component
0	sea-level condition
acc	Acceleration phase
BEM	According to Blade element theory
c	Control plane
cruise	Cruise phase
dec	Deceleration
f	fuselage
Glau	According to Glauert method
maxf	At never exceed speed
NE	Never exceed

Contents

1

INTRODUCTION

Leonardo da Vinci is considered to be one of the greatest inventors of all time. His designs inspired many modern day inventions. The aerial screw is one of his designs, a vehicle intended to perform vertical landing and take-off (VTOL), which eventually led to the helicopter of today. Although the concept of the aerial screw is as old as 500 years, it has never flown nor has been extensively researched with modern day technology, leaving a knowledge gap in the technical understanding of such a device. In honour of the 500th anniversary of Leonardo da Vinci, the 37th Annual Student Design Competition of the Vertical Flight Society (VFS) will consist of designing such a vertical flight and take-off vehicle, where thrust and lift is solely depended on one or more aerial screws. This design competition will aim to fill this knowledge gap by critically reviewing the feasibility of the aerial screw concept and extracting useful information for modern day applications.

The project objectives are part of designing the vehicle for the 37th VFS student design competition. The VFS competition requires the design of a Leonardo da Vinci-inspired aerial screw vehicle with a blade solidity equal or greater than, with a continuous surface and capable of carrying a pilot of at least 60 kg. The minimum mission profile includes the following; a vertical climb phase up to 1 meter, hovering for 5 seconds within 10 meters, covering 20 meters of distance and fly for at least 60 seconds, repeating the hover phase for 5 seconds and land vertically. The VFS competition is the foundation for this project and thus the mission need statement (MNS) and project objective statements are as follows.

Mission Need Statement

Provide an alternative rotor design in the form of an aerial screw for vertical take-off and landing vehicles to overcome limitations such as noise, maintenance and/or safety of current rotorcraft.

Project Objective Statement

To design an aerial screw-inspired vehicle and win the 37th Vertical Flight Society Competition 2019-2020, by ten undergraduate students in ten weeks.

This report serves as the fourth and final report of the DSE project. It summarises the entire progress of the first half of the DSE, this includes the project plan, baseline report and midterm report and furthermore describes the concluding weeks of the detailed conceptual design phase in full detail. The report is structured as follows; chapter 2 analyses the market in which the application of an aerial screw can be potentially an improvement on existing systems as was earlier described in the DSE project plan [2]. chapter 3 summarises the process performed to generate concepts and eliminate options to arrive at the final concept for the detailed phase of the project. This process is more elaborately described in the baseline report and midterm report [3, 4]. The sustainability development approach will be described in chapter 4. In order to converge to a finalised design, a iteration process has been developed as can been seen in chapter 5. The input for the iteration are the engineering tools developed to predict the SolidityONE's behaviour and performance. The tools consists of an aerodynamic (chapter 6), performance (chapter 7), power (chapter 8), control & stability (chapter 9) and structures tool (chapter 10). The overall design results are summarised in chapter 11, with the SolidityONE's predicted mission performance in chapter 12. Verification and validation of the entire SolidityONE can be found in chapter 13, where compliance with the requirements is confirmed. The remaining chapters describes the future of the SolidityONE beyond the DSE project. The production process, operations and logistics can be found in chapter 14, the future development strategy follows in chapter 15 and chapter 16 shows the costs and environmental impact. This report will be concluded in chapter 17, where the results are summarised and discussed.

2

Market analysis and proposition

To be able to direct the design effort in this project in the right direction, a market analysis was executed. Afterwards a proposition was made on how the characteristics of this project fit into this market.

2.1. Market analysis

To see where opportunities lie in the helicopter market and to find out what needs to be achieved to outperform competitors, a market analysis has been executed.

2.1.1. Opportunities in the helicopter market

As stated by the Green Rotorcraft project within the Clean-Sky joint undertaking, the largest challenge lies in a market with a large opportunity and is: *"the challenge of minimising the impact of the sharply increasing rotorcraft traffic expected in the future"* [5].

Noise reduction is one of the main sustainability objectives from the Green Rotorcraft project (GRC). Their goal is to reduce the average noise level by 10 dB of rotorcraft operations. Within this project, one main objective is innovative rotor design, the GRC1 [5]. This confirms the market need for adding to the current options for rotor designs. Furthermore, low noise can be suitable for applications in which stealth is desired.

Next to noise improvements, also an emission reduction is a current aim of the helicopter industry as the Green Rotorcraft program (led by Airbus Helicopters and Leonardo Helicopters [6]) state the following: *"In detail, taking into account year 2000 as baseline, the objectives of the GRC ITD and concurrent activities in other Clean Sky ITDs are to reduce CO2 emissions by 26-40 % and NOx emissions by 53-65 %, according to vehicle and technologies used"* [5].

Furthermore, opportunity lies in the helicopter market being an expanding market. While the market is already in the maturity phase, the rotorcraft market is still a growing sector every year with an expected growth from 31.7 billion USD in 2019 to 37.4 billion USD in 2025. This is a growth of 2.8% a year [7].

2.1.2. Market identification

The diversity of the application of rotorcraft is confirmed by the Cleansky joint undertaking, as they state *"Rotorcraft, thanks to their distinctive capability to take off and land vertically in tight situations, play an important role in the world of aviation and, apart from their purely commercial value, in numerous humanitarian uses: search and rescue, air ambulances, police and customs operations or providing access to otherwise remote areas"* [6]. For the personal transport market a Malaysian case study showed a large potential as 85% of the questioned want a personal flying vehicle if it is around the same price as a high-end brand car [8]. Combined, possible markets have been identified with many different needs and are listed below.

- Law enforcement
- Tourism
- Emergency transport
- Luxury taxi
- Aerial observation
- Personal transport

- Agriculture
- Military

2.1.3. COMPETITIVE ANALYSIS

To be able the have a complete overview of the performance of competitors, statistics have been analysed. In this analysis, mostly the small rotorcraft are investigated as the VFS competition aims at a small rotorcraft with the ability of carrying a 60 kg human payload [9]. Reference [10] states that: "*tip speed should be-...-low for low noise*", which is the reason it was included in the analysis below. From this same reference, the following parameters have been distilled:

- The lowest tip-speed for all different rotor diameters is 150 m/s where most are around 230 m/s.
- Most entries for rotor angular velocity are between 200 and 600 RPM.
- Most entries for rotor diameter are between 6 and 20 meter rotor diameter.

There are several companies trying to bring alternatives to the rotorcraft market for small vehicles. A number of these concepts have been analysed. Most of them are still in the designing phase. One lightweight helicopter is already for sale, the Mosquito XE[1]. Unlike the other concepts, this one has a conventional configuration. A number of these concepts are shown in Table 2.1 with their most significant characteristics. These characteristics are chosen as they were the most interesting for the comparison and the data was taken either from their own website or from eVTOL.news.

Table 2.1: Characteristics of lightweight rotorcraft

Name	MTOW (kg)	OEW (kg)	Payload (kg)	Propulsion types	Speed (km/h)	Time/dist
Talaria Hermes II	230	130	100	Electric 2x 60kW	80	30 min
Flysilverwing S1	N/A	N/A	90	Electric 2x	140	30 min
Volocopter	900	700	200	Electric 18x	110	35km
Curti Zefhir	700	N/A	2 passengers	Turboshaft	185	320km
Bell Nexus	2720	N/A	6 passengers	Hybrid-electric 6x	288	241km
Kittyhawk Flyer	205	113	1 passenger	Electric 10x	32	20 min
Opener Blackfly v3	255	142	110	Electric 8x	100	40km
Airbus Vahana	815	700	1 passenger	Electric 8x 45kW	220	50km
Surefly	1090	840	2 passengers	Hybrid 8x	112	2.5 hours
EHang 184	360	N/A	100	Electric 8x 152kW	100	23 min
Mosquito XE	277	135	112	rotorradial 48kW	130	2.2 hours

From the comparison of the lightweight rotorcraft, the following observations were made:

- Almost all the small rotorcraft use electric propulsion.
- Most of the single-passenger vehicles have a MTOW under 300kg and have a top speed around 100km/h.
- For vehicles with two passengers, the MTOW increases by 200% compared with a single-passenger rotorcraft.
- The flight time for electrical vehicles is significantly shorter than vehicles with hybrid or combustion propulsion.

2.2. MARKET PROPOSITION

In the market analysis, some significant drawbacks of modern rotorcraft rotors were found: they have a large diameter; produce a lot of noise and are a fairly unsustainable way of transport with respect to ground

[1] From URL: https://www.mosquito-europe.com/index.html#modeles(accessed 19/11/2019)

transportation. These drawbacks apply for all users, despite their different demands. Therefore, in this section, the market proposition is elaborated on, as summarized in Figure 2.1.

The opportunity of the aerial screw is to provide a new alternative. This unevaluated concept will entail flight characteristics which were unknown before this project. Due to the unpredictability of the characteristics of the vehicle and the limited resources in this project, only a **proof of concept at small size will be designed**. The vehicle will carry a minimum of 60 kg occupant and will be designed for a range of at least 20 m and a the minimum flight altitude will be 1 m. All these figures are in line with the mission set out by the VFS [9]. Overachieving these minima is desired for increasing the competitiveness of the concept.

The product in this project thus comes down to providing the customer with a new alternative for existing rotors. The vehicle is solely tailored to this purpose: providing a platform to show the customer how the aerial screw performs. This expected customer will be helicopter manufacturers. The helicopter manufacturer that has this new technology in hands can produce vehicles with new characteristics. As a result, the helicopter manufacturer can take over markets that are now filled by vehicles with 'regular' high aspect ratio rotors.

With this in mind, the vehicle was designed to be able to show the capability of the aerial screw and not to be used on a daily basis by a market of end-users. As an example, resources were more valuable spent at improving rotor characteristics than at designing rain covering. This design thought can be recognized throughout the entire report.

With the discovery of one or more unique features that the aerial screw has and existing rotors do not have, helicopter manufacturers can tailor a vehicle to a market to increase their market share in this market of end-users.

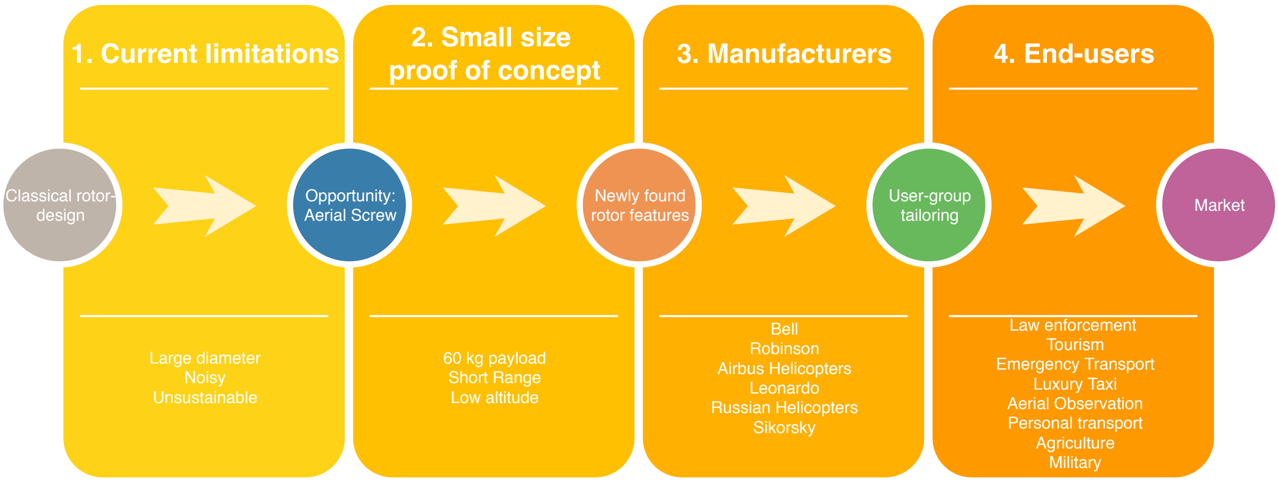

Figure 2.1: The value chain for the aerial screw vehicle

3

CONCEPT SELECTION

Before the creative process of generating concepts could start, the requirements needed to be created. This was followed by a trade-off, after which a concept is selected to start the design iterations with. The minimum prescribed mission is shown in Figure 3.1 and consists of a 5-second hover, a 20-metre flight in 1 minute, followed by another 5-second hover. Exceeding these minimums is favourable for scoring [9].

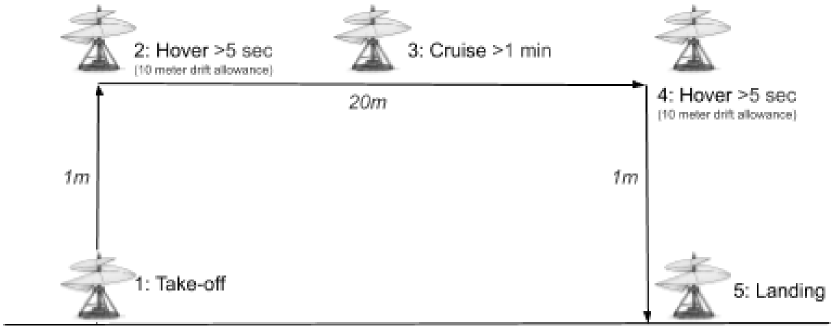

Figure 3.1: Mission phases

3.1. REQUIREMENTS

Before the design started, a list of requirements had to be created. This list helped to guide the design process and enabled validation of the design by ensuring that the product fulfills the needs of the customer. The requirements come from different sources such as VFS mission objectives, airworthiness regulations and sustainability.

3.1.1. KEY REQUIREMENTS

The majority of the design drivers stem from the VFS competition rules and are listed below.[1]

Key requirements

Sc-F-Mis-Takeoff *The vehicle shall be able to take-off vertically*
Sc-F-Mis-Hover-1 *The vehicle shall be capable of hover*
Sc-F-Mis-Hover-2 *The vehicle hover shall maintain its horizontal position to 10 m accuracy*
Sc-F-Mis-Cruise1 *The vehicle shall be able to fly at an altitude of at least 1 m*
Sc-F-Mis-Cruise2 *The vehicle shall fly for at least 1 min*
Sc-F-Mis-Cruise3 *The vehicle shall have a range of at least 20 m*
Sc-F-Mis-Landing *The vehicle shall be able to land vertically*
Sc-F-VFS-2 *The vehicle shall carry at least one occupant of 60 kg*
Sc-F-VFS-4 *The vehicle shall rely for its lift and thrust solely on one or more aerial screws*
Sc-C-VFS-5 *The aerial screw shall have a single blade*
Sc-C-VFS-6 *The aerial screw blade shall have continuous surface*
Sc-F-VFS-7 *The aerial screw shall have a blade solidity of at least 1*
Sc-F-VFS-8 *The vehicle shall fly without tethered power*
Sc-N-Sust-Cost-1 *The vehicle shall not cost more than €200,000*

[1] From URL:https://vtol.org/files/dmfile/leonardo-rfp_-vfs-sdc-2019_final.pdf.pdf, accessed 21 Nov 2019

These requirements set a baseline of performance and functional requirements for the flight mission. In subsection 5.2.3, the strategy for meeting and exceeding these minimum requirements is discussed. The lifting performance of the aerial screw is the main subject of the design exercise and therefore has a separate requirement.

3.2. DESIGN OPTIONS

In order to create a design that complies with all requirements, the design option tree (DOT) was constructed to analyse different design options. A design option tree shows all the options that were considered for each subsystem of the vehicle. First, non-feasible options were removed from the trees based on system requirements. It was concluded that the rotor options, power options and material options were the most critical for this project. Other parameters are considered at a later stage in the design process. Therefore, design decisions for these subsystems were made based on literature study and additionally obtained knowledge.

3.2.1. THRUST IMPROVERS

Within the usage of an aerial screw, different rotor options were available. The room for choice mostly was in increasing lift additional to lift generation of the surface of the screw.

DUCTED FANS

The subject of ducted fans has been a promising design option for the described mission profile, due to its excellent hover performance and increased efficiency. A ducted fan is defined as having a cylindrical shroud around the fan, with a narrow gap around the blade tips. The benefits of having a duct with respect to an open rotor are listed below [11–13].

- **Improved efficiency due to the prevention of tip vortex generation.** The tight clearance between the tips of the fan (or screw) and the duct walls prevents the air from the high pressure area to flow to the low pressure area and form a vortex. Some leakage will be present, but to a lesser extent. This provides for a more sustainable design as the fuel consumption will be decreased.
- **The intake of the duct can be designed to operate as a wing (intake lip) and thus produce additional thrust.** Due to the suction of the air into the duct and a wing-shaped inlet lip, the air flow will be accelerated around the inlet lip. This creates a low pressure area. The static pressure pushes the duct up at the inlet lips and creates extra thrust. This phenomenon has been visualised in Figure 3.2a.
- **Improved safety.** A duct can prevent objects striking the blade when flying at low altitudes. This creates a safer working environment for ground personnel when the engine is running. Internally, the duct acts as a shield in case of blade failure or separation. This is considered as an improvement in the social aspect for a more sustainable design.
- **Provides an alternative type of vehicle control.** The in- and outward flow of the duct can be vectored with the use of vanes or control surfaces to manoeuvre the vehicle. This introduces a torque that tilts the duct into the forward velocity and thus provides forward thrust. This reduces complexity since no other type of control is needed. This potentially reduces weight since less components are required.
- **Noise reduction.** The tip vortices produce noise and by reducing them significantly, decreases the noise production of the aerial screw. Furthermore, the duct itself provides some acoustic shielding. Shaping the duct exit to decelerate (e.g. a divergent duct exit) the flow provides even more noise reduction. (An accelerating convergent duct exit will improve efficiency, but is more prone to separation.) Furthermore, as the ducts reduce noise this is also considered to be a more sustainable design option than without ducts.
- **Inherent stability.** Ducted fans having a previously mentioned inlet lip are inherently stable. They tend to remain in vertical position when tilting the duct away from vertical. Since the forward velocity will accelerate the flow at one side of the inlet lip and decelerate the flow at the other side, this results

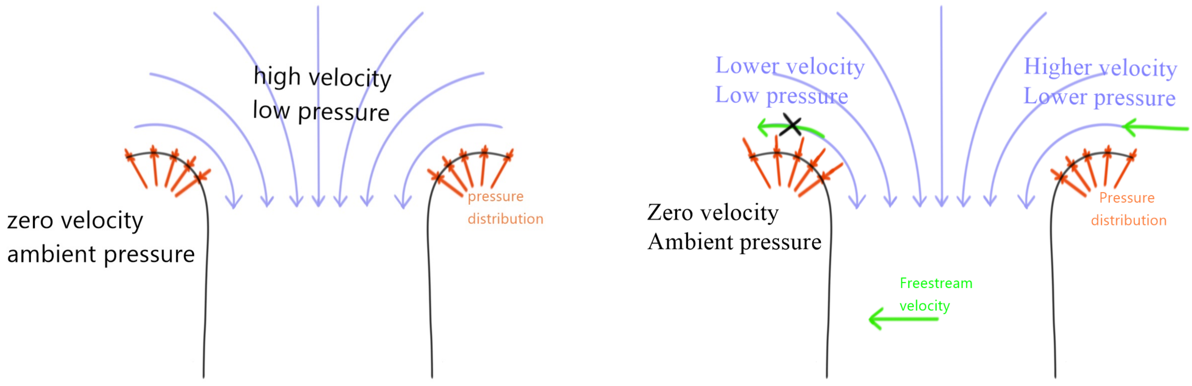

(a) Duct inlet lip mechanics for hover providing extra thrust (b) Duct inlet lip mechanics for forward flight introducing a moment

Figure 3.2: Duct inlet lip mechanics

in a difference of lift between the two sides that will rotate the ducted opposite to the velocity. The calculations for this restoring moment are shown in subsection 9.3.3 and visualisation can be viewed in Figure 3.2b.

To conclude, ducted fans have more sustainable potential as there is an increase in efficiency and safety and a reduction of noise. It has been determined that for a propeller of the same size, a ducted propeller is around 30% more power efficient when producing the same amount of thrust (for the ideal case of steady one-dimensional, incompressible, irrotational flow) [11]. This can be translated to a disc area reduction of a half with respect to an open rotor to produce the same amount of thrust [11]. This can potentially reduce the weight further. However, the duct has some limitations which are listed below and should be taken into account when making design decisions [11–13].

- **Weight increase.** Although previously it was stated that the duct can induce weight loss in multiple areas, the weight of the duct itself could dramatically increase the overall weight. This may be a reason that ducts are not widely adopted. Carefully selecting materials and designing the duct can mitigate this effect.
- **Increase in drag.** The size and shape of the duct is highly influencing the drag it causes. A ducted fan has a large drag when moved perpendicular to the airflow. This drag limits the horizontal speed it achieves.
- **More prone to crosswinds.** Due to the size and shape of the duct, the vehicle will be more prone to drift caused by crosswinds. This is closely related to the drag of the duct. For now this effect is not taken into account since flying indoors is required for the VFS competition (no wind) [9].
- **Impaired manoeuvrability.** Since the duct inherently opposes movement when in near-vertical position, it requires a large external torque to tilt the duct into the airflow. Together with the drag, having a duct placed in vertical position is not suited for flying horizontally at high speeds.
- **Authenticity.** The ducted screw is not true to Da Vinci's design and is thus a potential risk in terms of the VFS competition particcipation [9].

By applying these benefits and deficiencies to the provided mission profile, a ducted aerial screw seemed to be more suited than an open screw. The deficiencies are either not applicable to the mission profile or can be mitigated by various means. There are a few parameters to consider when designing the duct, these are more elaborated upon in chapter 6. The moment and stability provided by the duct lips are further explained in chapter 9.

WING TIP DEVICES

Wing tip devices can be an alternative in case the ducts turn out to be too heavy. Wing tip devices are already commonly used for conventional aircraft, marine propeller screws, and rotorcraft. The wing tip devices are all designed to fulfill the same general purpose, with some minor discrepancies related to their application. The benefits of having a wing tip device are similar to that of a ducted propeller; the devices are mainly used to improve propulsive efficiency by the reduction of tip vortices, resulting in less noise and fuel consumption [14, 15].

The largest disadvantage is that the wing tip device is attached to the wing tip, where it will experience high centripetal forces (approximately 500 g) depending on the RPM and radius. Decreasing the RPM is unfavourable for aerodynamic performance, and increasing the radius causes a drastic mass increase and increase of size of the device. This limits the size of the wing tip devices. Also, the wing tip device needs to be attached around the entire circumference of the screw which will make the weight of the wing tip device also significant. Furthermore, the increased thrust due to an intake lip is not present. Following the reasoning described above, it was concluded that ducted fans are more favourable than wing tip devices for the aerial screw and this particular mission profile.

3.2.2. POWER OPTIONS

The rotorcraft power train consists of a few components: the engine, fuel system, gearbox and a transmission system between the engine, gearbox and rotor. The gearbox is required to efficiently gap the difference in RPM between electric motor and rotor. The engine types considered at this stage were electric motors, two-stroke piston, Wankel-rotary, turboshaft, and four-stroke piston engines. The power-to-weight ratios of the engine types and their respective fuel types are shown in Table 3.1, not including batteries, motor controllers, fuel and fuel systems. The ratios indicated change with the addition of fuel and fuel system masses, especially when targeting longer flight durations as a result of increased fuel mass and the associated fuel tank sizing. Note that in Table 3.1 the energy storage for electric motors is provided in terms of the specific energy of batteries, which is used for mass estimation. Since the combustion engine fuel consumption is provided in terms of fuel volume over time, the a mass per unit volume is provided.

Table 3.1: Engine types considered, the dry engine power-to-weight (P/W) ratio and fuel consumed

<table>
<tr><th>Engine Type</th><th>Power-to-weight ratio (kW/kg)</th><th>Energy storage</th></tr>
<tr><td>Electric</td><td>4:1 [16]</td><td>Electricity; 4 kg/kWh [17]</td></tr>
<tr><td>Two-stroke piston</td><td rowspan="2">2:1 [18, 19]</td><td rowspan="2">Gasoline with two-stroke oil; 720 g/L [20]</td></tr>
<tr><td>Wankel-rotary</td></tr>
<tr><td>Turboshaft</td><td>2:1 - 9:1 [21]</td><td>Jet-A1, Diesel; 820 g/L [22]</td></tr>
<tr><td>Four-stroke piston</td><td>1:1 [23]</td><td>Avgas; 720 g/L [24]</td></tr>
</table>

From a sustainability perspective, electric motors are favourable due to the reduced emissions and the business models that accompany the new innovations [25]. Additionally, the newer generation lithium-based batteries have an approximately halved equivalent carbon footprint compared to Nickel-Cadmium batteries, where the largest contribution to the footprint results from the usage [26]. Least favourable are the two-stroke and Wankel engines, due to the exhausted oil contents, which results from a mix of fuel and oil for lubrication of the engine. This can be prevented partially by the addition of a catalytic converter [27].

COMBUSTION PROPULSION

Combustion engines include reciprocating and gas turbine engines. These were assumed to be supplied by the manufacturers as a complete functional module, unless indicated otherwise, with the exception of controllers and monitoring hardware, which is to be installed in the cockpit. Excluded, however, is the fuel system. For this, the mass estimation method for the fuel system by Torenbeek was used [28].

ELECTRIC PROPULSION

Electric motors are powered via a controller or inverter, which converts DC electric energy to three-phase sinusoidal waves, with the frequency dependent on the actual and target RPM of the motor. The electric energy is supplied by either batteries or hydrogen fuel cells.

Notably the lithium-based batteries have achieved specific energy of approximately 250 Wh/kg.[2] Currently, lab-tests show that solid-state batteries approach a specific energy of up to 500 Wh/kg [17]. Due to the uncommonness of commercially available high specific energy batteries, 250 Wh/kg is taken as a realistic value. Significant downsides to battery-technology are the battery weight for longer flight durations, in addition to the material-cost and flammability risks [29, 30].

Hydrogen fuel cells are a sustainable alternative to battery systems, however are too heavy for consideration. Namely, the fuel cell mass required for a certain electric power output exceeds the battery mass required for the required flight time of less than two minutes, as shown in Figure 3.3. This figure shows the lithium battery mass compared to a bare PowerCell S3 hydrogen fuel cell [31]. The hydrogen tank and its contents are omitted, since little data on mass is available for this power range, favouring the hydrogen option in the figure. The energy density used is the lower heating value of liquid hydrogen at 8491 Wh/L [32] and a tank mass estimation based upon linear regression of data found for tanks at an assumed 100% efficiency.[3]

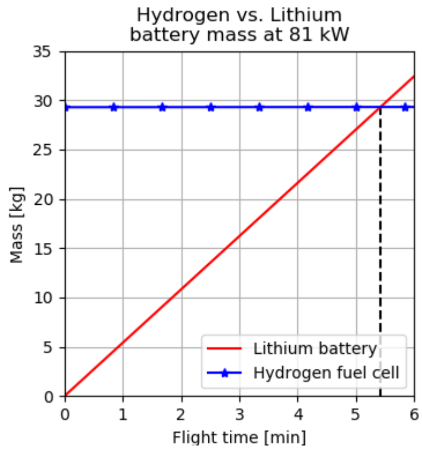

Figure 3.3: Powercell S3 Hydrogen Fuel cell mass compared to lithium battery mass versus flight time[4]

From the previous discussion, it can be concluded that electric propulsion is the preferable option in terms of sustainability. When the required power increases, turboshafts may become relevant. Hydrogen fuel cells are not favourable until flights become longer. Hydrogen also imposes a safety risk since it is very flammable.

3.2.3. MATERIAL OPTIONS

To pick the right materials for the rotorcraft, a material selection study has been performed. The program CES EduPack [33] allows the user to select from a list of aerospace materials and order them according to the

[2]From: https://cleantechnica.com/2019/01/28/tesla-model-3-battery-pack-cell-teardown-highlights-performance-improvements/ (04/12/2019)
[3]From: https://www.fuelcellstore.com/hydrogen-equipment/hydrogen-storage (12-12-2019)
[4]From: https://www.powercell.se/wordpress/wp-content/uploads/2018/12/S3-Produktblad-190430.pdf (04/12/2019)

most important parameters. To ensure that the right materials are chosen for both core and skin, different selection criteria have been used.

To determine the best performing core materials, a shear strength over density graph is plotted in Figure 3.4. Core materials are mainly used to create an offset between the two skins to improve stiffness of a sandwich structure whilst not adding too much weight. This means that the cores main function is to transfer shear forces through the sandwich panel. The best performing materials are towards the top left corner of the graph.

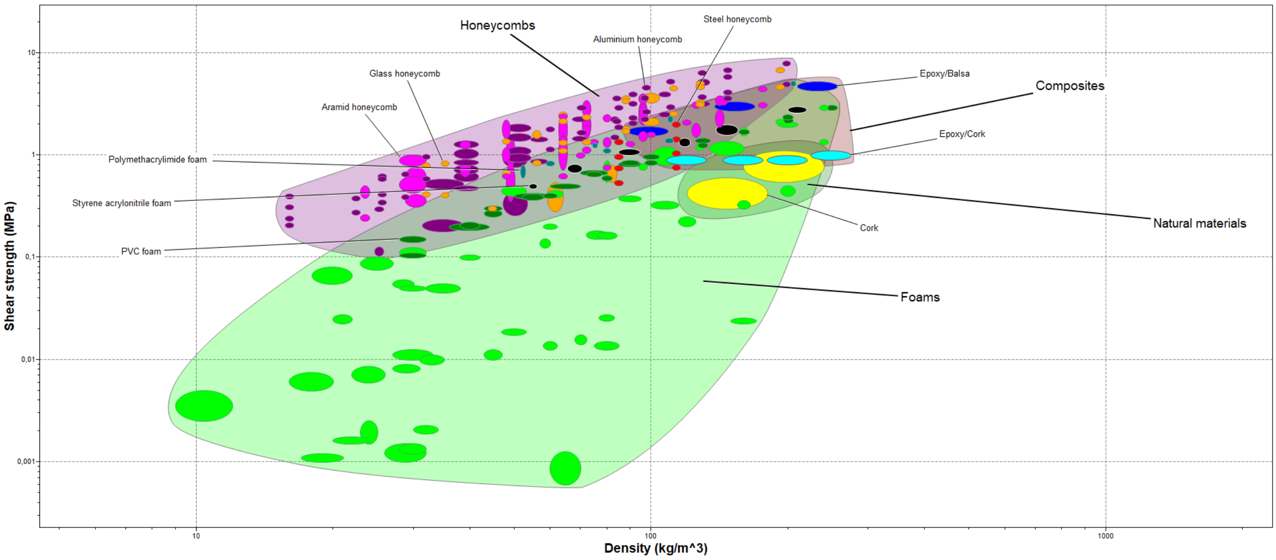

Figure 3.4: Shear strength compared to density of core materials

To determine the best performing skin materials, a specific strength versus specific stiffness graph is plotted in Figure 3.5. To make sure both stiffness and strength requirements will be met, the structure of the vehicle will be designed for both stiffness and strength whilst being as light as possible. The best performing materials can be found in the top right corner of the graph.

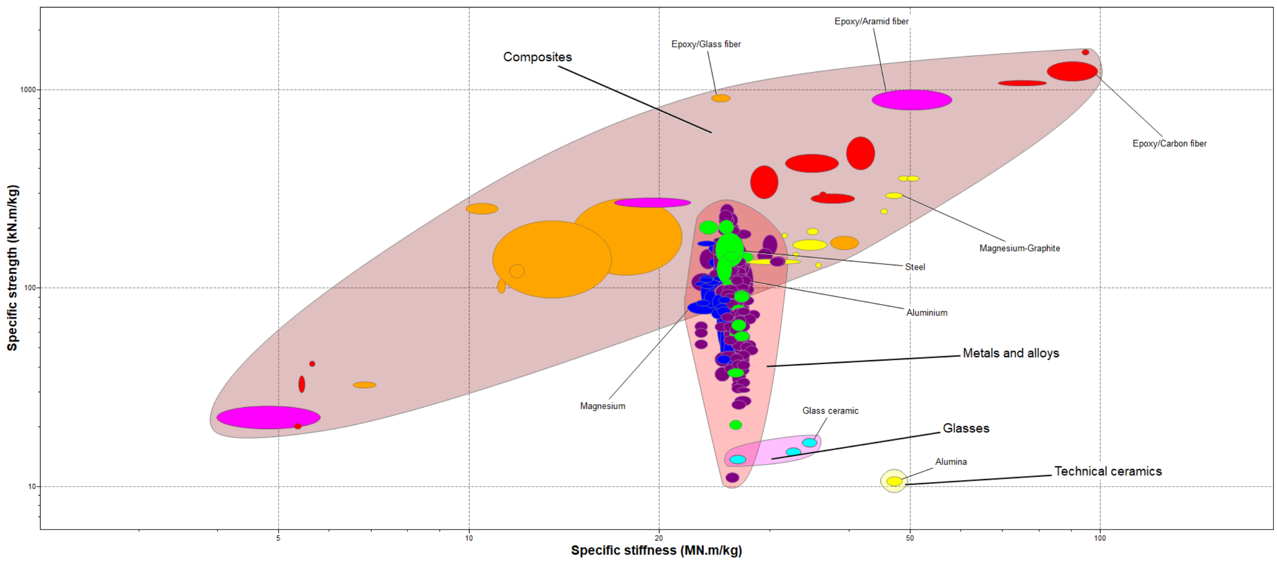

Figure 3.5: Specific strength compared to specific stiffness of aerospace materials

The best performing skin and core materials are chosen according to criteria mentioned above. However, to be able to make a proper trade-off, sustainability also had to be taken into account since the economic and environmental aspects of the design could be greatly affected by the material choice. Therefore the cost, CO_2 emissions, energy consumption for the production, manufacturability, recyclability, and biodegradability are also considered when making decisions on material. The final materials table is shown in Figure 3.8.

3.3. TRADE-OFF AND SELECTION

Figure 3.6 shows initial raw sketches of three of the concepts that were accumulated from the design option trees. These concepts differ in rotor configurations. A complete list of all the concepts considered is shown in Figure 3.7. The concepts feature a configuration, a name and a principle of control. The configuration and control principle are closely interrelated and therefore cannot be considered separately. Other options such as materials, pilot positioning, structure type of the rotor, rotor geometry and landing gear are not shown in the table, since these options are applicable to all these concepts. A selection among these was made based on the following characteristics: non-lifting power, mass performance, development risk, controllability, aesthetics, maintainability and demonstrability.

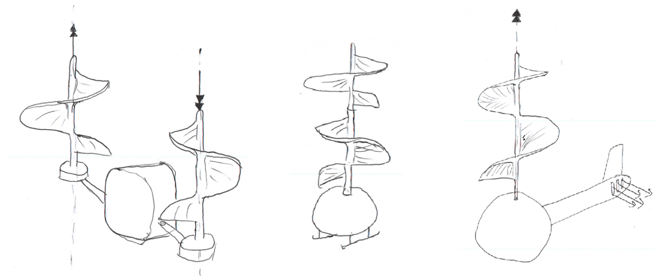

Figure 3.6: Initial concept sketches from left to right: twin rotor, coaxial and conventional

The trade-off in Figure 3.7 shows that the only concepts without any unacceptable characteristics are the coaxial and twin rotor configurations (tandem and side-by-side). The nested coaxial was selected to analyse coaxial options. The twin rotors were selected for their ability to counter the torque and because they are less complex than the coaxial configuration. The tandem with vanes and the tandem with tilt were selected to analyse different control mechanisms and the side-by-side was selected to analyse the control in another orientation.

Material	Cost (EUR/kg)	Density (kg/m^3)	E-modulus (GPa)	Yield strength (MPa)	Tensile strength (MPa)	Compressive strength (MPa)	Shear modulus (GPa)	Shear strength (MPa)	CO2 footprint (kg/kg)	Production energy (MJ/kg)	Recyclability	Biodegrade
Metals and alloys												
Titanium, alpha-beta alloy, Ti-6Al-2Sn-2Zr-2Mo, solutio	20	4550	124	1260	1340	1260	47	-	34	594	yes	no
Aluminum, 7068, T6511	5	2850	75	756	797	764	30	-	14	199	yes	no
Aluminum, 8009, rapid solification	10	2950	92	420	510	420	35	-	16	239	yes	no
Aluminum, 2090, T83	15	2610	80	483	531	490	31,5	-	14	219	yes	no
Maraging steel, 300, maraged at 482 celcius	33	7960	192	2000	2070	1940	74	-	5	70	yes	no
Intermediate alloy, Fe-5Cr-Mo-V aircraft steel, quenche	19	7820	218	1660	1930	1790	80	-	4	47	yes	no
Low alloy steel, AISI 4340, oil quenched & tempered at	1	7900	213	1850	2070	1850	83	-	3	34	yes	no
Magnesium, ZC71	3	1880	46	320	345	325	18	-	45	317	yes	no
Magnesium, ZK60A-T5	3	1840	46	304	366	310	18	-	46	332	yes	no
Magnesium, Elektron ZW3, F	3	1810	46	280	355	262	18	-	48	342	yes	no
Fiber composites												
PEEK/IM carbon fiber, UD prepeg, UD lay-up	102	1570	149	N.A.	2430	1200	5,5	-	54	781	no	no
Epoxy/HS carbon fiber, UD prepeg, UD lay-up	36	1580	154	N.A.	2170	1690	6,3	-	51	723	no	no
Epoxy/HS carbon fiber, woven prepeg, biaxial lay-up	50	1610	69	N.A.	910	937	3,5	-	47	679	no	no
Epoxy/S-Glass fiber, UD prepeg, UD lay-up	27	1970	48	N.A.	1760	1190	4,75	-	6	106	no	no
Phenolic/E-glass fiber, woven prepeg, biaxial lay-up	25	2000	39	N.A.	520	460	98	-	7	100	no	no
Epoxy/aramid fiber, UD prepeg, UD lay-up	67	1380	80	N.A.	1380	275	2,1	-	13	243	no	no
Plastic												
PA66 (30% long carbon fiber)	12	1300	24	330	350	410	9	205	28	432	no	no
PA66 (40% long carbon fiber)	14	1350	38	310	320	400	13	200	34	516	no	no
PEKK (40% long carbon fiber)	62	1460	49	272	342	-	18	155	40	608	no	no
Foams												
Alumina foam (99.8%)(1.2)	45	1220	34	64	64	85	13	-	7	134	no	no
PC foam (structural, 0.85)	5	860	2	25	41	25	1	12,5	8	125	no	no
Polymethacrylimide foam (rigid, 0.200)	64	205	0,4	6,6	6,9	9,6	0,15	5,2	29	348	no	no
Polymethacrylimide foam (rigid, 0.051)	107	51	0,075	0,8	1,65	0,9	0,024	0,8	29,1	348	no	no
Expanded PS foam (closed cell, 0.050)	2,62	53	0,03	1	1,2	1	0,01	0,5	2,49	92,1	no	no
Honeycombs												
Aluminum 5052 honeycomb (0.198), W direction	24	202	0,04	0,37	0,44	19,2	0,471	5,2	28	441	yes	no
Aluminum 5052 honeycomb (0.198), L direction	24	202	0,02	0,41	3,31	19,2	1,52	8,33	28	441	yes	no
Aluminum 5056 honeycomb (0.13), L direction	31	132	6,00E-03	0,21	0,97	13,8	1,04	6,68	29	451	yes	no
Aluminum 5056 honeycomb (0.13), W direction	31	132	1,20E-02	0,19	0,22	13,8	0,37	3,91	29	451	yes	no
Aluminum 5056 honeycomb (0.016), L direction	31	16,3	1,18E-05	0,00319	0,00182	0,434	0,109	0,416	29	451	yes	no
Glass/phenolic honeycomb, 0/90 fabric (0.192), L direct	94	196	0,03	1,72	5,16	18,2	0,32	7,12	5	116	no	no
Glass/phenolic honeycomb, 0/90 fabric (0.192), W direc	94	196	0,03	1,72	5,16	18,2	0,2	4,89	5	116	no	no
Aramid paper/phenolic honeycomb (0.176), L direction	36	180	0,01	0,35	1,21	19,5	0,2	4,63	17	349	no	no
Aramid paper/phenolic honeycomb (0.176), W direction	36	180	0,01	0,35	1,21	19,5	0,12	3,26	17	349	no	no

Figure 3.8: List of accumulated optional materials from material maps

<table>
<tr><th>Configuration</th><th>Concept name</th><th>Lift power efficiency</th><th>Mass performance</th><th>Development Risk</th><th>Controllability</th><th>Aesthetics</th><th>Maintainability</th><th>Demonstrability</th></tr>
<tr><td>1 main rotor, with tail rotor</td><td>Conventional tilt</td><td rowspan="3">2. Rotor will require a lot of torque, so tail rotor will use lots of power</td><td rowspan="2">5. Very minimal airframe possible, small tail boom</td><td rowspan="2">5. Proven concept</td><td rowspan="2">1. No conventional control methods apply</td><td rowspan="2">1. Not very renewing</td><td>4.</td><td>5</td></tr>
<tr><td>1 main rotor, with tail rotor</td><td>Conventional CG</td><td>5.</td><td>5</td></tr>
<tr><td>1 main rotor, 3 assist rotors</td><td>Assist rotors 1+3</td><td>3. Needs booms for each assist rotor</td><td>4. Investigated on small scale</td><td>4. Worse than quadrucopter</td><td>1. 3 long booms</td><td>5.</td><td>5</td></tr>
<tr><td>1 main rotor, exhaust jet in tail</td><td>NOTAR</td><td>5. Turbine exhaust air used</td><td>1. Turbine needed, which is heavy.</td><td>5. Proven concept</td><td>1. Requires helicopter controls</td><td>2. Blunt tail required.</td><td>5.</td><td>5</td></tr>
<tr><td>Coaxial, stacked on top of each other, tilt rotor</td><td>Stacked coaxial tilt</td><td rowspan="2">4. Possible loss due to turbulent effects</td><td rowspan="2">5. Very minimal airframe possible, small/no tail boom</td><td rowspan="2">1. Interference between rotors difficult to quantify</td><td>5. Easy to control</td><td rowspan="2">3. Very tall configuration</td><td>1.</td><td>5</td></tr>
<tr><td>Coaxial, stacked on top of each other, cg shift</td><td>Stacked coaxial CG</td><td>4. Easy but limited authority</td><td>4.</td><td>5</td></tr>
<tr><td>Coaxial, inner rotor nested in ducted outer rotor, tilt rotor</td><td>Nested coaxial tilt</td><td rowspan="12">5. Torque is counteracted by lift-generating rotors</td><td rowspan="3">3. Big structure needed for the double ducted fan</td><td>3. Nested rotor and tilting system structurally complex</td><td>4. Easy but slow control</td><td rowspan="3">5. Nested rotor looks interesting</td><td>4.</td><td>2</td></tr>
<tr><td>Coaxial, inner rotor nested in ducted outer rotor, CG shift</td><td>Nested coaxial CG</td><td>3. Nested rotor and cg-shift system structurally complex</td><td>4. Easy but limited authority</td><td>4.</td><td>2</td></tr>
<tr><td>Coaxial, inner rotor nested in ducted outer rotor vanes below rotor</td><td>Nested coaxial vanes</td><td>4. Nested rotor structurally complex</td><td>5. Quick and direct control</td><td>5.</td><td>2</td></tr>
<tr><td>Twin-rotor, side by side, tilt rotor</td><td>Twin-rotor side by side tilt</td><td rowspan="6">4. Long structure needed between the two rotors.</td><td>4. Tilting system structurally complex</td><td>4. Easy but slow control</td><td rowspan="3">5. Quite novel look</td><td>4.</td><td>4</td></tr>
<tr><td>Twin-rotor, side by side, CG shift</td><td>Twin-rotor side by side CG</td><td>5. Pilot shifts weight</td><td>3. Easy but limited authority</td><td>4.</td><td>4</td></tr>
<tr><td>Twin-rotor, side by side, vanes below rotor</td><td>Twin-rotor side by side vanes</td><td>5. Stator vanes are fairly simple</td><td>5. Quick and direct control</td><td>5.</td><td>5</td></tr>
<tr><td>Tandem tilt rotors</td><td>Tandem tilt</td><td>4. Tilting system structurally complex</td><td>4. Easy but slow control</td><td rowspan="3">5. Looks like a hoverbike</td><td>4.</td><td>5</td></tr>
<tr><td>Tandem CG shift</td><td>Tandem CG</td><td>5. Pilot shifts weight</td><td>3. Easy but limited authority</td><td>4.</td><td>5</td></tr>
<tr><td>Tandem, ducted with vanes below rotor</td><td>Tandem vanes</td><td>5. Stator vanes are fairly simple</td><td>5. Quick and direct control</td><td>5.</td><td>2</td></tr>
<tr><td>2 main rotors, 1 additional rotor away from center</td><td>Tricopter 2+1</td><td rowspan="3">1. Big structure needed for connecting all rotors.</td><td rowspan="2">1. Challenging control system</td><td rowspan="2">2. Bad DOF coupling</td><td rowspan="2">5. Quite novel look</td><td rowspan="2">4.</td><td>2</td></tr>
<tr><td>2 main rotors, 1 additional rotor away from center CG shift</td><td>Tricopter 2+1 CG</td><td>2</td></tr>
<tr><td>4 rotors placed symmetrically, 2 different spin directions</td><td>Quadrucopter</td><td>5. Proven concept</td><td>5. Easy to control</td><td>4. Suggests drone function</td><td>5.</td><td>1</td></tr>
</table>

Legend:

5: Excellent	4: Good	3: Moderate	2: Bad	1: Unacceptable

Figure 3.7: Trade-off table of evaluated concepts

3.4. FINAL TRADE-OFF RESULT

Figure 3.9 shows detailed sketches of the feasible candidates that were accumulated from the previously described trade-off process. To be able to pick a concept to be designed further in detail the overall

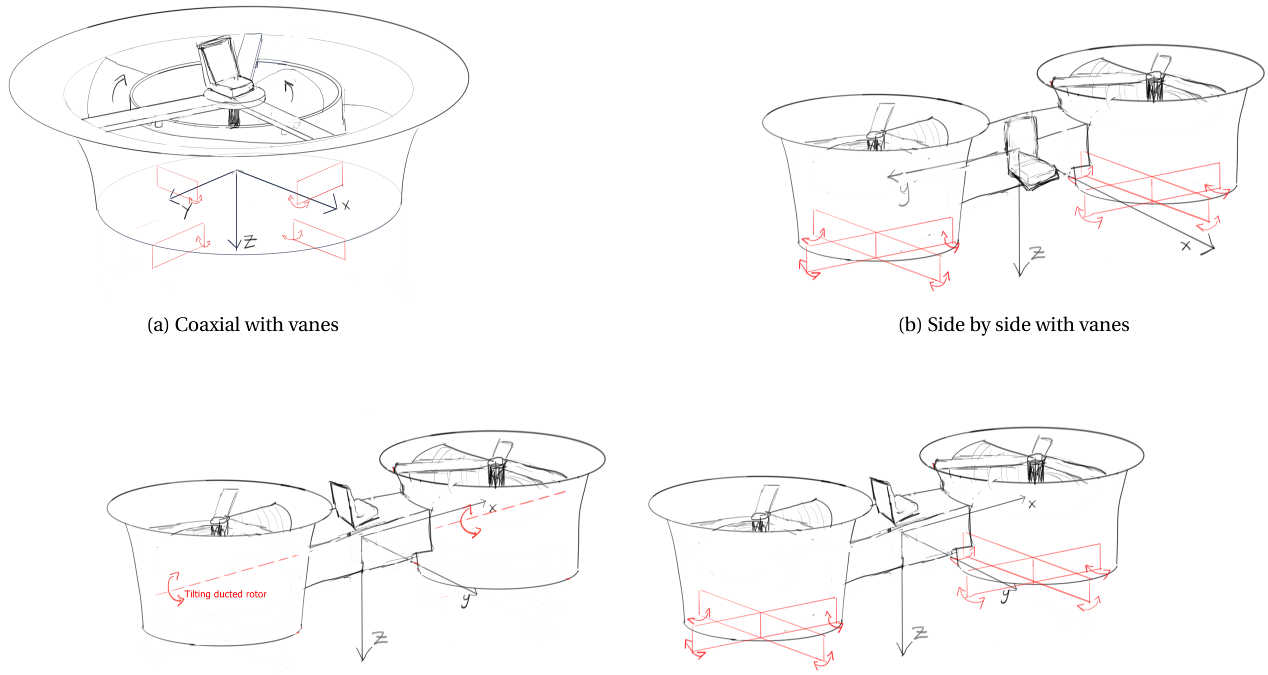

(a) Coaxial with vanes

(b) Side by side with vanes

(c) Tandem with tilt

(d) Tandem with vanes

Figure 3.9: Concept sketches

The method applied for the trade-off was the use of a standard weighted sum matrix analysis for each concept [34]. The result of this analysis is shown in Table 3.2. It can be seen that the highest importance is given on the performance criteria which ensures that the aerial screw can perform its mission. The trade-off resulted in that the tandem configuration controlled by vanes scored the highest and was therefore chosen to be designed further in detail. This is mainly because it has a higher controllability than the other twin rotors, is less complex and has a higher range than the coaxial.

Table 3.2: Trade-off between the feasible candidates

Criteria	Importance	Coaxial	Side-by-side	Tandem with vanes	Tandem with tilt
Hover power	2	-4	-3	-3	-3
Noise production	3	5	5	5	5
Design complexity	3	-4	-2	-2	-3
Aesthetics	1	3	3	3	3
Maintainability	2	1	3	3	2
Demonstrability	1	-1	0	2	2
Velocity	2	3	2	5	5
Range	5	3	2	5	5
Hovering endurance	5	5	5	5	5
Max hover altitude	5	3	1	1	1
Controllability	5	2	2	2	-3
Costs	2	-3	-3	-3	-3
		64	**60**	**83**	**56**

4

Sustainable development approach

Sustainability is increasingly being recognized as a vital component of a good design. Designers are trying to implement consciousness around sustainability at every step in the design process. A design is considered fully sustainable if it adheres and contributes to the three pillars of sustainability: people, planet and profit. This chapter first describes the tools applied to result at a sustainable design. Where after a description of the analysis method for sustainability is given.

4.1. Sustainability engineering

The first step in achieving a sustainable design was produced in the baseline phase, which was establishing requirements for sustainability. These requirements are described in chapter 13 and were applied as guidelines to which the design should adhere to for being sustainable.

Secondly, a budget breakdown was applied in which the weight, power and costs are tracked with design decisions and iterations. This eliminated waste in resources and resulted in a more efficient design.

At last a MAI-plan was made, which is the manufacturing. assembly and integration plan. The MAI-plan is a measure to eliminate the waste of resources, because a well formulated and well organised MAI-plan will ensure a cost and time effective production process. This MAI-plan is given in Appendix B.

4.2. Sustainability analysis

In order to assess sustainability throughout the final design phase sustainability analysis methods had to be applied.

Life cycle assesment is applied to anaylse sustainability throughout the product life. The product life consists of the phases as depicted in Figure 4.1. The goal of this life cycle assessment is to convert from a linear economy to a circular economy by minimising waste, recycling, remanufacturing, and extending the product life. This life cycle assesment is chiefly visible in the market and enivironmental impact.

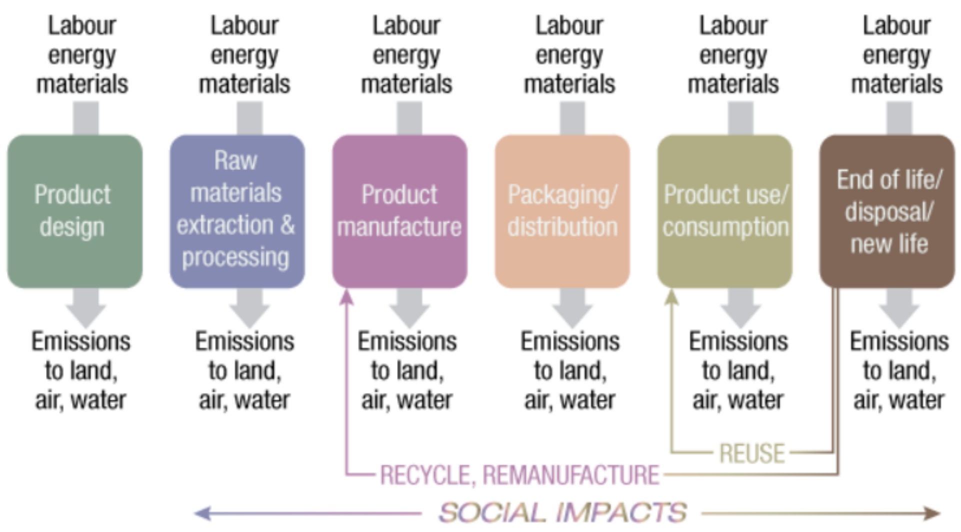

Figure 4.1: Life cycle of a product[1]

A material map was constructed to provide a clear overview, which materials could be applied. This increased the consciousness of applying sustainable materials by not only evaluating for weight, stiffness and strength, but also the cost, CO_2 footprint and the recyclability. This material map is given in Figure 3.8.

A parts map was constructed, which included all the parts of the vehicle. This map was used to have a clear overview for analysing all the different parts on their cost, environmental impact, reliability and reusability. This parts map is given in Appendix A.

RAMS was constructed in section 14.4 to evaluate the reliability, availability, maintainability and safety, which are important sustainability measures. Reliability of a system is defined as the probability that a system does not fail during a predetermined operating period. This has a significant effect on the sustainability, because when the vehicle fails it could have an big impact on the environment and the people. Availability is the time the vehicle could be operated. If it has a high availability less vehicles need to be made which has an impact on the environment. Maintainability is the ability to maintain the vehicle and increase the product life. Hence less vehicles have to be made, which is beneficial for the environment. At last safety is an important sustainability parameter, as the loss of a life has a high social impact and should be avoided at all time.

A cost analysis was constructed to evaluate the economical impact of the SolidityONE. Consideration of costs is of fundamental importance at all phases of the rotorcraft design process. The success or failure of a project is significantly dependent upon the cost associated with its initial acquisition and operation. The selling price of an aircraft is largely determined by market forces. To be profitable for the manufacturer it must be possible to produce it for less than the market price. Furthermore, the cost analysis was performed over the entire life cycle of the product from development until the end of life. This cost analysis is described in detail in section 16.1.

An environmental impact analysis was constructed to evaluate the effect of the SolidityONE on the environment. The environmental impact consisted of two factors; the emissions and the noise produced by the vehicle, which are described in section 16.2 and section 16.3 respectively.

Emissions are caused by either the vehicle or the production process related to the vehicle. In industry the CO_2 equivalent is used to account for all emissions such as CO_2, NO_x and PM. Hence emissions will be described as CO_2 production. The CO_2 is mainly produced by the materials used, the operations and the end of life of the vehicle.

Noise is an important environmental factor, because too much noise will have a negative influence on the environment and society. The main contribution of noise will be from the rotor, which produces rotational and vortex noise.

[1]From URL: https://www.lifecycleinitiative.org/starting-life-cycle-thinking/what-is-life-cycle-thinking/ (21/11/2019)

5 ITERATION PROCESS

The goal of the iteration process was to find the optimal design within the design space determined by the chosen concept. The iteration process comprised two main elements. The first element is the linkage between the different engineering disciplines to synthesize designs following varying sets of input parameters. This element is represented by the design iteration N2 chart. The second element is the comparison of these different designs and the ability to point out where the design process would need to go, to be able to find the optimal design. This element is the result of the multi objective design strategy.

5.1. DESIGN ITERATION N2 CHART

Figure 5.1 describes the iteration process in which, system engineering (SE), Performance (Perf), aerodynamics (Aero), structures (STR), power (POW) and control and stability (C&S) represent the different engineering disciplines. This process was deliberately documented in separate disciplines for ease of communication between the separate engineering teams.

Input ↓

Expected MTOW	Target altitude and hover time	Target cruise velocity	Rotor radius and rotor pitch					→ Output
SE: Weight	MTOW	MTOW						Remaining mass budget
	Perf: Hover		Thrust required at hover altitude		Hover time			Actual hover altitude
		Perf: Cruise	Target velocity and thrust required at cruise velocity at cruise altitude		Cruise time		Cruise velocity, cruise time	Actual cruise velocity
			Aero: Screw and drag	Dimensions of the rotor; hover and cruise RPM; Aerodynamic loads at the screws; Drag force	Hover and cruise power required	Dimensions of the rotor, tilt angle, cruise velocity, torque due to RPM variation		Noise
Screw, duct and airframe mass				**STR: Screw, duct, airframe**				
Motor and battery mass					**POW: Power system**			Power consumption and actual endurance
Vane mass, controller mass				Control forces		**C&S: Control and stability**		Pitch rate and settling time
							Range	Actual range

Figure 5.1: Design iteration process N2 chart

For each iteration, the engineering teams were given targets by the systems engineer: a hover altitude and time, a cruise velocity and altitude. In order to find the right rotor radius and pitch, these were given as an input and tracked to couple these values to performance values. To be able to start the calculations, also an expected MTOW was given. For each iteration, the steps in the N2-chart were followed at least once, where at the end of the iteration-loop the value in *SE: Weight* is the actual MTOW instead of the expected MTOW. If it this value was too far off, the loop was repeated until the actual versus expected MTOW were converged to a satisfactory extent.

The outputs of the process were the following performance parameters: actual hover altitude; actual cruise velocity; noise production; power consumption; actual endurance; pitch rate; settling time and the actual range. Also, the remaining mass budget was an output. This remaining mass budget was defined as the mass that could be added to the vehicle while still being able to perform according to the set targets. If this value was positive, the value could be used in the upcoming iteration to optimize the design. Options were to increase the hover altitude, the battery mass (thus endurance) or the velocity (reducing the mass carrying capability). If the value was negative, one or more targets would not have been met.

5.2. MULTI-OBJECTIVE DESIGN STRATEGY

During this project, multiple objectives indicated the performance of the mission. As the design space prohibited the achievement of maximal values for the complete set of these objectives, the design had to compromise between the different objectives. To evaluate which compromise between the different objectives performed best overall, a multi-objective design strategy was set up. In this method, different existing methods were adopted and tailored to the project of the aerial screw. This method simply is a trade-off in values of design and performance parameters.

The multi-objective design strategy incorporates all relevant objectives and scores designs on overall performance. This method also describes this overall performance and enables the designer to identify the parameters that have the most negative effect on this performance. It greatly aids the distribution of resources to where they have the largest improvement.

5.2.1. METHOD OF IMPRECISION

As during the conceptual design phase, the design space was not fully defined yet and the objectives could not be fully defined. It was not yet known what would be achievable. The method of imprecision suits this situation. It is a "method suitable for representing and manipulating uncertainties in preliminary design, to formalize the process of making these trade-off decisions", as stated in *Trade-off strategies in engineering design* [34].

In this design effort, an overall optimal performance was desirable. Namely, the mission had to be executed in an overall satisfactory way. For this, the performance on one parameter should be able to compensate for the performance on other parameters. Yet, if one parameter would cause mission failure, this should be incorporated in the scoring of the design. This design strategy is mathematically formalized in the aggressive design strategy, which is the method that was chosen from reference [34]. As for different parameters, different weights were determined, the weighted aggressive design strategy from the method of imprecision was adopted to suite this analysis [34], is represented in Equation 5.1 and further elaborated on in this section. Also the weighting of parameters and the chosen method are explained further in this section.

$$\mu(\vec{DP}^*) = max\left[\prod_{i=1}^{q+n} \mu_i^{\omega_i}\right] \tag{5.1}$$

In the method of imprecision, the full set of design parameters and performance parameters describe a concept. The design parameters were listed from DP_1 to DP_n and the performance parameters were listed from PP_1 to PP_q. In this analysis they were bundled in a design parameter vector $\vec{DP}$ and performance parameter vector $\vec{PP}$. The optimized vectors are denoted by the sign $*$. This optimized vector would be the ideal design. Both design and performance parameters can be scored on designer preference.

Within the method of imprecision, but specifically for the aggressive design strategy, ω_i is the normalized weight for the i'th parameter, with the sum of all weights always being 1. Next to this, μ_i is the preference value for the i'th parameter and $\mu(\vec{DP})$ is the preference of the design, as summarized in $\vec{DP}$. The preference value μ_i describes to what extent a value of a design parameter is preferred. All of these values are within a range between zero and one. The design metric of maximizing this value within the design space is formalized in Equation 5.1. Where q is the number of performance parameters and n is the number of design parameters.

5.2.2. PREFERENCE FUNCTIONS

As Equation 5.1 requires a preference value for all of the parameters on a scale from zero to one, all parameters had to be changed to this scale. To do this, a method based on the principles of fuzzy mathematics was used. This resulted into the preference functions. Fuzzy mathematics in general, normalises variables on a wide range to a variable between zero and one [35]. A preference of zero means that this would jeopardize the mission. For example, for the hover altitude, all hover altitudes of lower than one metre would have a preference value of zero since it would not meet the standards set by the VFS [9]. On the other hand, a preference value of one means that the 'ideal' value is reached, and increasing the value of the parameter more in this direction will not increase the preference anymore.

The fuzzification of the parameters was done by the fuzzy approach to multi objective decision making [35]. How the preference of the values of a parameter are modelled, is a designer preference and is elaborated on in the latter of this section.

LINEAR PREFERENCE FUNCTIONS

The most basic function to express the varying preference of a varying parameter, is the linear preference function. It means that for a designer defined range, the preference varies linearly with the value of the parameter. A linear preference function needs an upper and lower boundary as input for ranking the parameter for which the preference is analysed throughout the range of the parameter.

Linear fuzzification was executed as in *Linear membership for a fuzzy objective function* with Equation 5.2 [35]. Here $\mu_i(X)$ is the preference of variable X, linearized between the chosen boundaries f_i^{max} and f_i^{min}, where $f_i(X)$ is the value of the parameter.

$$\mu_i(X) = \begin{cases} 0, & f_i(X) \geq f_i^{max} \\ \frac{-f_i(X)+f_i^{max}}{f_i^{max}-f_i^{min}} & f_i^{min} < f_i(X) < f_i^{max} \\ 1, & f_i(X) \leq f_i^{min} \end{cases} \tag{5.2}$$

The linear theory described in [35] is only able for low parameter values to yield high preference values and vice versa. In practice, this would mean that only low parameter values can have a positive scoring and high parameter values would have a negative scoring. For example, this would apply to noise, but not to velocity. As compared to this theory, the function is adapted to be able to use it in situations where either the upper or the lower limit can be the desired value. In other words, this also allows monotonically increasing preference functions instead of monotonically decreasing preference functions only.

QUADRATIC PREFERENCE FUNCTIONS

As linear preference functions limit the modelling of designer preference to having a constant slope, some situations do not fit this function. The usage of quadratic preference functions enables concave or convex preference functions.

Next to upper and lower boundaries, a quadratic preference function needs a third value to describe the preference. As in reference [35], the value for which a preference of 0.5 is obtained was used as this third value. The lower limit was defined as z_{min}, the average preference as z_{avg} and the upper limit as z_{max}. The function is shown in Equation 5.3 and evaluates the preference $\mu_{\tilde{z}}$ as a function of z. Here a, b and c were obtained by solving the three equations in Equation 5.4. These were bundled in a matrix multiplication and then solved in Equation 5.5. In the tool that was build, these functions were solved for each parameter for which quadratic fuzzification was chosen.

$$a \cdot z^2 + b \cdot z + c = \mu_{\tilde{z}} \tag{5.3}$$

$$\begin{aligned} a \cdot z_{min}^2 + b \cdot z_{min} + c &= 1.0 \\ a \cdot z_{max}^2 + b \cdot z_{max} + c &= 0.0 \\ a \cdot z_{avg}^2 + b \cdot z_{avg} + c &= 0.5 \end{aligned} \tag{5.4}$$

$$\begin{bmatrix} a \\ b \\ c \end{bmatrix} = \begin{bmatrix} z_{min}^2 & z_{min} & 1 \\ z_{max}^2 & z_{max} & 1 \\ z_{avg}^2 & z_{avg} & 1 \end{bmatrix}^{-1} \begin{bmatrix} 1 \\ 0 \\ 0.5 \end{bmatrix} \tag{5.5}$$

5.2.3. APPLICATION

During the application of the multi-objective design strategy, parameters had to be tracked and analysed in order to compare different designs. These parameters were selected to support the quick convergence to a design matching or exceeding requirements. The goal was to be able to see how design parameters can be varied in order to achieve desirable performance parameters.

As in reference [34], an importance ranking from 1 to 5 was used, this is depicted in Table 5.1. In Table 5.2 the tracked parameters without importance weighting are displayed. These parameters are design parameters which do describe the design but do not dictate performance in itself and thus have no importance weighting. Only for the tracked parameters that were given an importance, it was necessary to state which parameter values had which preference. These parameters are displayed in Table 5.3.

Table 5.1: Importance ranking trade-off

Value	**Importance**
1	Vehicle performance marginally influenced and changes can be made with a marginal amount of resources.
2	Vehicle performance slightly influenced and changes can be made with a small amount of resources.
3	Vehicle performance significantly influenced and changes can only be made with significant amount of resources.
4	Vehicle is strongly influenced and changes can only be made with a large amount of resources.
5	Vehicle performance is crucially determined and changes need large resources.

For each parameter in this table, the value of the importance is elaborated on along with the values of the parameter to set up the preference functions. This list indicates the designer preference, so the values for which it is expected to define a *"good"* vehicle. For a few parameters, the values are from concrete sources, for other parameters they are based on an estimation of what defines *"good"*. As elaborated on in subsection 5.2.2, linear preference functions only needed an ideal value (for which $\mu_j = 1$) and an undesired value (for which $\mu_j = 0$). Quadratical preference functions additionally needed a value for which a preference of 0.5 is obtained ($\mu_j = 0.5$). Thus, the quadratical preference functions can be identified by having a value filled in for the average preference value.

A notable missing parameter is the cost of the vehicle. Cost for the overall design was evaluated after the design converged. This was in order to save resources during the iteration process. This could be done as the vehicle will be a one-off proof of concept which reduces the importance of costs. However, for material selection, cost was taken into account throughout the iteration process.

In order to increase the efficiency of the iteration process, a few simplifications have been made on how the parameters in Table 5.3 were represented in the analysis. These simplifications are listed below.

- *The maximum range at cruise velocity at cruise altitude*: This is simplified by neglecting the hover time (two times five seconds) in the mission stated by the VFS. This results in the range being the multiplication of the cruise velocity with the endurance.
- *Controllability, pitch rate*: It is assumed that the controllability of the vehicle is influenced to the largest extent by the pitch rate and thus solely represents the controllability of the vehicle.
- *Sustainability, power consumption (at cruise)*: It is assumed that the most significant power consumption, is the power consumption at cruise velocity.
- *Stability, settling time*: It is assumed that the stability of the vehicle is influenced to the largest extent by the settling time and thus solely represents the stability of the vehicle.
- *Hover altitude:* The goal was to escape out of ground effect. This was assumed to happen for the maximum assumed radius of 2 metres at an hover altitude of 4 metres or higher. If this was the case, 4 metres was denoted in the design tool. This also was the case for high hover altitudes.

Table 5.2: Parameters tracked in the iteration process without importance ranking

Parameter	**Unit**
Ideal RPM at hover	min^{-1}
Torque at ideal-RPM at hover	Nm
Rotor-radius	m
Tip-speed	m/s
Torque at cruise RPM	Nm
Lift at hover power without ground effect	N
Drag at cruise velocity	N
Screw weight (sum of hub, blade and duct weight)	kg
Engine weight including battery	kg
Control system weight	kg
Airframe weight (sum of struts, truss structure, landing gear and auxiliaries)	kg
Thrust over weight ratio at hover power without ground effect	-
Total vehicle height	m
Payload	kg
Max take-off weight	kg
Endurance at cruise velocity	s
RPM at cruise power	min^{-1}

Table 5.3: Parameters tracked in the iteration process with importance ranking

Parameter	Unit	Weight	Ideal value	Average preference value	Undesired value
Hover altitude at hover power	m	5 as escaping from ground effect is crucial for the ability to compete.	4 as this means that the vehicle can escape ground effect	3 as this gives a convex preference function.	1 as set by the VFS [9]
Maximum range at cruise velocity and altitude	m	5 as a large range increases the usability on a crucial extent	20000 as this is achievable but makes the vehicle usable	1000 as this is the bottom-line for usability of the vehicle.	20 as set by the VFS [9]
Sustainability: Noise at SEL	dB	3 as this is a figure the helicopter industry wants to improve on [5]	70 as industry wants 10 dB reduction [5]		82 as this is required by regulations
Stability: settling time	s	3 as control and stability together are crucial for the vehicle (thus score 5 together) where stability is more important for safety.	5 as this indicates a stable vehicle		120 as this is unacceptable
Controllability: Pitch rate	deg /s	3 as control and stability together are crucial for the vehicle (thus score 5 together) where stability is more important for safety.	30 as this indicates a fast responding vehicle	10 as this produces a concave plot.	1 as this means to little control authority
Cruise velocity	m/s	2 as this is not a part of the mission set by the VFS [9] but increases competitiveness	20 as this is deemed fast for what is achievable	6 as exceeding the minimum already is satisfactory.	4,3 as set by the requirements
Endurance at cruise velocity	sec.	2 as range is more relevant to get from one place to another	1800 as a high goal is appropriate.	120 as doubling the minimum is satisfactory	60 as set by the VFS [9]
Sustainability: Maintainability	-	2 as it is not very relevant for a proof of concept	5 for the manual scoring scale		-5 for the manual scoring scale
Sustainability: Safety	-	2 as most safety measures have limited impact on performance of other parameters	5 for the manual scoring scale		-5 for the manual scoring scale
Sustainability: Power consumption (at cruise)	kW	1 as it is only relevant in future development.	0 as a lower value, should score higher	100 as this would be an acceptable power consumption	250 as this is inefficient for a 60kg payload
Aesthetics	-	1 as this does not influence the functioning of the vehicle, but aids in marketing	5 for the manual scoring scale		-5 for the manual scoring scale
Sustainability: Manufactu-rability	-	1 as it is only relevant in future development	5 for the manual scoring scale		-5 for the manual scoring scale

Table 5.4: Definitions used for manual scoring

	Maintainability	Aesthetics	Safety	Manufacturability
5	Cleverly placed maintenance holes are present. Parts can easily be reached. Most maintenance task can be performed by the user. Widely available materials for maintenance are used and are purchasable at specialized stores.	Target group has been extensively researched and needs are implemented. Innovative design. All subsystems are tightly packaged and neatly finished. Sizing between parts makes sense.	Crash is very unlikely, back-up systems are present for all propulsive and control systems. If a crash happens, pilot is safe. Pilot can not be hurt in operation.	Existing machinery and widely available materials are used. Manufacturing times are short.
3	Maintenance holes are present. Most parts can be easily reached. Most maintenance task can be performed by the user after consulting the manufacturer. Maintenance materials are available at some specialized stores.	Tightly packaged subsystems. Target group needs has been taken into account.	Extra safety measures have been taken. Crash risk is less dependent on piloting skills. Crash risk is unlikely. Verification and validation have been performed.	Machinery only slightly modified. Few exotic materials.
0	Some maintenance task can be performed by the user. Most critical parts can easily be reached. Maintenance materials can only be purchased at a few specialized shops per continent with short (<6 months) delivering times .	Some efforts are made for an aesthetically pleasant design. Target group needs has been taken into account. Similarities in shape with existing vehicles.	The safety measures for certification are implemented. Under normal circumstances crash risk is unlikely and dependent on pilot skills. Prescribed safety factors are used. Verification and validation have been performed.	Modified machinery has been used. Some exotic materials are used. Manufacturing times are moderate (1 year per vehicle).
-3	Most parts are hard to reach. Maintenance task can only be performed by mechanics at few companies. Maintenance parts can only be purchased from a few stores throughout the world with long (>6 months) delivering times.	Designed for performance, target group has been considered.	High crash risk with possibly fatal results. Some moving part are exposed.	New tools and modified machinery used. Many exotic materials used.
-5	Maintenance holes are lacking and parts are hard to reach. Maintenance tasks can only be performed by expert personnel from the manufacturer. Maintenance parts can only be purchased from the company with long waiting times (»6 months).	Designed just for performance, target group not taken into account, aesthetics not considered. Sizing of vehicle is out of proportion and does not make sense for a personal aerial vehicle.	High crash risk with fatal results. Pilot and environment is exposed to moving parts. Environment is at risk. Verification and validation of safety measures is lacking.	New tools and machinery need to be developed. Mostly exotic materials are used. Manufacturing times are long (»1 year per vehicle).

6

Aerodynamics

To determine the capabilities and power requirements of the aerial screw vehicle several steps were taken and are described throughout this chapter. Preliminary estimates of helicopter trust and power behaviour rely on actuator disc and momentum theory. Numerous assumptions incur inaccuracies, however these calculations give good preliminary estimates and more importantly, an ideal hover power and induced velocity.

Next to hover, the vehicle shall be able to change attitude and fly forward during flight. These flight mechanics and how this influences the aerodynamics around the rotor can be described through the analysis of the equation of motions.

The flight mechanics and improved lift and power calculations are used in the blade element theory (BET). In this BET, blades are analysed per section and integrating yields a total lift and required power. However, this theory only applies for slender blades. Marine propellers use an altered version of this theory and the lift and power calculations are also inspired by this version.

The aerodynamic properties of ducts and their shape are analysed and fitted such that they remain lightweight, while contributing to the overall lift. Besides the positive effect of ducts, negative effects on rotary wings, such as tip losses are quantified.

The calculations are verified by computing the trust and power of propellers of which these numbers are already known. Moreover, tests have been performed with 3d printed scale-models of the propellers.

6.1. Actuator disc/Momentum theory

The power required and the induced velocity for hover can be estimated with the actuator disc momentum theory. It is the simplest form of power required calculations and it assumes that the propeller is a rotating disc that gives axial momentum to the airflow going through the disc [36]. This theory is applicable for every kind of rotor and forms a basis for the more elaborate methods described later on in this chapter, namely the blade element theory. The actuator disc theory is also applicable for ducted propellers or screws when some minor adjustments are made to the formulas [11]. For the actuator disc momentum theory, the following assumptions should be taken into account [36]:

- The rotor is a permeable disc, infinitely thin and loaded uniformly
- The axial pressure includes no contribution of the pressure on the duct skin
- Laminar, incompressible and inviscid flow

The actuator disc momentum theory for both the open rotor and ideal ducted case is visualised in Figure 6.1.

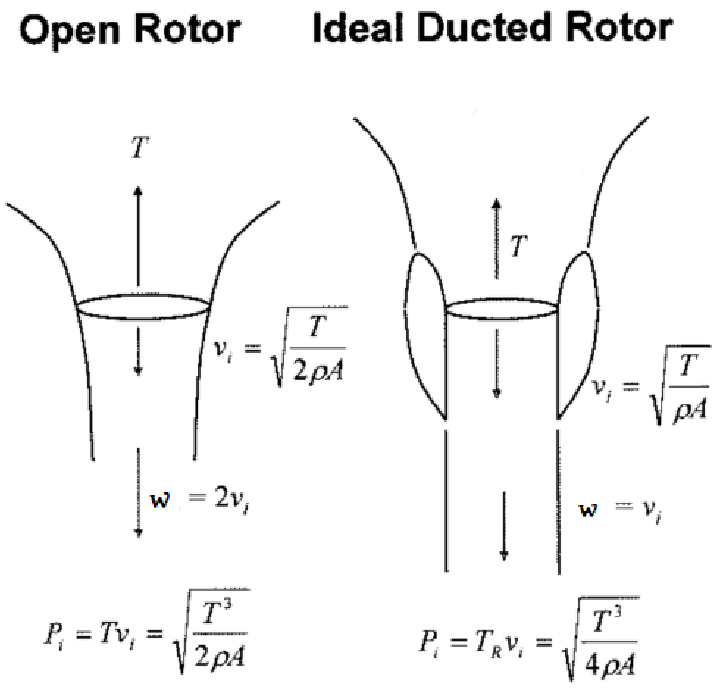

Figure 6.1: Actuator disc and momentum theory for open rotor and ideal ducted case [11]

The actuator disc momentum theory rely on the principles of conservation of mass and conservation of momentum. Doing the derivation for the actuator disc results in that the wake velocity w is twice the amount of the induced velocity v_i as seen in Equation 6.1 [36].

$$w = 2v_i \tag{6.1}$$

For an ideal ducted propeller these two velocities will be equal, see Equation 6.2. The difference comes from the increase of thrust due to the duct itself. [11].

$$w = v_i \tag{6.2}$$

Continuing the derivation, Equation 6.3 can be derived for the induced velocity v_{i_O} for an open rotor in hover [36]. Where T is the thrust, ρ the air density and A the area of the disc.

$$v_{i_O} = \sqrt{\frac{T}{2\rho A_{disc}}} \tag{6.3}$$

Again the same derivation, but then with the use of Equation 6.2 for the ideal ducted case it results in a slightly different formula, see Equation 6.4 [11].

$$v_{i_{duct}} = \sqrt{\frac{T}{\rho A_{disc}}} \tag{6.4}$$

The equations Equation 6.3 and Equation 6.4 conclude that the induced velocity for a ducted propeller or screw, $v_{i_{duct}}$ will be higher than that for an open rotor v_{i_O} depending on how ideal the rotor is (which is at most 41%), as can be seen in Equation 6.5 [11].

$$\frac{v_{i_{duct}}}{v_{i_O}} = \sqrt{2} = 1.41 \tag{6.5}$$

The induced velocity equations will furthermore be used for the aerodynamic calculations with the use of blade element (momentum) theory. The thrust will be set equal to the maximum take-off weight of the vehicle for the power calculations in order to obtain the ideal power to hover and calculate the Figure of Merit (FM) later on to check the hover efficiency.

For the power calculations (P_{id}, ideal power) the conservation of energy was included. Combining this principle with the earlier described results in Equation 6.6 for the ideal open rotor case and in Equation 6.7 for the ideal ducted rotor as power can be calculated by multiplying the thrust with the induced velocity [11, 36].

$$P_{id_O} = T v_{i_O} = \sqrt{\frac{T^3}{2\rho A_{disc}}} \tag{6.6}$$

$$P_{id_{duct}} = T v_{i_{duct}} = \sqrt{\frac{T^3}{4\rho A_{disc}}} \tag{6.7}$$

Comparing the two equations for ideal power leads to a decrease of around 30% in ideal power for the ducted case, as can be seen in Equation 6.8 [11]. Thus, making the ducted case more efficient.

$$\frac{P_{id_{duct}}}{P_{id_O}} = \frac{1}{\sqrt{2}} = 0.707 \tag{6.8}$$

The outcome of the actuator disc momentum theory are the induced velocities and ideal powers. These values will be used for calculating the hover performance. The hover performance is expressed in the FM. The FM is the ratio of the theoretical minimum power or ideal power P_{id} to hover with respect to the actually required power or hover power P_{hov}. Where the former is calculated with the actuator disc theory as described above and the latter with the blade element (momentum) theory following in the next section, see Equation 6.9 [36].

$$FM = \frac{P_{id}}{P_{hov}} \tag{6.9}$$

The FM is a value between 0 and 1, where 1 is an ideal rotor with no losses and drag. Furthermore, the lower the FM, the higher the power required [36].

6.2. BLADE ELEMENT THEORY

To be able to determine the geometry and calculate the power required to achieve the necessary thrust a Blade Element Theory (BET) tool was developed. BET is a method of calculating the forces and torque generated by a rotor by analyzing it as a series of two dimensional blade elements treated as if flying straight. Each blade element has its own local radius, local lift and drag coefficient, own air velocity coming in at an angle of attack. In this section it is explained how the classical helicopter blade element theory is adapted and applied to the aerial screw.

6.2.1. BLADE ELEMENT THEORY FOR AN AERIAL SCREW

Blade Element Theory analyses a conventional helicopter rotor by first dividing it along the span of the rotor blade with a series of straight cuts as can be seen in Figure 6.2. Each of these blade elements have a local tangential velocity due to rotation, the lift and drag forces of each element are calculated and summed up to finally get the total thrust, torque and power of the rotor.

While making such straight cuts is trivial for a typical rotor, it is incompatible with an aerial screw which sweeps a full rotation between leading and trailing edges. This issue was solved by using the same approach taken in marine propeller design[37]. The difference lies in how the blade elements are cut. Instead of straight cuts, in marine Blade Element Theory, the rotor is cut apart into curved blade elements by cylindrical cuts. Similar cuts can also divide an aerial screw into curved blade elements, this can again be seen in Figure 6.2.

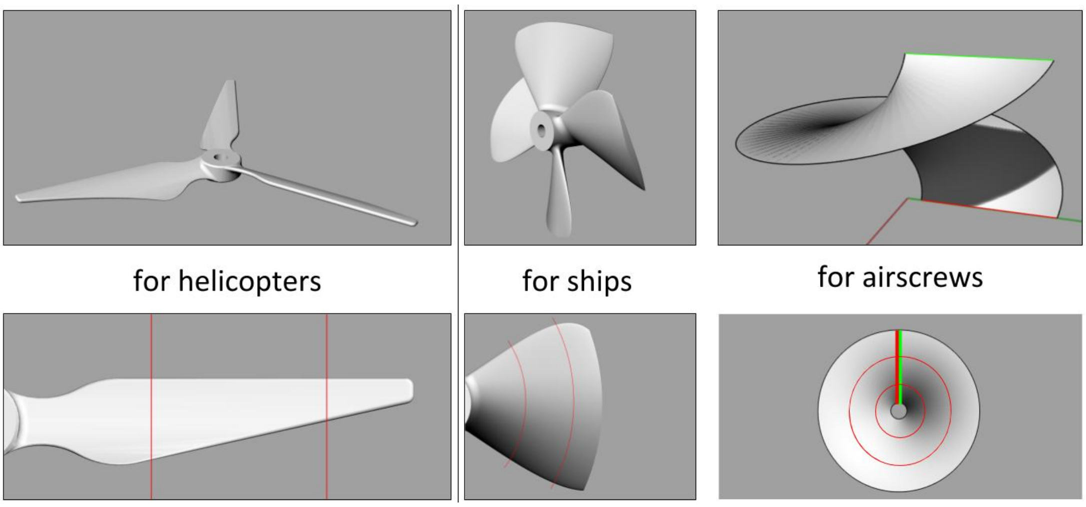

Figure 6.2: Differences within Blade Element Theory for different screw types

The leading and trailing edge of the blade segment is separated vertically by a distance known as the pitch p (not to be confused with blade pitch angle θ) and horizontally by the circumference of a full 360^o sweep, $2\pi r$. The diagonal distance between the leading and trailing edge then is the chord length c given in Equation 6.10a. These geometric parameters are also illustrated in three dimensions in Figure 6.3.

It is possible to analyse the cross-sections from Figure 6.2 individually by transforming them into a 2D shape. These 2D blade elements then appear as in Figure 6.4a.

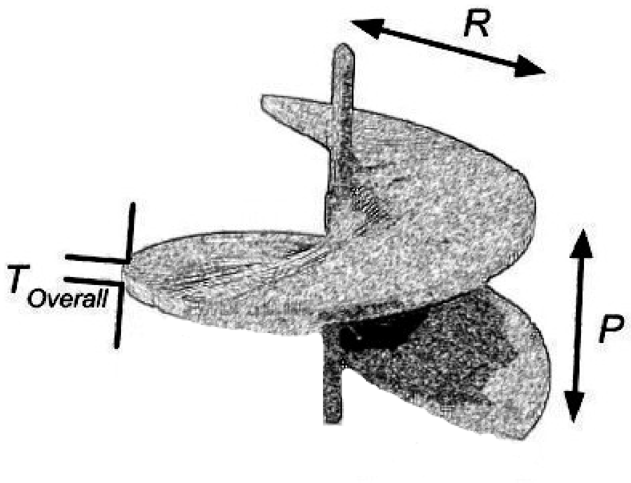

Figure 6.3: Aerial screw geometric parameters

$$c = \sqrt{p^2 + (2\pi r)^2} \tag{6.10a}$$

$$\theta = \arctan \frac{p}{2\pi r} \tag{6.10b}$$

The reference angle formed between the plane of the rotor disc and the chord line is the blade pitch angle θ which can be calculated with Equation 6.10b. Also depicted is the zero-lift angle α_{0L}, the angle of attack where no lift is generated. This value is zero and the line coincides with the chord line for a symmetrical airfoil but is not the case for a cambered airfoil.

The thrust calculation at every element was executed with Equation 6.14c. This formula was adjusted to comply with the aerial screw geometry in every flight phase i.e. hover, climb flight and forward flight. Due to the aerial screw geometry the chord c varies with the radius. The lift coefficient C_l varies radially by Equation 6.13c, as the angle of attack α changes, because the pitch creates a varying geometric twist θ and inflow angle ϕ. Further the velocity was generalised to implement all the different flight phases.

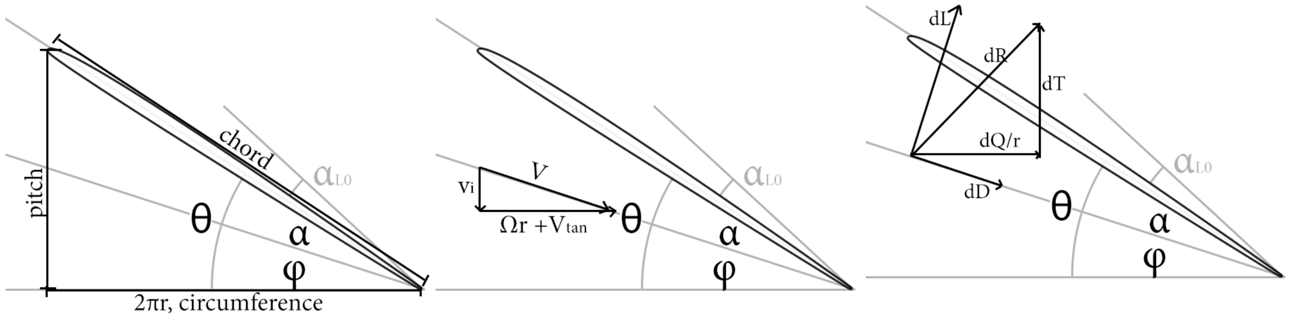

(a) Aerial screw geometry definitions

(b) Aerial screw angle definitions

(c) Conversion of forces from air velocity to rotor coordinate system

Figure 6.4: Aerial screw geometry definitions and force conventions

First, the induced velocity v_i at every section had to be calculated in order to calculate the lift coefficient and the velocity. The induced velocity was calculated by Equation 6.11 [38]. This formula was constructed by equating the momentum equation with the lift equation and includes non-uniformity and the additional axial velocity due to climbing from Equation 7.8b. Ω' as in Equation 6.12a is the angular velocity corrected for the incoming tangential velocity as given by Equation 7.8a. Finally, the resultant velocity was calculated with Equation 6.12b.

$$v_i = \frac{-\left(\frac{\Omega'}{2} C_{l_\alpha} c + 4\pi V_{axial}\right) + \sqrt{\left(\frac{\Omega'}{2} C_{l_\alpha} c + 4\pi V_{axial}\right)^2 + 8\pi\Omega'^2 C_{l_\alpha} cr\left(\theta - \alpha_{0L} - \frac{V_{axial}}{\Omega' r}\right)}}{8\pi} \tag{6.11}$$

$$\Omega' = \frac{\Omega r + V_{tan}}{r} \tag{6.12a}$$

$$V = \sqrt{v_i^2 + (\Omega r + V_{tan})^2} \tag{6.12b}$$

Equation 6.13a was applied to calculate the inflow angle depicted in Figure 6.4b. From this the angle of attack by Equation 6.13b was calculated and finally with Equation 6.13c the lift coefficient was determined at every element, in which the Prandtl-Glauert compressibility correction are implemented [39]. Different lift curve slopes C_{L_α} were applied for different elements, because the relative thickness of the airfoil decreases radially and the Reynolds number and Mach number increases radially.

$$\phi = arctan\frac{v_i}{\Omega r + V_{tan}} \tag{6.13a}$$

$$\alpha = \theta - \phi \tag{6.13b}$$

$$C_l = \frac{C_{l_\alpha}(\alpha - \alpha_{0L})}{\sqrt{1 - \frac{(\Omega r)}{a}^2}} \tag{6.13c}$$

6.2.2. CALCULATION OF THRUST AND POWER IN BET

Each radial position has a blade element of surface area dS, Equation 6.14a, and an airflow of velocity V flowing at a local inflow angle ϕ. The blade element is at a certain pitch angle therefore it has a certain angle of attack relative to the inflow angle and a lift coefficient C_l which causes a lift force dL to be produced perpendicular to the inflow, Equation 6.14b. This lift has a vertical component which is parallel to the axis of the rotor, which is the thrust dT, Equation 6.14c.

$$dS = cdr \tag{6.14a}$$

$$dL = \frac{1}{2}\rho V^2 C_l dS \tag{6.14b}$$

$$dT = dL\cos\phi \tag{6.14c}$$

Each element also produces drag dD, Equation 6.15a,which contributes to the rotor's profile torque dQp, Equation 6.15b. The horizontal component of the lift force, parallel to the rotor disc plane, also contributes to torque and is known as induced torque dQi, Equation 6.15c.

$$dD = \frac{1}{2}\rho V^2 C_d dS \qquad (6.15a)$$

$$dQp = dDcos(\phi)r \qquad (6.15b)$$

$$dQi = dLsin(\phi)r \qquad (6.15c)$$

Finally all the element thrusts dT and torques dQ are integrated into the total thrust T and torque Q of the rotor, as can be seen in Equation 6.16a and Equation 6.16b. Finally the rotor's power P is calculated by multiplying the torque with the rotational velocity, as can be seein in Equation 6.16c.

$$T = \int_0^R dT(r)dr \qquad (6.16a)$$

$$Q = \int_0^R dQi(r) + dQp(r)dr \qquad (6.16b)$$

$$P_{total} = (Q)\Omega \qquad (6.16c)$$

The relevant equations are given in Equation 6.14a to Equation 6.16c where the chord c, air velocity V, lift coefficient C_l, drag coefficient C_d, inflow angle ϕ are all functions of the local radius r; and Ω is the angular velocity of the rotor. The geometry of the forces involved are also illustrated in Figure 6.4c where dL and dD are shown perpendicular and parallel respectively to the air velocity vector which comes in at inflow angle ϕ. Combined they result in the resultant force dR which can also be decomposed perpendicular and parallel to the rotor disc as thrust dT and torque dQ/r (torque divided by radius r to be represented as a force instead of torque).

6.2.3. CORRECTION FACTORS

The calculations discussed in subsection 6.2.2 give the ideal thrust for a rotor with no tip losses, while the aerial screw is a non-ideal shrouded rotor. First Prandtl's tip-loss [40] factors were calculated for and applied to each blade element's section lift such that$dL = FdL_{ideal}$ where $F = \frac{2}{\pi}cos^{-1}e^{-f}$ and $f = \frac{1-\frac{r}{R}}{2\frac{r}{R}\phi}$

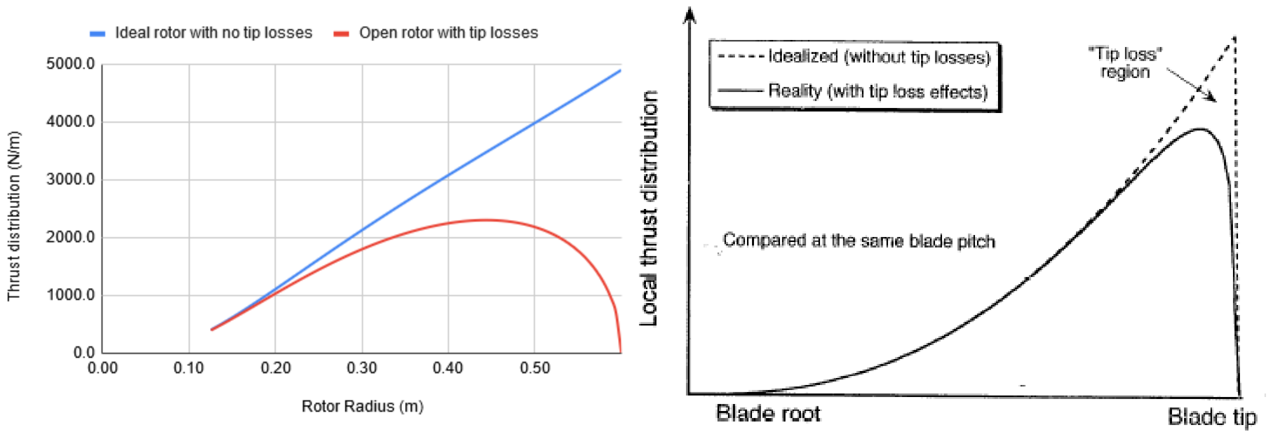

(a) Lift distribution across the rotor span before and after tip-loss

(b) Tip-loss of an example conventional rotor [40]

Figure 6.5: Tip loss comparison between conventional rotor and aerial screw

Figure 6.5a depicts the thrust distribution of an aerial screw of total radius 0.6 m in hover before and after tip loss factors are applied. (Note that the data starts at 0.12m because this is where the hub ends and the rotor blade begins.) Approximately 40% of the total thrust is being lost. For comparison Figure 6.5b from Leishmann[40] shows a typical rotor's tip loss, note that far less thrust is being lost.

Finally the aerial screw is required to fly at a low altitude of one metre. The rotor will be in ground effect, where the ground poses a constraint on the wake development. This has a positive effect on the rotor performance.

Ground effect is the effect of the ground on the rotor performance, due to the constraint on the rotor wake development. Because at the ground surface the downward velocity of the wake is reduced to zero, the wake expands horizontally and causes an increase in pressure in the wake, which results in a lower induced velocity for a given thrust. This decreases the power required to hover. This effect is most significant when the rotor height above the ground is less than the rotor diameter [38]. Therefore, the vehicle designed for the VFS competition can experience significant benefits from the ground effect, if the radius is larger than 0.5 m [40].

The increase in thrust for a constant power can be calculated with Equation 6.17, which gives the relation between the thrust with ground effect over the undisturbed thrust and can be used until the height of the bottom of the rotor is two times the rotor radius. After this, the effect of the ground on the wake will be negligible. The formula comes from an analysis of Cheeseman and Bennett on the ground effect [41].

The ground effect results in a higher thrust at the same power level, this is most significant if the height is smaller than the rotor diameter. The additional thrust in ground effect is calculated with Equation 6.17. However, this effect is on the rotor and not the combination of the shrouded rotor. Therefore, the thrust of the rotor in the duct had to be determined. This was executed by multiplying a correction factor of the thrust coefficient of only the rotor in the ducted case over the open rotor with the thrust of the open rotor, as given in Equation 6.25, which is described in detail in section 6.5 [42].

$$\Delta T_g = T_{rotor}\left(\frac{1}{1-\frac{R}{4h^2}}-1\right) \tag{6.17}$$

6.3. AIRFOIL SELECTION

In the concept phase the blade was modelled as a flat plate. Although, for optimising the design of the blade an airfoil could have a significant effect on the performance of the blade. The application of an airfoil will result in different zero lift angle of attack, lift curve slope and stall angle. Hence the application of a suitable airfoil could result in higher lift coefficients at a desired angle of attack. First, different airfoil parameters i.e. thickness and camber were analysed and how they affected the lift coefficient over angle of attack graph. After which the angle of attack and Reynolds number (as calculated in Equation 6.18 with air density ρ, velocity V, reference length L and dynamic viscosity μ) for the aerial screw were analysed and a decision was made for the optimal airfoil.

$$Re = \frac{\rho V L}{\mu} \tag{6.18}$$

Four-digit NACA airfoils with data from Javafoil [1] were used. The NACA 4-digit series consist of 4 digits indicating different parameters. The first digit indicates the maximum camber as percentage over the chord. The second digit describes the distance of maximum camber from the airfoil leading edge in tenths of the chord. The last two digits indicate the thickness over the chord, where the maximum thickness is at 30% of the chord. A NACA 0000, a flat plate; a NACA 0005, a symmetrical airfoil with 5% thickness; a NACA 5500, a flat plate with 5% camber; and a NACA5505, a 5% cambered airfoil with 5% thickness from Javafoil are depicted in Figure 6.6, Figure 6.7, Figure 6.8 and Figure 6.9 respectively for illustrative purposes.

6.3.1. THICKNESS

The thickness has a significant effect on the $C_l - \alpha$ curve, as shown in Figure 6.10a. This graph displays the NACA 0001 with green, NACA 0002 with red, NACA 0004 with purple and NACA 0008 with blue. This are all symmetric airfoils, where only the thickness is increased. From this it could be concluded that increasing the thickness increases the $C_{l_{max}}$ and the α_{stall}. However, changing the thickness does increase the weight and does not affect the C_{l_α}.

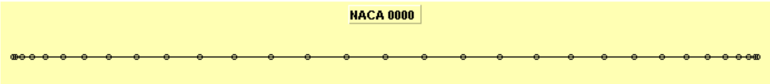

Figure 6.6: NACA0000, no camber, no thickness

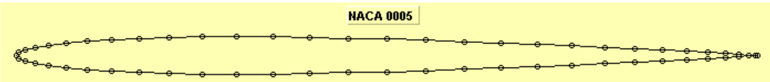

Figure 6.7: NACA0005, no camber, 5% thickness

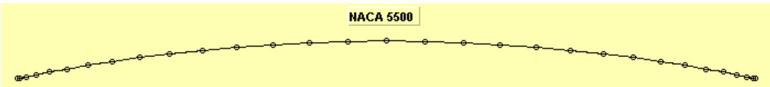

Figure 6.8: NACA5000, 5% camber, no thickness

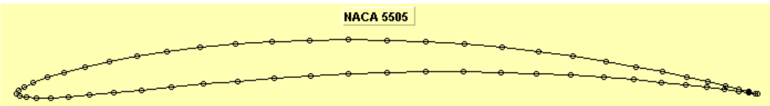

Figure 6.9: NACA5505, 5% camber at 50% position, 5% thickness

6.3.2. CAMBER

The camber is the asymmetry between the two surfaces of the airfoil. Camber is defined by two parameters in the 4 digit NACA airfoil; the location of the maximum camber and the camber. Figure 6.10b displays the effect increasing the camber, where the green line with squares indicates the NACA 1404, red with circles the NACA 2404, purple with pluses the NACA 4404 and blue with crosses the NACA 8404. From this figure it was concluded that increasing the camber resulted in a increase of the $C_{l_{max}}$ and decreased the α_{0L} and the C_{l_α} and the α_{stall} remains constant. Therefore, increasing the camber results in a higher C_l for the same α. Figure 6.10c displays the effect of changing the location of the maximum camber, where the green line with squares is the NACA 4204, red with circles the NACA 4304, purple with pluses the NACA 4404 and blue with crosses the NACA 4504. This figure presents that increasing the location of the camber shifts the graph to the left.

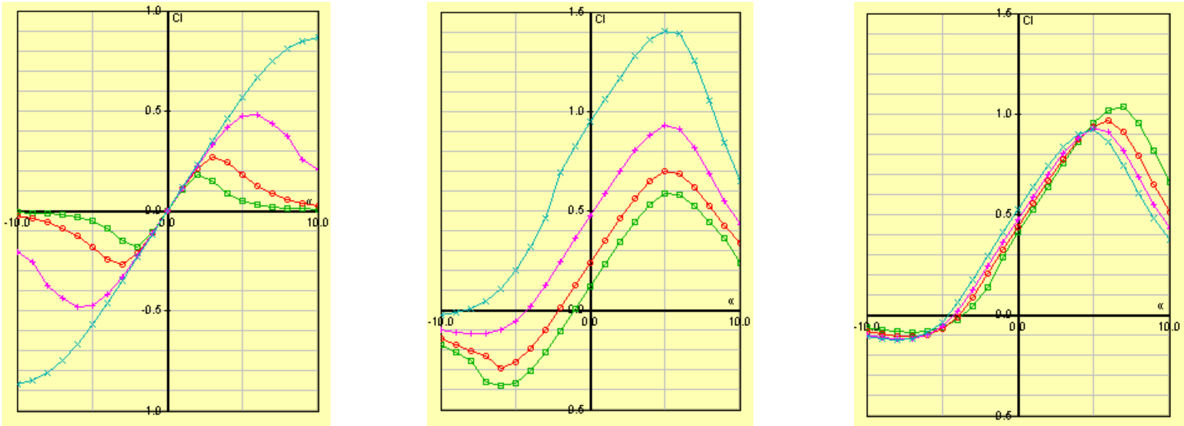

(a) Effect of thickness on C_l-α

(b) Effect of camber on C_l-α

(c) Effect of camper location on $C_l - \alpha$

Figure 6.10: Effect of changing airfoil parameters on the $C_l \alpha$ curve [1]

6.3.3. AIRFOIL INTERPOLATION

Instead of finding relevant airfoil data for every single blade element, data was obtained by interpolating between a limited number of data points. Data for airfoils of 1 to 10% t/c were acquired at 1% intervals. The blade elements were assigned a certain thickness based on a continuous function, then the relevant aerodynamic coefficients were looked up by linearly interpolating between the two closest airfoils.

6.3.4. FINAL AIRFOIL SELECTION

Analysis of the aerodynamic program concluded that the angle of attack was between the 4 degrees near the root and rapidly decreased to approximately -3 degrees at 70% of the radius and increased again to -2 degrees at the tip. Since these are low angles it was decided to implement a higher camber of 8% as this increases the lift coefficient significantly for these low angles of attack. However, increasing the camber further resulted in a higher drag and a complex aerial screw geometry. The location of the camber was decided to be at the middle of the chord, as this increases the C_l at low angles. At last it was decided to have a decreasing thickness. From a thickness at the root 8% to 1% at the tip. This decision was made, because at the root it has to have a high thickness, due to the angles of attack of 4 degrees, as it would stall with a thickness of 1%.

However, further to the tip, this high thickness is not required as it has an α of -2 degrees, hence it will not stall. Further, the thickness of 8% has no difference in C_l in comparison with a thickness of 1% at α of -2 degrees, as shown in Figure 6.11a. Hence it will only increase the weight.

To summarise the NACA 8508 is applied at the tip, which decreases exponentially to the NACA 8501, this is visualised in Figure 6.11b. The lift curve of these airfoils are shown in Figure 6.11a, where green indicates the NACA 8501, red the NACA 8502, purple the NACA 8504, light blue the NACA 8506 and dark blue the NACA 8508.

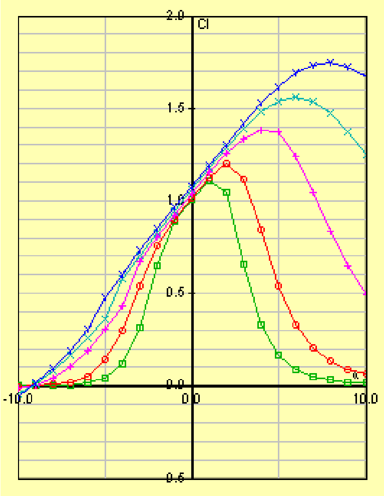

(a) Lift curve of the NACA 850X used [1]

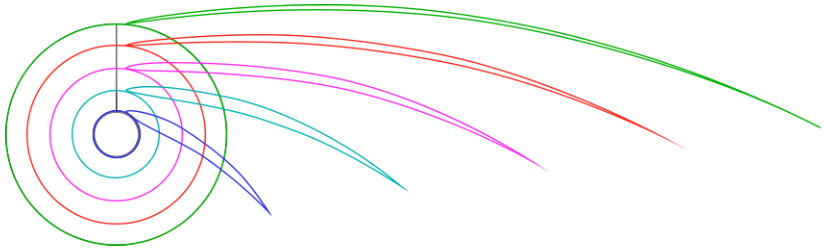

(b) NACA 8508 through 8501 airfoil in their respective radial positions

Figure 6.11: SolidityONE airfoil design

6.4. BLADE SOLIDITY

Blade solidity is defined as a ratio of the blade area to disc area as in Equation 6.19. It was required to calculate this because the VFS requested a solidity of at least 1.

$$\sigma = \frac{A_{blade}}{A_{disc}} \tag{6.19}$$

For a conventional rotor blade with no camber and constant chord the blade area may be calculated with Equation 6.20.

$$A_{bladeconventional} = ncR \tag{6.20}$$

However to calculate the area of a blade with varying chord it is necessary to integrate Equation 6.10a along the radius to become Equation 6.21 (shown from 0.12 to 0.6 m as the rotor's blade hub ends and the blade starts at 0.12 m and ends at 0.6 m).

$$A_{bladevaryingchord} = \int_{0.12}^{0.6} c(r)\mathrm{d}r = \int_{0.12}^{0.6} \sqrt{p^2 + (2\pi r)^2}\mathrm{d}r = 0.9991 \tag{6.21}$$

The SolidityONE's blade represented as a simple helicoid formed by the chord line has a solidity just under 1. However this is not the blade's true surface area. As can be seen by comparing Figure 6.6 and Figure 6.8, the centerline of an airfoil with camber has more length and therefore surface area than the chord line. If the camber line is modelled as a circular arc, the ratio between the arc length and chord can be calculated as Equation 6.22.

$$\frac{length_{camberline}}{length_{chord}} = \frac{(c/2)^2 + f^2}{cf} sin^{-1} \frac{cf}{(c/2)^2 + f^2} \tag{6.22}$$

And finally the chord area can be multiplied with this multiplier to yield the true surface area of a cambered blade.

$$A_{bladeactual} = A_{bladevaryingchord} \frac{length_{camberline}}{length_{chord}} \tag{6.23}$$

6.5. DUCT AERODYNAMIC DESIGN

Following up from the trade-off performed in the midterm phase a ducted configuration was the obvious choice to enhance the performance of the aerial screw for the provided mission profile [4]. The benefit of having a duct for screw type propellers became more apparent due to the above mentioned tip losses in Figure 6.5. In order to utilise the performance gains obtained from adding a duct to the aerial screw, the duct should be designed carefully. To summarise, the following duct design parameters are considered in this section: tip clearance, inlet lip radius, diffuser angle and diffuser length. This section will be concluded with the estimated effects the adding of the duct has on the overall performance.

6.5.1. DESIGN APPROACH

Choosing the wrong set of parameter values results in not utilising the possible performance gains or even worsening the overall performance of the vehicle due to an increase of weight. The process of optimisation and converging towards an optimum set of parameters is a complex process for multiple reasons. Firstly a certain optimum parameter set is only valid for a certain rotor, which in case of the yet unproven concept of the aerial screw results in an unique set of parameters [42]. Furthermore since formulas describing duct performance is limited to only actuator disc and momentum theory and these formulas are not describing duct performance parameters, this set of optimum parameters can only be obtained experimentally [11]. However due to the time span of only 10 weeks for the DSE project, experiments providing adequate information on duct performance parameters including aerial screw testing is not feasible, but are recommendations for further proceedings. Lastly the effect a certain duct performance parameter has on the overall performance is dependent on the other parameters and rotor design, therefore a clear relationship a certain duct performance parameter has on the overall design is difficult to predict [42].

In order to still be able to design the duct and find the required set of parameters, experimental data from literature has been consulted [11, 42]. Although this approach will most likely not give accurate results due to the before mentioned reasons and since the aerial screw is vastly different than conventionally used rotor designs. It has been assumed to give sufficiently accurate results for now, until future experiments are conducted. The experimental data from Pereira is primarily used, since these experiments describe the effects of all the duct design parameters individually [42].

6.5.2. DESIGN PARAMETER SELECTION

As stated before the following design parameters are being considered: tip clearance, inlet lip radius, diffuser angle and the diffuser length. These parameters are visualised in the figure below, see Figure 6.12. The duct inlet diameter D_t is also indicated.

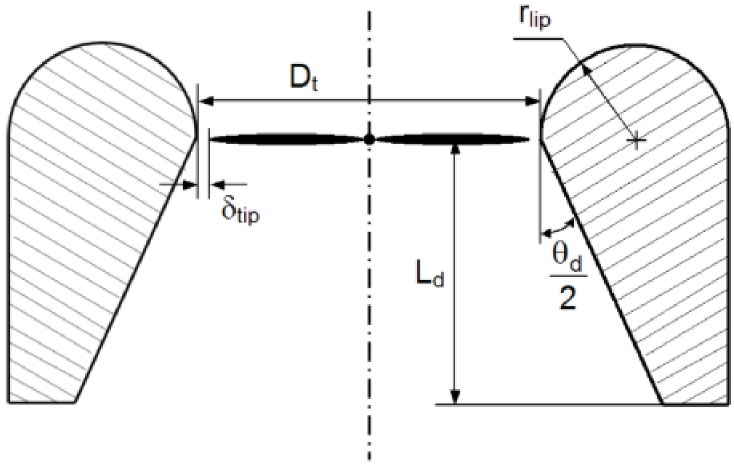

Figure 6.12: Duct design parameters influencing duct performance [42]

DUCT INLET DIAMETER

The duct diameter is determined by the rotor design and the tip clearance. Hence it depended mostly on the rotor design.

TIP CLEARANCE

Increasing the tip clearance (δ_{tip}) has adverse effects on performance [42].

- A decrease in maximum C_T/C_P (Thrust coefficient over power coefficient).
- A decrease in maximum figure of merit (FM).
- A decrease in $C_{T_{SR}}/C_{T_{OR}}$ (shrouded rotor thrust over open rotor thrust) at constant C_P.
- An increase in $C_{P_{SR}}/C_{P_{OR}}$ (shrouded rotor power over open rotor power) at constant C_P.

Furthermore it was stated that the increase in performance was more prominent when the other parameters are worse (e.g. no or small lip radius, no or small diffuser etc.) or when the open rotor case was performing better [42]. This is not a surprise since the gains are not unlimited and if a certain rotor is already performing with low losses, it is more difficult to gain significant margins on performance. Thus concluding the tip clearance should be as small as possible, resulting in a recommended optimum value of $0.1\%D_t$, which is also the lowest tip clearance tested [42].

INLET LIP RADIUS

The change of inlet lip radius has significant effects on duct performance [42].

- An increase in maximum C_T/C_P (Thrust coefficient over power coefficient).
- An increase in maximum figure or merit (FM).
- An increase in $C_{T_{SR}}/C_{T_{OR}}$ (shrouded rotor thrust over open rotor thrust) at constant C_P.
- An decrease in $C_{P_{SR}}/C_{P_{OR}}$ (shrouded rotor power over open rotor power) at constant C_P.

Furthermore it was stated that less power was provided by the rotor itself, resulting in an increase of off-loading of the rotor by the duct [42]. Moreover the inlet lip radius is not dependent on the other design parameters. Thus concluding the lip radius should be as large as possible. However since the experiments conducted by Pereira where up to a lip radius of $13\%D_t$ (the available data) and at this value the duct was performing the best, the lip radius has been set to this value [42].

DIFFUSER

The diffuser is a combination of two design parameters, the diffuser angle θ_d and the diffuser length L_d. The effect of these two design parameters are expressed in the expansion ratio of the diffuser σ_d. The expansion ratio is calculated with Equation 6.24.

$$\sigma_d = \left((1+2\frac{L_d}{D_t}tan(\frac{\theta_d}{2})\right)^2 \tag{6.24}$$

According to the experimental data from Pereira an optimum expansion ratio was found to be at around 1.2. This includes a diffuser angle staying constant at an optimum of 10 degrees and an increasing diffuser length (approximately $50\%D_t$ to approximately $70\%D_t$) to reach the desired expansion ratio of 1.2 [42].

However as shown in Figure 6.12 the diffuser (length) is defined to start after the rotor. Applying this knowledge to the aerial screw case it becomes clear that it will add around a radius length to the duct height, which is undesirable. It approximately doubles the height of the vehicle and doubles the weight of the duct. Furthermore according to the experimental data from Pereira, having an expansion ratio of 1 (no diffuser, see Equation 6.24 for $\theta_d = 0$ degrees and $L_d = 0$ m, σ_d becomes 1) will result in an decrease of performance, but only slightly (approximately 10% average) [42].

This results in the decision to not add a diffuser to the duct design for now. If future experiments are conducted for ducted aerial screws, adding a diffuser is recommended to fully understand the performance effects of adding a diffuser has on screw propellers.

CONFIGURATION

To summarise the acquired optimum configuration from literature the parameters can be found in Table 6.1 and are visualised in Figure 6.12.

Table 6.1: Chosen optimum duct design parameters

Duct design parameters	Chosen optimum design parameters
Duct inlet diameter D_t	- (Dependent on rotor design)
Tip clearance δ_{tip}	$0.1\%D_t$
Inlet lip diameter r_{lip}	$13\%D_t$
Diffuser angle θ_d	- (No diffuser, otherwise 10 degrees)
Diffuser length L_d	- (No diffuser, otherwise $50\%D_t$)
Diffuser expansion ratio σ_d	1 (No diffuser, otherwise 1.2)

6.5.3. ESTIMATED DUCT EFFECTS ON PERFORMANCE

The aerodynamic tool has been designed to calculate the thrust and power for the open rotor case. In order to estimate the performance effects the duct has on the open rotor case, the calculated values for the open rotor case are being multiplied by duct performance constants. These constants have been determined by setting the duct design parameters to the chosen values, as seen in Table 6.1, and then determined with the use of the experimental data from Pereira [42].

The following relations were obtained from the graphs shown in the experimental data from Pereira, $C_{T_{SR}}/C_{T_{OR}}$, $C_{T_{Rotor}}/C_{T_{OR}}$ and $C_{P_{SR}}/C_{P_{OR}}$ at the chosen optimal duct design parameters [42]. These relations describe the amount of thrust the duct rotor combination is providing compared to the open rotor, the fraction the rotor (with duct) is providing of the thrust compared to the open rotor and the amount of power the ducted rotor combination is using compared to the open rotor case. These relations give insight on the amount of thrust that is contributing towards the ground effect (rotor thrust) as well as an estimate on the total performance increase in thrust and decrease in power compared to the open rotor case.

The experimental data from Pereira has been provided at four different amounts of collective pitch [42]. The second graph at a collective pitch of 20 degrees has been chosen, since for the aerial screw case the bulk of the thrust is produced at approximately 20 degrees. Furthermore in each graph multiple duct rotor combinations where tested and the worst one was chosen due to the lack of data of a no diffuser duct rotor combination and the uncertainties considering the aerial screw.

The duct performance constants are listed below in Table 6.2. An example of the data from Pereira is given below in Figure 6.13, with use of the above described procedure all three duct performance constants can be determined [42]. From the example shown the $C_{T_{SR}}/C_{T_{OR}}$ relation has been determined.

Table 6.2: Duct performance constants

Duct performance constant	[-]
$C_{T_{SR}}/C_{T_{OR}}$	1.30
$C_{T_{Rotor}}/C_{T_{OR}}$	0.61
$C_{P_{SR}}/C_{P_{OR}}$	0.68

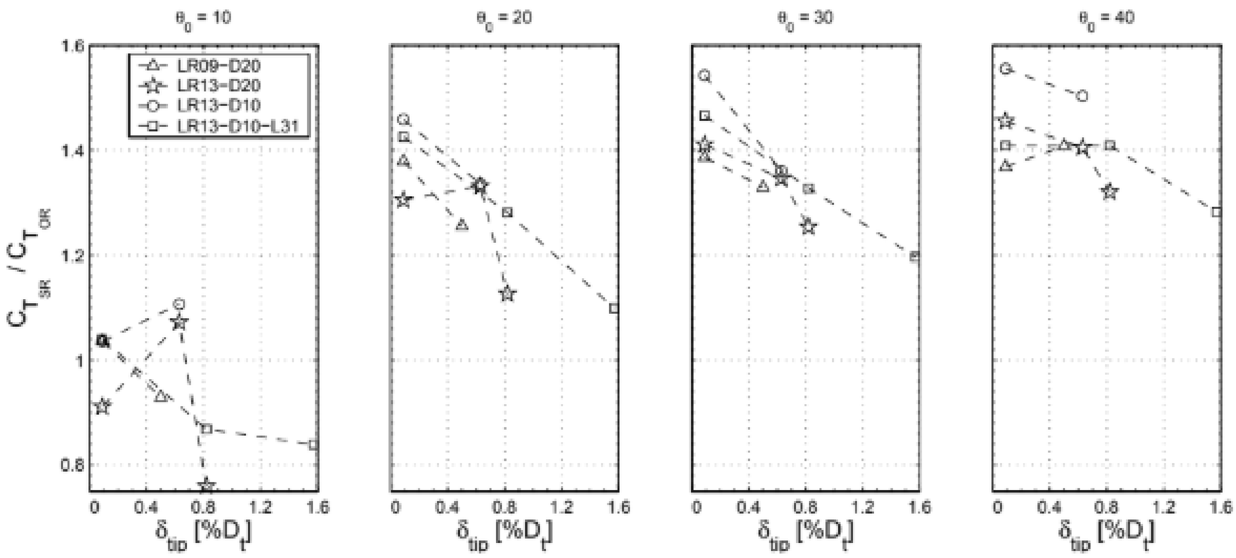

Figure 6.13: Example data for duct performance constant determination, data shown for $C_{T_{SR}}/C_{T_{OR}}$ [42]

The open rotor thrust value calculated in Equation 6.16a is multiplied by the relevant duct performance constants to estimate the same rotor's thrust when ducted, Equation 6.25 as well as the contribution to the thrust from the duct's lips themselves, Equation 6.26.

$$T_{rotor} = T_{OR}\frac{C_{T_{Rotor}}}{C_{T_{OR}}} = 0.61\,T_{OR} \tag{6.25}$$

$$T_{duct} = T_{OR}\frac{C_{T_{SR}} - C_{T_{Rotor}}}{C_{T_{OR}}} = 0.69\,T_{OR} \tag{6.26}$$

Separating the thrust into the rotor contribution and the duct contribution is necessary, since the rotor thrust can be used for ground effect calculations and duct thrust can be used to calculate duct moment for stability as was described earlier. To conclude this section, the total thrust then follows from Equation 6.27.

$$T_{total} = T_{rotor} + \Delta T_g + T_{duct} = T_{rotor}\left(\frac{1}{1-\frac{R}{4h^2}}\right) + T_{duct} = T_{OR}\left(\frac{C_{T_{ROTOR}}}{C_{T_{OR}}}\left(\frac{1}{1-\frac{R}{4h^2}}\right) + \frac{C_{T_{SR}} - C_{T_{ROTOR}}}{C_{T_{OR}}}\right) \tag{6.27}$$

6.6. VERIFICATION AND VALIDATION

The verification and validation methods used for the aerodynamic calculations are described in this section. Starting of with the verification followed by the validation to conclude the section.

6.6.1. VERIFICATION

The formulas applied in the BET tool were analysed and compared with manual computations for an individual blade section by a team member, who did not write the program, to check that the formulas were input correctly. Sanity checks and limit checks were also applied to ensure no obvious calculation flaws existed.

The formulas themselves, especially the ones taken from literature but modified to fit the aerial screw's geometry, were checked for logical consistency but they include some assumptions which are as follows.

It was assumed that an aerial screw blade can be modelled with blade element theory after having sections untwisted into a two dimensional blade. In reality air would gain momentum in the tangential direction and airstreams would not stay at the same radius as the rotor's long blade chord rotates. This then could mean the air instead flies over a modified section instead of the designed airfoil for that radius. The effect of this would be that the air travels along a longer airfoil (and so the effective surface area increases) as it crosses the blade diagonally but the airfoil experienced has less thickness and camber, and therefore a lower lift coefficient.

An assumed induced velocity based on the lift gradient of the airfoils along the radius from Prouty was used as in Equation 6.11 [38]. This is not the true induced velocity but an estimation based on momentum theory. However due to evidence from literature showing that this simplified momentum method is as accurate or even more accurate than more complex methods for determining the induced velocity, this was deemed sufficiently accurate for preliminary performance calculations [38, 43]. However it is recognized that this may not hold for an aerial screw rotor, namely a single bladed rotor with blade solidity exceeding 1.

In regions of reversed flow (see Figure 7.2) near the root on the retreating blade the lift produced was simply set to zero whereas in reality there would be negative thrust generated there, however this would be very low. Vortices caused by the change in flow direction is also neglected.

Finally the optimal duct parameters from Pereira [42] were assumed to be optimal and applicable to the aerial screw as well. It is also assumed that the effects of the duct walls and lips could be implemented by calculating for an open aerial screw rotor and then multiplying with a correction factor. Since data presented by Pereira differed for different rotors of only blade pitch angle, there is some doubt as to whether this holds.

6.6.2. VALIDATION

To validate the thrust generation simulated by the aerodynamic tool of the aerial screw a test was executed. The parameters of interest were solely the RPM versus thrust due to the nature of the experiment as is elaborated in this report.

EXPERIMENT

The experiment was executed at the propeller test setup at the High Speed Lab facility from the TU Delft. This test setup measured the following parameters: RPM, current, voltage and thrust force [44].

To validate this test-setup a rotor was used for which performance data was available. This propeller was the '7x4 propeller' manufactured by APC Propellers, a 7 inch propeller with a 4 inch pitch.

The test specimens were 3D printed models of two variants of the aerial screws. These were printed in a stereolithography printer (SLA) at the structures facility of the TU Delft. The SLA printer was desired for its high printing accuracy and smooth surfaces. A non-ducted and a ducted model were printed as shown in Figure 6.14. To reduce the complexity of the test setup of the ducted model, the duct and rotor were fabricated in one piece meaning that the duct spun along with the rotor. For the ducted rotor, this disabled the possibility of validating the torque needed to spin the rotor.

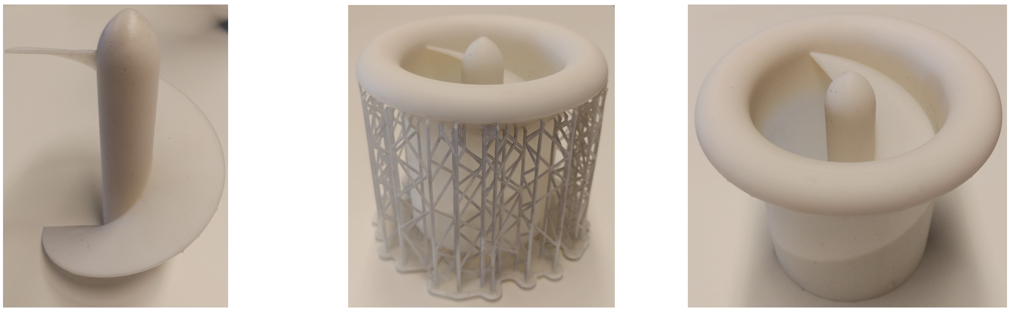

(a) Unducted aerial screw after removing support material

(b) Ducted aerial screw directly after printing

(c) Ducted aerial screw after removing support material

Figure 6.14: Test specimens for the experiment

As the outgoing shaft of the test-setup had M5 screw thread, a 15 mm long M5 nut was fixed in the models. For this, a hexagonal space was present on the inside of the hub. In this space, a 1 mm margin with regard to the space needed for the nut was present to compensate for printing inaccuracies. After printing, this turned out to be too large. To align the nut, aluminium tape was wrapped around the nut as it should provide the nut with a step-size thickness increase for each layer of aluminium tape. The thickness was increased until there would be no play between the nut and the hexagonal space, this can be seen in Figure 6.15a. Afterwards, the nut was secured by use of epoxy. As a last step, the two different models could be attached to the test setup as can be seen in Figure 6.15b and Figure 6.15c.

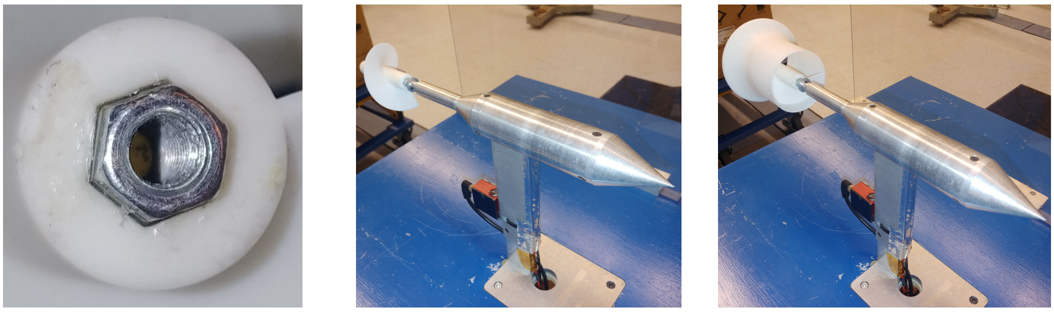

(a) Close up at the location of the hub where the nut is fixated

(b) Unducted aerial screw mounted in test setup

(c) Ducted aerial screw mounted in test setup

Figure 6.15: Fixation of test specimen

When the test-setup was switched on, it became clear that the alignment was imperfect and both models experienced great vibratory issues. These issues already occurred at RPM values of 200 or higher. The ducted aerial screw experienced the strongest vibratory effects as the lip of the duct was printed solid and thus had a high mass. The strategy was chosen to add counterweights to the specimen to balance them. This disabled the possibility for using this experiment the validate the torque needed to spin the rotor. To specify the desired location of the counterweights, the rotation was recorded with a high speed camera. A counterweight was added to the location opposite of the offset direction. Different weights were applied to different locations to be able to conclude the optimal mass and location for the counterweight. Small steel rings were used as counterweights, secured with tape as depicted in Figure 6.16. One larger and one smaller ring were used in such a way that the smaller ring could be used for trimming. It resulted in reachable RPM values of 2760 and 930 for the unducted and ducted screw, respectively.

Table 6.3: Test results

Unducted screw (radius: 33.8 mm)			
n (RPM)	**Thrust measured (N)**	**Thrust according to software (N)**	**Measured value over software value (-)**
2028	0.020	0.027	0.73
2400	0.029	0.038	0.78
2760	0.039	0.050	0.79
Ducted screw (radius: 33.8 mm)			
n (RPM)	**Thrust measured (N)**	**Thrust according to software (N)**	**Measured value over software value (-)**
930	0.029	0.007	4.02
Regular rotor (radius: 88.9 mm)			
n (RPM)	**Thrust measured (N)**	**Thrust according to datasheet (N)**	**Measured value over datasheet value (-) [45]**
930	0.020	0.040	0.49
2028	0.108	0.151	0.71
2400	0.157	0.247	0.64

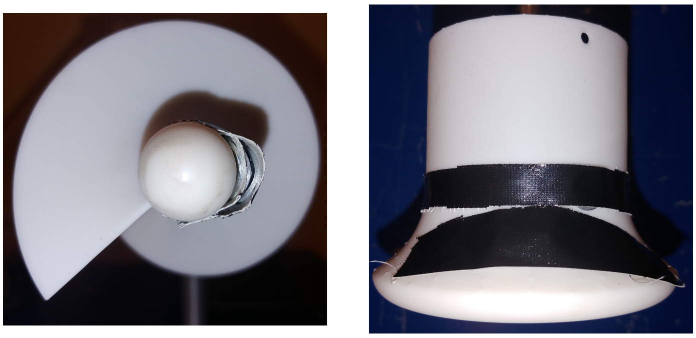

(a) Unducted aerial screw with balancing measures

(b) Ducted aerial screw with balancing measures

Figure 6.16: Balancing measures at the specimens

As can be seen in Table 6.3, both the unducted as the ducted screw generated more thrust in the test than according to the aerodynamic software developed in this project. For the unducted screw three different datapoints could be obtained at which approximately three times as much thrust was generated than the software expected. For the ducted screw, the vibratory issues limited the test to only one datapoint at which a thrust of 1.6 times the thrust that the software expected was obtained.

For the test setup, the thrust capability was validated. Due to the simplicity of the test setup, it was chosen not to validate the RPM count of the test setup. For the validation of thrust measuring capability of the test setup three different RPM's were measured and compared to specification values of the propellor [45]. In this process the measured value for 930 RPM and 2028 RPM were compared to the datasheet value for 1000 RPM and 2000 RPM, respectively. The 2400 RPM value was compared to the average value of the value of 2000 and 3000 RPM. In this process the rounding-off errors were assumed to be negligible and the increase between 2000 and 3000 RPM was assumed to be linear and thus could be averaged for obtaining the value for 2500 RPM. As the rounding off is within 10 % of the value, the unreliability of the value is also expected to be within 10 %. The averaging of the values between 2000 and 3000 RPM was done as there were only datapoints available at 2000 RPM and 3000 RPM and was expected to result in an error of the same order of magnitude. The thrust measured was approximately 0.6 times the thrust from the datasheet [45], meaning that the test setup measured less thrust than what was actually generated.

The test results indicate that the software is conservative for the ducted rotor as more thrust was measured during the test than was predicted by the aerodynamic software built during this project. This conclusion was emphasized by the validation of the test setup where it was found that more thrust was generated than what the measuring equipment states.

The results could be influenced by the effect of the weight of the test specimen on the test setup. This effect was not further investigated. The only mitigation taken for this, was zeroing of the measurement installation of the test setup before conducting the tests, but it is not certain that this was sufficient. Also as the RPM-count of the test setup was not validated, this could pose errors although this is not expected.

For future experiments, it is recommended to print with a margin of 0.2 mm at the location where the test specimen is attached to the nut. Furthermore action can be taken to reduce the duct mass of the ducted fan.

7
Performance

A performance analysis had to be applied to analyse how the SolidityONE behaves and its ability to execute the mission. For the performance analysis the hovering, forward flight, climbing and acceleration phase parameters were determined. This chapter describes the calculated parameters and how they are determined.

7.1. Equations of motion

Flight for the aerial screw differs from that of a conventional rotorcraft which achieves flight control by changing the collective and cyclic pitch of the rotor blades. Such changes in blade pitch is impossible for an aerial screw without a complex morphing wing system, as the blade forms a complex shape wrapped around the rotor axle without a simple rotational axis to pitch the blade about. Instead, the pitching moment to accelerate forward is achieved by applying differential thrust. The rear rotor spins at a faster RPM than the forward rotor which rotates in the other direction. This introduces a residual torque, which is compensated for using the vanes. This modifies the conventional calculations.

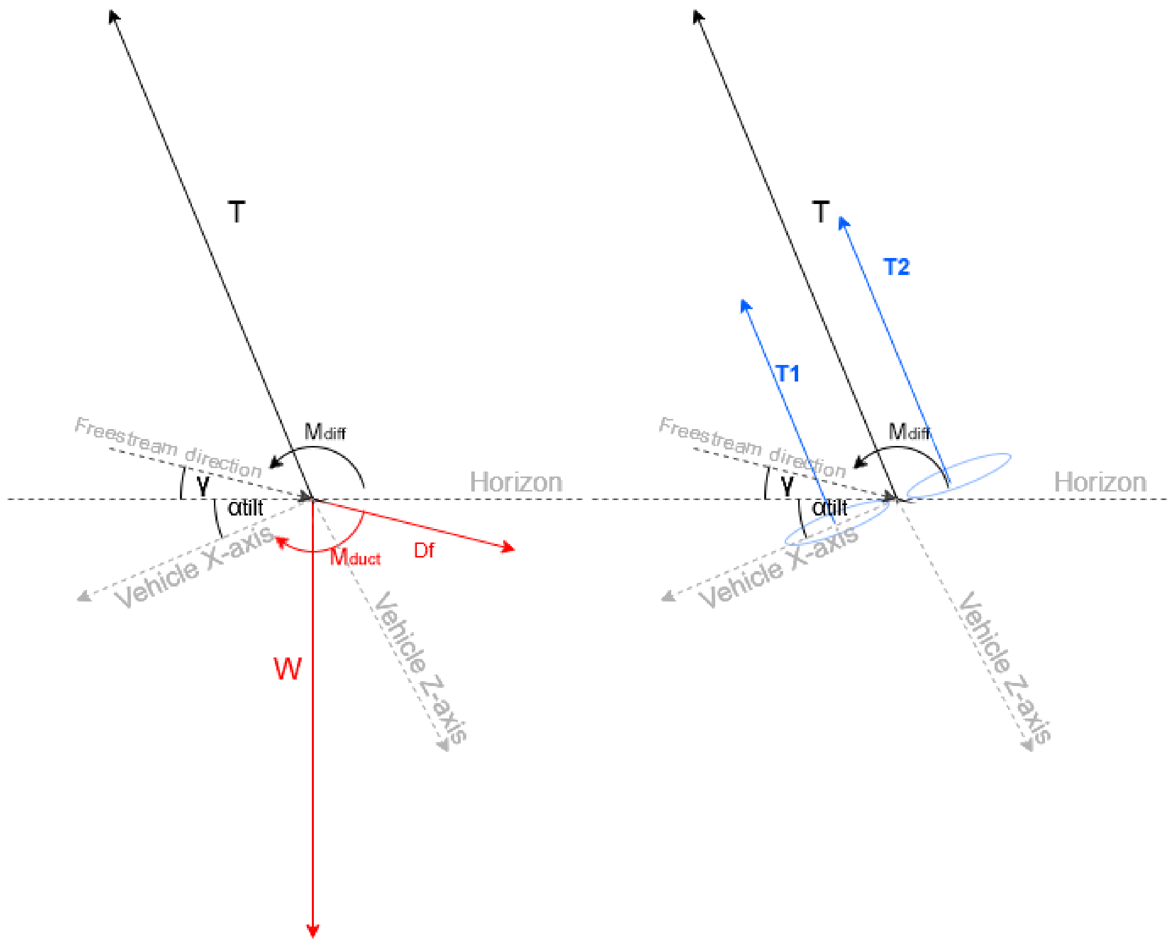

(a) Steady flight

(b) Decomposition of thrust into tandem thrust

Figure 7.1: Free Body Diagram

In Figure 7.1a a free body diagram of the vehicle in flight at a general velocity and flight path angle γ is given, as seen from the side. The vehicle tilts forward to fly forward which forms the tilt angle α_{tilt}. The disturbing forces and moments are given in red. These are the fuselage drag force D_f as given by Equation 7.1, the duct restoring moment M_{duct} discussed in subsection 9.3.3 and weight acting downwards due to gravity. To achieve steady flight these must be countered by a net thrust force T and moment M_{diff} which are given in black

$$D_f = \frac{1}{2}\rho C_D V^2 S \tag{7.1}$$

The tandem aerial screw vehicle has two rotors with thrust $T1$ and $T2$, spaced a certain distance away from each other. To achieve the net thrust T and moment M_{diff}, the sum of $T1$ and $T2$ must be equal to the value of T and the moment arm provided by the rotor spacing and the differential values between $T1$ and $T2$ provide the differential moment M_{diff}. This is illustrated in Figure 7.1b, the T and M_{diff} are given in red and also shown decomposed into $T1$ and $T2$, note that $T2$ is greater than $T1$ to produce M_{diff}.

When the sum of all forces is equal to zero for steady flight it can be seen that the thrust force required for flight is calculated with Equation 7.2a and the angle the vehicle has to tilt (α_{tilt}) is given by Equation 7.2b.

$$T = \sqrt{T_v^2 + T_h^2} = \sqrt{(W + D_f \sin\gamma)^2 + D_f \cos\gamma^2} \tag{7.2a}$$

$$\alpha_{tilt} = \arctan\left(\frac{D_f \cos\gamma}{W + D_f \sin\gamma}\right) \tag{7.2b}$$

7.2. HOVER

In hovering flight the velocity is zero thus fuselage drag is zero and Equation 7.2a simplifies to thrust being equal to the weight for a steady hovering case. The power required to provide this thrust with the rotor is described in section 6.2 and mainly consists of induced power which is caused by the induced velocity of the airflow tilting the lift vector back against the direction of rotation, and profile power which is caused by the aerodynamic drag forces of the rotor airfoil.

Furthermore, at higher altitudes the air is thinner and decreases the amount of thrust produced for a given RPM. To achieve enough thrust to hover with thinner air, induced velocity must increase to provide the same mass flow through the rotor. The decrease in air density for an increase in height was calculated with Equation 7.3, where g is the gravitational acceleration, M the molar mass, h the height, R^* the universal gas constant, T the temperature and the subscript 0 is the condition at 0 m, which was a temperature 288.15 K and a density of 1.225 kg/m^3 [39]. The hover ceiling is the height at which the density has decreased to the point where the rotor is at maximum power available to provide the required thrust.

$$\rho = \rho_0 \exp\left[\frac{-gMh}{R^* T_0}\right] \tag{7.3}$$

The disc loading and the power loading are also important design parameters and are calculated with Equation 7.4 and Equation 7.5 respectively [46]. The disc loading is an important parameter influencing the downwash and the power required to hover. A small rotor provides a high disc loading and a high induced velocity. This could create brown-out problems during hovering at a low altitude above dusty environments, which is the up swept of dust in the outwash and obscures the pilots vision [36]. The power loading is a parameter which indicates how much power is needed to lift a weight.

$$DL = \frac{W}{A_{disc}} \tag{7.4}$$

$$PL = \frac{P_{hov}}{W} \tag{7.5}$$

7.3. FORWARD FLIGHT

In forward flight the advancing blade has a higher velocity than the retreating blade, which is illustrated in Figure 7.2. The direction of flight is towards azimuth angle $\psi = 180^o$ and the arrows show the magnitude and direction of the airflow on the rotor blade, this is equal to ωR and for $\psi = 0^o$ and $\psi = 180^o$ the airflow from the velocity of flight is added. Near the root of the blade at $\psi = 270^o$ ωr is smaller than the velocity of flight and reverse flow occurs [38].

Since the relative speed between the blade and air differs around the rotor disc, the thrust had to be calculated as an average across the whole rotor disc, from azimuth angle 0 to 360 degrees. This was achieved by calculating the thrust value at azimuth angle 0, 90 and 270 with the local air speed. Then the azimuth thrust distribution was modelled as two half sine waves, with average value of T_0 and peak of T_{90} from 0 to 180 degrees and another sine wave with average value of T_0 and bottom of T_{270} for 180 to 360 degrees. These sine waves are integrated and divided by 2π to get the average.

$$\begin{aligned}T_{avg} = \frac{1}{2\pi}\int_{\psi=0}^{\psi=180} T_{\psi_0} + sin(\psi)(T_{\psi_{90}} - T_{\psi_0})d\psi \\ + \frac{1}{2\pi}\int_{\psi=180}^{\psi=360} T_{\psi_{180}} + sin(\psi)(T_{\psi_{270}} - T_{\psi_{180}})d\psi \\ = T_{\psi_0} + \frac{T_{\psi_{90}} - T_{\psi_0}}{\pi} + \frac{T_{\psi_{270}} - T_{\psi_0}}{\pi}\end{aligned} \tag{7.6}$$

Similar to thrust, the average torque for a full rotation of the rotor was calculated with Equation 7.7.

$$Q_{avg} = Q_{\psi_0} + \frac{Q_{\psi_{90}} - Q_{\psi_0}}{\pi} + \frac{Q_{\psi_{270}} - Q_{\psi_0}}{\pi} \tag{7.7}$$

The tangential velocity component of the flight velocity V_{tan} at different azimuth angles (ψ) is given by Equation 7.8a, where V is the cruise velocity and γ the flight path angle.

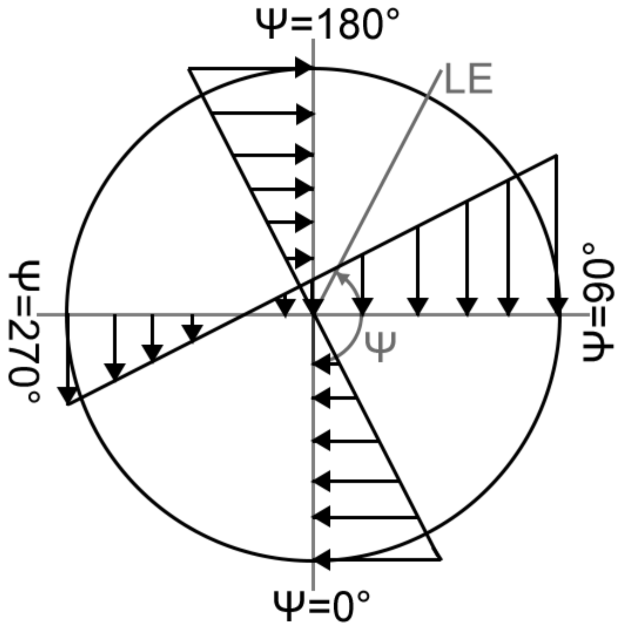

Figure 7.2: Tangential airflow at various azimuth angles

$$V_{tan} = V\cos(\alpha_{tilt} + \gamma)\sin\psi \tag{7.8a}$$

$$V_{axial} = V\sin(\alpha_{tilt} + \gamma) \tag{7.8b}$$

The cruise velocity increases the thrust of the advancing blade more than it decreases the thrust of the retreating side, it has a positive effect on the total thrust generation so the power required by the rotor decreases as velocity increases until an optimum is achieved. This optimum is the velocity for maximum endurance, after which the power increases again. The maximum forward velocity at level flight is the velocity, where the power-over-velocity ratio is minimal. This is found by drawing a tangent line from the origin to the total power curve [46].

Additionally, the forward tilt of the vehicle in forward flight creates an axial component of the flight velocity and is given by Equation 7.8b. This has the effect of increasing the induced power of the rotor.

The power curve was constructed by calculating the total power at every velocity. The total power consists of the induced power, profile power, the wake power and the parasite power. The calculation of the induced power, profile power and wake power are described in section 6.2. The parasite drag was computed with Equation 7.9a. Furthermore, the velocity will be given by μ, which is the advance ratio shown in Equation 7.9b.

$$P_{parasite} = D_f V \tag{7.9a}$$

$$\mu = \frac{V}{\Omega R} \tag{7.9b}$$

Furthermore, the maximum horizontal velocity V_{max} was limited by the duct moment and the power available to the rear rotor. Because the rear rotor will be on maximum power to produce as much thrust as possible. However, the front rotor has to be high enough to create the total thrust required, but also low enough to create the differential moment required to counter act moment from the duct. This was calculated by applying the aerodynamic program described in section 6.2. From the maximum velocity the never exceed speed V_{NE} was determined by multiplying the V_{max} with 0.9, which is a requirement stated by the FAR.

7.4. CLIMB & DESCENT

In climbing flight the flight path angle and the tilt angle as indicated in Figure 7.1a will be 90 and 0 degrees respectively. Hence climbing flight creates an axial velocity in the rotor as in Equation 7.8b. This axial velocity adds to the induced velocity and thus increases the inflow angle shown in Figure 6.4. Due to this increase in inflow angle the angle of attack will decrease, resulting in a decrease in thrust or an increase in power consumption.

The maximum rate of climb (ROC) is the maximum axial velocity the rotor can accept without exceeding the maximum power available while creating enough thrust to carry the weight of the craft. This rate of climb decreases with altitude, this is because to create the same thrust with thinner air requires higher induced velocity which reduces the angle of attack experienced at the blade and must be compensated by applying more RPM and power.

The time required to climb to an altitude is given by Equation 7.10, where the average rate of climb is calculated by dividing the difference between the rate of climb at the begin and end altitude by two.

$$t_{climb} = \int_{h_{start}}^{h_{end}} \frac{1}{ROC(h)} dh \tag{7.10}$$

In descent the opposite is true, the axial velocity acts upward, decreasing the inflow angle, increasing the angle of attack which increases the thrust, or decreases the power required to maintain thrust. If the rate of descent is close to the induced velocity of the rotor, a phenomenon called the vortex ring state occurs in which there is a very unstable non-continuous flow through the rotor. Therefore the rate of descent should not be allowed to exceed a quarter of the induced velocity during hover [38].

7.5. ACCELERATION

For the chosen combination of rotor and duct, the maximum vertical acceleration was limited by the maximum power available of the engine. First the thrust-to-weight ratio was determined by calculating the amount of thrust produced at maximum available power. From this the excess thrust available to accelerate was determined. Finally, the maximum vertical acceleration was computed with the second law of Newton.

The maximum horizontal acceleration was computed for the maximum velocity by calculating the counteracting moment at this velocity. Then the rear rotor was set to provide maximum thrust and the front rotor had to produce enough thrust that the moment, due to the differential thrust was equal to the moment of the duct. This resulted in the maximum thrust in forward direction. Then, by applying Newtons second law the maximum forward acceleration was calculated, as shown in Equation 7.11. The subscript maxf indicates at maximum forward velocity. In reality the acceleration could be a lot higher at a lower velocity, because the moment of the duct is a function of the velocity, thus it would be lower. Hence the front rotor could produce more thrust at lower velocity. Because the differential moment could be lowered, as the duct moment is lower. However, due to difficulties with trimming the moment of the differential thrust with the duct moment it was assumed to have a constant acceleration. Hence the lowest acceleration was decided to be the maximum.

$$a_{max} = \frac{\sqrt{T_{max}^2 - W^2} - D}{m} \tag{7.11}$$

Power consumption of the acceleration phase was determined by calculating the thrust needed to accelerate with the maximum acceleration at every timestep. Figure 7.3 shows all the forces acting on the vehicle during the acceleration phase, where F_a is the force applied to accelerate given by Newtons second law and the T_{Drag} and T_{Weight}, where the thrust required to overcome the drag and the weight respectively. From this free body diagram Equation 7.12a was derived, which was applied to achieve the thrust required to accelerate. From the thrust at every timestep the power corresponding to the thrust was calculated. Analysis of a power over thrust curve showed a linear relation between the power and the thrust for zero velocity, which was derived by interpolation. The velocity did have an effect on the power, due to the increase in parasite drag, which is the power needed to overcome the drag. This was added to the linear behavior for thrust over power. This resulted in a power for thrust at every timestep given by Equation 7.12b, which was averaged to indicate the power consumption given for the phase.

$$T = \sqrt{W^2 + (D_f + F_a)}^2 \tag{7.12a}$$

$$P = 32.9T - 26584 + D_f V \tag{7.12b}$$

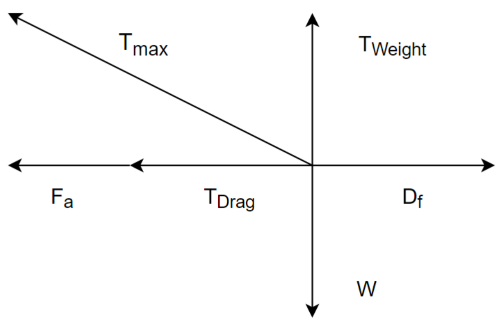

Figure 7.3: Free body diagram for acceleration phase

7.6. ENDURANCE AND RANGE

The endurance is limited by battery capacity and power consumption and is computed by applying Equation 7.13. The maximum endurance is achieved for the velocity at which the minimum power is required. As previously discussed the power required differs depending on the type of flight and velocity performed. Additionally there may be auxiliary electric systems which consume power.

$$t_{endurance} = \frac{C}{P} \tag{7.13}$$

The range is a sum of the distance covered by acceleration, cruise and then deceleration which may be calculated with Equation 7.14 and is a function of the horizontal acceleration and deceleration, cruise velocity and time which is limited by the endurance provided by the batteries, which are sized in chapter 8.

$$Range = s_{acc} + s_{cruise} + s_{dec} = 0.5a_{acc}t_{acc}^2 + V_{cruise}t_{cruise} + 0.5a_{dec}t_{dec}^2 \tag{7.14}$$

8
Power

The power system is a system that serves a few roles in the design of the SolidityONE. It provides the vehicle with a means of propulsion (excluding the rotor), and the means to control that propulsion. In addition, it ensures the availability of electrical power to the remainder of the vehicle. In this chapter, the calculations made for the sizing and component selection for the power system are described. Additionally, this chapter aims to describe the options considered for its components and why these were adopted or rejected. Lastly, the hardware, software and electrical interactions and interconnections between components in the SolidityONE are described and mapped in a block diagram.

8.1. Propulsion options

From existing aircraft and helicopters it can be found that four-stroke piston engines and turboshaft engines are predominantly applied to provide power. In contrast, electric motors have a very low adoption rate and can be found mostly in recent air-taxi concepts such as the Volocopter[1] and the Lilium Jet[2]. The majority of airworthiness regulations are based upon a combustion engine as a result [47, 48]. This section shortly discusses the options considered.

Parameters of interest during the selection and exclusion of system components include the following:

- Specific energy: energy per unit weight [$\mathrm{kWh\,kg^{-1}}$]
- Specific power: power per unit weight [$\mathrm{kW\,kg^{-1}}$]
- Energy density: energy per unit volume [$\mathrm{kWh\,m^{-3}}$]
- Power density: power per unit volume [$\mathrm{kW\,m^{-3}}$]

8.1.1. Engine types

Combustion engines include turboshaft engines, piston engines and rotary engines. These engines require petroleum-based fuels, where two-stroke piston and rotary engines require oil additives for lubrication. From engine data, it was found that turboshaft engines have high power density, in exchange for high fuel consumption. Piston engines are found to have low power density, with low fuel consumption. Additionally, two-stroke engines and rotary engines were found to have a higher specific power compared four-stroke engines [18, 19, 21, 23].

For electric motors, the options are brushed and brushless DC motors, in addition to AC (induction) motors: brushless DC motors utilize permanent magnets, which responds to the magnetic field generated by the electromagnets driven, whereas the AC motor consists of electromagnets only, resulting in losses in the magnetic field; it additionally requires inverters to be driven. Brushed DC motors require contact between the stator and commutator to drive the rotating electromagnets, wearing over time and adds mechanical friction losses. Brushless DC motors have the magnets mounted on the rotor, and require controllers to set the voltage per phase, which is dependent on rotor position: requiring a rotor position sensor [49].

Engine options reduction

Due to the clear advantage of brushless DC motors in achieved efficiency, the brushed DC motors and AC motors were not considered; this could otherwise have been concluded from iterations.

[1] https://www.volocopter.com/en/product/ (Retrieved: 14-01-2020)
[2] https://lilium.com/the-jet (Retrieved: 14-01-2020)

Oil particle exhaust caused by the oil additive required for two-stroke and rotary engines is considered a significant impact on the environment, and was thus concluded not viable for a sustainable propulsion system design, and were not analysed further.

Furthermore, since the mission flight time is in the order of magnitude of five minutes, the estimated total propulsion system mass of electric propulsion system options was found generally less than the engine mass before addition of a fuel system, for the power required. For this reason, combustion engines have been rejected as a viable option.

8.1.2. ENERGY STORAGE

Electric motors are powered by electricity, which requires an on-board storage. This storage can be solid, in the form of electrostatic storage, or electrochemical storage: super-capacitors are an example of a hybrid form. For fluid energy storage, hydrogen is considered. Energy provision from external sources (tethering) was not considered since power should be available for flight above multiple types of terrain, altitudes and velocities.

The energy storage is evaluated primarily on the specific energy. When multiple options are considered to be viable, the energy density can be evaluated to reduce the volume.

Electrostatic energy storage options include capacitors and super-capacitors, the latter being a hybrid of electrostatic and electrochemical storage. Advantages include rapid charge and discharge, since there is no chemical conversion taking place. Conversely, these devices have a low specific energy of less then 10 Wh kg^{-1} and are known to self-discharge at a higher rate than chemical alternatives [50].

Electrochemical energy storage, or batteries, require a chemical reaction to convert the stored energy to electricity. A distinction is made between primary (disposable) and secondary batteries (rechargeable). Batteries with a lithium anode have the highest specific energy (up to 265 Wh kg^{-1}), in addition to a high specific power; battery technology such as Li-$SOCl_2$ has a very high specific energy, but is a primary battery and especially unsustainable [17]. In the future, solid-state battery technology can be investigated to reduce the battery mass and size[3]; though it can be expected to be a more expensive alternative.

Furthermore, hydrogen was investigated for its applicability; requiring a hydrogen tank, fuel system and a fuel cell to generate electricity with hydrogen as fuel. Liquid hydrogen has a specific energy of 39.4 kWh kg^{-1}, which is 150 times more compared to batteries [32, 51]. This advantage is lost when considering the fuel cell mass.

STORAGE OPTION REDUCTION

Electrostatic storage and electrostatic-chemical hybrids avoided due to the low specific energy. Additionally, the power output forms a safety hazard: a short-circuit causes a current spike likely destroying all connected components.

Additionally, the hydrogen fuel cell was considered too high in mass: the fuel cell mass exceeds the lithium battery mass for the order of magnitude of five minutes of flight [31]. This excludes the additional mass associated with the hydrogen fuel and fuel system.

ENERGY TRANSFER

Energy transfer is performed by using cables sized appropriately for the application. Copper and aluminium have been considered as conductive materials. Due to the much lower density and slightly increased resistivity, copper was ruled out as an applicable conductor: 8960 kg m^{-3} and 1.7x$10^{-8}\Omega$m for copper compared to 2700 kg m^{-3} and 2.82-3.1 x$10^{-8}\Omega$m for aluminium [52, 53].

[3] https://sionpower.com/ (Retrieved: 15-01-2020)

8.1.3. GEARBOX TYPES

Since electric motors deliver a near-constant torque for a large range of speeds, high power output implicitly requires a high motor speed. Due to a higher rotational speed of the motor where it reaches its optimal power output, a reduction gearbox is required to drive the rotor, where the gearbox multiplies the torque and divides the RPM by the gearbox ratio, thereby maintaining a constant power (following Equation 8.1 where P is in W instead of kW). Some commercially available single-stage gearboxes in the range where the rotor was expected to perform were found. These are lightweight compared to results of preliminary sizing using the K-factor method described by Dudley [54, 55]. Due to the properties of electric motors, exclusively single-stage gearboxes have been considered, due to additional mass and losses associated with an additional gear stage. An additional preference is made towards planetary gearboxes using helical gears, due to the lower wear associated and concentric output axis [54].

$$P_{shaft} = \frac{2\pi Q_{shaft} RPM_{shaft}}{60} \tag{8.1}$$

8.2. POWER SYSTEM COMPONENTS SIZING AND SELECTION

For the selection of electric motors, controllers, gearboxes and battery cells, a database was constructed from which the optimal configuration could be found. If an efficiency rating was not provided by the manufacturer, a conservative efficiency of 90% was assumed for motors, controllers and gearboxes. Since most electric motors, controllers and gearboxes operate at 95% and higher efficiency, resulting in an overestimation of cable and battery masses [16, 54, 56, 57]. As a consequence, the assumption biased the results towards motors and controllers for which information is available. Furthermore, the power system components, sizes and quantities were determined using inputs from the rotor design and structural design:

- Maximum rotor RPM (RPM_{rotor}) [min^{-1}]
- Rotor power at maximum RPM (P_{rotor}) [kW]
  - Rotor torque can be determined with Equation 8.1
- Maximum total rotor power (P_{max}) [kW]
- Cable length (battery to controller) (L_{bc}) [m]
- Cable length (controller to motor) (L_{cm}) [m]

Additionally, the minimum flight time t was an input necessary to determine the battery mass, and has an impact on the mass estimation of the power cables.

The power system optimisation tool is structured to ensure all options are covered; such that every possible combination of motor, controller and gearbox is analysed separately. The battery and cables are sized as a result of the energy, power and current required. The motor, motor controller, gearbox and cables are sized for the required power and speed of one rotor, implying that the quantities and masses are to be multiplied by two after computation, before battery sizing.

8.2.1. GEARBOX

Gearbox sizing was initially attempted by performing a first-order K-factor estimation, however it was found to be in excess of three times the mass compared to existing gearboxes, such as the gearboxes by Anaheim Automation [54, 55]. Hence, the construction of a database of gearboxes with performance near the expected the performance required by the SolidityONE. In addition to gearboxes, the option for a straight connection between motor and rotor was added for completeness.

First each gearbox is checked for satisfying the required torque Q_{rotor} and speed RPM_{rotor} in Equation 8.2a and 8.2b. Following, the gearbox mass was added to the total system option mass; note that the mass of the gearbox m_{gb} was added twice: once per rotor. The power required by the gearbox P_{gb} was calculated using Equation 8.2c, which results from the power required by the rotor P_{rotor} and the gearbox efficiency η_{gb}.

$$RPM_{gb_{out}} \geqslant RPM_{rotor} \quad (8.2a)$$

$$Q_{gb_{out}} \geqslant Q_{rotor} \quad (8.2b)$$

$$P_{gb} = \frac{P_{rotor}}{\eta_{gb}} \quad (8.2c)$$

8.2.2. MOTOR

First, the maximum continuous mechanical power of the motor $P_{mot_{MC}}$ was compared to the maximum power required by the gearbox P_{gb}. If the motor was found insufficient, another motor of the same type was added (increasing the number of motors N_{mot}), after which the check repeats. The passing condition is shown in Equation 8.3a.

The accepted voltage range was passed to motor controller, cable and battery sizing. Additionally, the number of motors and power required by one motor P_{mot} additionally passed to motor controller sizing, which was calculated according to Equation 8.3b, incremented with the efficiency of the motor η_{mot}. The motor mass m_{mot} is then added to the total option mass following Equation 8.3c. When additional cooling is required, the power to dissipate was calculated with Equation 8.3d, which is an altered and rearranged version of Equation 8.3b.

$$N_{mot} \geqslant \frac{P_{mot_{MC}}}{P_{gb}} \quad (8.3a)$$

$$P_{mot} = \frac{P_{gb}}{\eta_{mot}} = \frac{P_{rotor}}{\eta_{mot}\eta_{gb}} \quad (8.3b)$$

$$m_{tot} = m_{tot} + 2m_{mot}N_{mot} \quad (8.3c)$$

$$P_{mot_{loss}} = \frac{P_{max}}{\eta_{gb}}\left(\frac{1}{\eta_{mot}} - 1\right) \quad (8.3d)$$

8.2.3. MOTOR CONTROLLER

The motor controllers were checked for compatibility of voltage and power for the motor analysed. If the voltage range did not match, the controller is skipped. Otherwise, controllers were added per motor until the maximum continuous power $P_{esc_{MC}}$ matched the motor power P_{mot}, passing the check in Equation 8.4a.

The total power required by the controllers P_{esc} could be calculated using Equation 8.4b; the power additionally includes the controller efficiency η_{esc} and the cable loss between the controller and motor $P_{cm_{loss}}$, which is described in subsection 8.2.4. Similar to motor cooling: if external cooling is required, the power to dissipate $P_{esc_{loss}}$ was found with Equation 8.4c. Last, the mass of the system configuration option could be updated using Equation 8.4d: note that N_{esc} is the amount of controllers required to drive one motor.

$$N_{mot} \geqslant \frac{P_{mot}}{P_{esc_{MC}}N_{esc}} \quad (8.4a)$$

$$P_{esc} = \frac{1}{\eta_{esc}}\left(\frac{P_{rotor}N_{mot}N_{esc}}{\eta_{gb}\eta_{mot}} + P_{cm_{loss}}\right) \quad (8.4b)$$

$$P_{esc_{loss}} = \frac{P_{max}}{\eta_{gb}\eta_{mot}}\left(\frac{1}{\eta_{esc}} - 1\right) \quad (8.4c)$$

$$m_{tot} = m_{tot} + m_{esc}N_{esc}N_{mot} \quad (8.4d)$$

8.2.4. CABLES

Cable size and mass have been estimated by limiting the temperature increase to 15 K over the flight duration to ensure low mass without overheating and potential fire risks. The base cable from Axon used as reference has a resistance R of 3.6 Ω km^{-1} and a mass of 34.3 kg km^{-1} for a conductor area A of 8.6 mm^2, from which a density ρ of 3985 kg m^{-3} is retrieved [53].

First, the base resistivity ρ_{res_0} is calculated using Equation 8.5a. Assuming that the energy loss is contained within the cable as heat, Equation 8.5c is necessary to calculate the next incremental temperature, knowing the specific heat of aluminium c_p of 900 J kg^{-1}K^{-1} [52, 58]. For the cables from controller to motor, the current is taken as its root-mean-square value due to its sinusoidal nature.

Adding a temperature correction for the resistivity is necessary to prevent underestimating since it increases with temperature. For this the temperature correction in Equation 8.5b was taken, where $T_0 = 293.15$ K and $T - T_0 = \Delta T$ [52]. Then combining Equation 8.5a, 8.5b and 8.5c yields Equation 8.5e, which calculates the necessary cable area to sustain the maximum expected current.

The power loss across cables between two components was calculated with Equation 8.5d, which was added in controller and battery sizing as P_{bc} and P_{cm}.

$$\rho_{res} = R\frac{A}{L} \tag{8.5a}$$

$$\rho_{res} = \rho_{res_0}(1 + \alpha_{tc}(T - T_0)) \tag{8.5b}$$

$$\Delta T = \frac{E}{c_p m} = \frac{I^2 R}{c_p m} t \tag{8.5c}$$

$$P_{cable_{loss}} = I^2 R N_{cable} \tag{8.5d}$$

$$A = \sqrt{\frac{\Delta t}{\Delta T} \frac{\rho_{res_0} I^2 (1 + \alpha_{tc} \Delta T)}{c_p \rho_{al}}} \tag{8.5e}$$

PROVISIONS FOR AUXILIARY EQUIPMENT

In addition to high power cables, signal cables and low power cables account for a low mass portion. The weight is approximately 4 to 12 kg km^{-1} for the sizes AWG 24 (0.21 mm^2) and AWG 18 (0.82 mm^2), respectively[4]. Since, at this stage, an estimate could not be made reliably (factors being amount of wires, power and shielding requirements and lengths and equipment), a fixed value of 1 kg was taken: between 83 and 250 m of wiring.

8.2.5. BATTERY

Battery sizing was performed by analysing each battery cell in the database for its nominal values of voltage, capacity, current, size and weight. An assumption made was that forward flight accounts for the majority of the mission, leading to a battery sized for this power requirement for the duration of flight. The assumption results in an overestimation of battery mass if the battery is sized for energy required in the flight phase. The power required for auxiliary equipment includes the flight computer, control servos, navigation lights and cooling equipment supplements was added as P_{aux}.

Two more assumptions were made: the battery mass was increased with 10% to account for battery linking, the battery container and other materials added during the construction of a battery. Additionally, the battery must have a battery management system (BMS), for which an additional mass of 2 kg was reserved. The battery box sizing and BMS are described further in subsection 8.2.6.

In order to find the ideal cell and configuration for the design, the following steps were taken for each cell:

1. Calculate the acceptable range of cells in series, N_S, using Equation 8.6a, knowing the voltage range of the motor and motor controller. Cells placed in series are henceforth named a battery bank.
2. Calculate the number of battery banks in parallel, N_P, for each possible value of N_S. This is determined by the maximum value of:

[4] https://www.habia.com/product-overview/single-wires/ (Retrieved 18-01-2020): PTFE // E, types: E 2419, E 1819

(a) The number of battery banks required to meet the energy required for the duration of flight, determined by Equation 8.6b.
(b) The number of battery banks required to meet the power required for the maximum power requirement, determined by Equation 8.6c.

3. Calculate the battery mass with Equation 8.6d. The battery configuration for which the lowest m_{bat} was calculated was then added to the system option mass.

$$\frac{max(U_{mot,esc})}{U_{cell}} \geqslant N_S \geqslant \frac{min(U_{mot,esc})}{U_{cell}} \quad (8.6a)$$

$$N_P \geqslant \frac{C_{cell} U_{cell} N_S}{(P_{esc} + P_{aux})\, t} \quad (8.6b)$$

$$N_P \geqslant \frac{I_{cell} U_{cell} N_S}{P_{esc} + P_{aux}} \quad (8.6c)$$

$$m_{bat} = 1.1 m_{cell} N_S N_P + 2 \quad (8.6d)$$

8.2.6. ADDITIONAL COMPONENTS AND AUXILIARY POWER

This subsection describes the selected components which were not sized in detail. Especially the battery container, BMS and cooling were assumed: these assumptions are checked against the values of the components chosen, and is reflected upon.

The battery itself should be placed in a secondary structure which protects the batteries from impact and weather and provide cooling for the battery cells. Additionally, the structure should provide containment or venting in the case of fire or explosion. Combined, a battery box made of 1 mm thick aluminium was chosen, since this limits the deformation of the box under the weight of the batteries. Internally, it should be lined with fire-resistant or fire-retarding material, such as aramid paper: hence, 0.5 mm thick Nomex 410 is chosen [59]. Combined, a mass of approximately 2.5 kg can be expected, which is included in the mass estimation for the battery.

Cooling of the motor, motor controller and battery is important to ensure continuous operation; hence a preliminary estimate of 4 kg was made. This estimate results from the identification of radiators and pumps, prematurely assuming that the motors would be air-cooled.

The motor is set-up to be air-cooled using the inflow velocity above the duct, requiring and receiving 20 and 30 m s^{-1}, respectively (as calculated in chapter 6)[16]. Contrarily, the controller is liquid-cooled: the heat power to dissipate, $P_{esc_{loss}}$, may increase up to 2 kW. For this, a 45 mm thick radiator, to which four 140 mm diameter fans are mounted, was selected. This radiator weighs approximately 2.1 kg[5] for a cooling capacity of approximately 100 W K^{-1}[6]. Meaning that the liquid temperature should stabilise at approximately 20 K above ambient. In order to circulate the liquid, a pump is required, which accounts for an additional 0.75 kg[7]. The battery was chosen to be cooled with two fans similar in size to the radiator-mounted fans: combined, six fans weigh approximately 1.8 kg [60]. Combined, a cooling system mass of 4.65 kg excluding hoses and coolant liquid indicates that the system itself was underestimated.

The BMS is required to maintain consistent voltages across battery banks and cells, and is used to charge and discharge the battery. The Elithion Lithiumate BMS is capable of monitoring and controlling 255 cell banks, while weighing only 0.68 kg; leaving 1.3 kg of the reserved 2 kg for connections, mounting of the BMS and cell-connection PCBs or the discrepancy in the estimate made for cooling [61]. As a measure to protect battery banks from over-current, high current fuses are added in series to each battery bank.

Additional components not discussed in detail include the flight information display and navigation lights: the total weight of which was found at at 0.1 kg and 0.2 kg[8], respectively [62]. The front-view camera is considered negligible[9].

[5] https://www.ekwb.com/shop/ek-coolstream-ce-560-quad (Retrieved 17-01-2020)
[6] https://www.ekwb.com/blog/radiators-part-2-performance/ (Retrieved 17-01-2020)
[7] https://eveurope.eu/en/product/12v-water-pump-for-cooling-fluid/ (Retrieved 15-01-2020)
[8] https://aeroleds.com/products/pulsar-ns-01-1280-b-12/ (Retrieved 20-01-2020)
[9] https://www.raspberrypi.org/documentation/hardware/camera/ (Retrieved: 20-01-2020)

Combined, the power for auxiliary components listed in this section reaches at most 185 W, of which 120 W is assigned to cooling of the motor controllers and battery. However, the power system is sized for 200 W: this leaves a 15 W reserve for other components without impact on the power system. The power required for the cooling system can decrease when reducing the currently oversized radiator and coolant pump. Additionally, the power required by the fans is at the maximum operational speed, which may not be required to attain an acceptable fluid temperature.

8.3. COMPONENT CONNECTIONS AND INTERACTIONS

In this section, the interactions between different components are described on a hardware, software and electrical level. This is culminated into a block diagram displayed in Figure 8.1. Note that, due to the electrical nature of the propulsion system and control system (described in chapter 9), the electrical and hardware connections and interactions are almost identical.

Externally, a charger is connected to the electric grid or a sustainable alternative such as solar panels. This charger is then connected to the vehicle through a cable to the vehicle. Another external interaction is with a programmer or PC for performance data analysis. Within the SolidityONE a few groups of components can be made, namely:

- Energy storage subsystem: includes the battery and BMS
- Propulsion subsystem: includes the rotors, motors, motor controllers and gearboxes
- Control system: includes control input encoders, servos and the flight computer
- Avionics: includes the display, camera and navigation lights
- Mechanical: includes everything that is not electrically connected or controlled and overlaps with the propulsion subsystem.

The links defined in Figure 8.1 are based on power and signal: this is both electrical and mechanical. The components and interactions have been divided into blocks of signal data, actions, physical properties and components.

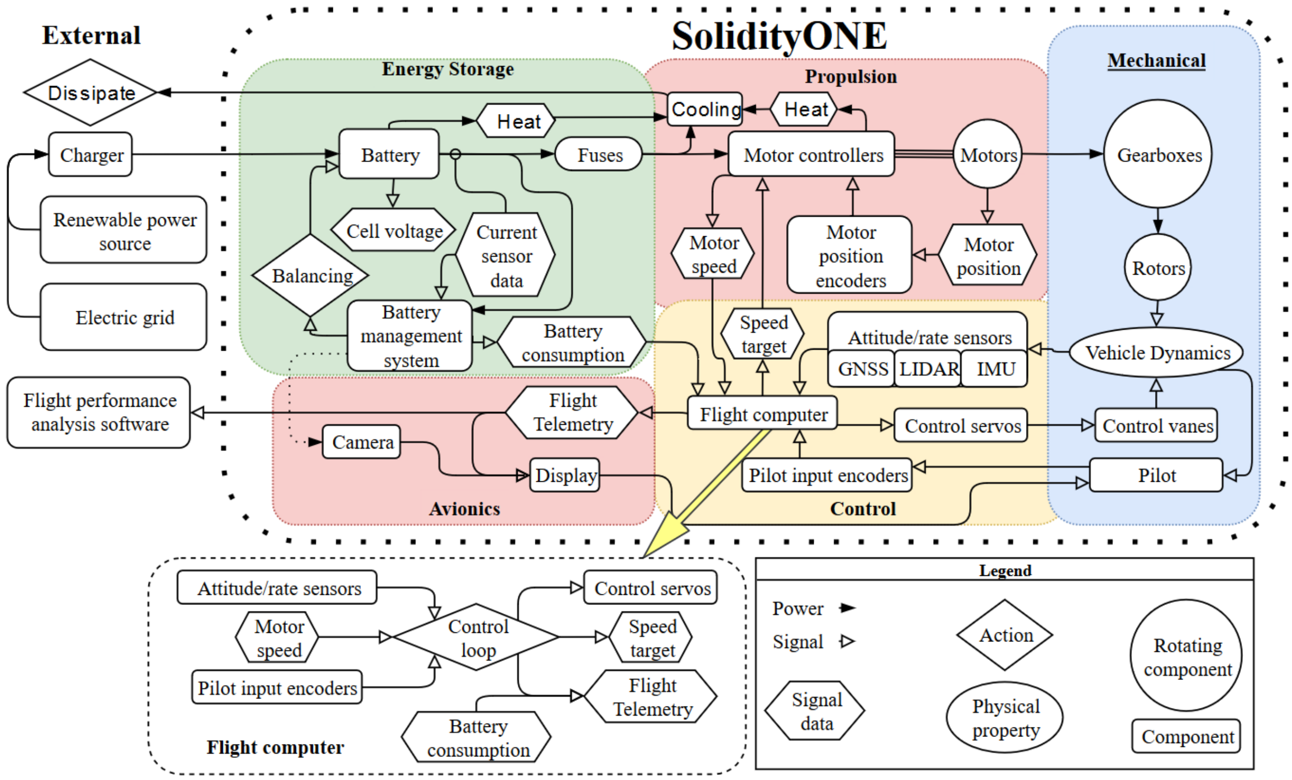

Figure 8.1: Block diagram containing electrical, hardware and software connections and interactions for the SolidityONE

9

Control and Stability

In order to be able to fly, the chosen device needs to be controllable and preferably stable. Most helicopters have a tail rotor and use a combination of collective and cyclic input which is not possible for the screw design. Therefore a new way of controlling had to be designed.

9.1. Control options

As shown in section 3.4, the two main options for control were to either tilt the ducts or install control vanes below the rotor similar to the Hiller platform [1]. The tilt mechanism was quickly eliminated since the rotors contribute to most of the weight, resulting in the choice for the use of control vanes as explained in chapter 3.

For pitch control, differential RPM was considered to improve cruise velocity and remove pitch vanes. The disadvantage of this is that it would introduce a differential torque, but this can be counteracted with the vanes. The advantage is that the pitch vanes are no longer required, reducing the weight and control complexity while still keeping authority in all degrees of freedom.

To keep the pilot interfaces manageable, a fly-by-wire system is implemented. This allows the control coupling to be automatically compensated for. A mechanical system using cables or pushrods was also considered, but such a system would be difficult to implement without taking up too much space and thus disturbing the rotor wake. The six degrees of freedom and their respective control mechanisms are listed below:

Pitch: differential RPM change
Yaw: asymmetric control vane deflection
Roll: symmetric control vane deflection
Forward translation: maintaining a pitch angle to tilt the thrust vector forward
Lateral translation: maintaining a bank angle to tilt the thrust vector sideways
Vertical translation: symmetric RPM change

9.2. Control layout

This section describes the layout of the control system. This includes the external forces on the vehicle, loads and mass estimation, and the pilot interfaces. The controls are similar to that of current helicopters, with the fly-by-wire system reducing workload.

9.2.1. Vanes

As can be seen in Figure 9.2, the induced velocity, which was calculated with Equation 6.11 is about 60% larger at the outside of the rotor compared to 20% of the rotor radius, where the hub ends. Since the vane effectiveness is proportional to the square of the induced velocity, the vanes are about 2.5 times as effective when placed in this outer region.

[1] ("Hiller Model 1031-A-1 Flying Platform." Smithsonian National Air and Space Museum. Retrieved: 7 January 2020.)

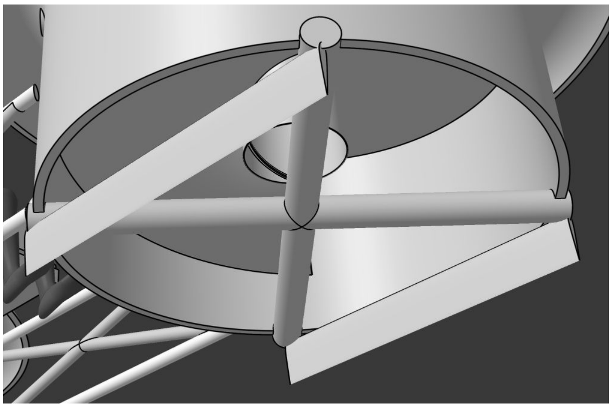

Figure 9.1: Render showing the position of the vanes

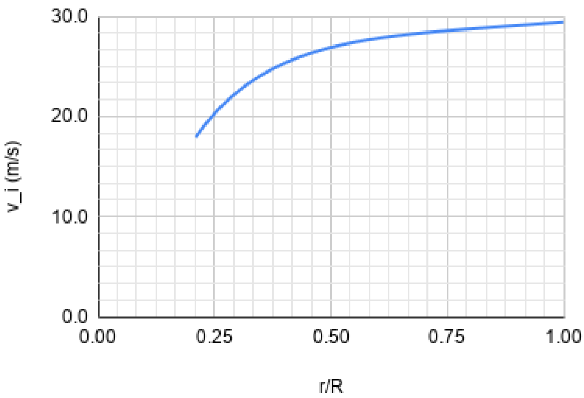

Figure 9.2: Induced velocity versus radial position in hover

The vanes are connected to duct struts, where the loads can easily be introduced to the structure, as shown in Figure 9.1. There are two vanes per rotor, both aligned parallel to the longitudinal axis of the vehicle. The centre of each vane is situated at $\frac{1}{\sqrt{\pi}}$ of the radius, seen from the centre. The Eppler 473 is chosen as the airfoil for the vanes, which is shown in Figure 9.4. It is suitable for its high maximum lift coefficient. The Reynolds number of the vanes is calculated to be in the order of 500,000, with a velocity equal to the rotor induced velocity and a vane chord in the order of 20 cm. The deflection of the vanes is limited to 12°, where the lift slope can still assumed to be linear, as seen in Figure 9.3.

9.2.2. LOADS AND SIZING

The lift forces generated by the vanes are offset from the centre of gravity of the vehicle. When the front and rear vanes are deflected opposite to each other, a yawing moment is created. This yawing moment must be larger than the maximum torque imposed due to differential RPM, such that the vehicle is able to counter this torque and is able to yaw with sufficient authority. The vane chord is sized according to this, since the lift force is proportional to the area. This is the parameter that is used to size the control system.

The vanes are actuated by a servo. To size this servo, the moment coefficient is used. For this airfoil, C_m has a maximum value of 0.045 at an angle of attack of 16°. This moment coefficient results in a hinge moment of 0.48 Nm at an induced velocity of 30 m s^{-1}. Including a safety factor of 1.5, an off-the-shelf servo can be chosen. A servo that fulfills this requirement is the DA-20-12-2515 by Volz Servos[2]. This actuator has a rated torque of 0.80 Nm, and has a mass of 88 g. Four servos are used: one per vane. The servos are powered by the BMS as described in section 8.3. The hinge line is placed at a chordwise location just in front of the aerodynamic centre to ensure a negative moment coefficient with respect to the deflection.

[2]From: https://volz-servos.com/produkte/, (Retrieved: 17 January 2020)

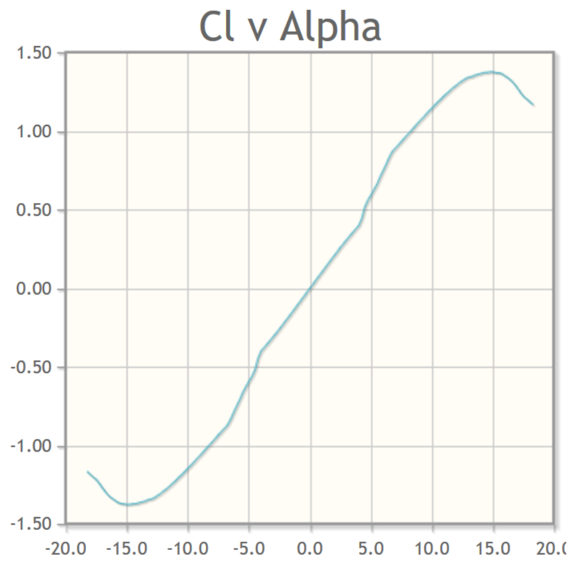

Figure 9.3: Lift slope of Eppler 473 airfoil at Re = 500,000[1]

9.2.3. MASS ESTIMATION

For a vane where the length, cord, profile and loading are known, it is possible to make an estimate of the mass. The chosen airfoil has a high thickness to cord ratio of 16.2%, which is favourable because of its large moment of inertia. Because airfoils are slender, they are not as resistant to bending in the x axis as in the y axis, shown in Figure 9.4.

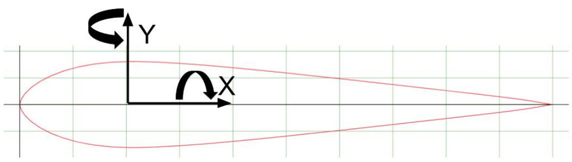

Figure 9.4: Bending moments on the Eppler 473

The vane is not allowed to bend significantly. Bending the wing when under a load would mean its lift and drag get more difficult to estimate precisely. The vane is designed that it will not plastically deform or bend more than 1.0 cm under its highest load. The profile works well up to 12° angle of attack. When the airfoil is physically constrained to less than 16°, the airfoil is not able to rotate more and act as as flat plate in the wake.

The lift at 12° is calculated and assumed to act as a distributed load on a simply supported beam where the distributed load is $w = \frac{\sqrt{2}L}{F_{Vane}}$; ignoring finite wing effects. The moment of inertia is calculated from the Steiner terms of 200 coordinates from Xfoil[3].

It is a relatively easy shape to produce this component from both carbon fiber composite with a foam core, or from an aluminium sheet. Aluminium is preferable since it can be recycled. If the mass budget does not fit and it is required to reduce weight, making the vanes out of carbon fiber would reduce their weight by 23 % compared to aluminium.

[3]From: http://airfoiltools.com/airfoil/details?airfoil=e473-il, (Retrieved: 17 January 2020)

9.2.4. CONTROL INTERFACES

The control is fully fly-by-wire with an autopilot for pitch, altitude, and yaw. This reduces mechanical complexity and can be used to increase vehicle stability. The input from the pilot will go through a controller, to 4 servos (1 for each vane), and to the motor controllers. The fly-by-wire system is selected A PixHawk 4[4] is used as flight computer. In Figure 9.5, an N2 chart of the control architecture is shown. It shows the interaction between the different components and their respective inputs and outputs.

Executing mission

Input ↓ → Output

Pilot	Altitude, velocity, yaw input, roll								
Control feedback	**Control input devices (yoke, pedals)**	Desired altitude	Desired velocity, desired yaw rate						
		Altitude controller		Desired engine RPM					
			Attitude controller	Desired engine RPM	Desired control vane deflection				
				Engine controllers			Engine thrust		
					Control vane actuators	Hinge moment			
			Control vane position			**Control vanes**	Control moment		
							Vehicle dynamics		Pitch attitude
		Altitude, climb rate	Rates, accelerations					**Gyroscope, accelerometer**	Rates, accelerations
Position, attitude and rate data									**Displays, observations**

Data collection and mission analytics

Figure 9.5: N2 chart of control architecture and data handling

9.2.5. PILOT FACILITIES

The inputs from the pilot need to be translated to the vehicle. The central processor of the vehicle takes these inputs. For this interface, the following facilities are available:

SEATING

For the seating, a simple bucket seat was chosen, mostly to save mass. Since the design is only a proof of concept, there is no need for heating, leather cover, and other luxuries. The weight of this seat is estimated around 2 kg.

CONTROL STICK

The final design has a control yoke. This provides roll and velocity control. Pitch is controlled by an autopilot. Since there is no collective control, both hands can be used on the yoke. This also provides more possible button options, for example: autopilot, trim, etc. The estimated mass for this is 2 kg. The yoke provides a signal to the flight computer.

[4] https://docs.px4.io/v1.9.0/en/flight_controller/pixhawk4.html (Retrieved 21-01-2020)

PEDALS

The final design has pedals for yaw control using a sliding mechanism. The pedals provide a signal to the flight computer.

DISPLAY

The display shows the following information: front camera display for enhanced forward visibility, airspeed, altitude, rotor RPM, warning lights, battery status, and power use. The exact layout is subject for the detailed design phase. Its mass and power have been described in subsection 8.2.6.

9.3. STABILITY EFFECTS

There are several effects that influence vehicle stability. Each of these effects is included in the flight mechanics model in section 9.4. They are explained in the following subsections.

9.3.1. GROUND EFFECT

When the vehicle is flying close to the ground and with a pitch angle, the lower rotor experiences more ground effect and thus more lift. This effect only occurs at low altitudes and acts like a spring, causing a longitudinal oscillation.

9.3.2. INDUCED VELOCITY

When the vehicle has a pitch rate, the rotors experience a different axial velocity since the rotors placed at opposing sides of the centre of mass. The effect is similar to apparent climbing and descending flight on each respective rotor, as analysed in subsection 6.2.2. The up-going rotor thus has less lift, and the down-going rotor more. This is a damping effect, reducing the pitch rate.

9.3.3. LIP RESTORING MOMENT

The flared duct inlet lips contribute a significant amount of lift to a stationary ducted fan. This is caused by the pressure above the lip surface dropping because of the induced velocity of the air. This increase in lift has an additional effect when the duct has a velocity orthogonal to its orientation. To quantify this effect, the following steps are taken:

First, the total thrust of the duct has been calculated in section 6.5 and was called T_{duct} in Equation 6.26. It is assumed that this thrust can be equated to a general lift equation with a so-called duct-lift-coefficient as shown in Equation 9.1.

To simplify the calculations, the lift of the duct was assumed to act on the thin rim of the duct, on the circumference of length $2\pi r$ instead of the area of the duct lip. Note that this has the consequence of $C_{L_{duct}}$ not being non-dimensional but this is compensated for later by again not using the area but using the circumference again.

$$L_{duct} = \frac{1}{2}\rho v_i^2 C_{L_{duct}} \cdot 2\pi r \tag{9.1}$$

This equation models the duct as distributed lifting load, which acts evenly at the rim of the duct and this lift is caused by the duct having a so-called duct lift coefficient being exposed to air velocity across the lips equal to the value of the induced velocity of the rotor inside the duct.

The induced velocity and the rotor lift are given from the rotor performance calculations so Equation 9.1 can be rearranged to give the duct lift coefficient:

$$C_{L_{duct}} = \frac{2L_{duct}}{\rho v_i^2 \cdot 2\pi r} \tag{9.2}$$

The duct lift can now be explicitly expressed as a distributed load by replacing the 2π with variable θ, the azimuth angle, and replacing the constant induced velocity V_i with the velocity expressed as a function of the azimuth angle $V(\theta)$. This results in Equation 9.3a. θ is defined such that for an angle of $\pi/2$, the section of the duct is in the direction of flight and free stream velocity. This velocity function is a sum of the free stream velocity vector and the induced velocity as shown in Equation 9.3b. The highest velocity is at $V(\frac{\pi}{2})$ and lowest at $V(\frac{3\pi}{2})$. This differential causes a reaction moment.

Figure 9.6 illustrates the velocity and lift distribution. The two sketches on the top row show the static case. The upper left duct depicts air coming in from the sides evenly at induced velocity, the upper right duct shows the resulting even lift distribution. The two ducts on the bottom row show ducts flying to the left. They experience a resulting wind blowing to the right. Now the left side of the duct has both the free stream velocity and the induced velocity acting on the duct lip, while the right (rear) side has induced velocity minus the free stream velocity acting on it. This has the consequence of a skewed distributed lift, the front-left side generates a lot more lift than the rear-right side. This imbalance of lift causes a moment which tries to pitch the ducts away from the direction of travel, which will reduce speed and stabilise the vehicle to the stationary state.

$$\frac{dL_{duct}}{d\theta} = C_{L_{duct}} \frac{1}{2} \rho V(\theta)^2 r \tag{9.3a}$$

$$V(\theta) = v_i + V_\infty sin(\theta) \tag{9.3b}$$

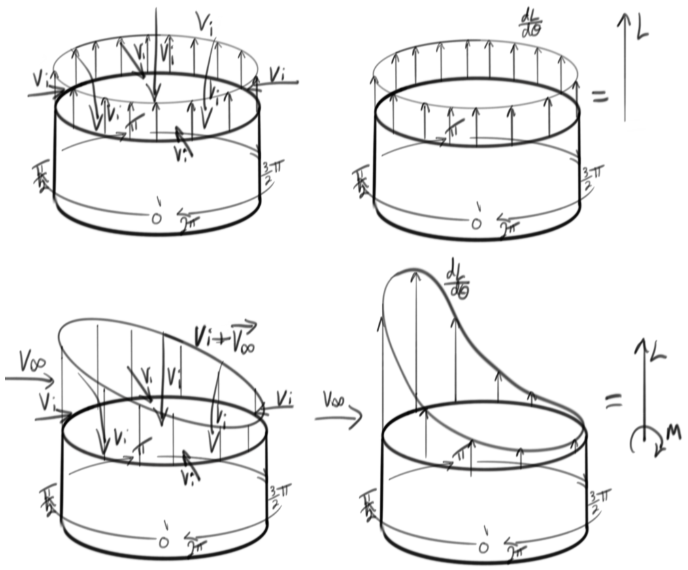

Figure 9.6: Radial velocity and lift distribution on the duct inlet lip for the stationary and dynamic case

This distributed lift function Equation 9.3a can be integrated around the full circumference of the duct to yield the total lift for a given induced velocity and horizontal free stream velocity.

$$L_{duct} = \int_0^{2\pi} \frac{1}{2} C_{L_{duct}} \rho (v_i + sin(\theta) V_\infty)^2 r d\theta = \frac{1}{2} C_{L_{duct}} \rho r (2\pi v_i^2 + \pi V_\infty^2) \tag{9.4}$$

Similarly, the total moment caused by the uneven lift distribution can be calculated by integrating the product of the lift distribution and moment arm to yield Equation 9.5.

$$M_{duct} = \int_0^{2\pi} \frac{1}{2} C_{L_{duct}} \rho r (v_i + sin(\theta) V_\infty)^2 r^2 sin\theta d\theta = C_{L_{duct}} \pi \rho v_i V_\infty r^2 \tag{9.5}$$

Finally in the case of the rotor being tilted by some angle ψ relative to the velocity vector, it is necessary to correct the free stream velocity by replacing it with $V_\infty cos\psi$ to yield Equation 9.6.

$$M_{duct} = C_{L_{duct}} \pi \rho v_i V_\infty \cos(\psi) r^2 \tag{9.6}$$

9.3.4. YAW TORQUE

When the rotors spin at different speeds to create a pitching moment, the torque of the rotors does not cancel anymore and a resulting torque acts on the vehicle, making the vehicle yaw. The control vanes have to be deflected to counter this effect. Also, when the vanes are deflected to counter the yaw torque due to differential rotor speeds, they still should have sufficient authority to yaw the vehicle.

The moment of inertia of the vehicle about the yaw axis is 305 kg m^2. This was calculated by taking the Steiner terms of each individual component, using the masses and distances from the centre of mass of the vehicle. The vanes can deliver a maximum torque of 112 Nm. With this data, the angular acceleration can be found, as well as the time to yaw the vehicle. From a standstill, it takes 4.1 seconds to yaw the vehicle 180°.

9.4. FLIGHT MECHANICS MODEL

This section describes the model used for the flight mechanics calculations. The model is longitudinal, with 3 degrees of freedom. Namely, horizontal velocity (u), vertical velocity (w) and pitch angle (θ_f). In this case pitch is defined as the angle that the device makes with respect to an inertial reference frame. The model is not yet expanded to more degrees of freedom as it is not required in this stage of the design. However, the control-ability of these additional degrees of freedom are taken into account when designing the control system. In future development, these additional degrees of freedom should be included in the simulation.

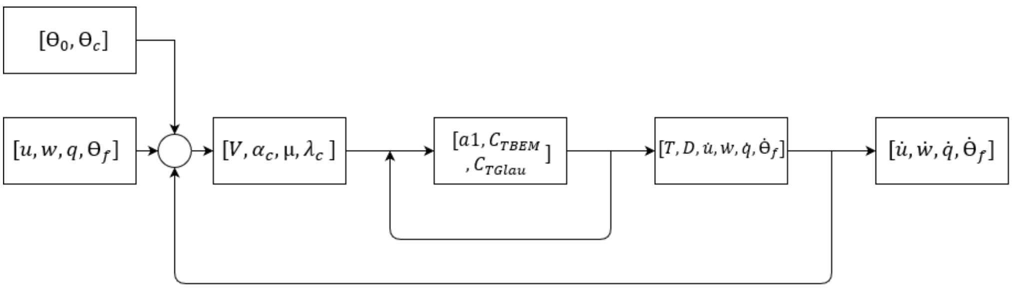

Figure 9.7: Block diagram of flight mechanics model

The simulation can be simplified to Figure 9.7 where Θ_0 and Θ_c are the collective and cyclic inputs respectively. Firstly, the total velocity V, control plane angle with respect to the fuselage α_c, advance ratio μ and non-dimensional inflow velocity λ_c are calculated according to [46]:

$$V = \sqrt{u^2 + w^2} \tag{9.7a}$$

$$\alpha_c = \theta_c - \arctan\frac{w}{u} \tag{9.7b}$$

$$\mu = \frac{V}{\Omega R} \cdot \cos\alpha_c \tag{9.7c}$$

$$\lambda_c = \frac{V\sin\alpha_c}{\Omega R} \tag{9.7d}$$

Next, the thrust coefficient (C_T) is calculated using the Blade element theory and Glauert method. λ_i is the non-dimensional induced velocity and is chosen until C_{TBEM} and C_{TGlau} converge [46].

$$a_1 = \frac{\frac{8}{3}\mu\theta_0 - 2\mu(\lambda_c + \lambda_1) - \frac{16}{\gamma}\frac{q}{\Omega}}{1 - \frac{1}{2}\mu^2} \tag{9.8a}$$

$$C_{TBEM} = \frac{1}{4} c_{l\alpha}\sigma\left[\frac{2}{3}\theta_0\left(1 + \frac{3}{2}\mu^2\right) - (\lambda_c + \lambda_1)\right] \tag{9.8b}$$

$$C_{T\,\mathrm{Glau}} = 2\lambda_1\sqrt{\left(\frac{V}{\Omega R}\cos(\alpha_c - a_1)\right)^2 + \left(\frac{V}{\Omega R}\sin(\alpha_c - a_1) + \lambda_1\right)^2} \tag{9.8c}$$

$$F(\lambda) = C_{TBEM} - C_{TGlau} \tag{9.8d}$$

When $C_{T_{BEM}}$ and $C_{T_{Glau}}$ are within 0.0001 of each other. The values of $C_{T_{BEM}}$ and α_1 are used to calculate Thrust T, Drag D, and the system states. The following equations are the equations of motion for a standard helicopter. These are only used for the verification process [46].

$$T = C_T\rho(\Omega R)^2\pi R^2 \tag{9.9a}$$

$$D = C_D\frac{1}{2}\rho V^2 S \tag{9.9b}$$

$$\dot{u} = -g\sin\theta_f - \frac{D}{m}\frac{u}{V} + \frac{T}{m}\sin(\theta_c - a_1) - qw \tag{9.9c}$$

$$\dot{w} = g\cos\theta_f - \frac{D}{m}\frac{w}{V} - \frac{T}{m}\cos(\theta_c - a_1) + qu \tag{9.9d}$$

$$\dot{q} = -\frac{T}{I_y}h \cdot \sin(\theta_c - a_1) \tag{9.9e}$$

$$\dot{\theta}_f = q \tag{9.9f}$$

As described in section 9.1 the SolidityONE does not have a collective and cyclic input, thus θ_0 and θ_c are set to 0. Furthermore, the other effects stated in section 9.3 are also included in the model so that it would be compatible with the SolidityONE. Furthermore, since the thrust calculations have been done before in chapter 6, the iteration process replaced by a constant C_T of 0.074. which is derived from the calculations in chapter 6 with the previous calculations. This changes the formulas to:

$$T_{1,2} = \frac{C_T\rho(\Omega R)^2\pi R^2}{1 - \frac{R}{4z^2}} \tag{9.10a}$$

$$D = C_D\frac{1}{2}\rho V^2 S \tag{9.10b}$$

$$\dot{u} = \frac{T_1 + T_2}{m}\sin\theta_f - \frac{D}{m}\frac{u}{V} \tag{9.10c}$$

$$\dot{w} = (T_1 + T_2)\cos\theta_f - \frac{D}{m}\frac{w}{V} - g \tag{9.10d}$$

$$\dot{q} = -\frac{T_2 - T_1}{I_y} D_{cg} - M_{duct} \tag{9.10e}$$

$$\dot{\theta}_f = q \tag{9.10f}$$

In Equation 9.10a, the factor for ground effect is incorporated in the denominator. Where T_1 and T_2 are the thrusts for the front and back rotor respectively, D_{cg} is the distance from the centre of the rotor to the centre of gravity which is assumed to be in the middle for the purpose of simplification. The exact cg locations are shown in Table 11.2. This shows that the assumption is reasonable.

9.4.1. PHUGOID

The phugoid is an aircraft mode where the aircraft generally shows a pitch oscillation. It is induced by introducing a sudden pitch control. Either by a cyclic input for a conventional rotor or a differential RPM input in the SolidityONE. The simulation of the phugoid of the SolidityONE can be seen in Figure 9.8. From the graph it can be seen that the motion is unstable, since the amplitude and the frequency of the motion increase after the input has ended, therefore a controller is required. This is more explained in subsection 9.4.3

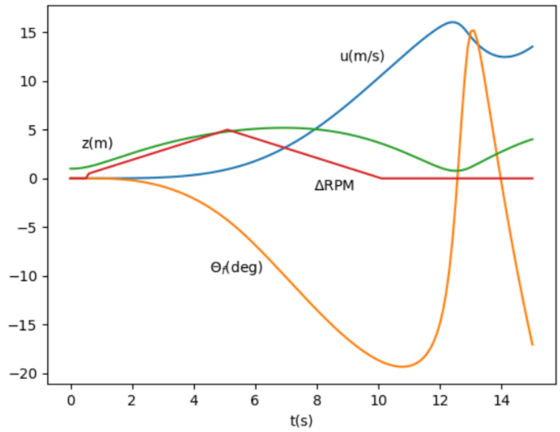

Figure 9.8: Instability in the hover after a differential rpm input (RPM input is shown divided by 10)

9.4.2. SHORT PERIOD

The short motion is a rapid pitching of an aircraft, initiated by applying a sudden increase in pitch due to a either a cyclic or differential rpm input in the case of the SolidityONE. The result of the differential input is shown in Figure 9.9. It shows a decaying oscillation after the input. As indicated in the graph, the short-period motion is stable with a half time of approximately 6 sec. Therefore a controller is not required to further dampen the motion.

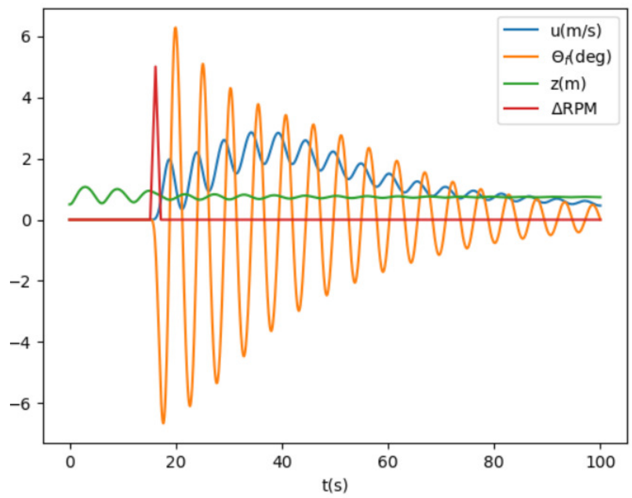

Figure 9.9: Hover after a short impulse in differential input (RPM input is shown divided by 5)

9.4.3. P-CONTROLLER

As been discussed in Figure 9.8, the device is slightly unstable in the phugoid motion. This is true for the case of most helicopters without controller[46]. There are 3 different kinds of controller that could be used: Proportional (P), Integrator (I) or Differential (D). Since there is only a slight instability, a simple P-controller is used to simulate the pilot. For t>15sec; $\Delta_{RPM} = 100 * \Theta_f$ (deg). The result of this is depicted in Figure 9.10 the motion stabilises after a few oscillations.

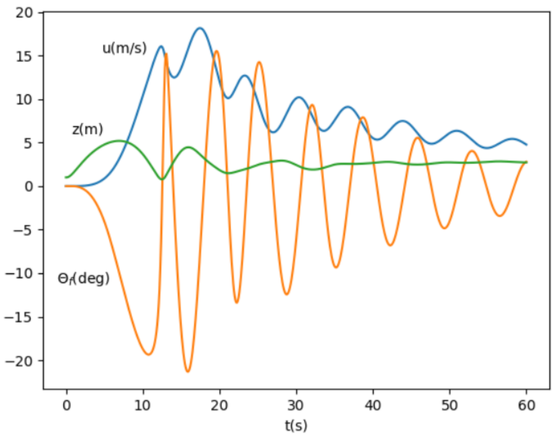

Figure 9.10: Simple pilot feedback for stabilization for hover. The input is equal to Figure 9.8

From Figure 9.10, the phugoid motion is now stable with a half time of approximately 17 sec. In the future, a more sophisticated controller can be designed if more damping is required.

10
Structure

The mid-term concept design phase results in a vehicle depicted as in Figure 10.1. There are two ducted rotors, each has a rotor with an axle called the rotor hub. The rotor and hub are supported by so-called duct struts and an electric motor is mounted on the top of these struts. The two ducts are connected to each other by a truss structure called the airframe, which also serves as the pilot compartment and contains various power storage and control systems.

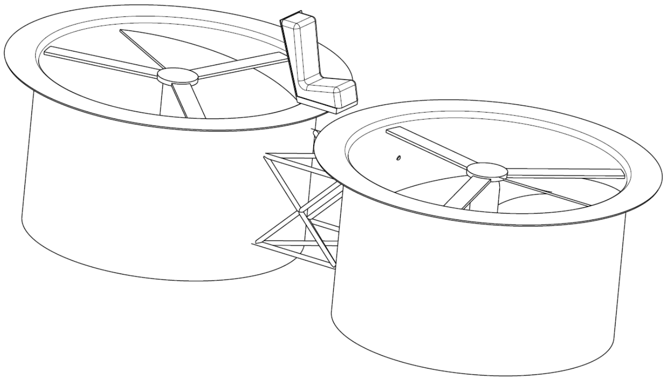

Figure 10.1: Concept render of the tandem

In the final preliminary design phase the airframe truss ends and duct struts were designed so loads from the rotor can be transferred directly to the airframe instead of being carried by the duct walls. This is illustrated by Figure 10.2. The two duct struts closer to the airframe are primary load carrying and the two struts farther away only serve to secure the duct wall from deflecting so they are called the primary and secondary duct struts respectively. Detailed discussion of the loads designed for can be found in the following sections.

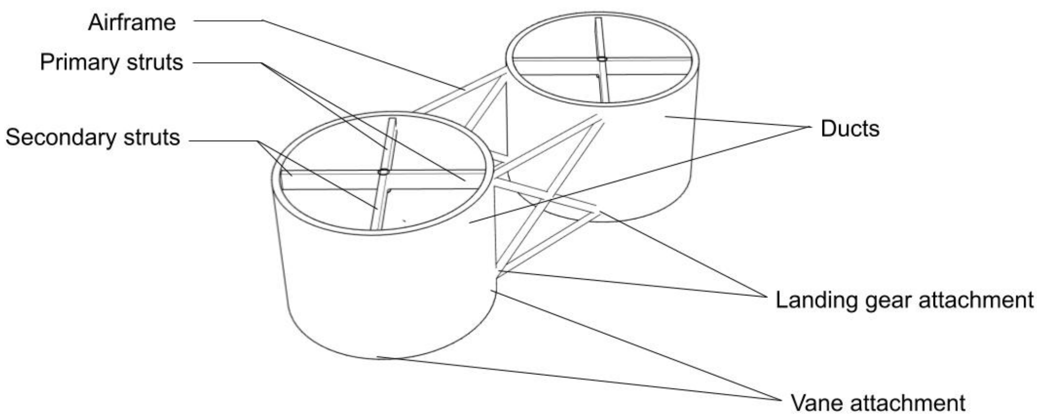

Figure 10.2: Updated overall lay out of structure

10.1. ROTOR BLADE DESIGN

In this section the design process for the rotor blade, excluding the hub, is elaborated upon. First, the loads acting on the part are explained. Then, a structure selection is made based upon a trade-off. Next, the calculation and verification method applied during the design process are clarified. Lastly, the selection of material is justified.

10.1.1. LOADS

Figure 10.3 depicts the forces acting on the rotor blade. F_c is the centrifugal force on the blade due to the rotation. This force is calculated with Equation 10.1, where m is the mass of each blade element, ω the RPM of the blade and r the distance of each blade element to the center of the hub.

$$F_c = m\omega^2 r \tag{10.1}$$

This force can be decomposed into two forces and this decomposition is dependent on the anhedral angle Γ. The component parallel to the rotor blade will cause an elongation of the blade whereas the component perpendicular will contribute to the bending moment acting on the blade which is also caused by the lift force on the blade. The determination of the lift force of each blade element is explained in section 6.2. The rotor structure must be designed to be stiff enough to prevent deflection and making contact with the duct wall.

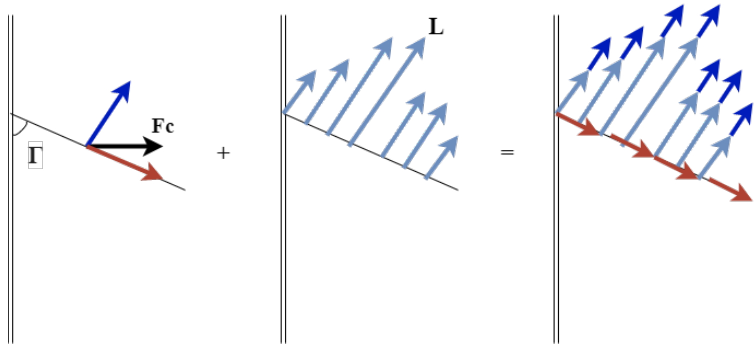

Figure 10.3: Schematic drawing of loads on the rotor blade

Furthermore, the aerodynamic moment acting on the blade was also considered. Because a cambered airfoil was used, the blade experiences a nose-down pitching moment. A nose-down deflection could cause significant loss in angle of attack and thrust. The moment is calculated separately for each element using Equation 10.2 where C_m is the moment coefficient imported from the aerodynamic department. S is the surface of the element which is determined multiplying the width of an element with the chord.

$$M = C_m q S c = C_m \frac{1}{2}\rho(\omega r)^2 S c \tag{10.2}$$

10.1.2. STRUCTURE SELECTION

To be able to select an efficient structure type for the rotor blade a trade-off was performed. Options that were taken into consideration were a solid blade, a hollow blade with and without sandwich structure. Solid blades were dismissed because this would result in a comparably heavy rotor due to its volume. This would limit the radius size because the volume increases cubically with the radius. Hollow blades were dismissed since for large airfoil thicknesses the structure would need to be stiffened, which would make the design and production complex. Hence, a sandwich structure was deemed the most efficient way to make it lightweight and stiff. To protect the rotor from particle impact damage, eroding the composite at the leading edge, leading edge tape was applied.

10.1.3. CALCULATION METHOD

STRESSES

To be able to calculate the different deflections and stresses, the rotor blade is divided into 100 equally wide elements (the same amount as the aerodynamics BEMT sections, described in subsection 6.2.1) along the radius. From the aerodynamics department values for radius, thrust, RPM, pitch angle and airfoil data such as chord, thickness-to-chord ratio, camber and camber location for each section were imported. Calculating the tensile stress caused by the bending of the blade by the lift and perpendicular centrifugal component on it has been done using Equation 10.3.

$$\sigma = \frac{My}{I} \tag{10.3}$$

$$M = (L + F_c \cdot sin(\Gamma)) \cdot r \tag{10.4}$$

Per section, it's area moment of inertia and highest vertical distance to the centroid is calculated. The bending moment M in this equation is calculated for each element by summing up the corresponding lift and perpendicular component of F_c and multiplying this with the radius as shown in Equation 10.4.

The other force that was considered to cause tensile stress on the blade is the parallel component of F_c. For each section the parallel component was calculated and used to calculate the tensile stress by dividing it by the skin profile area Equation 10.5. The profile area is calculated per section and then summed.

$$\sigma = \frac{F_c \cdot cos(\Gamma)}{A_{skin}} \tag{10.5}$$

Then, summing op the tensile stresses obtained from Equation 10.3 and Equation 10.5 per element and adding them up from tip to root gives the bending moment distribution along the blade.

Lastly, the shear stresses on the blade were analysed. This is done simply by dividing the sum of the lift force and the perpendicular component of F_c by the core area of the blade element as shown in Equation 10.6. This gives the average shear stress along each element. Similarly, adding these up from tip to the root gives the average shear stress distribution. It was determined that the average shear stress is negligibly low, hence more engineering effort was not put into determining the maximum shear shear stress.

$$\tau_{average} = \frac{L + F_c \cdot sin(\Gamma)}{A_{core}} \tag{10.6}$$

DEFLECTIONS

Due to the lift forces being low a conservative approach was taken to calculate the deflection of the blade in the vertical direction due to bending. This was done by introducing the total lift force of the blade at the tip and use the lowest moment of inertia out of the hundred elements. Then, the deflection was calculated using Equation 10.7, which is the standard formula for a cantilever beam with a point load at the free end.

$$\delta_{max} = \frac{PL^3}{3EI} \tag{10.7}$$

The elongation of the blade was calculated separately for each element with Equation 10.8 where σ is the stress obtained from Equation 10.5 and L the width of an element. Then, all the elongations of each element were summed up to arrive at the total elongation of the blade. This needed to be determined to know if the blade would touch the duct while spinning at max RPM.

$$\delta = \frac{\sigma}{E} L \tag{10.8}$$

Lastly, the angular deflection due to the aerodynamic moment has been looked at. It was computed separately again for each element with Equation 10.9, where T is the aerodynamic moment acting on each element and L the distance of the element from the hub. Adding all these deflections from root to tip gives the angular deflection along the rotor blade.

$$\theta = \frac{TL}{GJ} \tag{10.9}$$

10.1.4. VERIFICATION

Verification of the tool for the rotor blade has been done by developing a slightly different tool first. The difference from the final tool is that this tool performed the calculations for each element with a hollow rectangular cross section instead of an airfoil. The height of each hollow rectangular cross section corresponds with the maximum profile thickness of the airfoil of each element and the width with the chord as shown in Figure 10.4. The thicknesses of both were also kept the same. Manual calculations could be performed for a particular rectangular element which would help verifying the tool. After the verification of the rectangle tool with manual calculations, the more accurate airfoil tool could be verified by comparison to the rectangle tool. It was expected that the mass and the moment of inertia of the airfoil would be slightly less than that of the rectangular cross section, which would result in slightly higher stresses. As this was the case after comparison the tool was considered verified.

Figure 10.4: Hollow rectangular cross section in comparison to the airfoil

10.1.5. MATERIAL SELECTION

The aerodynamic properties of the rotor blade are a function of the shape of the blade. Thus, stiffness is an important factor in rotor material selection. The weight of the rotor is also important, since increasing the weight increases the centrifugal forces, which in turn increases the weight even further. Also, increasing the weight gives an increase in moment of inertia of the blade and since the rotor rotates with nearly 2000 RPM this has a significant effect on the control & stability of the vehicle. Due to the complexity of the shape of the rotor a fiber material is chosen for the skin, since this can be easily formed into any shape. Out of the fiber materials listed in Figure 3.8 it was chosen to go for *Epoxy/HS carbon fiber, woven prepeg, biaxial lay-up* to be able to get an quasi-isotropic lay-up and still have enough stiffness in all directions. Because the volume of the skin is significantly lower than other parts of the vehicle the cost and CO_2 footprint of the material was not considered a decision driver.

For the core, foam is chosen over a honeycomb, since foam can also be easily formed into any shape with a CNC machine. From Figure 3.8 *Expanded PS foam (closed cell, 0.050)* was picked because it is the cheapest and has the lowest CO_2 footprint out of all the optional foams. It is slightly weaker than the other foams out of the list but because the shear stresses were calculated to be low it was chosen to pick the cheapest and most sustainable option.

The leading edge tape protects the carbon fibre at the leading edge from eroding due to dust particles and small stones. The material used is a off-the-shelf tape *3M Polyurethane Protective Tape 8674*.

10.2. ROTOR HUB DESIGN

In this section the design process for the rotor hub is elaborated upon. First, the loads acting on the part are explained. Then, a structure selection is made based upon a trade-off. Next, the calculation and verification method applied during the design process are clarified. Lastly, the selection of material is justified.

10.2.1. LOADS

The same loads that introduce centrifugal and lift forces on the rotor blade as shown in Figure 10.3, also introduce shear forces and a bending moment in the rotor hub respectively. Due to the complex shape of the rotor blade, the distribution of these forces and moments along the chord of the blade is highly asymmetrical. To be able to calculate the deflection and the stresses in the hub, the load case is simplified into the free body diagram of Figure 10.5c.

For the simplification of the loads, the blade is divided into two sections Figure 10.5a, where the loads due to lift L are assumed to be point loads at half radius Figure 10.5b. This will overestimate the moments that will act on the hub in the real case. Since, the forces would normally be a more distributed load along the length of the hub. Thus, this will be a conservative estimate of the deflection and the stresses that will act on the hub. Furthermore, the centrifugal force is taken at one-third radius as a result of the center of mass for a semi-circle.

The ends of the hub are assumed to be fixed, since the hub is only able to rotate freely around its longitudinal axis but fixed in all other degrees of freedom. In Figure 10.5c the rotated free body diagram of this simplified case is given. Where point D is the top attachment to the duct struts and point A is the bottom attachment. At both ends of the of the hub, there are reaction forces and moments. These are shown as $R1$, $R2$ and $MR1$, $MR2$ in the figure respectively. Since the hub rotates around the z-axis, the reaction forces and reaction moments will also rotate around the z-axis. This introduces reaction moments of the hub into the primary duct struts which will be elaborated on in section 10.3.

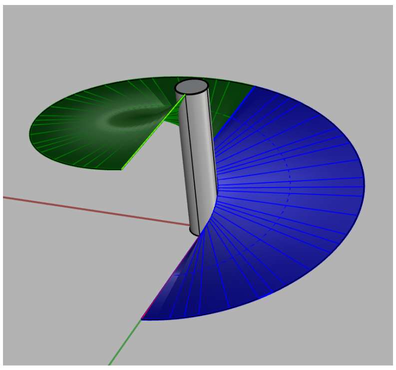

(a) Isometric view of split rotor surfaces

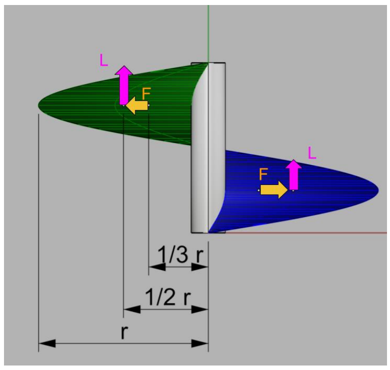

(b) 3D view of simplified rotor analysis

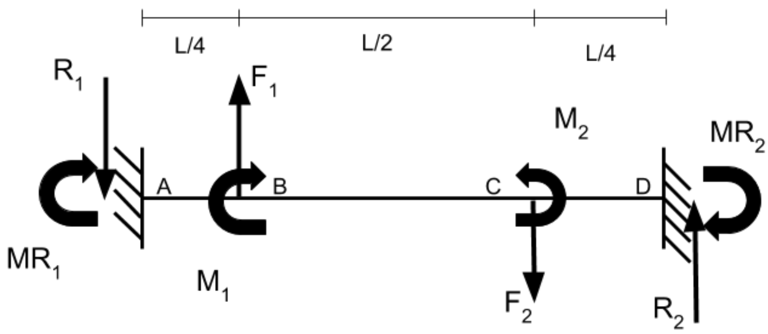

(c) FBD of simplified loading case

Figure 10.5: Load case of rotor

The above simplified loadcase covers the largest part of the loads acting on the hub. However, the hub also needs to transfer the torque provided by the motor into the rotor blade to be able to make it rotate. To make sure the shaft does not fail under operation conditions, the torque on the shaft is assumed to be the maximum torque required in any operating condition times a safety factor of 1.5. Also the torque of the rotor is assumed to be introduced into the hub at the middle point of the hub. In the real case the torque will be distributed along the hub where the centre of these torques will be closer to a quarter of the span. Thus, the deflection calculated in this manner will be overestimated.

10.2.2. STRUCTURE SELECTION

The rotor hub is a thin tube because the stiffness-to-weight ratio is higher compared to that of solid shafts. This makes sense since the moment of inertia of a thin tube scales with R^3 (Equation 10.10) and the weight scales with R^2 (Equation 10.11). Furthermore, a tube is more efficient at carrying torsional loads than any other kind of shape since the shear stress distribution is uniform along the radius of the shaft [63]. Also, is there no distortion or change in volume of the shaft sections due to torsion.

$$I = \pi R^3 t \tag{10.10}$$

$$m = 2\pi R \cdot L \cdot t \tag{10.11}$$

10.2.3. CALCULATION METHOD

Using the simplified load case of the hub as in Figure 10.5c and the deflection equation Equation 10.12, the moment and deflection distribution along the span can be calculated. Since this is a statically indeterminate problem, the boundary conditions needed to be used to be able solve this equation. Since the ends of the hub are fixed, the boundary conditions are zero deflection at $x = 0$ & $x = L$ and zero slope at $x = 0$ & $x = L$. Furthermore, if the material and geometry are constant along the length of the hub, the Young's modulus E and the moment of inertia I can be assumed as constants. In order to get the deflection along the span, the moment needed to be integrated over the span twice.

$$\frac{d^2\delta(x)}{dx^2} = -\frac{M(x)}{EI} \tag{10.12}$$

To find the maximum deflection $\delta_{(x)_{max}}$, Equation 10.12 needs to be solved for zero slope at $0 < x < L$. Where x is the distance along the hub, measured from the bottom attachment. To calculate the stress distribution in the hub, the moment distribution needs to be implemented in Equation 10.3. This will result in Equation 10.13. To determine the maximum stress the maximum moment needs to be inserted.

$$\sigma(x) = \frac{M(x)y}{I} \tag{10.13}$$

To compute the maximum angular deflection of the hub Equation 10.14 is used. Where T is the maximum torque at span location L, G is the shear modulus of the tube and J is the polar moment of inertia

$$\theta = \frac{TL}{GJ} \tag{10.14}$$

To find the maximum shear stress due to the motor torque Equation 10.15 is used. Where τ is the shear stress, T is the maximum torque, R is the radius of the hub and J is the polar moment of inertia.

$$\tau = \frac{TR}{J} \tag{10.15}$$

Lastly, to make sure the thin tube does not collapse under the combination of the previously mentioned loads the design approach stated in *Buckling of thin-walled circular cylinders* by NASA is used [64]. This approach uses statistical data to calculate the maximum stress of thin tubes under various combinations of loads.

10.2.4. VERIFICATION

To verify the calculations a Finite Elements Analysis (FEA) was performed with the program Abaqus [65]. Where the deflections calculated with the method mentioned above is checked with the deflections calculated by the program. In the program the hub is modelled as a wire, with the previously determined properties and cross-section assigned to it. The deflections calculated with Abaqus can be seen in Figure 10.6 where the deflections is given in millimeters. The difference between the calculated above and the deflection determined by the program is less than 14%.

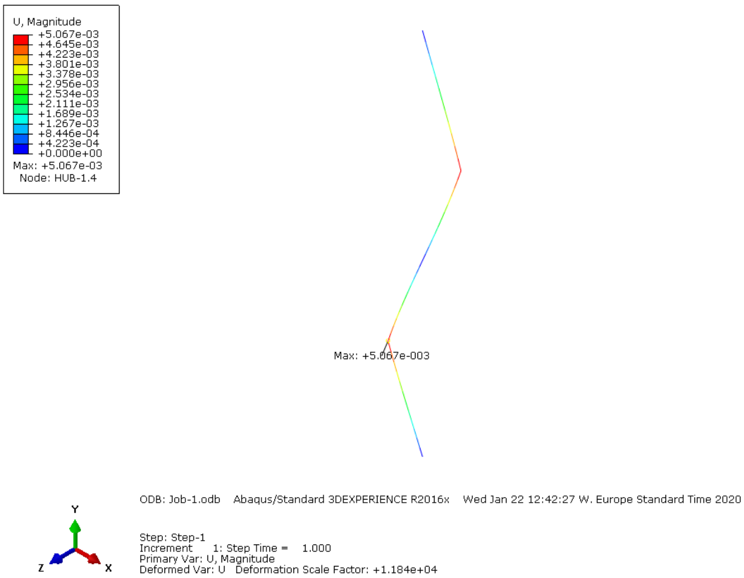

Figure 10.6: Deflections of the hub as simulated in Abaqus

10.2.5. MATERIAL SELECTION

Since the hub introduces all the loads to the rest of the structure a material with high stiffness and strength was looked for. The density of the material was not a decision driver because the two hubs in the vehicle are considerably small parts. Therefore, steel was chosen to be the material over aluminium and carbon fiber. Out of Figure 3.8 *Low alloy steel, AISI 4340* was chosen because it is the cheapest and most sustainable out of all the steel options.

10.3. DUCT STRUTS DESIGN

In this section the design process for the duct struts is elaborated upon. First, the loads acting on the part are explained. Then, a structure selection is made based upon a trade-off. Next, the calculation and verification method applied during the design process are clarified. Lastly, the selection of material is justified.

10.3.1. LOADS

To ensure the attachment of the control vanes and a proper transfer of loads from the struts to the airframe, the configuration shown in Figure 10.2 for the duct struts has been chosen. Each duct will contain eight struts where four of them will be on the top and four under the duct. The four struts that are attached to the airframe structure are called primary struts, whereas the four outer struts are called secondary struts from now on. The primary struts are assumed to carry all the loads from the hub to the airframe.

The two primary struts will be subjected to three different loads as shown in Figure 10.7a. P is the maximum vertical force of the rotor, T is the engine of the motor and M_{hub} is the rotating reaction moment that the hub is introducing to the struts. Because the reaction moment M_{hub} is rotating together with the hub it subjects a torsion to one primary strut while subjecting a bending moment to the other at one point of time and at another moment in the same revolution vice versa.

The duct struts were assumed to be cantilever beams with free ends for load P and M_{hub} whereas simply supported for engine torque T as shown in Figure 10.7b. This is because T acts in the horizontal plane whereas the other forces act in the vertical plane. Furthermore, for load P is it assumed that the load is equally distributed over the four (two top and two bottom) primary struts on each duct. For load M_{hub} is it assumed that one strut needs to be able to carry all the load because this load rotates from strut to strut. Lastly, the engine torque T is assumed to be distributed equally along two primary struts because the engine will only subject torsion to the two struts on the side it is attached to.

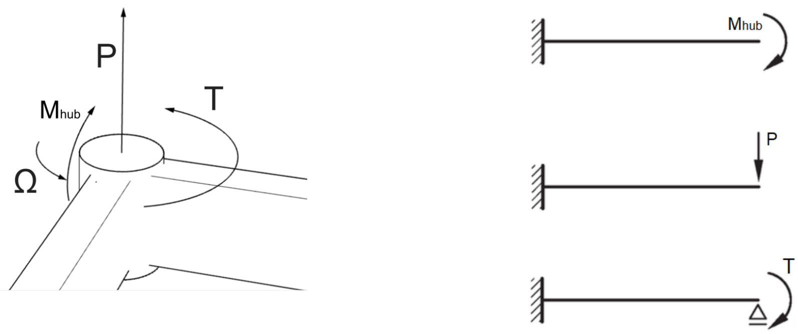

(a) Forces and moments on the primary struts

(b) Simplified load case

Figure 10.7: Loads on duct struts

10.3.2. STRUCTURE SELECTION

From initial calculations it was determined that the critical load case for the duct struts is the combination of the bending caused by load P and M_{hub}. Therefore, the decision was made to use an hollow rectangle cross-section for the duct struts. The hollow inside can be used to cover cables and are rectangular section is better at torsion than an I-beam for instance. Furthermore, limits to the size of the beams were set during the design process to ensure the size of the beams are proportional to the size of the rotor. Lastly, the decision was made to cover the beams for both top and bottom with aerodynamic fairings to not disrupt the in- and outflow and create unnecessary drag. The shape of the fairings are two semi-ellipses on top and bottom of the beams such that the total height of the beams become 1.3 times the height of the beam.

10.3.3. CALCULATION METHOD

The magnitude of M_{hub} was calculated while sizing the hub in section 10.2 and the maximum engine torque T from the power department. Determining load P has been done by taking the maximum of three different considered load cases which are; standing still on the ground with engines off, during flight and during landing. For landing the FAR requirements states that *the vehicle shall be capable of landing with 2/3 of the maximum weight supported by lift* [47]. For each iteration the tool determined the highest load out of the three cases which could differ each time depending on the weight the duct struts need to be able to carry. During the iterative process this weight would be the weight of the engine and the screw because they are attached to the duct struts.

After having determined load P the dimensions of the beam were optimized for a certain deflection limit and size limit. The deflection due to the combination of load P and bending moment M_{hub} is calculated by using the standard formulas from mechanics for a cantilever beam with a point load at the free end and with a bending moment at the free end. Adding these two up as in Equation 10.16, gives the total deflection due to combination of load P and bending moment M_{hub}. The deflection due to the engine torque T has been computed using Equation 10.17. Lastly, the angular deflection due to the torsion caused by M_{hub} is calculated using Equation 10.18.

$$\delta_{total} = \frac{PL^3}{3EI} + \frac{M_{hub}L^2}{2EI} \tag{10.16}$$

$$\delta = \frac{TL^2}{32EI} \tag{10.17}$$

$$\theta = \frac{M_{hub}L}{JG} \tag{10.18}$$

For the set deflection limit, the tool runs trough all possible beam cross section configurations within the size limit and collects all configurations which comply to the deflection limit. Once the weights of the screw and the engine were determined within a certain range it was noticed that the bending moment caused by the combination of P and M_{hub} is the critical case for the size and thickness of the cross section. Within the group of the configurations that comply to the deflection limits the tool picked the one that has the least mass. This way it has been made sure to have an optimized cross-section for the duct struts. The deflection limits were determined by the gap between the duct struts and the rotor.

10.3.4. VERIFICATION

Verification of the tool for the duct strut has been done by using a similar verification method as described in subsection 10.1.4. First, verification of code segments has been done by means of manual calculations. Verification for the entire duct strut tool has been done by developing similar tools for different cross sections such as a hollow cylinder, I-beam and an H-beam. Knowing the strengths and weaknesses of these profiles and their behaviour with certain loads it was possible to compare the results. As results turned out to be as expected the tool was considered verified.

10.3.5. MATERIAL SELECTION

Because there are 16 duct struts with a significant size a material with high specific strength and specific stiffness has been searched for that is also cheap and sustainable. Aluminium was chosen over carbon fiber because the increase in stiffness does not outweigh the increase in cost. Also, aluminium is recyclable whereas carbon fiber is not. Out of Figure 3.8 *Aluminium 7068 T6511* was chosen as material for the duct struts, because it is the cheapest and most sustainable out of all the aluminium options.

10.4. DUCT DESIGN

In this section the design process for the ducts is elaborated upon. First, the loads acting on the part are explained. Then, a structure selection is made based upon a trade-off. Next, the calculation method applied during the design process is clarified. Lastly, the selection of material is justified.

10.4.1. LOADS

The loads on the duct are simplified into the free body diagram of Figure 10.8. Due to the design of the structure of the vehicle, the duct needs to carry its own weight (F_g). This force is at its maximum during the landing of the vehicle. Furthermore, the duct also has to be able to transfer the bending moments introduced by the duct lips, M_{lip}, into the structure. The maximum momemt is used, which is created during the maximum forward flight speed. Lastly, the duct is subjected to a local pressure force, D, introduced by the pressure drag of the duct. The maximum drag is created during maximum forward flight speed. All of these forces are introduced into the rest of the structure at the simply supported points 1 and 2. The reaction forces at these points are given by F_{x1} and F_{x2} for the x-direction and F_{z1}, F_{z2} for the z-direction.

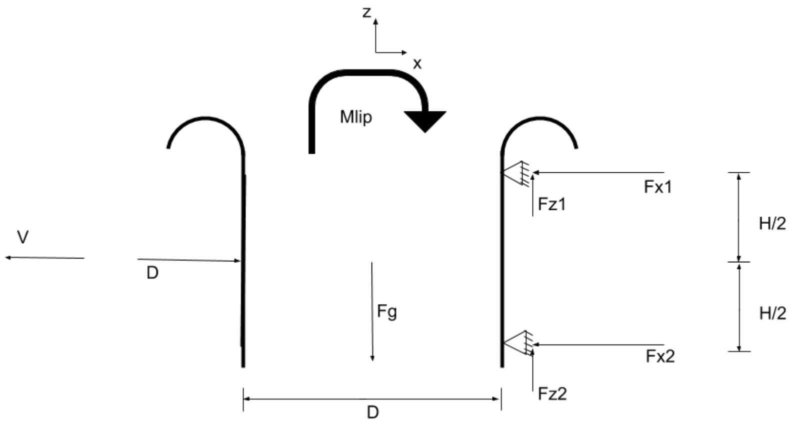

Figure 10.8: Free body diagram duct

10.4.2. DUCT STRUCTURE SELECTION

For the ducts a trade-off has been performed between two structure types which were a sandwich panel and a solid skin. A solid skin would need a higher thickness compared to a sandwich structure to be able to not collapse or fail in buckling. This would make the duct heavier which is not desired because the ducts have a relatively big size. Although the skin could be kept thin with stiffeners this was not considered A worthy option because placing the stiffeners inside the duct would not be possible without increasing the tip clearance and placing them outside the duct would increase the drag of the vehicle. Furthermore, would it decrease the aesthetic performance. However, a sandwich structure can provide a high stiffness while also having a low weight. Therefore, the ducts were designed to be sandwich panels.

10.4.3. CALCULATION METHOD

The formulas for the stresses calculated in the duct lip are retrieved from *Buckling of thin-walled circular cylinders* by NASA [64]. This paper estimates the maximum buckling stresses for a thin-walled cylinder under different loading conditions. Equation 10.19 [64] gives the estimates the buckling stress, where E is the Young's Modulus, μ is the Poisson's ratio, t is the wall thickness and r is the duct radius. γ is given by Equation 10.20 for axial loading and by Equation 10.21 for bending. ϕ is determined by Equation 10.22 for all load cases.

$$\sigma = \frac{\gamma E}{\sqrt{3(1-\mu^2)}}\frac{t}{r} \tag{10.19}$$

$$\gamma = 1 - 0.901(1-e^{-\phi}) \tag{10.20}$$

$$\gamma = 1 - 0.731(1-e^{-\phi}) \tag{10.21}$$

$$\phi = \frac{1}{16}\sqrt{\frac{r}{t}} \tag{10.22}$$

10.4.4. MATERIAL SELECTION

Materials for duct sandwich panel skin were selected to have a high specific stiffness because of the tight tip clearance set by the aerodynamics department. Furthermore, due to the relative big size of the two ducts compared to other parts, the material density was also a decision driver. Therefore, carbon fiber was chosen for the duct. Since the duct is loaded in axial and radial direction, it was deemed necessary to have quasi-isotropic lay-up of the carbon fiber skins. Therefore, the same carbon fiber (*Epoxy/HS carbon fiber, woven prepeg, biaxial lay-up*) was chosen as for the rotor blade.

As for the core, the decision was made to use honeycomb for the straight part of the duct and foam for the lips. This is because production costs would be higher for a honeycomb core in the shape of the duct lip.

10.5. AIRFRAME DESIGN

In this section the design process for the airframe is elaborated upon. First, the loads acting on the part are explained. Then, a structure selection is made based upon a trade-off. Next, the calculation method applied during the design process is clarified. Lastly, the selection of material is justified.

10.5.1. LOADS

The critical loads cases on the airframe can be divided into two different flight phases. The first is forward flight at maximum speed, the free body diagram is shown in Figure 10.10. The second loadcase is landing at two-thirds of the lift, the free body diagram for landing is shown in Figure 10.9. At maximum forward speed the engine torque Te, the thrust, the drag and the torque about the longitudinal axis are at their maximum. The torque about the longitudinal axis is caused by the aerodynamic moment created by the duct lip, for a more detailed explanation see chapter 9. For the landing load case the large deceleration increases the bending forces in the introduced into the airframe.

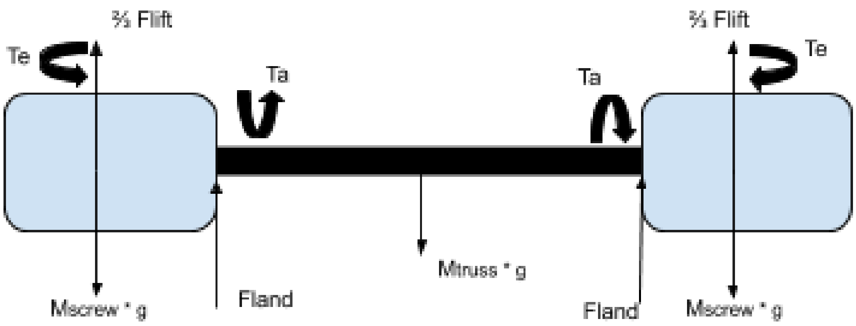

Figure 10.9: Free body diagram landing

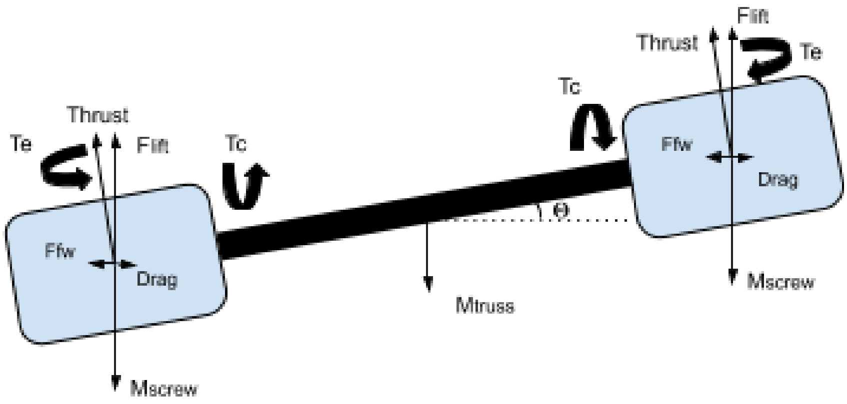

Figure 10.10: Free body diagram for forward flight

To simplify the airframe design process the airframe is simplified into two different 2D truss structures, where the loads of the two different load cases are combined.

One for the zx-plane Figure 10.11, where the moments about the y-axis and the forces in z-direction dominate the design. To be able to fly forward, differential thrust is used (L_2>L_1). This causes a moment around the y-axis, which tilts the vehicle forward.$Mduct1$ and $Mduct2$ are the moments around the y-axis caused by the duct lips. In chapter 9 a detailed explanation is given on how this moment is created. At constant maximum speed the moments created by the ducts are equal and opposite to the resultant moment created by the difference in thrust. For landing these moments are almost zero, since there is almost no horizontal movement in the vehicle. However, for landing the FAR requirements states that *the vehicle shall be capable of landing with 2/3^{rds} of the maximum weight supported by lift* [47]. Due to the deflection in the landing gear this comes down to a deceleration of 3.3g. Therefore, the gravitational forces F_{gcomb1}, F_{gcomb2} and F_{gcomb3} need to be multiplied by 3.3.

The second for the xy plane Figure 10.12, for which the moments about the z-axis and the forces in y-direction determine the design. In this figure T_{e1} and $Te2$ are the engine torques introduced into the airframe. For forward flight the engine torque of the rear (T_{e2}) is larger than the torque in the front (T_{e1}) and to balance the control surfaces create reactions forces F_{c1} and F_{c2}. This is explained more in detail in chapter 9. The moment around the longitudinal axis, Tc in Figure 10.10, is introduced into the structure as shear force F_{m1} and F_{m2}.

The loads introduced in the section above can be devided by two, since the 3D airframe is two 2D truss structures next to each other. Furthermore, the torsional moments around the x-axis are added in the 2D structure as shear forces.

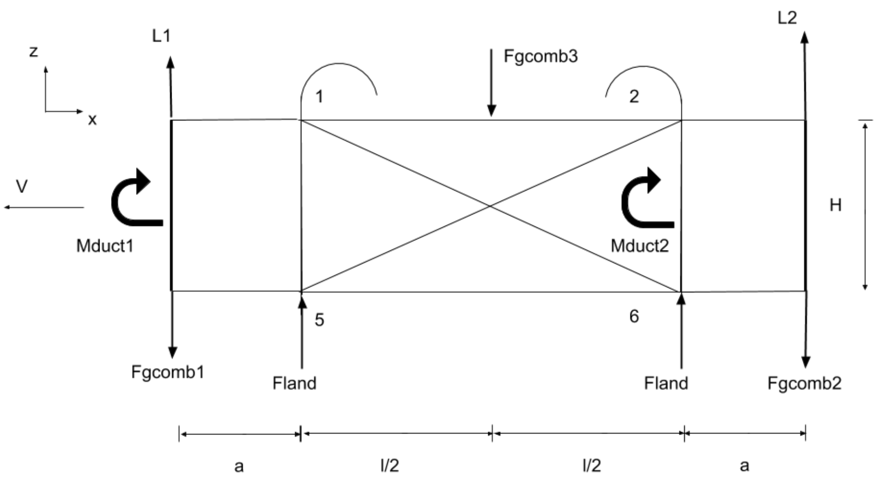

Figure 10.11: 2D Free body diagram in zx-plane

$$F_{gcomb1} = F_{gcomb2} = (m_{rotor} + m_{hub} + m_{engine} + m_{gearbox} + m_{struts})g \tag{10.23}$$

$$F_{gcomb3} = (m_{pilot} + m_{battery} + m_{controllers} + m_{avionics} + m_{extra})g \tag{10.24}$$

$$2F_{land} = (F_{gcomb1} + F_{gcomb2} + F_{gcomb3})3.33 - (F_{gcomb1} + F_{gcomb2} + F_{gcomb3})0.66 \tag{10.25}$$

$$2F_{land} = (F_{gcomb1} + F_{gcomb2} + F_{gcomb3})2.66 \tag{10.26}$$

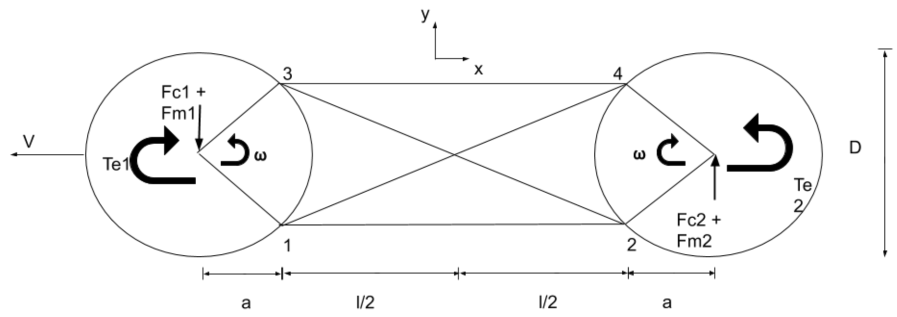

Figure 10.12: 2D Free body diagram in xy-plane

$$T_{e2} - T_{e1} = F_{c1}(a + \frac{L}{2}) + F_{c2}(a + \frac{L}{2}) \tag{10.27}$$

$$F_{m1} = F_{m2} = \frac{T_c}{\frac{H}{2}} \tag{10.28}$$

10.5.2. STRUCTURE SELECTION

For the airframe two different structure types were considered which were a truss structure and a monocoque structure. Monocoque is a structural system where loads are supported through an object's external skin whereas for a truss structure loads are supported through beams. A monocoque structure is more difficult to produce hence increases the producing costs. Also, does it require a higher design effort. Furthermore, is a monocoque structure more difficult to access for the pilot and during maintenance of the vehicle. Therefore, it was chosen to design a truss structure for the airframe.

10.5.3. CALCULATION METHOD

For 2D truss structure the method of joints can be used to determine the tensile and compressive forces in each member separately. For calculation the truss structure is simplified into the two 2D truss structure's Figure 10.11 and Figure 10.12. The method of joints is applied to calculate the tensile and compressive loads in each member for both FBD's. Then, to calculate the total force acting through one member, these different loads are added. To calculate the compressive and tensile stress for each member, Equation 10.29 is used. Where A is the area of the tube and F is the load.

$$\sigma_n = \frac{F}{A} \tag{10.29}$$

Since the members used in the truss are made of thin-walled, slender tube sections, it is a possibility that the members fail in buckling. To prevent this from happening, the Euler buckling load has been calculated for each member, using Equation 10.30. The safety factor of the airframe can be determined by Equation 10.31. The safety factor should be at least 1.5, according to FAR27 requirements.[47]

$$\sigma_{cr} = \frac{\pi^2 EI}{L^2} \tag{10.30}$$

$$SF = \frac{\sigma_{cr}}{\sigma_n} \tag{10.31}$$

10.5.4. MATERIAL SELECTION

For the truss structure the same material (*Aluminium 7068 T6511*) was chosen as for the duct struts. This is mainly due to the same reasons, such as that the airframe is of significant size and thus the material needs to have a high specific strength and specific stiffness while also being cheap and sustainable.

10.6. LANDING GEAR

In this section the design process for the landing gear is elaborated upon. First, the loads acting on the part are explained. Then, a structure selection is made based upon a trade-off. Next, the calculation and verification method applied during the design process are clarified. Lastly, the selection of material is justified.

10.6.1. LOADS

FAR states that *the vehicle shall be capable of landing with 2/3 of the maximum weight supported by lift* [47]. Using classical mechanics, the velocity during the impact can be calculated. A strategy has been chosen which involves setting a deceleration distance and from there, accelerations, forces and stresses are calculated.

The larger the deceleration distance is, the lower the actual deceleration will be. Furthermore, increasing this distance improves the pilot comfort during landing. When the distance and thus the acceleration is known, landing gear and structures can be designed for this impact.

10.6.2. STRUCTURE SELECTION

The landing gear acts like a damper when landing. Flying vehicles can have various landing gear configurations. Most of them can be split up in three different categories. Non-damping, mechanically damping and flexible damping.

(a) Not damped

(b) Flexible materials

(c) Mechanically damped

Figure 10.13: Different landing gear configurations and their application

Designing a stiff landing gear, such as in Figure 10.13a, will cause higher impact forces through-out the structure and is therefore not preferred. Mechanical damped landing gear involve more moving parts than flexible beams. If it is possible to design a beam that can deflect enough while landing, there is no need for a mechanical system.

A possible solution is a landing gear inspired by traditional helicopter landing skids, designed for the deflection at the worst case scenario landing conditions as described by certification legislation [47]. When looking at the airframe structure, attachment points for the landing gear should be able to carry away the loads easily. The four points where the two longitudinal bottom tubes meet the ducts are good points to attach the landing gear. Both the loads from the airframe as from the duct can be carried away directly.

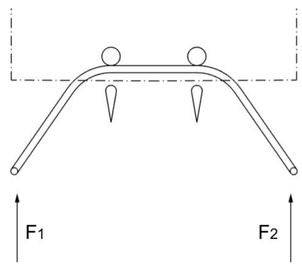

Figure 10.14: Forces and moments on the struts

The dimensions are based upon other dimensions in the vehicle, the radius and the thickness however are calculated based upon stresses and deflection. The horizontal distance between the skids has an effect on the longitudinal tip over angle. In case the vehicle is landing under an angle, it should not tip over. To stay out of the wake, the horizontal distance of the skids is set to the duct diameter. The height of the landing gear is mostly based on the vane cord. Furthermore, the vanes should remain at least five centimeters of the ground when the crossbars are maximum deflected to account for an uneven landing surface.

10.6.3. CALCULATION METHOD

A landing can get harsh and the landing gear must not fail when the landing is not vertical. The landing gear is designed to sustain a landing on one of it's four feet. To select a suitable landing gear tube and material, a Finite Element Method analysis, Abaqus[65], is used to be confident in the expected deflection and stresses. It could have been designed using the deflection formula for a simple cantilever beam, however three assumptions would make this calculation unreliable.

- Using a cantilever beam, attached to the main frame would introduce torsional forces and bending into the frame. This would require a heavier air frame.
- Stress concentrations in case of cantilever beam. Fixing the landing gear introduces stress concentrations near the intersection with the main frame, using this approach the stresses remain lower.

- During bending, the moment arm increases and therefore the moment at the intersection. Performing FEM analysis gave insights in this behaviour.

The color scale in the image below refers to the vertical deflection. The section is designed in such a way that the deflection is trimmed to the required deflection and the stress limits remain under the yield strength.

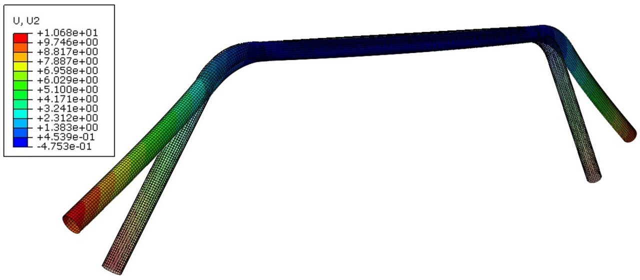

Figure 10.15: Forces and moments on the landing gear

10.6.4. VERIFICATION

Verification has been performed by analysing the deflections and stresses using simple calculations for cantilever beams. A free body diagram of the simplified load case is depicted in Figure 10.16. The P force is set to the force that is required to decelerate a mass m within a distance δ_x. Multiple cases for different combinations of I, E, θ and L are analysed. As expected, the stresses in the FEM analysis are lower. When iterating, this calculating will also be performed to avoid the risk of having constraint errors in the FEM analysis.

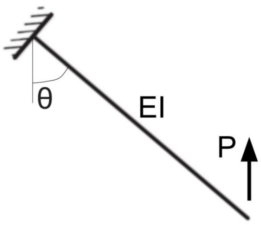

Figure 10.16: Simplified load case for landing gear

10.6.5. MATERIAL SELECTION

The primary function of the landing gear is to absorb the kinetic energy of the vehicle during landing in deflection. The deflection is a function of the force and the displacement and these are a function of the stiffness of the structure. The stress in the structure is determined by the geometry of the beam. Using the finite element analysis described in subsection 10.6.3 it was found that *Aluminium 7068 T6511* had the right properties for the required energy absorption.

10.7. GEARBOX, ENGINE AND ROTOR ATTACHMENT

In this section the design process for the gearbox, engine and rotor attachment is explained. First, the critical loads acting on the part are explained. Next, the calculation method applied during the design process is clarified. Lastly, the resulting shear stresses are elaborated upon.

10.7.1. LOADS

The critical load case for the motor and gearbox attachment is determined by the FAR requirements. The requirements state that: *"The rotor/transmission/motor shall be restrained from injuring an occupant under an ultimate inertial load of 16g forward"* and *"The rotor/transmission/motor shall be restrained from injuring an occupant under an ultimate inertial load of 20g downward"* [47] Since the motor and transmission are fixed to the rest of the structure by bolts, it is assumed that if the bolts fail, the attachment is deemed not unsafe. Thus, the bolts need to be able to carry the inertial force introduced by the motor and gearbox 16g forward (maximum inertial load in x- and y-direction) in shear. Furthermore the bolts need to be able to carry the inertial force introduced by the rotor, motor an gearbox 20g downward (maximum inertial load in the z-direction) in tension. The motor and gearbox are attached with 4 bolts to the duct struts to have a symmetrical load distribution over the two primary duct struts.

10.7.2. CALCULATION METHOD

The load a single bolt needs to be able to carry can be calculated with Equation 10.32, where m is the total mass of the engine, gearbox and rotor. Since the motor and gearbox are attached with 4 bolts, the total force needs to be divided by 4.

$$V_{max} = \frac{mgLF}{4} \tag{10.32}$$

The shear force a single bolt is able to carry is calculated with Equation 10.33, where τ is the shear strength of the material and A is the stress area of the bolt. The tensile force of a single bolt can be calculated using Equation 10.34, where σ is the tensile strength of the material and A is the stress area of the bolt.

$$V_{max_{bolt}} = \tau_{bolt} A_{bolt} \tag{10.33}$$

$$V_{max_{bolt}} = \sigma_{bolt} A_{bolt} \tag{10.34}$$

To prove that the requirements mentioned earlier are met an example calculation is performed. The motor is attached to the duct struts using 4 M6 bolts and the gearbox is attached to the struts using 4 M4 bolts. The motor mass is 7 kg and the gearbox mass is 3.6 kg. With Equation 10.32, the shear force introduced in each M6 bolt is 0.27 kN and the tensile force introduced on each bolt M6 is 0.34 kN, due to the inertial load of the motor. With Equation 10.32, the shear force introduced in each M4 bolt is 0.14 kN and the tensile force introduced on each bolt M4 is 0.18 kN, due to the inertial load of the motor.

For 12.9 grade steel M4 bolts and M6 bolts the shear force is 6.4 kN and 14.7 kN respectively (with Equation 10.33). The tensile force is calculated with of 12.9 grade steel M4 bolts and M6 bolts is 10.7 kN and 24.5 kN respectively (with Equation 10.34).

Since the bolts are able to carry shear and tensile forces that are a order of magnitude higher than the shear and tensile forces introduced by the inertial loads, it can be concluded that the attachment will not fail.

10.8. FURTHER RECOMMENDATIONS

In this section further recommendations in verification is presented for the duct and airframe. Also, in this section further recommendations for certain other parts in the vehicle are elaborated upon such as; secondary duct struts, aerodynamic fairing of the duct struts, duct strut attachment parts, roll cage and fairing of the vehicle.

10.8.1. VERIFICATION OF DUCT AND AIRFRAME

Due to lack the of resources, verification of the duct and airframe has not been performed in this phase. It is recommended for future development to analyse the ability of these structural parts by the means of the finite element method. The calculations in section 10.5 on the airframe can also be verified by using a different calculation method such as the Macaulay's step function method and comparing the results.

10.8.2. OTHER PARTS

In this section recommended design strategies for other parts of the vehicle are presented such as for; secondary duct struts, duct strut attachment parts, roll cage and fairing. Furthermore, are different considerations elaborated upon that should be taken into account during future development of these parts.

SECONDARY DUCT STRUTS

During the design of the the duct struts it was assumed that all loads would be carried by the primary duct struts. Hence, an analysis of the loads on the secondary struts has not been performed. It is recommended to determine the critical loads on the secondary struts and design for this. Furthermore, is it important to bear in mind that the main function of these secondary struts is to contribute to the stiffness of the duct.

DUCT STRUT ATTACHMENT

The bending, compressive and tensile forces acting in the duct struts need to be transferred into the airframe. One should bear in mind during future development that the structure of the vehicle should also be removable for maintenance. Furthermore, the sandwich structure duct is in between the duct struts and the airframe which adds extra complexity. It is recommended to look further into possible attachments. A recommended solution is bolting the duct struts and airframe together and reinforcing the sandwich structure of the duct with reinforcement patches and inserts in the core.

ROLL CAGE

To ensure the safety of the pilot a roll cage needs to be designed. It is recommended to design this roll cage for the extreme case of the vehicle flipping upside down at cruise altitude and accelerating to the ground with both rotors on. In this case the pilot should be protected by the roll cage. It is recommended to design the roll cage to be a part of the airframe main structure. Verification of the roll cage design can be performed analysing the airframe and the roll cage together with the finite element method.

VEHICLE FAIRING

The main function of the fairing is to protect the pilot and the systems inside of the airframe. Furthermore, does a good looking fairing increase the aesthetic performance of the vehicle. It is recommended to design a light nonstructural fairing in an aerodynamic shape from duct to duct.

11 DESIGN RESULTS

The knowledge accumulated in this project was used to synthesize a design. This process was iterative and is presented in this chapter along with the detailed description of the result.

11.1. SENSITIVITY

A sensitivity analysis on the aerodynamic performance was applied to identify, how the radius, the pitch and the hub affected the performance, while the maximum power and mass was kept the same 30 kW per rotor and 200 kg respectively. This information was applied in the iteration process, to converge faster to an optimal rotor design.

The first performance parameter analysed was the maximum level flight speed. The result of this analysis is shown in Figure 11.1. Figure 11.1a displays the effect of changing the radius on the velocity, from which it could be seen that it has approximately a square root relation. Hence increasing the radius has the highest positive influence until a radius of 1 m after, which the effect is less positive. Figure 11.1b displays the effect of changing the ratio of the pitch-to-radius, which shows that having a pitch higher than the radius would be beneficial, where pitch is the height between the leading edge and the trailing edge. The explanation for this is that increasing the pitch would increase the angle of attack and for that reason the thrust increases, resulting in a higher maximum velocity. Finally, Figure 11.1c displays the effect of increasing the ratio of the hub over radius, which shows that until a hub-radius ratio of 0.25 does not have a large effect on the performance, but thereafter it decreases more. Because until 0.25 the velocity is low and therefore does not create much lift, but after the 0.25 the sections do create a significant amount of lift.

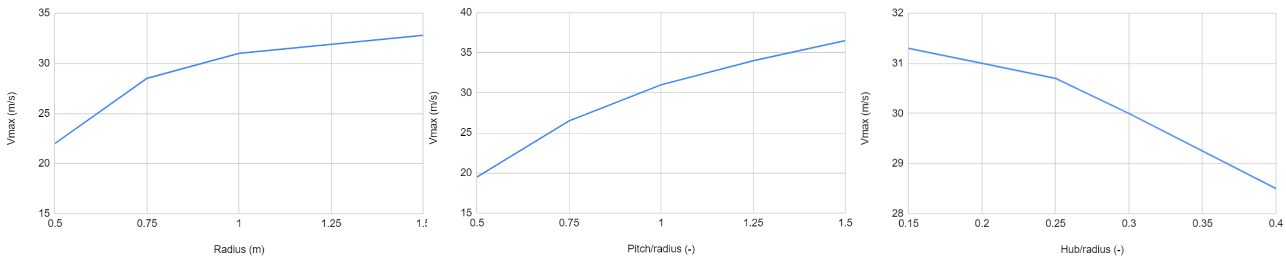

(a) V_{max} for different radii (b) V_{max} for different pitch-radius ratio (c) V_{max} for different hub-radius ratio

Figure 11.1: Sensitivity analysis V_{max}

Further the maximum acceleration, hover ceiling and maximum rate of climb where analysed. However, this resulted in approximately the same result, because the increase in weight was not taken into account. Hence for this analysis all these parameters were only dependent on the ability of the blade to create thrust for the given power and not the combination of the increase in thrust production and in crease in weight. Nevertheless it provides a good insight in how rotor geometry changes the amount of thrust produced.

11.2. EXECUTED ITERATION CYCLES

In this section, the execution of the method set up in chapter 5 is reported. The strategy for the iteration process was to first find correlations on how altering different design parameters result in values for the different performance parameters. This was executed in iterations 1 to 5. After this was done, optima could be found. This was done in iterations 6 to 8 where in iteration 8, the design result was found. The strategies and significant events per iteration are noted below with the values noted in Table 11.1 and the evolution of four significant parameters in Figure 11.2. For each iteration, the total preference of the set of design parameters $\mu(\vec{DP})$ is noted.

- **Iteration 1:** $\mu(\vec{DP}) = 0.034$
  - To investigate how the tools evolved, the result of the iteration performed for the trade-off between different concepts was used as the input for the first iteration.
  - As velocity could not be computed at the time of the first iteration, the importance was set to 0 instead of 2 and the importance of the range to 0 instead of 5.
  - In the first iteration it was seen that the power available is strongly influenced by RPM. As a result, the catalog value of 72 kW was not taken, but 20 kW which is suitable to the RPM in this iteration.
- **Iteration 2:** $\mu(\vec{DP}) = 0.511$
  - In the first iteration, the thrust to weight ratio out of ground effect was less than one. This resulted in a hover altitude of just 1 metre. Also the rotor was very heavy due to the large radius. To overcome this, the strategy for this iteration was to keep the hover thrust the same but decrease the rotor radius.
  - The expected MTOW was far off from the actual MTOW so the design was not optimized for the weight it had. The actual MTOW was only 64% of the expected MTOW. The following iterations were used to converge on mass value to see the potential of the design with these dimensions.
- **Iteration 3:** $\mu(\vec{DP}) = 0.486$
  - For the reason named in iteration 2, the third iteration was used to converge on mass value. The result was that the expected mass was closer to the actual mass but still the actual MTOW was 67 % of the expected MTOW.
- **Iteration 4:** $\mu(\vec{DP}) = 0.310$
  - The goal of this iteration was to converge on mass value. The mass successfully converged as there only was a 2% difference between the actual versus expected MTOW.
  - From this iteration on, the duct strut height was reduced from 20 cm to 10 cm to reduce the overall size of the vehicle and to keep it proportional to the rotor height, this increased the structural mass.
- **Iteration 5:** $\mu(\vec{DP}) = 0.489$
  - As the result of iteration 4 had a thrust to weight value of less than one, the pitch is increased for the same radius. This increased the thrust with more than 10% with increasing the MTOW by less than 5 %.
  - From this iteration onwards auxiliaries were added to the airframe weight.
  - The difference between cruise and hover RPM was now added to the parameter tracking.
  - Maintainability and safety features were now included into the design. This increased weight but also increased the scoring of the design.
- **Iteration 6:** $\mu(\vec{DP}) = 0.605$
  - This iteration was the result of a separate analysis performed on the structure. The remaining mass budget for different values of pitch and rotor radius and with constant values for velocity, power and altitude were calculated being 5 m s^{-1}, 60 kW and 4 metres, respectively. In this analysis, an efficient design was a design that was able to have a large remaining mass budget for the input parameters set. The result of this analysis was the ability of fixing the radius and pitch of the vehicle. In the following iterations, this remaining mass budget was utilized to optimize the scoring of the design.

  - As the landing gear location turned out to be at the place of the vanes, the location had to be altered. This alteration resulted in a higher structural weight for all iterations that followed.

- **Iteration 7:** $\mu(\vec{DP}) = 0.649$
  - The remaining mass budget was large enough to be able to double the battery mass, significantly the scoring of the design. In the next iteration, the optimizing of the battery mass was analyzed more in depth.

- **Iteration 8:** $\mu(\vec{DP}) = 0.721$
  - The optimal battery mass for large range was found as elaborated on in section 12.2. For this configuration, batteries with a higher energy density could be chosen.
  - Cruise velocity was increased for optimal range with a safety margin as the maximum velocity was divided by 1.1 Vne.
  - The power was now calculated for the different flight phases separately.

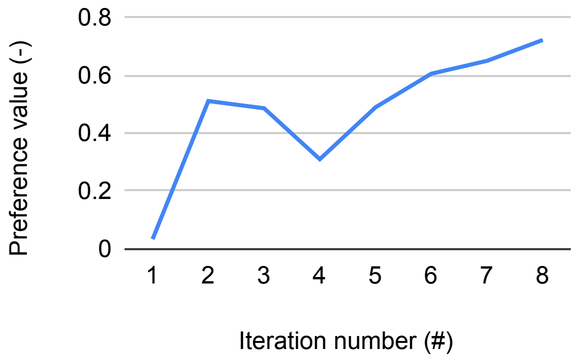

(a) Total preference value throughout the iteration process

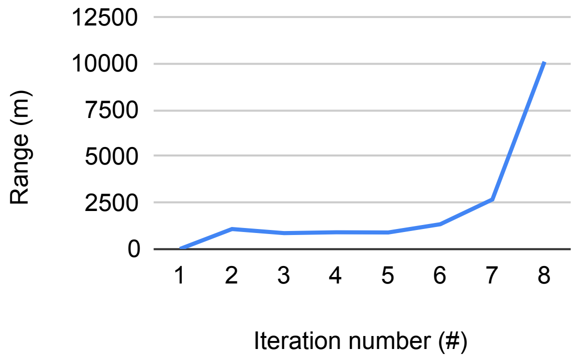

(b) Range throughout the iteration process

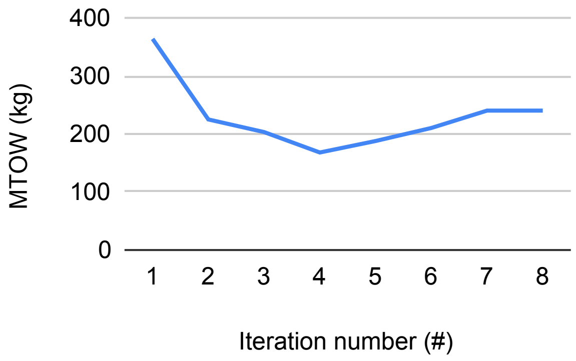

(c) MTOW throughout the iteration process

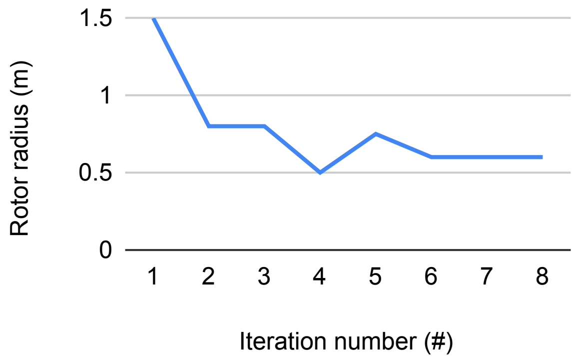

(d) Rotor radius throughout the iteration process

Figure 11.2: Evolution of parameters throughout the iteration process

The most significant parameter tracked throughout the iteration process was the overall preference for the design $\mu(\vec{DP})$ as this represents the performance of the entire design. In Figure 11.2a it can be seen that the strategy in the first 5 iterations was to find correlations and only from iteration 5 to 8 the preference value was optimized. Furthermore in Figure 11.2b it can be seen that the utilization of the lifting capability for extending range, paid off significantly. From the combinations of Figure 11.2a, Figure 11.2c and Figure 11.2d it could be concluded that a minimal rotor-radius is needed for performance, but increasing the rotor radius by a too large extent will dramatically increase the MTOW. This conclusion was emphasized by the analysis executed in iteration 6.

Table 11.1: Parameter values throughout iteration cycles

Parameter	Unit	1	2	3	4	5	6	7	8
Ideal-RPM at hover	min-1	361	903	721	1190	1045	1712	1787	1712
Torque at ideal-rpm at hover	Nm	386	310.6	165.1	131.3	140.4	142.8	154.4	142.8
Rotor-radius	m	1.5	0.8	0.8	0.5	0.75	0.6	0.6	0.6
Tip-speed	m s^{-1}	56.7	75.6	60.4	62.3	82.1	112.3	112.3	112.3
Torque at cruise rpm	Nm	20	32.1	25.2	22.7	178.7	157.2	158.2	157.2
Lift at hover power without ground effect	N	3260	3433	2261	1621	1864	2560.41	2560.41	2560.41
Drag at cruise velocity	N		137.8	73.5	69	51.45	22	22	283
Screw weight (sum of hub, blade and duct weight)	kg	156.9	46	45.9	26	30.4	21.3	21.3	21.3
Engine weight including battery	kg	73.2	86.9	70.9	58.2	62.2	74.5	104.5	104.5
Control system weight	kg	5	4	4	4	4	4	4	4
Airframe weight (sum of struts, truss structure, landing gear and auxiliaries)	kg	69	28.15	22.45	19.8	31.2	50.5	50.5	50.5
Thrust over weight ratio at hover power without ground effect	-	0.91	1.55	1.13	0.98	1.01	1.24	1.11	1.11
Total vehicle height	m	2.86	2.22	2.22	1.11	1.32	1.67	1.67	1.67
Hover altitude at hover power	m	1	4	4	1.5	4	4	4	4
Max range at cruise altitude and velocity	m	0	1075	855	900	890	1335	2670	10100
Controllability: Pitch rate	deg s^{-1}	1.3	12	11	11	6	6	6	6
Sustainability: Noise at SEL	dB	80	62	60	58	58	67	67	65
Cruise velocity	m s^{-1}	0	5	5	5	5	5	5	15.2
Endurance at cruise velocity	sec.	127	215	171	180	178	267	534	785
Sustainability: Maintainability	-	-4	-4	-4	-4	-4	3	3	3
Sustainability: Safety	-	-3	-4	-4	-4	-4	3	3	3
Sustainability: Power consumption (at cruise)	kW	24.5	29.4	24.9	22	25.8	56.7	60	56.7
Aesthetics	-	-4	-3	-3	-2	1	2	2	2
Sustainability: Manufacturability	-	2	2	2	2	2	2	2	2
Payload	kg	60	60	60	60	60	60	60	60
Max take-off weight	kg	364.1	225.1	203.2	168	187.8	210.3	240.3	240.3
Stability: settling time	s	35	35	35	35	35	35	35	35
RPM at cruise power	min^{-}1	-	-	-	-	1330	1806	1806	1806
Total preference $\mu(\vec{DP})$:	-	0.034	0.511	0.486	0.310	0.489	0.605	0.649	0.721

11.3. FINAL DESIGN RESULTS

The final design was dubbed the SolidityONE in reference to its high blade solidity rotors. The vehicle was drawn in CAD and a render of the overall vehicle is provided in Figure 11.3. The weights, dimensions and CG locations (from the center of the airframe truss structure) are presented in Table 11.2.

Figure 11.3: The SolidityONE

Table 11.2: Dimensions of the SolidityONE

Parameter	Value
Operating weight	240 kg
MTOW	260 kg
Length	4.60 m
Width	1.83 m
Height	2.21 m
X_{CG}	-152.0 mm from centre
Y_{CG}	-1.5 mm
Z_{CG}	59.7 mm

Figure 11.4 shows the internals of the airframe. It includes some off-the-shelf components such as lithium batteries, two motor controllers, a radiator for liquid cooling of said motor controllers, yaw pedals, yoke and seat[1][2][3][4][5], but the electrical cabling and cooling fluid pipes are missing.

[1]From: https://grabcad.com/library/pc-fan-140mm-arctic-f14-pwm-1 (21/01/2020)
[2]From: https://grabcad.com/library/saitek-pro-flight-rudder-pedals-1 (21/01/2020)
[3]From: https://grabcad.com/library/saitek-pro-flight-cessna-yoke-system-1 (21/01/2020)
[4]From: https://www.cascadiamotion.com/pm-family-low-volume.html (21/01/2020)
[5]From: https://grabcad.com/library/ek-coolstream-ce-420mm-radiator-3x-140mm-1 (21/01/2020)

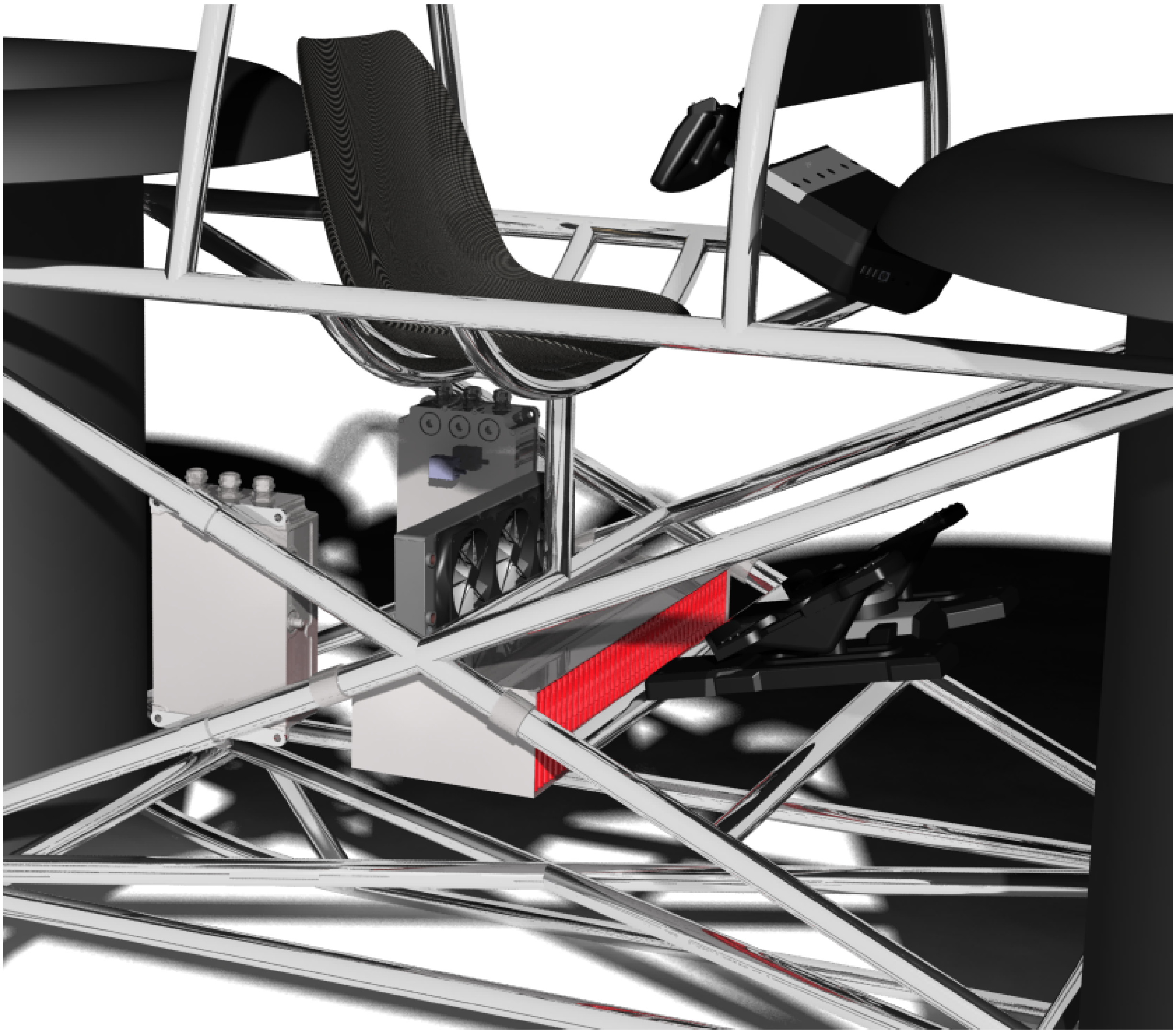

Figure 11.4: Internals of the airframe

Table 11.3: Power design results

Component	Name	Total mass	Quantity	Performance
Motor	Emrax 188	14 kg	2	64 kW, η =95%
Motor controller	Cascadia PM100DZ	15 kg	2	144 kW, η =97%
Gearbox	Anaheim GBPS-0901-NM-004	7 kg	2	500 kW, η =97%
Battery cells + container	Sony VTC6 18650 Li-ion	47.5 kg	900	10.3 kWh, 370 V 66.6 kW
BMS	Elithion Lithiumate	0.7 kg	1	-
Cooling radiator	EK CE 560	2.1 kg	1	$100\ \mathrm{W\,K^{-1}}$
Cooling fans	Noctua IndustrialPPC NF-A14	1.8 kg	6	$1600\ \mathrm{m^3h^{-1}}$
Wiring (controller-motor)	48 $\mathrm{mm^2}$ aluminium	2.3 kg	6	-
Wiring (battery-controller)	62 $\mathrm{mm^2}$ aluminium	0.3 kg	4	-
Additional components	Wiring, avionics, cooling	2.1 kg	-	-

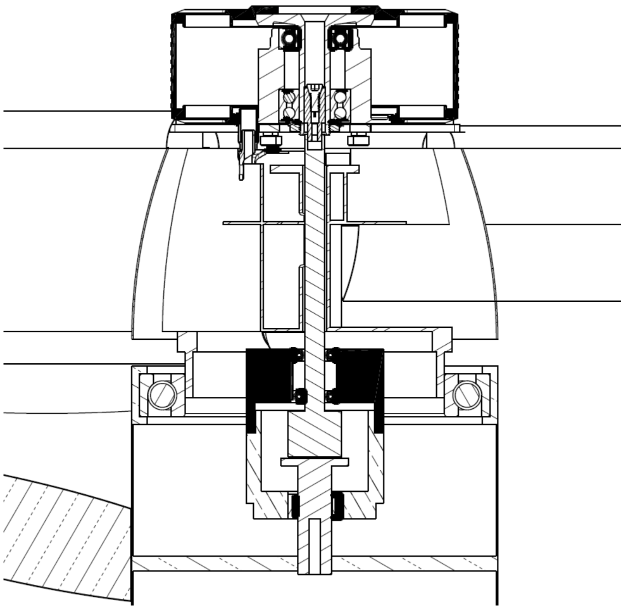

Figure 11.5: Cutout drawing of the drivetrain

The motor is mounted above the top struts and a planetary gearbox is mounted under the struts. A shaft goes through the strut structure to connect the motor to the gearbox and a keyed output shaft then finally connects to the rotor hub. The composition of the powertrain is displayed in Table 11.3.

The properties of the final aerial screw rotor is presented in Table 11.4 and the exposed rotor with the duct removed is shown in Figure 11.6 and Figure 11.5 shows the drive train. The rotor has a cylindrical hub which is supported at the center point of the duct struts, a ball bearing at the top and bottom of the hub ensures smooth operation.

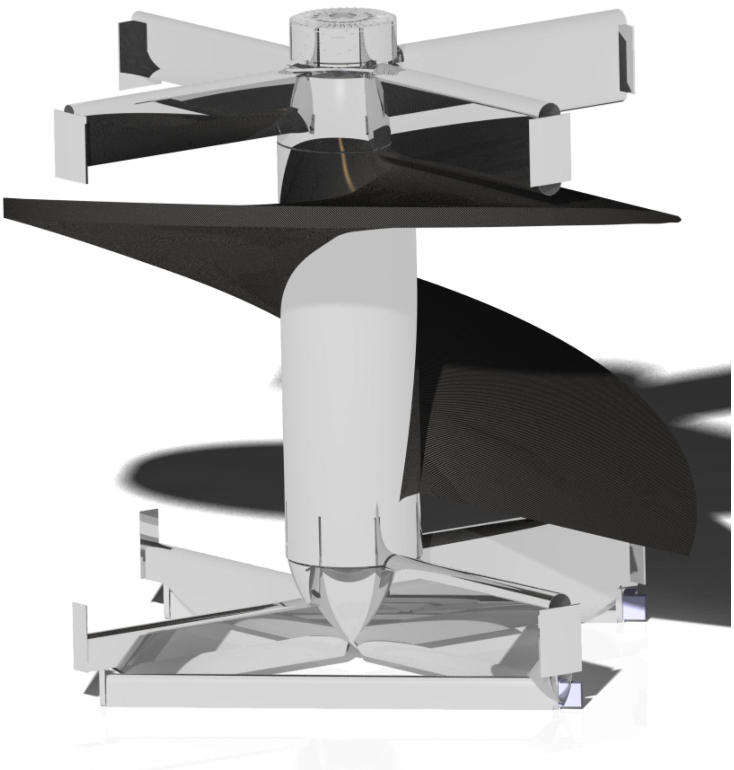

Figure 11.6: Render of an exposed rotor with supporting struts

Table 11.4: Ducted rotor design results

Parameter	**Value**
Number of rotors	2
Rotor radius	0.6 m
Rotor pitch	0.6 m
Hover RPM	1712 min^{-1}
Max RPM	1806 min^{-1}
Figure of merit	0.68
Blade solidity	1.016
Hover tip speed	108 m s^{-1}
Torque at max RPM	158 Nm
Tip clearance	1.2 mm
Inlet lip radius	156 mm
Diffuser expansion ratio	1 -
CG location	1.48% of radius
Downwash velocity	24.7 m s^{-1}

Table 11.5: Design results for each structural part

Part	**Type of structure**	**Dimensions**	**Material**	**SF**
Rotor hub	Thin-walled hollow cylinder	radius: 12 cm thickness: 1 mm	Low alloy steel, AISI 4340	350
Rotor blade	Sandwich structure	skin thickness: 0.3 mm core thickness: varying	Skin: Epoxy/HS carbon fiber Core: Expanded PS foam	12
Duct	Sandwich structure	skin thickness: 0.3 mm core thickness: 10 mm	Skin: Epoxy/HS carbon fiber Core: Aluminium 5056 honey-comb Core lips: Expanded PS foam	10
Duct struts (primary)	Hollow rectangle beams with aerodynamic fairing	12 cm x 5 cm flange thickness: 2 mm web thickness: 2 mm	Aluminium, 7068, T6511	1.5
Duct struts (secondary)	Hollow rectangle beams with aerodynamic fairings	5 cm x 3 cm flange thickness: 3 mm web thickness: 3 mm	Aluminium, 7068, T6511	1.5
Airframe	Truss-structure thin-walled hollow cylinders	radius: 4 cm thickness: 1 mm	Aluminium, 7068, T6511	44
Landing gear	Skids thin-walled hollow cylinders	radius: 4 cm thickness: 2 mm	Aluminium, 7068, T6511	2.6

Details of the structural parts are given in Table 11.5 and mass breakdown of the structural airframe and overall vehicle are given in Table 11.6 and Figure 11.7 respectively. Additionally 3 view drawings are available in Figure E.1.

Table 11.6: Mass for each structural part

Part	Amount	Mass per part [kg]	Total mass [kg]
Rotor hub	2	2.7	5.3
Rotor blade	2	3.5	7
Duct	2	8.5	17
Duct struts (primary)	8	0.56	4.5
Duct struts (secondary)	8	0.2	1.6
Airframe	1	13.4	13.4
Landing gear	1	6.6	6.6

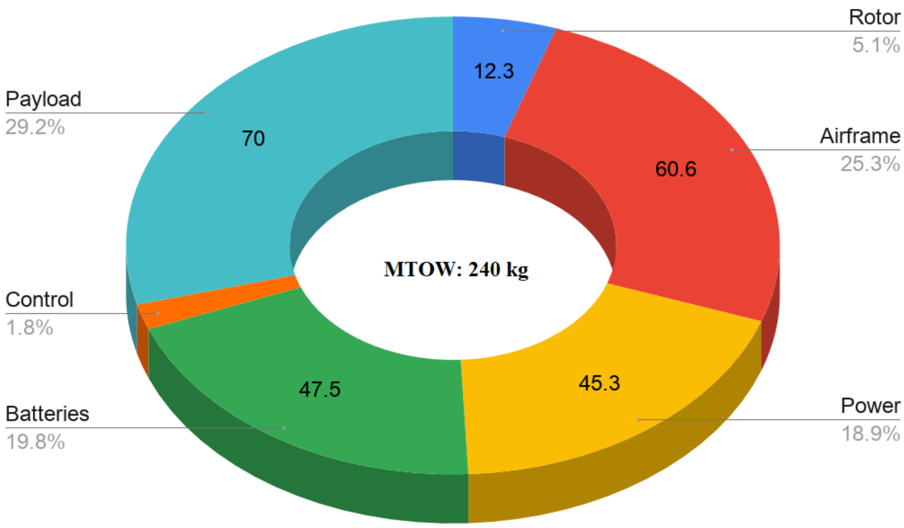

Figure 11.7: SolidityONE mass distribution

11.4. CHARACTERISTICS OF SOLIDITYONE

The aerial screw vehicle has some interestingly different characteristics from conventional rotorcraft. These characteristics and their possible consequences will be briefly discussed.

The SolidityONE flies with a Reynolds number of 27 million at the tip in hover. Although the tip speed is Mach 0.3, which is significant lower than for conventional rotorcraft, which have a tip speed of Mach 0.8, the aerial screw's 3.8m long chord at the tip results in very high Reynolds numbers. Such high Reynolds number results in a lower drag coefficient and turbulent flow [38] with good flow attachment. This results in lower relative profile power.

The aerial screw consists of a single blade per rotor. Having only one blade results in little to no blade vortex interaction (having a duct also greatly reduces tip vortices to begin with) which results in a more quiet rotor. However the thrust produced by the aerial screw is inherently off balance as the center of lift is offset, this may create vibratory noises, control and structural issues.

The aerial screw's shape is quite complex and three-dimensional, this means a variable blade pitching mechanism would be complex and require blade morphing. Instead the SolidityONE's rotor is unable to adjust blade pitch to increase thrust or apply cyclic pitch for control. This means in forward flight one side of the rotor will generate more lift than the other and a rolling moment is created, this is why the vehicle is equipped with two counter rotating rotors so this rolling moment is cancelled out. However this means there is torsional stress on the airframe in X-direction.

The SolidityONE achieves pitching control by applying differential RPM; more power and RPM is applied to one rotor than the other which causes a pitching moment. However this also causes coupling because different torques will be applied to the two rotors, the difference in torque will yaw the vehicle. This must be corrected by applying yaw with the control vanes.

Due to not having an adjustable blade pitch angle, the SolidityONE is limited in velocity by axial velocity due to flight (because the vehicle flies tilted) increasing the inflow angle and reducing the angle of attack which leads to a reduction in thrust. This is in contrast to a conventional helicopter which is often limited by the tangential velocity causing the advancing rotor blade to be limited by mach effects.

The aerial screw has inverse taper, the taper ratio (the ratio of tip chord over root chord length) is 3.8. A conventional rotor may have lift distribution which is a function of the radius squared because the lift produced is a function of $(\Omega R)^2$, to lower losses it is necessary to relieve the tip by lowering the blade pitch angle by twisting the blade or applying taper. However for the aerial screw adjusting the blade pitch angle is problematic and the inverse taper means the lift distribution is cubic with respect to the radius. This causes disproportionally high tip losses and having a duct is more useful.

To generate more lift with a smaller rotor the aerial screw was designed with high camber, 8% of the chord. This however also meant the critical mach number of the rotor tip at the relevant angle of attack is quite low at 0.45, while the tip speed is 0.33 Mach. The camber also causes relatively high aerodynamic moment coefficient $C_{m_0.25}$ of -0.2.

Very low aspect ratio of 0.3, results in very low bending stress along the radial direction but also found quite high torsion from aerodynamic moment which could cause structural issues from aerodynamic flutter. This is made worse by critical mach number being reached if the airfoil pitches down by more than 1.5 degrees.

Though the disc loading is similar to that of the V-22 Osprey, use of a duct which increases lift at the duct lips without moving additional airflow down means induced velocity is quite low and additionally results in the wake not contracting significantly, such that the downwash velocity is even lower compared to the Osprey [66].

The highest tip speed of the aerial screw is 133 m s^{-1} (0.33 Mach) which is almost a third of what is typical. This means the SolidityONE's rotors only produce 67 dB of noise at 150m distance, well under the 82 dB required by regulations.

12

Mission performance

After the iteration process, the optimal rotor geometry and engine were established, after which a more extensive performance analysis was performed. First, an additional analysis was performed in which the final variables were set and performance parameters were established. Secondly, the conformance to the mission profile was described in detail. Lastly, the remaining parameters are described.

12.1. Performance iteration

From the iteration it was concluded that the pitch and the radius were set at 0.6 metres and the maximum available power for a rotor would be 30 kW. From this it could be determined that at maximum power, the vehicle could lift an additional 50 kg and still perform the minimum mission. This excess thrust could be used in multiple ways. Therefore, an analysis on multiple options was performed. First, the decrease in performance by adding weight was analysed. The results of this analysis is shown in Table 12.1. The forward power in Table 12.1 corresponds with a velocity of 5 m s^{-1}, as this is the maximum speed for the heaviest configuration. It was concluded that adding mass results in a close to consistent decrease in performance per added 10 kg.

Table 12.1: The effect of adding weight to the performance

Added weight [kg]	**T/W**	**P_{hov} [kW]**	**V_{max}**	**P_{cruise}[kW]**	**ROC [m s^{-1}]**	**a_V [m s^{-2}]**	**h_{max} [km]**
0	1.27	20.9	23.3	21.9	9.5	2.7	7.3
10	1.21	22.4	21.7	23.4	8.2	2.1	6.0
20	1.16	24	19.5	25	7.0	1.6	4.7
30	1.11	25.5	16.7	26.5	5.1	1.1	3.3
40	1.07	27.1	12.5	28.1	3.6	0.7	2.1
50	1.03	28.8	5.0	29.8	1.3	0.3	0.8

Furthermore, an analysis was performed on how much the flight time and the range would increase if the added weight consisted of batteries. Utilising the additional weight the vehicle can lift with batteries, resulted in a significant increase in endurance and range. The vehicle initially had 21 kg of batteries to get to the maximum power output of 30 kW. This resulted in a flight time of 267 seconds. However, adding 50 kg of batteries resulted in a flight time of 950 seconds at maximum power. The range was calculated in order to find the optimum amount of additional batteries. The range was computed at maximum velocity and at a velocity of 5 m s^{-1}. The results are plotted in Figure 12.1. It was concluded that flying at maximum velocity with an additional battery mass of 30 kg resulted in the highest range.

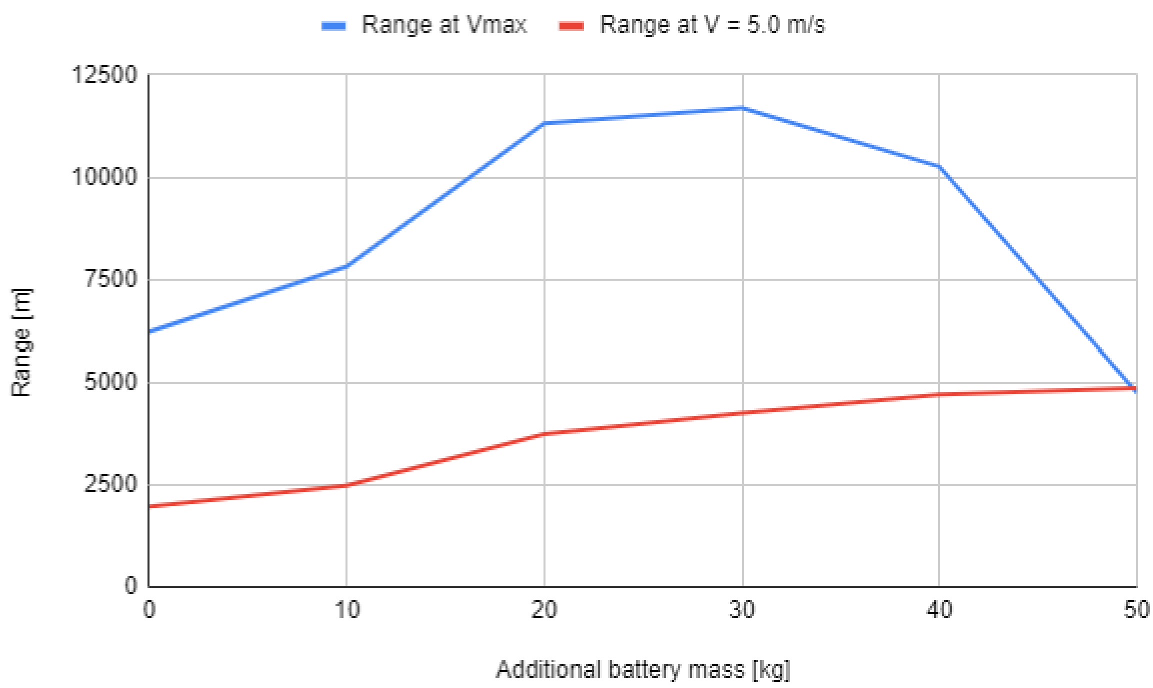

Figure 12.1: Range for additional batteries

12.2. MISSION PERFORMANCE

To improve the range of the vehicle the decision was made to add the 30 kg of additional batteries to the vehicle for the reasons discussed in the previous section. This resulted in a final design with a mass of 240.3 kg. The performance of the final design was analysed for all mission phases and the results are shown in Figure 12.2. It was decided to perform the minimum requirements for all the phases except for the forward flight phase. For the forward flight phase the decision was made to reach maximum range, as the VFS will score the design on range.

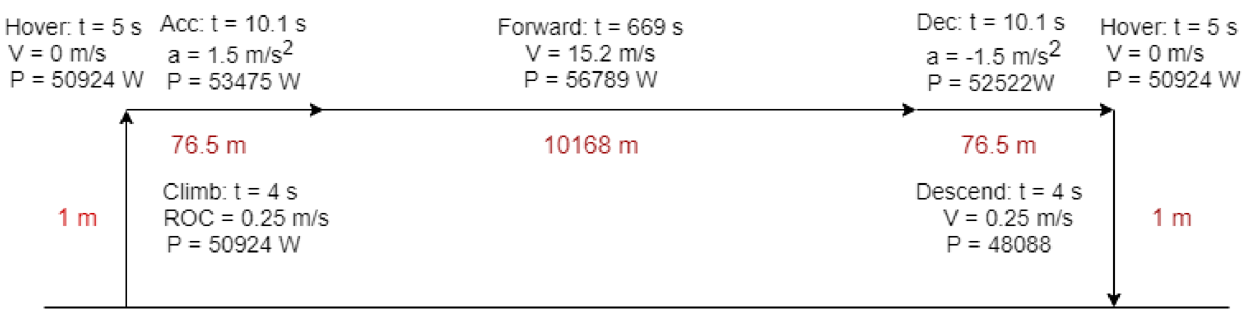

Figure 12.2: Mission profile

The first mission phase is the take-off phase and climbing to a height of at least one metre. This climbing phase was achieved with the use of ground effect. The ground effect provides a 30% increase in thrust on the ground and decreases to 0% when the height is the same as the rotor diameter, which is 1.2 metres. This additional thrust made it possible to set a nominal hover RPM of 1712. Depending on weight, a different RPM can be set by the closed-loop controller. Also, will it automatically accelerate and decelerate to hover at 1 metre. The second mission phase is hovering for 5 seconds. During hover, the thrust and RPM remain the same for both rotors.

The third phase is the forward flight phase. During forward flight, the purpose was to achieve the highest range possible. Figure 12.3 shows the power curve of the vehicle. From drawing a tangent line from the origin to the total power curve, was it determined that the velocity for optimum range was higher than the V$_{max}$, which is indicated by the green dot. This indicates that cruising at V_{NE} is the optimum for

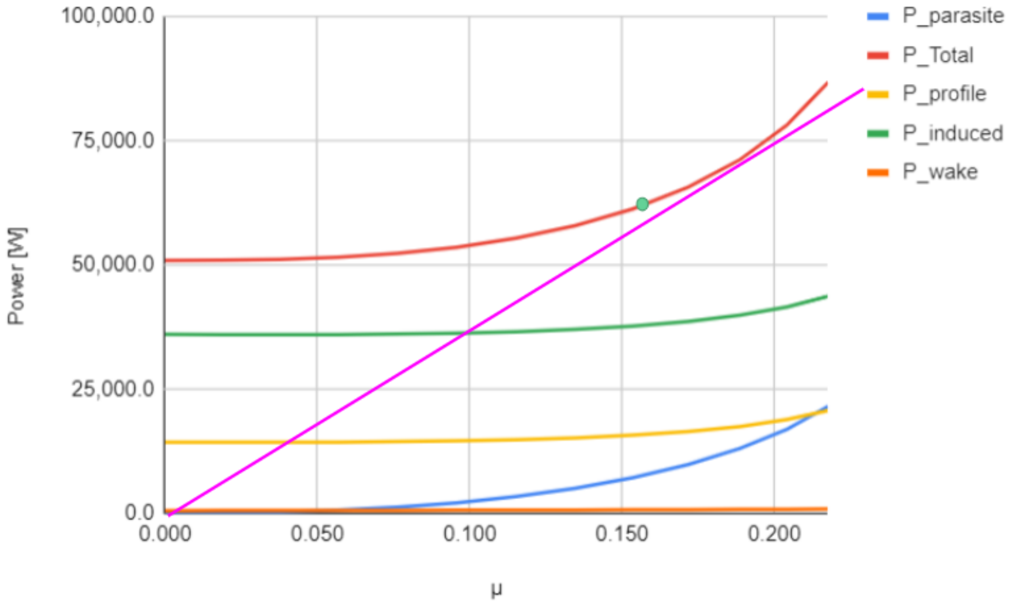

Figure 12.3: Power curve. The green dot indicates the maximum velocity.

maximum range. Hence the vehicle will fly at the never exceed speed, which was a velocity of 15.2 m s^{-1}. The performance of this phase is shown in Figure 12.2. The time the vehicle could fly was calculated by calculating the energy consumed by all the other flight phases. The remaining amount of energy in the batteries was divided by the energy consumption of the forward flight phase,. This resulted in a cruise flight time of 669 s. The maximum range was calculated for this cruise flight time, which resulted in a range of 10.2 km.

The acceleration to achieve this velocity will be the forward acceleration. This was an acceleration of 1.5 m s^{-2}. This result in a acceleration phase of 10.1 s. The power consumption of this phase is shown in Figure 12.2. The RPM of both rotors during this phase are variable. Because the both RPMs first increases to create more thrust, where the RPM of the rear increases more to counter the duct moment and to increase the angle of the vehicle. However, the front RPM will decrease again with increasing velocities to counteract the duct moment.

The deceleration phase is decided to take again 10.1 s. Therefore, the vehicle had to decelerate with 1.5 m s^{-2}. This resulted in a lower power required than for acceleration as the drag contributes to the deceleration. In order to decelerate the Solidity one has the tilt backwards instead of forwards. Hence for decelerating the rear thrust had to be decreased and the front thrust had to increase. This resulted in an average power as indicated in Figure 12.2.

After which it has to hover again for five seconds and at last it has to descend. For descending the RPM is lowered to 1680, which is the RPM at which the vehicle will just lift of with the effect of the ground. This RPM is too low for the hovering flight so will accelerate downward, due to the weight. This increases the descend velocity which in combination with the increasing effect of the ground on the rotor will increase the lift. This results in a deceleration of the descend velocity until zero precisely at the ground. This results in the power consumption as shown in Figure 12.2.

12.3. PERFORMANCE ANALYSIS

The performance of the parameters are shown in Table 12.2. The two horizontal velocities and the range in the table are described in the previous section. The endurance time is the time spent in the air for maximum endurance. The power curve shows that there is not a decrease in total power when the velocity increases as is the case with conventional rotorcraft. So, the vehicle will hover for maximum endurance. This resulted in a endurance time of 785 seconds with a battery capacity of 11.1 kWh.

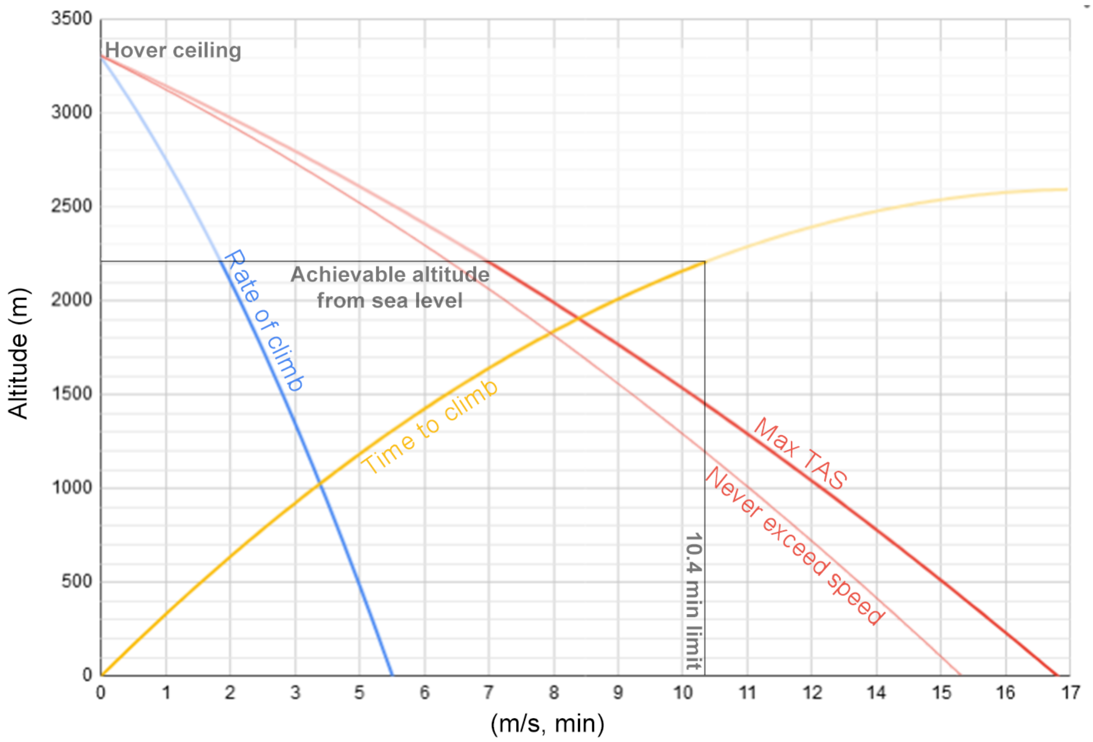

Figure 12.4: Performance over altitude

The rate of climb given in the table was the maximum rate of climb determined at an altitude of 4 m. This rate of climb decreases with height, as shown in Figure 12.4. This is a result of the lower thrust production at the same power, due to the decreased density. The rate of climb reduces to zero at the hover ceiling, which is at an altitude of 3.3 km, because here the rotors can produce exactly enough thrust to hover. However, for the applied battery capacity the vehicle could not achieve this height, because it will take the vehicle 22 minutes to climb to this altitude from sea level and the battery has only the capacity to fly 10.4 minutes at maximum power. Taken into account the battery capacity the maximum climbing distance is 2.2 km, which it achieves in 10.4 minutes with an average ROC of 3.5 m s^{-1}, as shown in Figure 12.4.

Similarly to the maximum rate of climb the maximum forward velocity decreases with an increase in altitude. The result of this is displayed in Figure 12.4, which shows that the rate of climb decreases to the same hover ceiling as for rate of climb, which indicates that the calculations are correct. Furthermore, it shows that at the maximum achievable altitude the vehicle could have a forward velocity of 6.5 m s^{-1}.

The accelerations the vehicle could achieve is 1.1 m s^{-2} for climbing and 1.5 m s^{-2} for level forward flight. The vertical acceleration was determined from the thrust-weight ratio (T/W), which was 1.11. The time needed to accelerate to maximum ROC is 4.6 s. The horizontal acceleration is the maximum acceleration at the never exceed speed. With this constant acceleration the vehicle takes 10.2 s to achieve the never exceed speed. However, the vehicle could accelerate faster at lower velocities. In theory the vehicle could accelerate 4.7 m s^{-2} at a velocity of 0 m s^{-1}.

Lastly, additional payload could be added to the base weight of 70 kg, which consists of a pilot of 60 kg according to the requirement and 10 kg for personal protection, as described in subsection 14.4.4. However, this decreases the performance significantly. The effect of the the additional payload on the range is shown in the payload-range diagram in Figure 12.5. This shows that the vehicle with a payload of 26 kg is only capable of lifting of and hovering, but could not obtain a horizontal velocity.

Table 12.2: Performance parameters

$\mathbf{V}_{max}$	16.7 m s^{-1}
$\mathbf{V}_{NE}$	15.2 m s^{-1}
$\mathbf{t}_{endurance}$	785 s
Range	10.2 km
ROC	5.1 m s^{-1}
$\mathbf{h}_{max}$	3.3 km
$\mathbf{a}_{V}$	1.1 m s^{-2}
$\mathbf{a}_{H}$	1.5 m s^{-2}
Figure of Merit	0.67
Disc Loading	1042 N m^{-2}
Power Loading	22 W N^{-1}

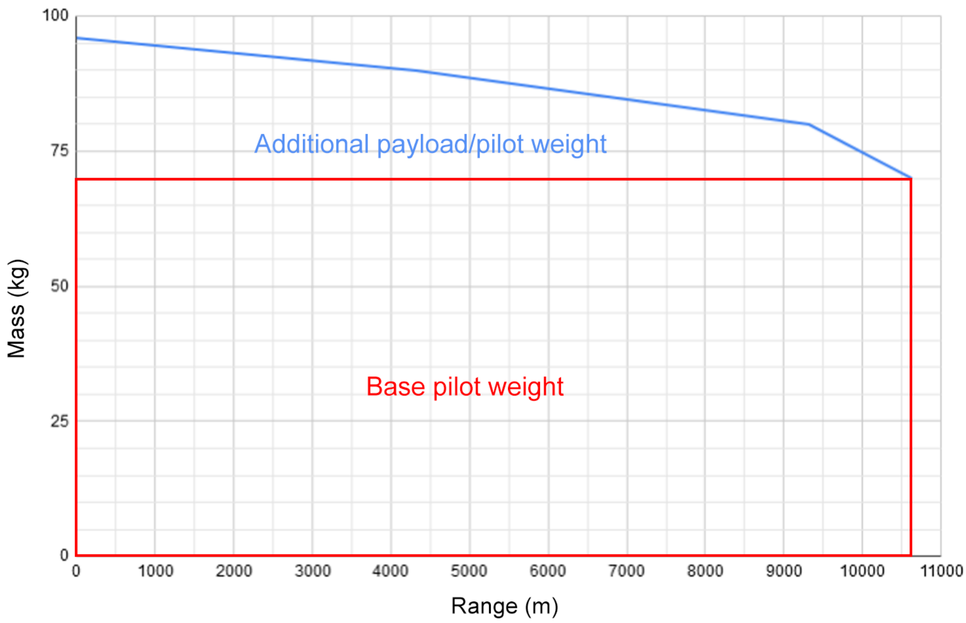

Figure 12.5: Payload-range diagram

13
System Verification and Requirements Compliance Matrix

This chapter describes the system verification against the requirements, providing a full list of requirements in a compliance matrix and details additional steps or modifications still required to meet any as of yet unfulfilled requirements.

13.1. Design verification

The requirements used during the design of the SolidityONE are given in a requirements compliance matrix in Table 13.1, Table 13.2, Table 13.3, Table 13.4 and Table 13.5. The matrix shows the name and text of the requirement, a checkbox showing if the requirement was met and the actual value of the vehicle or subsystem, and finally a reference indicating where in the report the discussion of this parameter can be found.

13.2. Unverified requirements

Several requirements cannot yet be verified for various reasons, they are listed below and the various ways they will be resolved are discussed in chapter 15.

Requires more analysis and testing

These requirements require more analysis but also need to be proved by flight testing, vibration and proving tests. The aerodynamic loads for every subsystem of the vehicle were not calculated and designed for and vibration analysis and testing is required to meet the vibration requirements.

- Sc-F-Ss-Structure-10 The vehicle shall survive aerodynamic loads at 1.3 VNE in a straight flight path
- Sc-C-FAR27.241.GR The vehicle shall have no tendency to oscillate during ground operation (ground resonance)
- Sc-C-FAR27.251a.PPR The power plant shall have no vibration (resonance) that can lead to direct failure
- Sc-C-FAR27.251b.RR The rotor shall have no vibration (resonance) that can lead to direct failure

Requires more detail in control system design

The control system was not designed in detail enough to meet the requirements of section 13.2. More detailed design and selection of components is required.

- Sc-F-Ss-Control-6 The vehicle shall be capable of 1 deg of attitude control
- Sc-F-Ss-Control-11 The vehicle shall be capable of 0.2 m of altitude control
- Sc-F-Ss-Control-3 The vehicle shall be capable of 1 m s^{-1} of velocity determination
- Sc-F-Ss-Control-36 The vehicle shall be capable of 0.5 deg of attitude determination
- Sc-C-FAR27.395a The control system shall not fail under pilot stick forces
- Sc-C-FAR27.395b The control system shall not fail under powered control actuators
- Sc-C-FAR27.671a Each control and control system shall operate with the ease, smoothness and positiveness appropriate to its function

REQUIRES MORE PROGRESS IN FLIGHT MODEL SYSTEM

The flight model showed that the duct lip moment was destabilizing in every direction, this is suspected to be caused by an error in the model as there is evidence from other ducted hover vehicles that show the duct lips are strongly stabilizing. Additionally the controller requires more work and only longitudinal flight was considered.

- Sc-F-SS-Control-lateral The vehicle shall be capable of at least 1 m s^{-1} of lateral translation
- Sc-F-Mis-Hover-2 The vehicle hover shall maintain its horizontal position to 10 m accuracy
- Sc-F-Ss-Control-2 The vehicle hover shall drift by less than 2 m s^{-1}
- Sc-F-Ss-Control-25 The control system shall be capable of turning maneuvers at 1.1 g
- Sc-F-Ss-Control-18 The vehicle shall be statically longitudinally stable
- Sc-F-Ss-Control-19 The pitch stability derivative dCm/dAlpha shall be negative
- Sc-F-Ss-Control-20 The vehicle shall be laterally stable
- Sc-F-Ss-Control-21 The roll stability derivative dCl/dPhi shall be positive
- Sc-C-FAR27.161a1 The trim control shall trim any steady longitudinal forces to zero in level flight at any appropriate speed
- Sc-C-FAR27.161a2 The trim control shall trim any steady lateral forces to zero in level flight at any appropriate speed
- Sc-C-FAR27.161a3 The trim control shall trim any steady collective forces to zero in level flight at any appropriate speed
- Sc-C-FAR27.161b The trim control shall not cause any undesirable discontinuities in control force gradients

REQUIRES CHANGES IN DESIGN

The current production cost estimate for the vehicle stands at just under €270,000, this is largely due to the high manufacturing costs attached to the extensive use of carbon fiber foam sandwich structures in the rotors and ducts and may be solved by changing the design.

- Sc-N-Sust-Cost-1 The vehicle production cost shall not cost more than €200,000

Table 13.1: Requirements Compliance Matrix Part I

Name	Requirement	Complied	Actual value	Reference
Sc-F-Mis-Takeoff	The vehicle shall be able to take-off vertically	TRUE	T/W>1	Table 12.1
Sc-F-Mis-Hover-1	The vehicle shall be capable of hover	TRUE	TRUE	Table 12.1
Sc-F-Mis-Cruise1	The vehicle shall be able to fly at an altitude of at least 1 m	TRUE	3.4 km	Table 12.1
Sc-F-Mis-Cruise2	The vehicle shall fly for at least 1 min	TRUE	785 s	Table 12.2
Sc-F-Mis-Cruise3	The vehicle shall have a range of at least 20 m	TRUE	10.1 km	section 12.2
Sc-F-Mis-Landing	The vehicle shall be able to land vertically	TRUE	TRUE	subsection 10.6.1
Sc-F-VFS-2	The vehicle shall carry at least one occupant of 60 kg	TRUE	70 kg	Appendix A
Sc-F-VFS-4	The vehicle shall rely for its lift and thrust solely on one or more aerial screws	TRUE	TRUE	chapter 11
Sc-C-VFS-5	The aerial screw shall have a single blade	TRUE	TRUE	chapter 11
Sc-C-VFS-6	The aerial screw blade shall have continuous surface	TRUE	TRUE	chapter 11
Sc-F-VFS-7	The aerial screw shall have a blade solidity of at least 1	TRUE	BS = 1.02	section 6.4
Sc-F-VFS-8	The vehicle shall fly without tethered power	TRUE	TRUE	chapter 8
Sc-F-DSE-Vehicle	The vehicle shall use no more than 4 aerial screws	TRUE	Two screws	chapter 11
Sc-F-VFS	The vehicle shall comply with the mission according to the 37th Vertical Flight Society Competition 2019-2020	TRUE	TRUE	Table 12.1
Sc-F-Ss-Structure-2	The structure of the vehicle shall not plastically deform under max operational engine power	TRUE	SF 1.5	chapter 11
Sc-F-Ss-Structure-6	The vehicle shall be structurally capable of a maneuver load factor of 1.1 to 0.9	TRUE	SF 1.5	chapter 11
Sc-F-Ss-Structure-9	The rotor shall not permanently deform at ultimate load of 1.65 time hover load (limit times safety factor)	TRUE	SF 1.5	chapter 11
Sc-F-Ss-Structure-10	The vehicle shall survive aerodynamic loads at 1.3 VNE in a straight flight path	FALSE	UNMET	
Sc-F-Ss-Propulsion-3a	The vehicle shall be capable of 4.3 m s^{-1} horizontal flight velocity	TRUE	VNE=15.2 m s^{-1}	section 12.2
Sc-F-Ss-Propulsion-4	The aerial screw diameter shall not exceed 3 m	TRUE	1.2 m	chapter 11
Sc-F-Ss-Propulsion-4b	The aerial screw height shall not exceed 2 m	TRUE	0.6 m	chapter 11
Sc-F-Ss-Propulsion-5	The rotor downwash shall not exceed 30 m s^{-1}	TRUE	24.7 m s^{-1}	Table 11.4
Sc-F-Ss-Propulsion-6a	The aerial screw shall have a figure of merit of at least 0.5.	TRUE	FM = 0.67	chapter 11
Sc-F-Ss-Propulsion-13	The rotor shall provide enough lift to maneuver the craft at 1.1 g	TRUE	T/W = 1.11 g	Table 12.1
Sc-F-Ss-Propulsion-14	The center of mass of each aerial screw shall not be more than 5% of the maximum radius away from the center of rotation	TRUE	1.5%	Table 11.4

Table 13.2: Requirements Compliance Matrix Part II

Name	Requirement	Complied	Actual value	Reference
Sc-F-Ss-Power-1	The power plant shall be capable of generating 50 kW power	TRUE	64 kW	chapter 11
Sc-F-Ss-Power-2	The power system shall output 200 W of auxiliary electrical power	TRUE	>1000 W	
Sc-F-Ss-Power-11	The power system shall be capable of spinning the rotor at 1300 RPM	TRUE	1810 RPM	chapter 11
Sc-F-Mis-Hover-2	The vehicle hover shall maintain its horizontal position to 10 m accuracy	FALSE	UNMET	
Sc-F-Ss-Power-16	The energy storage shall reserve at least 10 s of maximum power for hovering phases	TRUE	10 s	Table 12.1
Sc-F-Ss-Power-19	The energy storage shall store at least 2 kWh (120s of max power)	TRUE	10.3 kWh	chapter 11
Sc-F-Ss-Power-20	The rotor's induced power required shall not exceed 20 kW hover (<1 m s^{-1})	TRUE	18 kW per rotor	Figure 12.3
Sc-F-Ss-Control-2	The vehicle hover shall drift by less than 2 m s^{-1}	FALSE	UNMET	
Sc-F-SS-Control-lateral	The vehicle shall be capable of at least 1 m s^{-1} of lateral translation	FALSE	UNMET	
Sc-F-Ss-Control-6	The vehicle shall be capable of 1 deg of attitude control	FALSE	UNMET	
Sc-F-Ss-Control-10	The vehicle shall be capable of yawing 10 deg s^{-1}	TRUE	180 deg in 4.1 s	subsection 9.3.4
Sc-F-Ss-Control-11	The vehicle shall be capable of 0.2 m of altitude control	FALSE	UNMET	
Sc-F-Ss-Control-3	The vehicle shall be capable of 1 m s^{-1} of velocity determination	FALSE	UNMET	
Sc-F-Ss-Control-36	The vehicle shall be capable of 0.5 deg of attitude determination	FALSE	UNMET	
Sc-F-Ss-Control-13	The rate of climb at velocity of hover (<1 m s^{-1}) shall be at least 0.2 m s^{-1}	TRUE	5.3 m s^{-1}	Table 12.1
Sc-F-Ss-Control-15	The longitudinal CG location shall fall between within 10% of the total length from the center	TRUE	3.3%	Table 11.2
Sc-F-Ss-Control-16	The lateral CG location shall fall between within 10% of the total width from the center	TRUE	0.08%	Table 11.2
Sc-F-Ss-Control-18	The vehicle shall be statically longitudinally stable	FALSE	UNMET	section 9.4
Sc-F-Ss-Control-19	The pitch stability derivative dCm/dAlpha shall be negative	FALSE	UNMET	section 9.4
Sc-F-Ss-Control-20	The vehicle shall be laterally stable	FALSE	UNMET	section 9.4
Sc-F-Ss-Control-21	The roll stability derivative dCl/dPhi shall be positive	FALSE	UNMET	

Table 13.3: Requirements Compliance Matrix Part III

Name	Requirement	Complied	Actual value	Reference
Sc-F-Ss-Control-25	The control system shall be capable of turning maneuvers at 1.1 g	FALSE	UNMET	
Sc-F-Ss-Control-254	The control system shall be capable of accelerating at 0.2 g	TRUE	1.5 $m\,s^{-2}$	Table 12.2
Sc-N-Sust-Cost-1	The vehicle production cost shall not cost more than 200,000 €	FALSE	240,000 €	subsection 16.1.1
Sc-N-Sust-Emissions-7	The production of the material shall not emiss 45 $CO2_{eq}\,kg^{-1}$	TRUE	5 $CO2_{eq}\,kg^{-1}$	section 16.2
Sc-N-Sust-Materials-1	The vehicle shall not use more than 50 kg of nonrecyclable materials	TRUE	4 kg of Rohacell 51	section 16.2
Sc-N-Sust-Materials-3	The vehicle shall not be made of materials from exploited sources	TRUE	TRUE	chapter 11
Sc-C-FAR27.1a.MTOW	The vehicle shall have a maximum mass of 7000 pounds (3175 kg)	TRUE	240 kg	chapter 11
Sc-C-FAR27.33a	The power system shall provide the complete range of RPM required for the rotor	TRUE	TRUE	chapter 11
Sc-C-FAR27.33b	The transmission shall provide the complete range of RPM required for the rotor	TRUE	TRUE	chapter 11
Sc-C-FAR27.161a1	The trim control shall trim any steady longitudinal forces to zero in level flight at any appropriate speed	TRUE	Partial	section 9.4
Sc-C-FAR27.161a2	The trim control shall trim any steady lateral forces to zero in level flight at any appropriate speed	FALSE	UNMET	
Sc-C-FAR27.161a3	The trim control shall trim any steady collective forces to zero in level flight at any appropriate speed	FALSE	UNMET	
Sc-C-FAR27.161b	The trim control shall not cause any undesirable discontinuities in control force gradients	FALSE	UNMET	
Sc-C-FAR27.173a1	The vehicle's longitudinal control shall accelerate the vehicle for a forward stick deflection	TRUE	TRUE	subsection 9.2.5
Sc-C-FAR27.173a2	The vehicle's longitudinal control shall decelerate the vehicle for a rearward stick deflection	TRUE	TRUE	subsection 9.2.5
Sc-C-FAR27.241.GR	The vehicle shall have no tendency to oscillate during ground operation (ground resonance)	FALSE	UNMET	
Sc-F-Ss-Control-4	The vehicle shall be capable of accelerating at 0.2 $m\,s^{-2}$	TRUE	1.5 $m\,s^{2}$	Table 12.2
Sc-C-FAR27.251a.PPR	The powerplant shall have no vibration (resonance) that can lead to direct failure	FALSE	UNMET	
Sc-C-FAR27.251b.RR	The rotor shall have no vibration (resonance) that can lead to direct failure	FALSE	UNMET	
Sc-C-FAR27.303a.SF	The vehicle shall be designed with a factor of safety of at least 1.5	TRUE	TRUE	chapter 10

Table 13.4: Requirements Compliance Matrix Part IV

Name	Requirement	Complied	Actual value	Reference
Sc-C-FAR27.305a.LD	The vehicle's structure shall not plastically deform at limit loads	TRUE	SF 1.5	chapter 11
Sc-C-FAR27.305b.UF	The vehicle's structure shall not fail at ultimate loads	TRUE	SF 1.5	chapter 11
Sc-C-FAR27.395a	The control system shall not fail under pilot stick forces	FALSE	UNMET	
Sc-C-FAR27.395b	The control system shall not fail under powered control actuators	FALSE	UNMET	
Sc-C-FAR27.397	The foot control actuation forces required from the pilot shall be no higher than 130 pounds	TRUE	"FLY by WIRE "	subsection 9.2.4
Sc-C-FAR27.398a1	The stick control actuation forces required from the pilot shall be no higher than 100 pounds fore	TRUE	"FLY by WIRE "	subsection 9.2.4
Sc-C-FAR27.398a2	The stick control actuation forces required from the pilot shall be no higher than 100 pounds aft	TRUE	"FLY by WIRE "	subsection 9.2.4
Sc-C-FAR27.398a3	The stick control actuation forces required from the pilot shall be no higher than 67 pounds lateral	TRUE	"FLY by WIRE "	subsection 9.2.4
Sc-C-FAR27.473a	The vehicle shall be capable of landing with 2/3 of the maximum weight supported by lift	TRUE	TRUE	subsection 10.6.1
Sc-C-FAR27.547b	The vehicle's main rotor shall be able to withstand the engines limit torque at any rotational speed	TRUE	TRUE	chapter 10
Sc-C-FAR27.561a1	The rotor shall be restrained from injuring an occupant under an ultimate inertial load of 4g upward	TRUE	TRUE	section 10.7
Sc-C-FAR27.561a2	The rotor shall be restrained from injuring an occupant under an ultimate inertial load of 16g forward	TRUE	TRUE	section 10.7
Sc-C-FAR27.561a3	The rotor shall be restrained from injuring an occupant under an ultimate inertial load of 8g sideward	TRUE	TRUE	section 10.7
Sc-C-FAR27.561a4	The rotor shall be restrained from injuring an occupant under an ultimate inertial load of 20g downward	TRUE	TRUE	section 10.7
Sc-C-FAR27.561a5	The rotor shall be restrained from injuring an occupant under an ultimate inertial load of 1.5g rearward	TRUE	TRUE	section 10.7
Sc-C-FAR27.561b1	The transmission shall be restrained from injuring an occupant under an ultimate inertial load of 4g upward	TRUE	TRUE	section 10.7
Sc-C-FAR27.561b2	The transmission shall be restrained from injuring an occupant under an ultimate inertial load of 16g forward	TRUE	TRUE	section 10.7
Sc-C-FAR27.561b3	The transmission shall be restrained from injuring an occupant under an ultimate inertial load of 8g sideward	TRUE	TRUE	section 10.7

Table 13.5: Requirements Compliance Matrix Part V

Name	Requirement	Complied	Actual value	Reference
Sc-C-FAR27.561b4	The transmission shall be restrained from injuring an occupant under an ultimate inertial load of 20g downward	TRUE	TRUE	section 10.7
Sc-C-FAR27.561b5	The transmission shall be restrained from injuring an occupant under an ultimate inertial load of 1.5g rearward	TRUE	TRUE	section 10.7
Sc-C-FAR27.561c1	The engine shall be restrained from injuring an occupant under an ultimate inertial load of 4g upward	TRUE	TRUE	section 10.7
Sc-C-FAR27.561c2	The engine shall be restrained from injuring an occupant under an ultimate inertial load of 16g forward	TRUE	TRUE	section 10.7
Sc-C-FAR27.561c3	The engine shall be restrained from injuring an occupant under an ultimate inertial load of 8g sideward	TRUE	TRUE	section 10.7
Sc-C-FAR27.561c4	The engine shall be restrained from injuring an occupant under an ultimate inertial load of 20g downward	TRUE	TRUE	section 10.7
Sc-C-FAR27.561c5	The engine shall be restrained from injuring an occupant under an ultimate inertial load of 1.5g rearward	TRUE	TRUE	section 10.7
Sc-C-FAR27.661	There shall be enough clearance between the rotor blades and other parts of the structure to prevent the blades from striking any part of the structure during any operating condition	TRUE	TRUE	section 10.1
Sc-C-FAR27.671a	Each control and control system shall operate with the ease, smoothness and positiveness appropriate to its function	FALSE	UNMET	
Sc-C-FAR27.671b	Each element of each flight control system shall be designed or distinctively and permanently marked to minimize the probability of any incorrect assembly that could result in the malfunction of the system	TRUE	TRUE	subsection 14.1.2
Sc-C-FAR27.807	There shall be an emergency exit on each side of the cabin	TRUE	TRUE	chapter 11
Sc-C-FAR27.1521b1i	The maximum rotational speed shall not be greater than the maximum value determined by the rotor design or the maximum value shown during the type tests	TRUE	"Rotor survives motor's max RPM "	section 10.1
Sc-C-FAR27.1521c2	The continuous operation shall be limited by the minimum rotational speed under the rotor speed requirements	TRUE	TRUE	chapter 11
Sc-N-Sust-Noise-2	The vehicle noise shall not exceed 82 dB SEL (up to 787kg MTOW)	TRUE	67 dB	subsection 16.3.1

14
Production, operations and logistics

This chapter covers the life-cycle of the SolidityONE after the design phase from pre-operation processes to end-of-life and includes production, testing, functions and operations. To conclude the section a Reliability, Availability, Maintainability and Safety (RAMS) analysis has been performed.

14.1. Pre-operation

This section describes the manufacturing, assembly and integration plan for the SolidityONE. The three phases are individually covered and concludes the entire pre-operations processes.

14.1.1. Manufacturing

The manufacturing of the SolidityONE parts can be divided into three main categories: Composite part manufacturing, mechanical part manufacturing and off-the-shelf parts.

Composite part manufacturing

For the manufacturing process of the composite parts, pre-impregnated carbon composites are used (prepreg). These kind of composites are delivered with the resin impregnated with the fibers and can therefore be applied immediately on the moulds. Since the SolidityONE is an one of a kind vehicle (low production quantity) and with the complex shape of the rotor, hand layup has been chosen to reduce the cost of designing expensive machines. The foam cores required for a sandwich configuration are CNC milled to obtain high accuracy and reduce production time. The curing processes for the composite parts are done with an autoclave oven in order to improve the material properties and thus reduce weight. After the composite parts are cured, the parts will be post-processed. This includes: demoulding, removing breathers, removing deformities (e.g. edges and flanges) and drilling required holes. For the full manufacturing plan (MAI), see Appendix B.

The main composite parts to be manufactured are the ducts (CRFP sandwich structure), aerial screws(CRFP sandwich structure) and battery casing (aramid). Complex shapes like the aerial screw will be segmented and either glued (composites/foam) or welded together. The parts will be manufactured at the TU Delft Structures and Materials Lab or the TU Delft Dreamhall if permission is granted where the laminating, curing processes (autoclave) and post-processing can be performed. The part drawings are made with the use of CATIA V6.

Mechanical part manufacturing

For the mechanical part manufacturing of the complex parts, the raw materials will be CNC milled (e.g. complex brackets, inserts, etc.). The tubing and I-beams for the aircraft structure will be ordered from a manufacturer in the calculated dimensions. The mechanical parts will be either attached by welding(e.g., airframe) or bolted together (e.g., airframe-duct-duct strut assembly). The mechanical part manufacturing consists primarily out of the aircraft structure, brackets and inserts. The CNC milling and welding are performed at the TU Delft Structures and Materials Lab or the TU Delft Dreamhall if permission is granted. The part drawings are made with the use of CATIA V6 For the full manufacturing plan, see Appendix B.

OFF-THE-SHELF PARTS

The remaining parts of the SolidityONE are off-the-shelf and purchased from expert companies. These parts are the motors (Emrax), battery cells, bearings (SKF), transmission (Anaheim Automation), yoke (Saitek), pedals (Saitek), flight instruments, seat (Aircraft Spruce & speciality co.) and camera (GoPro). Buying off-the-shelf part reduces design complexity, but could increase the costs.

14.1.2. ASSEMBLY

The SolidityONE will be assembled digitally in (CATIA V6) to make sure everything fits together. The interface between the digital drawings and the real life production and assembly have to be checked frequently to achieve a smooth assembly and integration process.

The vehicle assembly should be carried out in a single location. Preferably a location with close access to test facilities and third parties that produce separate parts. The TU Delft Materials and Structures Lab or TU Delft Dreamhall suffice if permission is granted. This saves transportation cost and time. Before assembly can start, all parts need to be collected, measured, labelled and ordered per subsystem.
The physical assembly can be divided into two main categories, namely: the subsystem assembly and system assembly. The assembly starts with the assembly of the subsystems, these include the propulsion system (rotor, duct, hub, duct struts, engine, transmission, etc.), the electrical system (battery assembly, wiring, motor controllers, avionics etc.), airframe structure (landing gear, trusts structure, roll cage, seat, dashboard etc.) and control structure (flaps, servos, yoke, pedals, etc.). Assembly processes include welding and bolting for mechanical components, welding and gluing for electrical components and gluing and bolting for composite components. The finished parts and subsystems will be checked on the correctness of the dimensions, tolerances and overall imperfections. Finally, after the subsystems are successfully tested, they are assembled into the complete system. For the full assembly plan, see Appendix B.

14.1.3. INTEGRATION

The integration process is performed through out the manufacturing and assembly phases. During the manufacturing of the parts carefully checking CATIA part drawing dimensions and tolerances with the produced part is required before subsystem assemblies can be performed. This process repeats itself for the subsystem assemblies and total system assembly. Furthermore tests will be performed at multiple stages. Non-destructive testing like visual inspection, x-ray testing on welds and tab test for non-critical composite components will be performed as well as destructive testing to validate the calculated strength of structural critical components. The testing facilities required for these type of tests are all present at the Materials and Structures Lab of the TU Delft. However, other companies do provide the similar services. For the finished electrical subsystem the PCB (printed circuit board) will be unit tested and the entire subsystem will be integration tested. The entire finished system should be tested in a full scale flight test at an airport (preferable Rotterdam/The Hague Airport, due to close proximity), for safety purposes. The SolidityONE can be transported by truck from the assembly location to the airport. The SolidityONE's envelope is 4.604 m (length) x 1.830 m (width) x 2.210 m (height) acquired from CATIA and should be able to fit in the Eurotrucks 82 (EURO) 13.6 m (length) x 2.45 m (width) x 2.45 m (height) from FESS transport company [1]. For the full integration plan, see Appendix B.

14.1.4. MAI-PLAN

The above mentioned manufacturing, assembly and integration (MAI) plans are combined with the operations and logistic concept description of subsection 14.2.5. The top level diagram in Figure 14.1, shows the overlap between the MAI-plan and the operations and logistics concept description. A more detailed MAI-plan can be found in appendix Appendix B.

[1] http://fess.su/news/dimensions-and-sizes-of-trucks (16-01-2020)

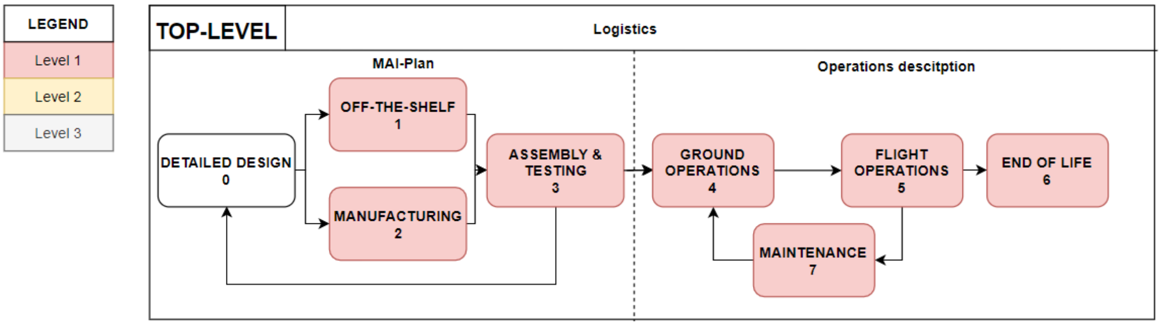

Figure 14.1: Top level MAI-plan and operations & logistics concept description

14.2. OPERATIONS

The operations of the SolidityONE follows from the pre-operational procedures, only when the final system test has been successfully performed the SolidityONE will be deemed ready for operation. This section describes the ground operations and in flight operations necessary to fully operate the vehicle through the required mission profile and are visualised in the operations and logistic concept description in Appendix B. The functions are visualised and described in the FFD (functional flow diagram) and FBS (functional breakdown structure).

14.2.1. GROUND OPERATIONS

The ground operations consists of getting the SolidityONE to the flight location, performing flight preparations, monitoring flight performance and post-flight operations. The logistics of getting the SolidityONE to the flight location and back will be done similarly as described in the integration plan by truck. The flight preparations include all the ground activities directly preceding flight phase of the vehicle. This includes the making of a flight plan, doing a pre-flight inspection, charging the batteries and checking the flight conditions. Then during flight the ground crew and pilot monitor the flight path, the flight conditions and all critical systems of the vehicle. After landing, a post-flight inspection is conducted and the vehicle is removed from the landing site.

14.2.2. FLIGHT OPERATIONS

The flight operations consists of getting the SolidityONE of the ground, hover, cruise, monitoring, perform the mission and land. During the total flight phase the pilot and the ground support crew monitor the flight path, the flight conditions and all critical systems of the aircraft. The mission that needs to be performed is stated in chapter 3.

14.2.3. FUNCTIONAL FLOW DIAGRAM

The Functional Flow Diagram (FFD) relates the flow between different system functions by showing the inputs and outputs. Each box shows a function of the systems and the arrows determine the flow direction. Next, lower-level divisions can be made. The complete FFD is found in Appendix C. The top-level FFD, which is shown in Figure 14.2 arises from the different flight phases during the mission of the SolidityONE.

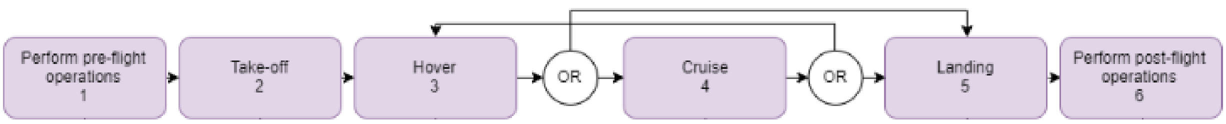

Figure 14.2: The top-level Functional Flow Diagram.

There is one main background functions that needs to be performed continuously during flight, which is the *vehicle stability & control* function. This function is an input for all the subsystem functions from take-off to landing. This is depicted with an arrow pointing into these subsystems marked by an *A* and an arrow pointing out a separate stability and control loop also marked by an *A*. Furthermore, each level within the FFD is depicted with a different colour. Top-level is depicted in purple, second level in blue, and third level in grey.

14.2.4. FUNCTIONAL BREAKDOWN STRUCTURE

The FBS is a breakdown of functions and its sub-functions from the highest level to the lowest level. It is an *AND*-tree which means that each element in the tree is equal to all the elements below it. The top-level FBS is shown in Figure 14.3. The grouping is kept similar to that of the FFD, which are the flight phases in chronological order during the mission plus the background function of *vehicle stability & control*. The complete FBS can be found in Appendix D.

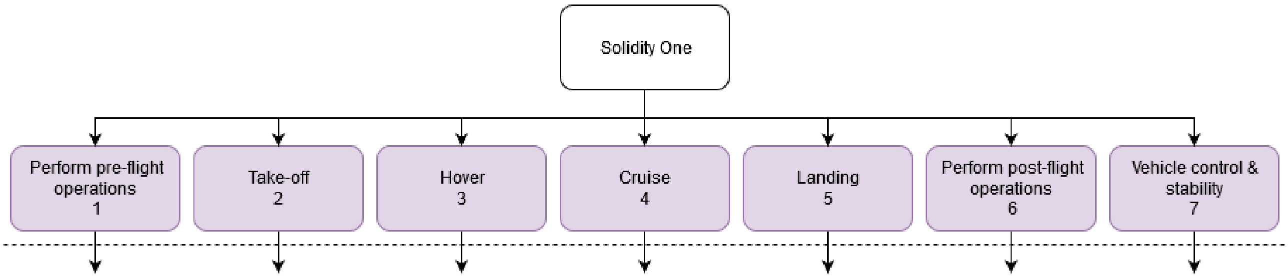

Figure 14.3: The top-level Functional Breakdown Structure.

14.2.5. OPERATIONS AND LOGISTIC CONCEPT DESCRIPTION

The operations and logistic concept description describes the logistics from the detailed design phase up to and including the end of life phase of the system. This is done to get a better understanding of how to allocate the resources and track sustainability of the system. In Figure 14.1, the top level flow diagram is shown including the overlap with the MAI-plan. The figure shows the logical flow of the activities to be performed after the detailed design phase, with first the manufacturing, assembly and testing/integration phase, also known as the MAI phase. The MAI phase is explained in detail in section 14.1. Then followed by the operational phase including the ground and flight operations, with the maintenance of the vehicle running in parallel. The operational phase is explained previously in section 14.2. Finally, the post-operational phase and the end-of-life phase of the system are explained in section 14.3. The full operations and logistic concept description can be found in Appendix B.

14.3. END-OF-LIFE

The end-of-life operations are divided into three different categories. If the parts lifespan is greater than the lifespan of the system, then the parts can be reused. A good example would be the electric motor, which can be reused for a new rotor craft or for another system entirely. If the parts cannot be reused, they can be checked for recycle-ability. If the parts cannot be recycled, they can be dismantled and the remaining valuable materials contained in the part can be recovered. All the parts that are left need to be checked for toxicity and then they can be thrown away. The full end of life process can be viewed in Appendix B.

14.4. RAMS

This section describes the process performed for the reliability, availability, maintainability and safety (RAMS) characteristics of the SolidityONE in order to determine the operational performance. The four topics are described in this section independently. The focus of the RAMS characteristics was put on the unique subsystem components of the SolidityONE, since the conventional components are already proven concepts. Furthermore the design is a prototype rotorcraft, so the RAMS aspects are of less importance than for commercially used rotorcraft.

14.4.1. Reliability

Reliability can be regarded as the probability of successful operation or performance of systems and their related equipment, with minimum risk of loss or disaster or of system failure. Designing for reliability requires an evaluation of the effects of failure of the inherent systems and equipment [67]. Since electrical propulsion is relatively new in the aerospace industry, it is considered a potential reliability risk. Parts of the electrical propulsion system that are considered are the motor, the battery, motor controllers and the sensors.

Looking at available research, the failure rate λ of a 3-phase electrical system is one failure per $6.5 \cdot 10^6$ hours [68]. Compared to a turbine ($3.75 \cdot 10^5$ hours)[69] and a piston engine ($3.2 \cdot 10^3$ hours)[69] this is a few orders of magnitude higher. One of the main reasons for this is, from a mechanical perspective, the electrical motors have less moving parts and therefore have less component wear. However, since there are no redundant motors, a failure of one engine would mean catastrophic failure of the entire system.

The reliability of the electrical system is also influenced by the battery. The battery is made out of 900 lithium ion cells build in series and parallel. The battery management systems are designed in such a way that, if one cell gives a too high or too low voltage, or a too high cell temperature, it needs to be powered down. Since the cells are connected with 99 other cells in series this whole segment needs to be powered down. This would mean that one of the 9 parallel battery packs would shut down. There are however 8 more parallel battery packs and the vehicle is still able too fly, albeit with a shorter range.

Another electrical component that influences the reliability of the system is the motor controller. Even though the motor controller was checked for compatibility of voltage and current of the picked motor, the controller is not from the same manufacturer as the motor. This means that the motor controller to motor interaction needs to be calibrated. This might cause unforeseen issues down the line. A motor controller failure would mean a motor stops delivering torque and this would mean a complete system failure.

The last part of the electrical system to be discussed are the sensors. After the unit tests and the electrical system integration tests, the negative effects of Electromagnetic Interference (EMI) and other noise sources are negated. Other inaccuracies are covered by using a redundant number of sensors to measure the same input and averaging the values. A redundancy in senors would also mean that there is a fail safe sensor system.

14.4.2. Availability

The *Handbook of Reliability, Availability, Maintainability and Safety in Engineering design* describes the availability as follows: "Availability is that aspect of system reliability that takes equipment maintainability into account. Designing for availability requires an evaluation of the consequences of unsuccessful operation or performance of the integrated systems and the critical requirements necessary to restore operation or performance to design expectations" [67]. This is explained as the percentage of the SolidityONE's operational lifetime, in which the total system is available for operational use. The downtime of the operational use is due to scheduled activities (e.g. charging, regular maintenance, checking fluids, changing batteries, etc.) as well as unscheduled activities (e.g. crashes, broken parts, environmental uncertainties etc.), but these are more difficult to quantify and thus not considered.

Scheduled activities

The largest downtime comes from charging the batteries and mandatory maintenance. The charging of the batteries takes approximately 94 minutes to fully charge, assuming using the provided 6.6 kW charger[2]. The maximum flight time on a fully charged battery while cruising is approximately 11 minutes as described in chapter 12.

The scheduled maintenance tasks are described below in subsection 14.4.3. The pre-flight checks take approximately 15 minutes before each flight. [3] The 100 hours inspection will be done ones a year or after every 100 hour of flight time. These inspection will take approximately 20 hours for small rotorcraft, unless flaws in the system are found. [4] The SolidityONE shall be operated twice every day, resulting in an overall flight time of 133 hours per year. This means the 100 hour inspection will be performed twice a year, resulting in a downtime of 40 hours per year. The pre-flight checks are done twice a day, resulting in a downtime of 30 minutes a day. The battery needs to be charged before every flight, resulting in a downtime of 188 minutes a day. The overall downtime of the vehicle due to scheduled activities will be approximately 1366 hours per year of the 8760 total hours per year. The availability of the SolidityONE is than equal to approximately 85% per year.

14.4.3. Maintainability

There are two types of maintenance, which are scheduled and unscheduled maintenance. Scheduled maintenance is an important aspect of owning a vehicle and is critical to maintaining the SolidityONE's value and ensuring it works in good order. Maintenance schedules are typically broken down by flight hours for aerial vehicles. Unscheduled maintenance is unforeseen and occurs anytime a component of the vehicle has malfunctioned or is suspected to be malfunctioning. This can occur after the vehicle owner finds a problem during the pre-flight checks or even during flight. An unscheduled maintenance can also occur as the result of problems found during scheduled inspections.

Scheduled maintenance

Three different types of scheduled maintenance have to be performed for the SolidityONE on different time intervals. These are: pre-flight checks, 100-hour inspections and annual inspections. What these consist of is explained below [70].

- **Pre-flight checks**: The pilot shall perform a daily pre-flight checks prior to the first flight of each day. During this check, different components of the vehicle shall be visually checked by the pilot. The pilot shall first inspect the landing gear, the ducts, the vanes, the struts and the airframe and the rotors for general damage. Then, the pilot shall also perform specific checks on certain parts. Proper attachment of the landing gear to the airframe shall be checked. Furthermore, shall the pilot check the rotor for tip clearance and perform a tap test on the carbon fiber to check for delamination. Also, shall the pilot check the leading edge tape for excessive wear. The vanes shall also be checked for actuation. Lastly, the pilot shall perform a check for critical systems inside the cockpit.
- **100-hour inspections**: An inspection is required after every 100 hours of flight time by the SolidityONE. During the 100-hour inspection the entire vehicle will be checked for cracks and damages with nondestructive testing methods and may be extended by at most 10 hours. Furthermore, will the entire vehicle be checked for proper functioning of each component. Also, preventive maintenance shall be performed which consists of lubrication, refinishing of decorative coatings, fairings, vanes, landing gear and cockpit interior. Furthermore, leading edge tapes, safety belts, navigation lights and batteries shall be replaced and serviced.

[2] From: https://eveurope.eu/product/lithium-oem-lader-66-kwatt-440-vdc-with-can-bus/ Retrieved 21 January 2020
[3] From: https://www.pprune.org/private-flying/63209-how-long-do-you-take-do-pre-flight-check.html Retrieved 21 January 2020
[4] From: https://www.pilotsofamerica.com/community/threads/c150-annual-inspection.60632/ Retrieved 21 January 2020

- **Annual inspections**: An annual inspection is similar to the 100-hour inspection and is required once every 12 calendar months. However, this is inspection must be performed by a licensed Airframe and Powerplant mechanic with Inspection Authorization. This inspection shall not be overflown. The annual inspection resets the interval of a 100-hour inspection.

14.4.4. Safety

"Safety can be classified into three categories, one relating to personal protection another relating to equipment protection, and yet another relating to environmental protection" as stated in reference [67]. Designing a vehicle for safety is integral with designing for maintenance and reliability. As explained in subsection 14.4.1, failure of a few parts in the electrical system would mean a complete system failure. This is because there is no sufficient redundancy. However these same systems are designed for high reliability and therefore safe operation can be guaranteed with regular maintenance of the critical parts.

For personal protection several safety precautions have been taken. Firstly, placing the pilot inside the roll-over protection envelope. This means putting the pilot inside the truss structure and roll cage, to prevent the pilot from being crushed in case of the vehicle rolling over or crashing into something. Secondly, shielding the pilot from a potential battery fire. The battery catching fire in itself is already highly unlikely due to the battery management system monitoring the cell temperatures and voltages for critical values. But in case of a fire, the aramid-aluminium fireproof casing of battery contains the fire sufficiently long for the pilot to get out of the vehicle. Thirdly, from calculations it became clear that, due to the close distance to the rotors the pilot will experience a high noise. As the rotational noise of the rotor is approximately the 104dBA and the vortex noise is approximately the 100 dB (from section 16.3). This has to be reduced, because noise levels above the 85 dB could result in hearing damage. Therefore, the pilot should wear a helmet with noise cancelling properties as this could reduce the noise by 26 dB [71]. As personal protection, the pilot wears a parachute, helmet, fireproof suit and underwear, which have a mass of 3 kg, 1.5 kg and 2 kg respectively. This results in an additional weight of 6.5 kg. Therefore, it is assumed to add a weight of 10 kg to the pilot of 60 kg to add a contingency.

Equipment protection of several safety critical systems is incorporated in the design. The same as for the pilot, most of the critical electrical components are placed within the roll-over protection envelope. These systems are the battery, motor controllers and all sensor nodes. Other critical systems such as the rotor and motors are protected from horizontal impact by the duct. However since the duct is not designed to withstand impacts this should be prevented all together. To make sure the pilot does not crash into an object out of line of sight, extra cameras and screens are provided for the blind spots.

Environmental protection relates to the prevention of failure of the vehicle's system that result in environmental problems associated with chemical substances and heat [67]. The only flammable and chemical substance present in the vehicle is the lithium-ion battery pack. As explained for the personal protection the battery pack of the vehicle is contained in a fireproof casing. This casing shields both the pilot, other vehicle systems and the environment from being damaged by a battery fire for a short duration. If possible the battery should be quickly extracted from the vehicle and doused with water [5]. As explained earlier, the battery management system should prevent the battery catching fire in the first place.

[5] From: https://batteryuniversity.com/learn/article/safety_concerns_with_li_ion Retrieved 21 January 2020

15
Future development

This chapter is twofold. Firstly, the trajectory for winning the VFS competition is described. Secondly, it is described how the current design is further developed to a stage where the prototype and concept idea can be sold to a helicopter manufacturer. The technical aspects of these processes are described in the previous chapter. However, the more practical aspects such as planning and risks are elaborated on here. This planning is concluded in a Gantt Chart. Finally, the risks for the future are analysed and migrated when necessary.

15.1. Vertical Flight Society: student design competition

The goal for the VFS competition is to demonstrate the physics and feasibility of an aerial screw rotor geometry. SolidityONE has such a level of detail and weight margin of 20 kilos, that this research provides a design that has the potential to fly. Additional steps will be taken to higher this level of detail and therefore decrease the uncertainties.

The VFS requires potential participants to send their letter of Letter of Intent no later than February 3, 2020. The final proposal is due 31st May, 2020. All research and engineering activities should be conducted and reported before then. The activities that raise the level of detail and overall level of the report can be summarized in four action points.

From the compliance matrix, requirements that are not met yet are listed in four lists. By performing one of those action points, the related list of unmet requirements are considered. As a result of performing one of those action points, the linked requirements are proven to be met.

FEM analysis and optimisation for total structure

Currently, all parts are individually designed for specific worst case scenarios and include a safety factor. A Finite Element Method analysis would provide insights in natural frequencies of the system. It has to be checked whether resonance is possible and if so, how the design should be altered to prevent resonance. Finally, this analysis can provide accurate overall deflections. As described earlier, tip clearance is a major parameter in the duct efficiency. FEM analysis can be used to optimise for a required design tip clearance to get it as small as possible, without the rotor makin contact with the duct.

Improve control simulation

Current control estimates are either bases upon a three degrees of freedom analysis or simple hand calculations. A full 6 degree of freedom simulation would gain more insights in the behaviour of the vehicle.

CFD analysis and optimisation for the rotors.

For wind turbines, Blade Element Theory (BET) and computational fluid dynamics (CFD) are often compared and their results can differ more than 10%. It would be interesting to compare the results from BET with numerically calculated values for such a rotor shape. There is one disadvantage of running such an analysis for the rotors, the costs will be substantial. Costs of CFD analysis scales with Reynolds number cubed [72]. As detailed in subsection 6.2.1, the Reynolds number will be much higher due to the large chord length and high velocity. Additionally, the analysis of the flow in the proximity of the rotors can provide insight in the controllability of the vehicle with RPM variations and airflow across the motors for cooling.

PERFORM MORE NEW TESTS

Testing provided insights that are applied throughout the design. However, the tests were not performed under the actual conditions and the values for thrust and power should not be considered as the 'ultimate' truth. Two main differences between the test and the actual load case is the hub is currently fixed at one point, in the real situation it will be fixed at both the bottom and the top and thus will behave, vibration-wise. The other main difference is that the duct is that the duct is attached to the rotor, this implies no tip losses due to tip clearance and the test will measure extra skin drag of the duct since it's rotation. A test should be designed keeping the limitations of the previous test in mind. As described in chapter 6, the vibrations limited the rotational velocity an therefore the test. A new test set up with a balanced rotor and fixed duct could lead to a proper validation of the calculations.

ITERATE TO MORE DETAILED DESIGN

With the new information, a better design can be made. Also, the design team of the SolidityONE can learn from its inefficiencies to get to a better design with more harmony between the design departments. The new information and experience lead to a design with more design detail, better performance which is more trustworthy. An example of such an improvement could be an enhanced duct strut fairing shape. Such a fairing can act as stator to thrust improver and reduce the resulting torque. All these activities to improve the overall quality of the design are planned and described in the Gantt Chart in section 15.3.

15.2. FURTHER DEVELOPMENT & PLANNING

To get to the point where a major helicopter manufacturer would be interested in buying the prototype and concept, more steps need to be taken. In chapter 14, manufacturing and the operations are described. Now, a clear planning and strategy is provided. The stages that this project is going to go through are listed below:

ACQUIRE INVESTMENT

Besides man hours, an investment is needed to build the SolidityONE and convince helicopter manufacturers that this concept has a future. In chapter 2 more on the investment acquisition can be found.

MANUFACTURING

The manufacturing of the vehicle is described in chapter 14. The duration assigned to the sub tasks is based on the planning of TU Delft dreamteams. This comparison is justified with the fact that dreamteams design, build and test high performance one-off products.

CONCEPT DEMONSTRATION & SELLING

This tasks requires preparations. First, companies should be contacted and get excited about this development. This requires good sales skills and a company that leave a decent and trustworthy impression at potential clients. The goal in the preparation stage is to get in touch with major aircraft manufactures or other potential buyers of the concept and schedule a demonstration.

In the demonstration & selling phase, the scheduled demonstrations are held. In this phase, companies should get enchanted by the demonstration and buy the concept and underlying theories.

15.3. PROJECT PLANNING

For the VFS competition, hard deadlines are provided. For the future planning on the other hand, no hard deadlines are present. The duration of the manufacturing stages are based upon in-house experience.

At this point, the stages, their containing activities and their expected duration is described. From here, a Gantt chart can be made.

Task Name	Duration	Start	Finish
VFS	**85 days**	**Mon 3-2-20**	**Sun 31-5-20**
Improve control simulation	2 mons	Mon 3-2-20	Fri 27-3-20
FEM analysis and optimalisation	3 mons	Mon 3-2-20	Fri 24-4-20
CFD analsysis and optimalisation	3 mons	Mon 3-2-20	Fri 24-4-20
Perform tests	1 mon	Mon 23-3-20	Fri 17-4-20
Improve Design	2 mons	Mon 16-3-20	Fri 8-5-20
Report	1 mon	Mon 27-4-20	Fri 22-5-20
Deadline VFS report	0 days	Sun 31-5-20	Sun 31-5-20
Acquire investment	6 mons	Mon 4-5-20	Fri 16-10-20
Detailed design	100 days	Mon 1-6-20	Fri 16-10-20
Manufacturing	**280 days**	**Mon 19-10-20**	**Fri 12-11-21**
Technical drawings	1 mon	Mon 19-10-20	Fri 13-11-20
Manufacturing	4 mons	Mon 16-11-20	Fri 5-3-21
Subsystem assembly	1 mon	Mon 8-3-21	Fri 2-4-21
subsystem tests	3 mons	Mon 5-4-21	Fri 25-6-21
assembly	2 mons	Mon 28-6-21	Fri 20-8-21
system tests	3 mons	Mon 23-8-21	Fri 12-11-21
Concept demonstation & selling	**247 days**	**Mon 24-5-21**	**Tue 3-5-22**
Prepare demonstations	6 mons	Mon 24-5-21	Fri 5-11-21
Demonstrate	6 mons	Wed 17-11-21	Tue 3-5-22
Return money to investors	1 wk	Wed 4-5-22	Tue 10-5-22

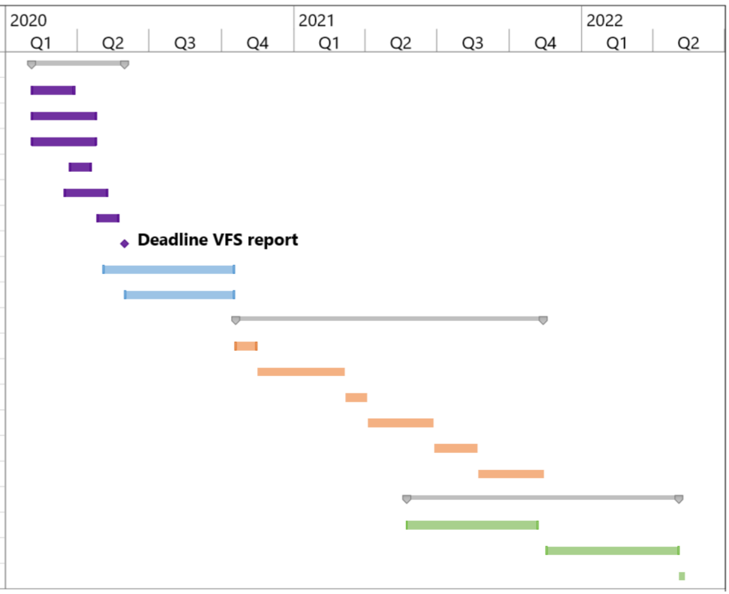

Figure 15.1: Gantt planning for future development

15.4. TECHNICAL RISK ASSESSMENT

In this section, the technical risks for the design and the next phases in the product life-cycle are analysed and assessed. If technical risks are found to be critical (high impact or likelihood) for the success of the phase, an approach for risk mitigation is discussed. These risks and explored mitigation are then projected in risk maps.

15.4.1. IMPACT CATEGORIES

Risks can be analysed in terms of time (or time to market), personal safety, and performance impact for the mission. The overarching impact is the financial cost associated with a risk: time, safety and performance all result in higher costs or decreased product pricing. Other impacts can be classified as environmental impact or component performance degradation and failure.

Impact classifications are denoted on a scale from low to very high, where a low impact has little influence on the impact categories, and a very high impact could require a completely new design of a system, as a result of mission failure.

15.4.2. DETAILED DESIGN AND PRODUCTION

Detailed design and production risk assessment are combined due to the interlinked nature of the two phases. The risk key associated with this category is **RM-DDP**. Some risks and mitigations are carried over from the preliminary design phase, whereas other risks originate from re-evaluation of the current concept and the associated design and production risks.

15.4.3. TESTING AND CERTIFICATION

Risks associated with testing and certification are given the key **RM-TC**. Testing allows validation of models and tools, which risks the need to refine the model or tool, which can impact the vehicle design. The worst case conclusion leading to scrapping the design: it is thus preferable to test as quickly into the design phase as possible; before parameters are frozen.

15.4.4. OPERATIONS AND END-OF-LIFE DISPOSAL

Risks with expected occurrence post-production and post-certification are keyed **RM-OPD**, and include the normal operations and end-of-life phases. Risks include fire, loss of power, and the environmental risk associated with battery disposal.

15.4.5. RISKS AND RISK MAPS

Listed below are the risks and their descriptions and proposed mitigations, which are then shown in risk maps before and after mitigation in Table 15.1 and Table 15.2.

RM-DDP-1 *Design oversights* Result in missing components or systems, where the true impact depends on the design modification to be made. The impact increases while the design becomes more complete.

RM-DDP-2 *Production cost* Extensive use of exotic materials causes a product cost increase, leading to an increased price and potential sales stagnation. Additionally, tooling and labour costs associated with CFRP is high: this can be prevented by considering the production during the design.

RM-DPP-3 *Manufacturing* Manufacturing itself has a risk associated: it may occur that a component or system cannot be created as a result of incompatibilities and design oversights. This is mitigable by considering tooling complications and partial production with assembly of more complicated components.

RM-DDP-4 *Design weight* The target operational empty weight of the design should be compared to the actual weight at every stage to prevent the snowball-effect, in order to prevent a mismatch which causes a potential mission failure. Additionally, it should be considered that the design can become heavier than anticipated due to production methods and inaccuracies such as excessive use of epoxy.

RM-TC-1 *Vibrations* Asymmetric rotor center of mass and aerodynamic center of lift positions can cause vibrations resulting in potential structural failure, Additionally, ground resonance should be anticipated. Designing a balanced rotor should be prioritised and can benefit from static testing.

RM-TC-2 *Rotor deformation* The rotor may deflect under flight loads, potentially resulting in decreased performance, structural failure of the rotor or contact with the duct. Since the rotor was designed with anhedral, both lift and centrifugal forces cause an upward deflection. To mitigate this risk, the rotor may require additional stiffening and the duct diameter can be increased.

RM-TC-3 *Aerial screw performance* The aerial screw performance is not yet proven and existing theories and models for rotor design explicitly state incompatibility with high disk solidity. Physical testing of aerial screws can be performed to verify or adjust models at an early stage.

RM-TC-4 *Vehicle noise* Testing may show that noise levels are higher than anticipated by models, which risks failure to meet the market proposition.

RM-TC-5 *Design uncertifiable* Due to limitations of the rotor and its controllability in the the case of rotor failure or power train failure, the occupant safety may be grounds for the rejection of type certification. The risk of which may be reduced by the implementation of a safety measure, such as a ballistic rescue system as developed by BRSAerospace [1].

RM-OPD-1 *Control complexity* A low-flying vehicle risks contact with obstacles as a result of pitching motion. Anti-torque depends on control inputs as a result of coupled motion. Mitigation is performed using a PID controller and simplifying the pilot controls to speed, yaw and roll.

RM-OPD-2 *Battery fire* The batteries used are Lithium-ion based, which are known to catch on fire if mistreated [30]. This is prevented by selecting battery cells for maximum continuous current, add sufficient cooling and fire protection in the form of a battery box lined with aramid paper.

[1] https://brsaerospace.com/ (Retrieved: 20-01-2020)

RM-OPD-3 *Power system overheating* Causes a temporary performance degradation or shutdown. This is mitigated by evaluating options for cooling where necessary.

RM-OPD-4 *Battery degradation* As a result of charge-discharge cycles, the battery capacity and possibly the power output degrades. At a certain point, this degradation causes loss of performance beyond acceptable means for the mission. Though not mitigable, the battery performance can be checked regularly to ensure its capacity.

RM-OPD-5 *Battery disposal* Lithium ion battery cells can be found in large quantities at landfills [73]. The risk is the unavailability of a recycling method, or the awareness of such a method. This can be prevented by spreading awareness to electric vehicle users and by setting up a battery reclaiming and recycling procedure.

Table 15.1: Risk map showing identified risks before mitigation for the remaining product life cycle (Note that the **RM** prefix is removed for clarity)

Impact	Very High	OPD-2	TC-3, TC-5	OPD-3	*red*
	High		DDP-4, TC-2	DDP-3, OPD-5	TC-1
	Medium		DDP-1, OPD-1	DDP-2, TC-4	
	Low	*green*			OPD-4
		Low	Medium	High	Very High
Initial	**Likelihood**				

Table 15.2: Risk map showing identified risks after proposed mitigation for the remaining product life cycle

Impact	Very High	OPD-3, TC-5			*red*
	High	OPD-2	DDP-4, TC-1, TC-2, DDP-3		
	Medium	OPD-1	DDP-1, DDP-2, TC-3	TC-4, OPD-5	
	Low	*green*	OPD-4		
		Low	Medium	High	Very High
Mitigated	**Likelihood**				

16

Market and environmental impact

The first cost of the prototype is divided in 3 parts; development cost, production cost and direct operational cost. Adding these prices comes to an investment fund required to build the vehicle. Furthermore, the total CO_2 emissions are estimated to build one prototype. According to the requirements in subsection 3.1.1 this should not be more than 45 times the vehicle mass. Finally the noise is calculated which should not exceed 82 dB at 150m according to the requirements in subsection 3.1.1

16.1. Cost analysis

Consideration of costs is of fundamental importance at all phases of the aircraft design process. The selling price of an aircraft is largely determined by market forces and to be profitable for the manufacturer it must be possible to produce it for less than the market price [74]. Since this project is only a proof of concept and not a market proposition, this requirement is not included. However, a cost estimation is still relevant.

16.1.1. First cost

The first estimation made of the costs for a design is referred to as the first cost. For a conventional design process, first cost is estimated in function of total mass or maximum cruise velocity [74]. These methods are often considered unreliable and very preliminary. Considering this reason and the uniqueness of the chosen design. These cost approximation methods were disregarded.

The preferred method of cost approximation was to estimate the material and production cost (or price for "off-the-shelf" products), for each part and add those together. The parts and their respective prices can be found in Appendix A. Total of which comes to €24.000 including "off-the-shelf" products.

According to Figure 15.1, the design would require around another 4 months to finish with a detailed design. Assuming the services from TU Delft can still be used during this period. It would require no extra cost to arrive at the detailed design. However the design could change in such a way that it would require more funds to build. An additional €4.000 is assumed as a contingency cost buffer for extra components such as fasteners and dials, which are not yet determined.

Finally, an additional €20.000 is estimated for organisational costs, transportation costs and travel expenses for demonstration purposes. This comes to a grand total of €90.000 in investments costs.

Summarizing, when the vehicle has to be produced, tested and demonstrated, 48.000 euro is required.

This money can be obtained in three different ways, or a combinations of them:

- Sponsorship of multiple suppliers, partners, small money investment that cover all costs up to the point the design and concept is sold.
- One major party that is able to invest the full sum.
- A potential client of the design and concept could do the initial investment. In return this party could then get a first change to buy the concept and design.

Furthermore, Figure 15.1 predicts an additional 280 days of manufacturing work after the VFS competition. Initially, this labour is not considered to be paid work because of the TU Delft Dreamteam structure. After the internal investment in made, the production of the vehicle can start and materials and parts can be ordered. When the vehicle would be sold and commerically endorced, it would be reasonable to take the labout into account when selling to a commerical party. Assumng working at an hourly rate of €15 per person, the labor costs would come to a total at €42.000. Some parts require special equipment or machining tools. The exact parts are explained in subsection 14.1.1. Assuming we could still use the services of TU Delft, this would only cost us around €100.00 for cncing the foam parts and carbon lay-up. But this can be neglected in the cost estimation. [1]. When a company would buy the prototype and design, the total costs would then be around €90.000.

The system would require testing and operational costs for another 3 months. The operational costs are estimated below.

16.1.2. OPERATING COSTS

For a more conventional aircraft. the considered operating costs are:

- Write off of the initial purchase price, or equivalent lease payment. This includes the cost of raising the purchase sum where relevant
- Insurance
- Crew costs
- Engineering replacement items
- Maintenance
- operational charges such as landing and en route navigation fees
- Fuel and other expendable items

Since this design is only a proven concept, only the maintenance and fuel costs are taken into account. Maintenance is more difficult to estimate, as it is unsure which parts will fail first. However, it can be said that any "off-the-shelf" parts should be replaced after failing instead of repaired to ensure the safety of the vehicle. Any part made either with carbon fiber or honeycomb composite should also be replaced after any visual sign of damage. Since every part can be removed separately, only the costs for the damaged part should be taken into account. These can be found in Appendix A.

The main operational cost of the SolidityONE will be the electricity required to power the vehicle. From chapter 8 the total power required for one flight is calculated to be 10.3 kWh.

The price per kWh in 2018 in the Netherlands is 0.12 EUR [75]. This comes to a total of 42 cents per flight cycle. Assuming the SolidityONE will be flown twice a day for a full year the total operational cost per year is 306.60 EUR.

16.1.3. LIFE CYCLE COSTS

The final cost is obtained by the first and operational costs minus the value at the end of life. Since it is required that 95% of each vehicle manufactured after January 2015 should be recyclable[76]. Much attention was brought to the recyclability of the SolidityONE. Therefore, there will be very little costs to the disposal of a vehicle.

Aluminium Can be fully recycled.
Carbon fibre Can be used in asphalt or used in concrete reinforced material but will return little to no value.
Control stick/pedals Can be re-used if checked. Estimated to reduce in value of 50%
Foam Must be disposed of. But yields no extra cost due to low mass
Batteries Can be re-used but will yield lower performance/capacity. Estimated loss of value at 50%
Motor Can be re-used if checked. Estimated to reduce in value of 50%

The total return value of the vehicle will be around €10.000. Therefore the final cost of the vehicle is estimated to be €30.000 for an estimated life time of 10 years.

[1] https://www.tudelft.nl/en/ide/about-ide/facilities/pb/facilities/

16.2. CARBON DIOXIDE PRODUCTION

One of parameters taken into account for the environmental impact of the SolidityONE is the total CO_2 emitted for the production and operation of one product. This is divided in the CO_2 produced for each material and the manufacturing of that product.

16.2.1. MATERIALS

For each material the CO_2 emission per kg was estimated using CES EduPack [33]. The results of which can be found in Appendix A. Adding these values gives a total CO_2 production of 1365 kg per SolidityONE build. The emissions for the parts of the shelf are ignored. Furthermore. The producing of the parts from raw materials also require electricity which would produce CO_2 to generate. These are however excluded as they only contribute to a fraction of the total emissions.

16.2.2. OPERATIONAL

The only operational emissions that are assumed is the CO_2 produced by the electricity generated to power the vehicle. For coal generated this is around 0.94kg per 1kWh according to CNCF[2] for one flight this would be 9.7 kg of CO_2 emissions. Assuming 2 flights per day, around 7068 kg per year.

16.2.3. END OF LIFE

At the end of life, some materials can be re-used and recycled. This can be seen as a negative CO_2 production. Since only the raw materials are considered to produce any CO_2. These are the only ones which will be analysed.

In the case for carbon fiber, the only commercialized method for composites to come from PAMELA research is grinding of thermoset composites into granules for use as filler materials (in asphalt, for example), while reclaimed short fibers are used to reinforce sheet molding compound and bulk molding compound (SMC and BMC). This will yield nor produce any CO_2.

In the case of aluminium, these can be fully recycled for its raw materials but need to be processed before. The energy required for this is negligible. The only material that is not recyclable is the foam core used in the structure, the total mass of which is around 4 kg. In conclusion, the total CO_2 produced for a single vehicle is estimated around 25,342 kg. This is around 10 times the value of the vehicle which is lower then the requirement of 45.

16.3. NOISE

The market analysis showed a trend in decreasing the noise produced by rotorcraft. This was considered an opportunity for the SolidityONE. Therefore, the goal was set to obtain the lowest noise level possible. The regulations on noise for aerial vehicles are set by the ICAO. The ICAO states in Annex 16 Volume I chapter 11 , that a small rotorcraft lighter than 788 kg shall not exceed 82.5 dBA SEL in overflight at a height of 150 m [77]. This was implemented as a requirement.

16.3.1. ROTOR ROTATIONAL NOISE

Noise for a rotor consists of two parts; rotational and vortex noise. The rotor rotational noise is calculated by applying analytical plots given in 'A review of aerodynamic noise from propellers rotors, and lift fans' Figure C.2[78]. This has as input the effective mach number M_E given by Equation 16.1a and the angle between the rotor point and the line joining the field point θ given by Equation 16.1b, where a is the speed of sound and x, y and z are the coordinates from the flight path the observer and i_d is the disc incidence. This provides the harmonic sound pressure levels, which are corrected for thrust and distance by Equation 16.2a and gives a fundamental frequency of Equation 16.2b [78]. Finally, this is in dB while the requirement is in A-weighted

[2] https://cncf.com.au/carbon-calculator/

decibels. Hence Equation 16.3b computes the A-weighted noise correction.

$$M_E = \frac{\frac{0.8\Omega R}{a}}{1 - \frac{V_f x}{ar}} \quad (16.1a)$$

$$\theta = \tan^{-1}\left[\frac{z}{\left(x^2+y^2\right)^{1/2}}\right] - i_d\left[\frac{x}{\left(x^2+y^2\right)^{1/2}}\right] \quad (16.1b)$$

$$SPL_N = \left[I_N + 11 + 10\log\frac{T}{r^2}\left(\frac{T}{A}\right)\right] \quad (16.2a)$$

$$f = \frac{\Omega}{2\pi\left(1 - \frac{V_F}{a}\cos\theta\right)} \quad (16.2b)$$

$$R_A(f) = \frac{12194^2 f^4}{\left(f^2+20.6^2\right)\sqrt{\left(f^2+107.7^2\right)\left(f^2+737.9^2\right)}\left(f^2+12194^2\right)} \quad (16.3a)$$

$$A(f) = 20\log_{10}\left(R_A(f)\right) + 2 \quad (16.3b)$$

16.3.2. VORTEX NOISE

In the axial direction there is vortex noise. The sound pressure level of vortex noise is given by Schlegel's equation for overall vortex noise at a distance r in feet for sea level conditions. This equation applies imperial units and is given by Equation 16.4, where $V_{0.7}$ is the velocity at 0.7 of the radius and A_{disc} is the disc plan form area . The fundamental frequency for the vortex noise was computed with Equation 16.5a, which was dependent on the projected blade thickness given by Equation 16.5b and the Strouhal number St, which is taken to be 0.28 [78].

$$SPL_r = 10(2\log V_{0.7} + 2\log T - \log A_{disc} - 3.57) - 20\log\frac{r}{300} \quad (16.4)$$

$$f = \frac{V_{0.7} St}{h} \quad (16.5a)$$

$$h = t\cos\alpha + c\sin\alpha \quad (16.5b)$$

16.3.3. RESULTS

The analysis on the rotational noise resulted for maximum forward velocity in an effective Mach number of 0.31 and a θ of 81.2 degrees. From these values the Sound pressure levels, frequencies and A weighted SEL were determined and are shown in Table 16.1.

Table 16.1: Rotational noise in overflight

Harmonic Order	**2**	**3**	**4**	**6**	**8**	**10**	**12**	**16**	**20**	**30**	**40**	**60**
SPL [dB]	76	70	66	59	56	54	52	47	42	41	36	31
Frequency [Hz]	72	108	144	216	288	360	432	576	720	1080	1440	2160
SEL [dBA]	52	52	51	49	49	48	48	45	41	41	37	32

In the axial direction the vortex noise resulted to be 64.3 dB SPL, the projected blade thickness was 0.35 m and the fundamental frequency was 58 Hz. The highest SEL was obtained at the 16th harmonic with a noise of 64.3 dBA. Adding both the noises resulted in a total noise of 65 dBA. Hence it fulfills the requirement. Furthermore, by comparison with the Robinson R22 and the Schweizer RSG LLC 269C-1, which are both small rotorcraft with a MTOW below 1000 kg, is the SolidityONE really quiet. As these rotorcraft have an overflight noise of 78.9 and 80.4 dB respectively[3].

[3]From URL:https://www.easa.europa.eu/easa-and-you/environment/easa-certification-noise-levels(accessed on 20-1-20)

16.4. MARKET POSITION

The SolidityONE is a cheap alternative to the conventional rotorcraft and although it does not meet the standard of those proven concepts yet, it has a place on the market. The SolidityONE is a device which is easy to fly due to the stability and controls incorporated. It has the capability to fly in small urban areas and is a great alternative for every day transportation. The device has a fun factor and uniqueness to it, which makes it more than suitable for rotorcraft enthusiast. The historic relevance of Leonardo Da Vinci makes it even more desirable.

17

CONCLUSION

This chapter concludes the report and provides recommendations for future work on SolidityONE. SolidityONE is a conceptual design for a Leonardo da Vinci-inspired aerial screw, designed for the 37th Annual Student Design Competition of the Vertical Flight Society (VFS).

The vehicle is designed in an iterative process, where multiple objectives are optimised according to the mission. Starting from a rough estimate, the accuracy of the design parameters increased with each iteration. The methods used in this process are validated by comparing them to existing models. In the end, it was checked that the design meets all requirements.

An overview of the design is given in Table 17.1. SolidityONE has tandem counter-rotating rotors to compensate for torque. The rotors are shrouded by a duct with an intake lip. This increases the generated thrust significantly.

The rotor design has been optimised with the use of blade element theory modified for aerial screw geometry. This resulted in circular blade elements which are stretched out compared to the conventional straight blade elements. The aerial screw differs compared to conventional rotors in longer chords (up to 3.8 m, resulting in thin airfoils), reversed taper (the tip length is 3.8 times larger than the root length), high blade solidity (>1), high Reynolds numbers (up to 30 million), high disk loading with low downwash velocity, high cambered airfoils (8%), no twisting of blades possible and low aspect ratio blade (0.3) in the SolidityONE's configuration. The airfoil chosen is the NACA 8508 (8% thickness at the root) to NACA 8501 (1% thickness at the tip). Furthermore the tip speeds is 0.33 Mach at most, resulting in low noise of the vehicle. At a distance of 150 meter the noise production is only 67 dB.

Control is provided by differential rotor RPM for pitch, and vanes below the rotor control yaw and roll. Using differential RPM allows larger velocities to be reached than vanes. A fly-by-wire system is used to enhance pilot control and reduce workload.

The structure is partially made from a carbon fibre composite to reduce the mass while keeping the structure stiff and strong. Where the mass is less critical, or manufacturing is complex, aerospace grade aluminium is used to reduce material and manufacturing costs, and improve environmental impact. Also, recyclability is taken into account in the material selection. Overall, the CO_2-production for a single vehicle is about 25 tonnes.

Propulsion is delivered by two 30 kW electric motors, which take their power from a lithium battery pack. This configuration was found to be optimal, both in terms of mass and sustainability.

The unit price of a SolidityONE is €270,000 for a series of 150. This includes costs for future engineering work and construction. Should a larger series or a longer return on investment time be an option, this price would be lower.

The design proves to be versatile enough that 50 kg of extra payload can be carried. When a part of this mass is used for additional batteries, either a larger range or a longer flight endurance can be achieved. Alternatively, the extra mass of 50 kg can be used as a design contingency for the detailed design phase.

In comparison with conventional helicopters, SolidityONE has shown to be relatively quiet. This could make the design suited for urban operations. An operations and logistics planning was made to demonstrate the vehicle to helicopter manufacturers, who can tailor the design to a specific market.

Table 17.1: Design overview

Parameter	**Value**	**Unit**
Rotor radius	0.6	m
Rotor pitch	0.6	m
Blade solidity	1.016	-
Airfoil	NACA 850X	-
Total power	60	kW
Endurance	785	s
Range	10.2	km
Never exceed speed	15.2	$m\,s^{-1}$
MTOW	260	kg
Payload	70	kg
Tip clearance	1.2	mm
Inlet lip radius	156	mm
Diffuser expansion ratio	1	-

Bibliography

[1] M Hepperle. Javafoil, 2018. [Computer software].

[2] E. Asir et al. Project plan - group 3. Technical report, Delft University of Technology, November 2019.

[3] E. Asir et al. Leonardo da vinci's aerial screw - baseline report - group 3. Technical report, Delft University of Technology, November 2019.

[4] E. Asir et al. Leonardo da vinci's aerial screw - midterm report - group 3. Technical report, Delft University of Technology, December 2019.

[5] S. et al Huber. *Periodic Report P7 (January 1st to December 31st, 2014), Publishable summary*. Green Rotorcraft ITD (GRC).

[6] G. Maoui. *INNOVATION TAKES OFF - Clean Sky European research for aeronautics*. Le cherche midi éditeur, 2016.

[7] Markets and markets. Helicopters market by point of sale (oem, aftermarket), oem type (light, medium, heavy), oem application (military, civil & commercial), oem component & system, aftermarket by component & system, and region - global forecast to 2025. Market research report AS5591, Markets and markets, Nov 2019.

[8] F. Romli et al. Market potential for personal air vehicle (pav) concept: A malaysian case study. *International Journal of Pure and Applied Mathematics*, 119:3755–3760, 01 2018.

[9] Vertical Flight Society. 37th annual student design competition 2019-2020 request for proposal, 2019.

[10] O. Rand and V. Khromov. Helicopter sizing by statistics. *JOURNAL OF THE AMERICAN HELICOPTER SOCIETY*, pages 300–317, jul 2004.

[11] Myers L.M. Aerodynamics experiments on a ducted fan in hover and edgewise flight. Technical report, The Pennsylvania State University, December 2009.

[12] L.P. Parlett. Aerodynamic characteristics of a small-scale shrouded propeller at angles of attack from 0°to 90°. Technical report, NACA, 1955.

[13] P. Martin and C. Tung. Performance and flowfield measurements on a 10-inch ducted rotor vtol uav. Technical report, American Helicopter Society 60th Annual Forum, June 2004.

[14] G. Gennaro and J. Gonzalez-Adalid. Improving the propulsion efficiency by means of contracted and loaded tip (clt©) propellers. Technical report, SINM srl and SISTEMAR, 2012.

[15] F.E. Hitchens. *The Encyclopedia of Aerodynamics*. Andrews UK Limited, digital edition edition, 2015.

[16] EMRAX. *Technical Data and Manual for EMRAX Motors / Generators*, aug 2018. Rev. 5.1.

[17] T. Placke et al. Lithium ion, lithium metal, and alternative rechargeable battery technologies: the odyssey for high energy density. *Journal of Solid State Electrochemistry*, 21(7):1939–1964, Jul 2017. DOI: 10.1007 s10008-017-3610-7.

[18] Austro Engine. *Engine Manual AE50R AE50RA AE50RAB*, mar 2011. Rev. 6.

[19] Solo Kleinmotoren GmbH. *Manual for the Engine SOLO type 2625 02 i*, dec 2018. Rev. 4.

[20] Lantmännen Aspen AB. Safety data sheet aspen 2, mar 2016.

[21] M. Daly. *Jane's Aero-Engines*. IHS Markit, 2019.

[22] J. Bacha et al. Diesel fuels technical review. Technical report, Chevron Corp., 2007.

[23] Lycoming. *Operator's Manual Lycoming O-320 Series*, 3 edition, oct 2006.

[24] Shell. Shell avgas 100ll piston engine aircraft fuel. Online, feb 1999.

[25] P. Fischer et al. Innovative electric motors for the future electric powertrain. In Liebl J., editor, *Der Antrieb von morgen 2017*, Wiesbaden, 2017. Springer Vieweg. DOI: 10.1007/978-3-658-19224-2_9.

[26] Y. Liang et al. Life cycle assessment of lithium-ion batteries for greenhouse gas emissions. *Resources, Convervation and Recycling*, 117(B):285–293, feb 2017. DOI: 10.1016/j.resconrec.2016.08.028.

[27] T. Ålander et al. Particle emissions from a small two-stroke engine: Effects of fuel, lubricating oil, and exhaust aftertreatment on particle characteristics. *Aerosol Science and Technology*, 39(2):151–161, 2005. DOI: 10.1080 027868290910224.

[28] E. Torenbeek. *Synthesis of Subsonic Airplane Design.* Springer, 1982. DOI: 10.1007/978-94-017-3202-4.

[29] X. Zeng et al. Commercialization of lithium battery technologies for electric vehicles. *Advanced Energy Materials*, 9(27):A2605–A2622, jun 2019. DOI: 10.1002/aenm.201900161.

[30] Q. Wang et al. Lithium ion battery fire and explosion. *Fire Safety Science*, 8:375–382, 2005. DOI: 10.3801/IAFSS.FSS.8-375.

[31] PowerCell. Powercell s3 product sheet. Accessed 03/12/2019.

[32] College of the Desert. *Hydrogen Properties*, 0 edition, dec 2001.

[33] Granta Design Limited. CES EduPack, 2019. [Computer software]. Cambridge, UK.

[34] K. N. Otto and E. K. Antonsson. Trade-off strategies in engineering design. *Research in Engineering Design*, 3(2):87–104, 1991.

[35] S.S. Rao and A.K. Dhingra. Applications of fuzzy theories to multi-objective system optimization. Technical Report NASA-CR-177573, Purdue Univ., West Lafayette, IN, United States, jan 1991. DOI: 19910006699.

[36] Th. Van Holter and J.A. Melkert. *Helicopter Performance, Stability and Control.* Faculty of Aerospace Engineering, Delft University of Technology, 2002.

[37] John Carlton. *Marine Propellers and Propulsion.* Elsevier, Oxfort, 2007.

[38] R.W. Prouty. *Helicopter Performance, Stability, and Control.* PWS Publishers, Boston, Massachusetts, 1986.

[39] J.D. Anderson. *Fundamentalsof aerodynamics.* McGraw-Hill, 2011. ISBN-13: 978-0-07-339810-5.

[40] J.G. Leishman. *Principles of Helicopter Aerodynamics.* Cambridge University Press, The Pitt Building, Trumpington Street, Cambridge, United Kingdom, 2000.

[41] I.C. Cheeseman and W.E. Bennett. The effect of the ground on a helicopter rotor in forward flight. Technical Report 3021, Aeronautical Research Council, 1955.

[42] J.L. Pereira. Hover and wind-tunnel testing of shrouded rotors for improved micro air vehicle design. Technical report, University of Maryland, 2008.

[43] O. Gur and A. Rosen. Comparison between blade-element models of propellers. Technical report, Technion Israel Institute of Technology, dec 2008.

[44] KNMI. *Daggegevens van het weer in Nederland Het weer op maandag 13 januari 2020 te Rotterdam*, jan 2020.

[45] APC PROPELLERS. *7X4 PROPELLER - PERFORMANCE DATA (VERSUS ADVANCE RATIO AND MPH)*, dec 2014.

[46] T. van Holten and J.A. Melkert. *Helicopter Performance, Stability and Control.* Faculty of Aerospace Engineering, Kluyverweg 1 Delft University of Technology, 2002.

[47] Federal Aviation Administration. *PART 27-AIRWORTHINESS STANDARDS: NORMAL CATEGORY ROTORCRAFT*, 3rd edition, nov 2019.

[48] European Aviation Safety Agency. *Certification Specifications and Acceptable Means of Compliance for Engines CS-E*, dec 2018. Amendment 5.

[49] M. Yildirim et al. A survey on comparison of electric motor types and drives used for electric vehicles. In *2014 16th International Power Electronics and Motion Control Conference and Exposition*, pages 218–223, Sep. 2014. DOI: 10.1109/EPEPEMC.2014.6980715.

[50] V. Khomenko et al. High-energy density graphite/ac capacitor in organic electrolyte. *Journal of Power Sources*, 177(2):643–651, mar 2008. DOI: 10.1016/j.jpowsour.2007.11.101.

[51] O. Gröger et al. Review-electromobility: Batteries or fuel cells? *Journal of the Electrochemical Society*, 162(14):A2605–A2622, 2015. DOI: 10.1149/2.0211514jes.

[52] R.A. Serway. *Principles of physics*. Saunders College Publishing, second edition, 1998.

[53] Axon. *Esa wires & cables and Axalu® aluminium wires*, nov 2010. Cable: AXL 1 M 8133 AS1.

[54] D.W. Dudley and S.P. Radzevich. *Handbook of practical gear design and manufacture*. CRC Press, second edition, 2012. pages 42-43, 207-216.

[55] Anaheim Automation. Gbpn-120 series - planetary gearboxes. Online, 2019. GBPS-0901-NM-003.

[56] D. Moreels and P. Leijnen. High efficiency axial flux machines. White paper, Magnax, jan 2018.

[57] Cascadia Motion. Pm100 propulsion inverter catalog. Online, 2019.

[58] E.H. Buyco and F.D. Davis. Specific heat of aluminum from zero to its melting temperature and beyond. *Journal of chemical & engineering data*, 15(4):518–523, oct 1970. DOI: 10.1021/je60047a035.

[59] DuPont. *DuPont Nomex 410 Technical Data Sheet*, 2016.

[60] Noctua. *NOCTUA NF-A14 industrialPPC-3000 PWM information sheet*.

[61] Elithion. *Lithiumate BMS Manual*, 2018.

[62] Texim Europe. *Product Specification CH056DLCL-002*, march 2011.

[63] T.H.G. Megson. *Aircraft Structures for Engineering Students*. Elsevier Ltd., United Kingdom, 2016.

[64] J.P. Peterson, Seide P., and Weingarten V.I. Buckling of thin-walled circular cylinders. Technical report, National Aeronautics and Space Administration, 1968.

[65] Dassault Systemes. Abaqus. [Computer software].

[66] M.D. Pavel. Rotorcraft mechanics ae4-213. TU Delft course presentation.

[67] R.F. Stapelberg. *Handbook of Reliability, Maintainability, Maintainability and Safety in Engineering Design*. Springer, London, 2009.

[68] I. Bolvashenkov, Kammermann J., Willerich S., and Herzog H.-G. Comparative study of reliability and fault tolerance of multi-phase permanent magnet synchronous motors for safety-critical drive trains. *International Conference on Renewable Energies and Power Quality*, 2016.

[69] S.E. Scates. Aerial perspective: Flying dollars and sense. *Professional Surveyor Magazine*, 2007.

[70] Federal Aviation Administration. *PART 91-GENERAL OPERATING AND FLIGHT RULES*, jan 2020.

[71] C. Brown and Gordon M.S. Motorcycle helmet noise and active noise reduction. *The Open Acoustics Journal*, March 2011.

[72] S.B. Pope. *Turbulent Flows*. Cambridge University Press, Cornell University, 1st edition, 2016.

[73] O. Velázquez-Martínez et al. A critical review of lithium-ion battery recycling processes from a circular economy perspective. *Batteries*, 5(4):68, nov 2019. DOI: 10.3390/batteries5040068.

[74] D. Howe. *Aircraft Conceptual Design Synthesis*. Professor Engineering publishing, St Edmunds, UK, 2000.

[75] Eurostat. Electricity prices components for household consumers. https://ec.europa.eu/eurostat/data/database?node_code=nrg_pc_204_c, nov 2019.

[76] EU parliament. The eu's end-of-life vehicle (eeev) directive. *European Union documents and publications*, sept 2000.

[77] International Civil Aviation Organization, Montreal. *Annex 16 - Environmental protection - Volume I - aircraft noise*, 2008. ISBN 978-92-9231-108-7.

[78] J.E. Marte and Kurtz D.W. A review of aerodynamic noise from propellers rotors, and lift fans. Technical Report 32-1462, NASA, Pasadena, California, jan 1970.

A

BILL OF MATERIALS

Part	Amount	Material	Weight per part [kg]	Weight total [kg]	Material cost [EUR]	Eq. CO2 footprint [kg]
Rotor hub	2	Low alloy steel, AISI 4340, oil quenched & tempered	2,65	5,3	26,5	74,2
Rotor blade skin	2	Epoxy/HS carbon fiber, woven prepeg, biaxial lay-up	1,1	2,2	110,0	103,4
Rotor blade core	2	Expanded PS foam (closed cell, 0.050)	2,4	4,8	12,6	11,952
Duct skin	2	Epoxy/HS carbon fiber, woven prepeg, biaxial lay-up	5,5	11	550,0	517
Duct core	2	Aluminum 5056 honeycomb (0.016), L direction	3	6	186,0	174
Duct struts	8	Aluminum, 7068, T6511	0,56	4,48	22,4	62,72
Duct struts sec.	8	Aluminum, 7068, T6511	0,2	1,6	8,0	22,4
Duct strut fairing	4	Expanded PS foam (closed cell, 0.050)	0,16	0,64	1,7	1,5936
Duct strut fairing sec	4	Expanded PS foam (closed cell, 0.050)	0,028	0,112	0,3	0,27888
Duct struts attachment	8	Aluminum, 7068, T6511	0,114	0,912	4,6	12,768
Airframe	1	Aluminum, 7068, T6511	13,4	13,4	67,0	187,6
Roll cage	1	Aluminum, 7068, T6511	0,7	5	25,0	70
Aerodynamic fairing	1	Phenolic/E-glass fiber, woven prepeg, biaxial lay-up	5	5	125,0	35
Bearing	2	Steel	4	8	1260,0	0
Landing gear	1	Aluminum, 7068, T6511	6,6	6,6	33,0	92,4
Control vanes	4	Expanded PS foam (closed cell, 0.050)	0,79	3,16	9,0	0
Sticks	1	HC 615-200	2	2	90,0	0
Pedals	1	HC 300-111	4	4	100,0	0
Control computer	1	Pixhawk 4	0,25	0,25	200,0	0
Engine	2	Emrax 188			7150,0	0
Gearbox	2		7,2	14,4	1000,0	0
Cooling	1		2	2	300,0	0
Engine bracket	2	Aluminium 7068 T6511	0,125	0,25	0,0	0
Gearbox bracket	2	Aluminium 7068 T6512	0,125	0,25	0,0	0
Controller	2	Rhinehart PM 100DZ	7,5	15	9500,0	0
fire casing	1	Aluminum, 7068, T6511	5	5	100,0	0
Battery	900	Lithium ion	0,05	45	2691,0	
Cabling	0		1	1	0,0	
Pilot with personal protection	1		70	70	0,0	0
Seat	1	plastic	2	2	20,0	0
Dashboard	1		1	1	50,0	0
Warning lights	1		0	0	0,0	0
Avionics	1		0	0	0,0	0
Vehicle access (stairs, doors)	1					0
Extra						0
Total				**240,354**	**23642,0**	**1365,31248**

Figure A.1: List of parts used

B

MAI-plan and Operations & Logistics Concept Description

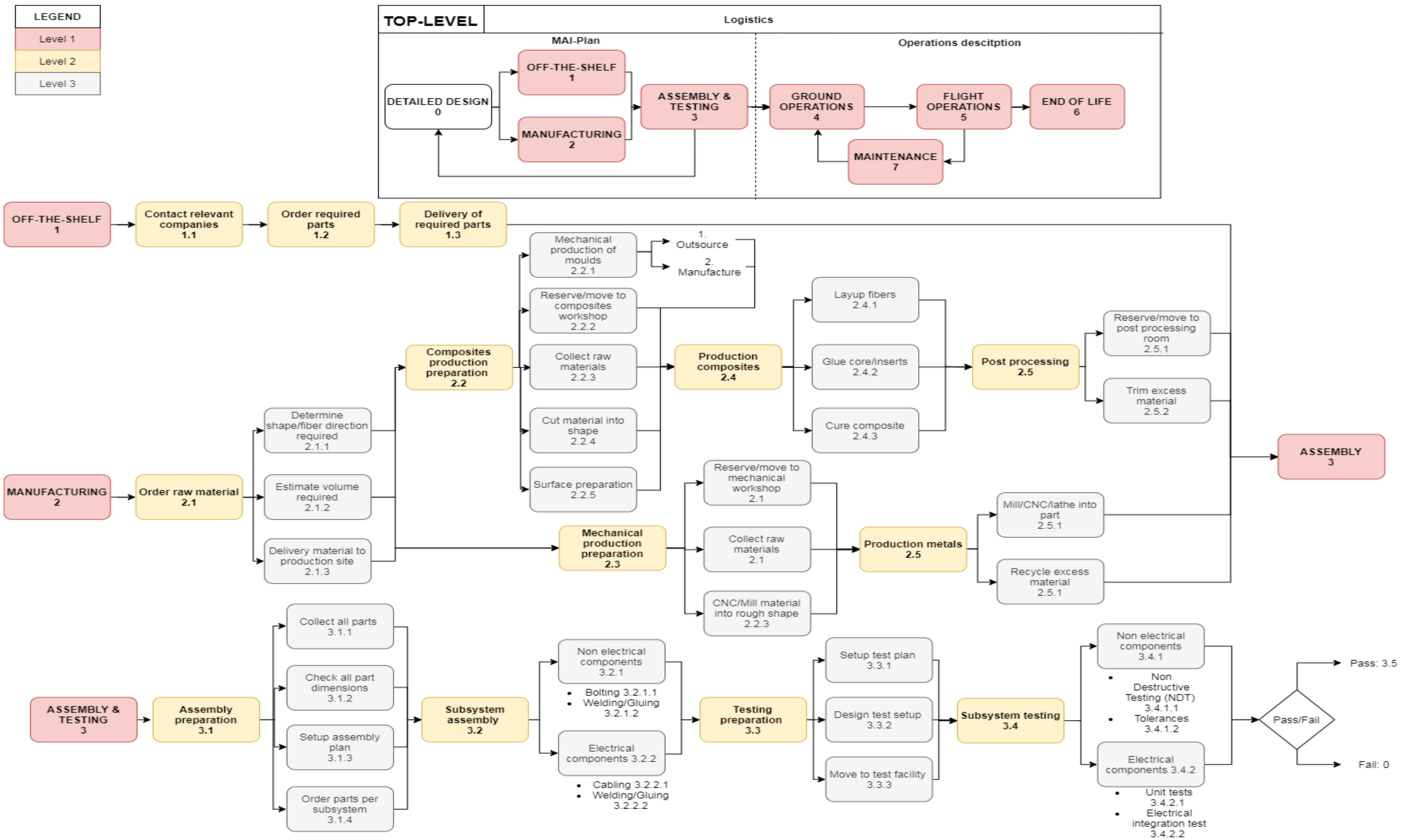

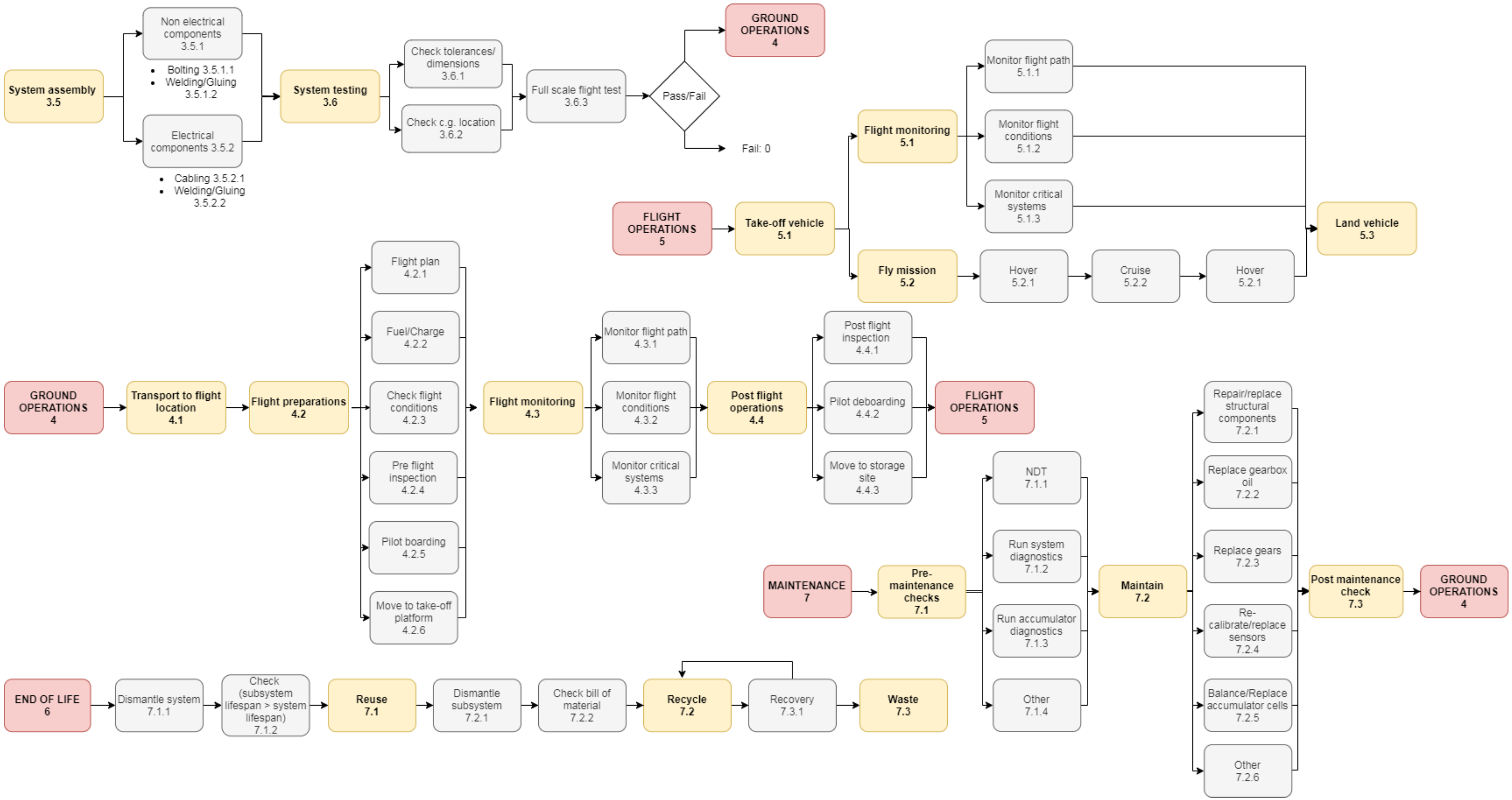

Figure B.1: MAI-plan and Operations & Logistics Concept Description

C

Functional Flow Diagram

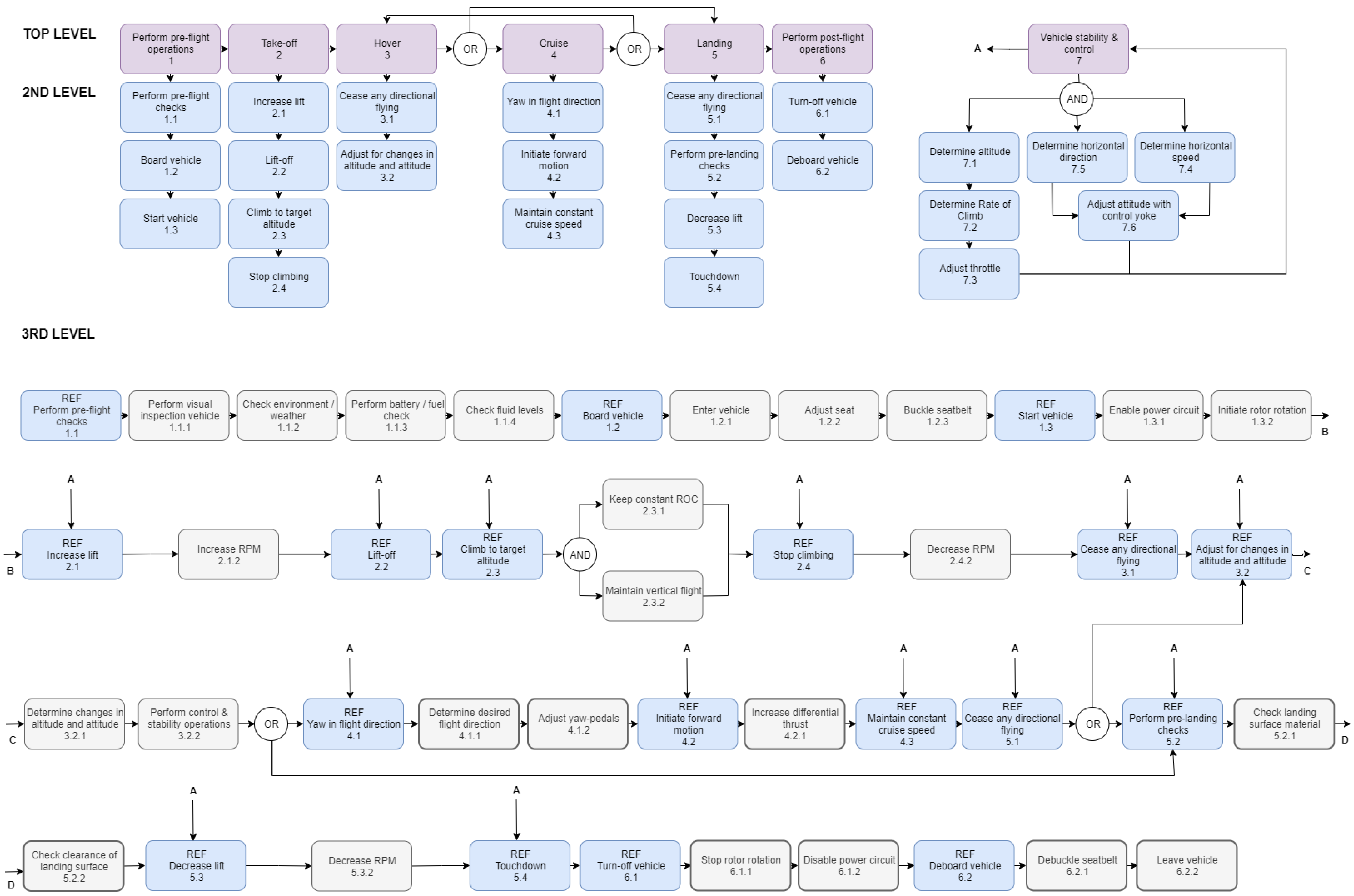

Figure C.1: Functional Flow Diagram.

D

Functional Breakdown Structure

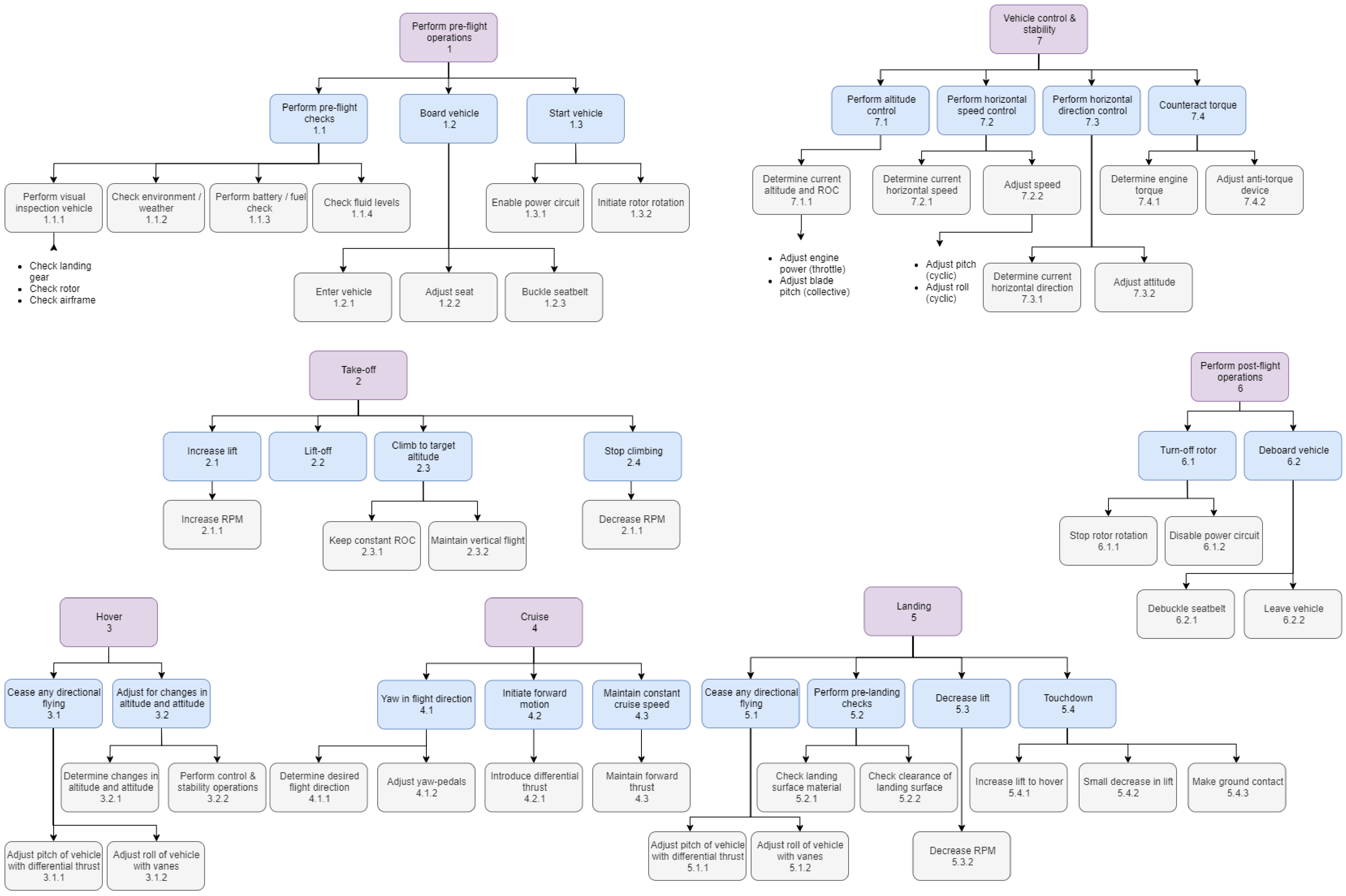

Figure D.1: Functional Breakdown Structure.

E

Three-view drawing

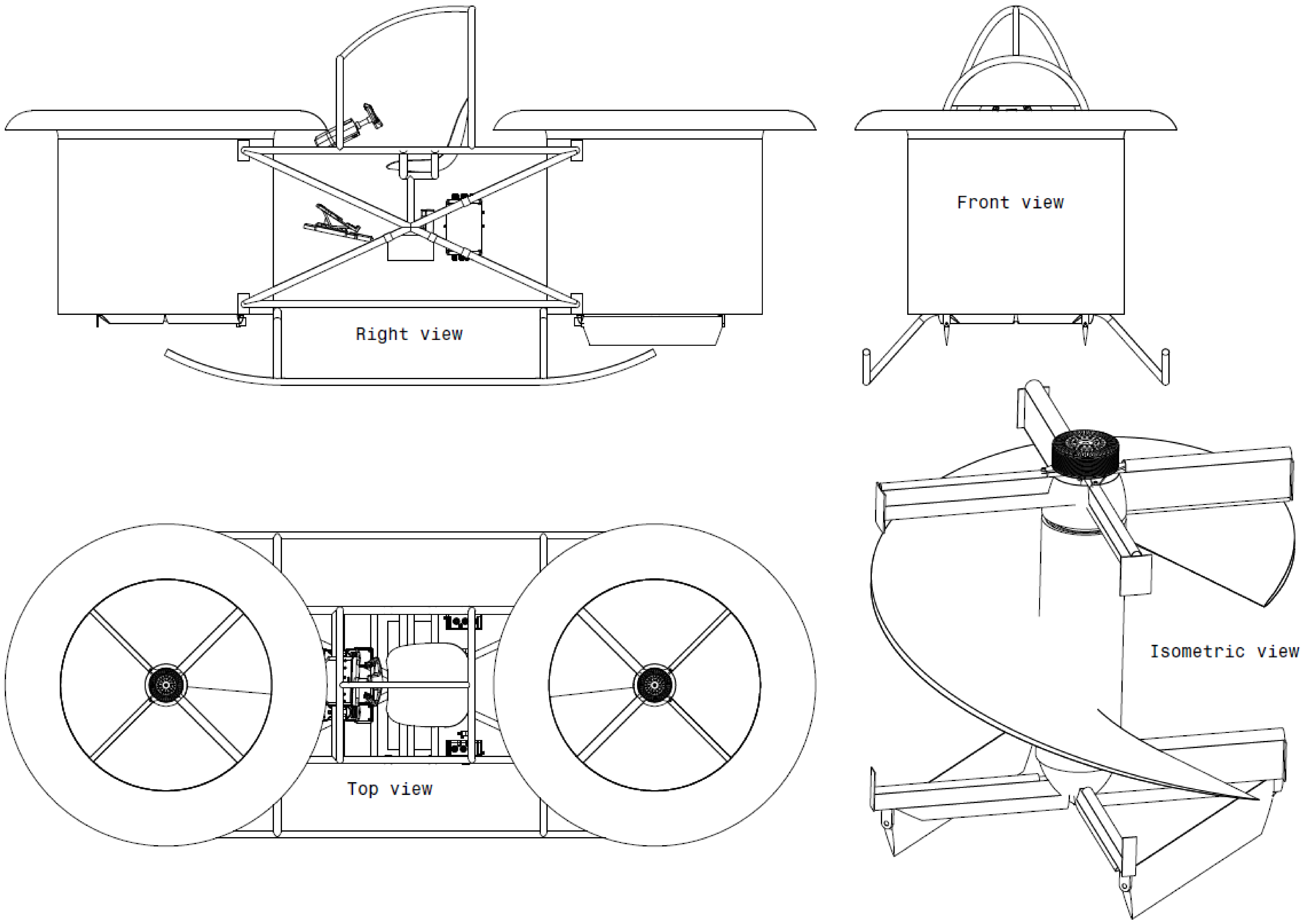

Figure E.1: Three-view drawing of the Solidity-1